Efficient measurement and data inversion strategies for large scale geoelectric surveys

A dissertation submitted to the
SWISS FEDERAL INSTITUTE OF TECHNOLOGY ZÜRICH
for the degree of

Doctor of Sciences

presented by

MARK BLOME

Diplom-Geophysiker (Dipl. Geophys.)
University of Göttingen (Germany)
born April 15, 1977
citizen of Germany

accepted on the recommendation of

Prof. Dr. Alan G. Green, examiner
Prof. Dr. Hansruedi Maurer, co-examiner
Prof. Dr. Stewart Greenhalgh, co-examiner
Prof. Dr. Andreas Weller, co-examiner

2009

Dedicated to Michel

But, sure, the sky is big, I said;
Miles and miles above my head;
So here upon my back I'll lie
And look my fill into the sky.
And so I looked, and, after all,
The sky was not so very tall.
The sky, I said, must somewhere stop,
And – sure enough! – I see the top!
The sky, I thought, is not so grand;
I 'most could touch it with my hand!
And reaching up my hand to try,
I screamed to feel it touch the sky.
I screamed, and – lo! – Infinity
Came down and settled over me;
Forced back my scream into my chest,
Bent back my arm upon my breast,
And, pressing of the Undefined
The definition on my mind.

excerpt from "Renascence"
Edna St. Vincent Millay (1892 – 1950)

Contents

Zusammenfassung

In den letzten zwei Jahrzehnten hat die Bedeutung der Geoelektrik in einer Vielzahl ingenieur- und umweltwissenschaftlicher Fragestellungen zur Untersuchung des oberflächennahen Untergrundes stark zugenommen. Der Erfolg der Geoelektrik kann weitestgehend auf die Verfügbarkeit (i) moderner Multielektrodeninstrumente, (ii) effizienter zwei- und dreidimensionaler Inversionsprogramme sowie auf (iii) vor kurzem vorgestellte neuartige Techniken zur Optimierung von Meßstrategien zurückgeführt werden. Obwohl die Forschung in den drei genannten Gebieten erstaunliche Fortschritte erzielt hat, gibt es noch erheblichen Weiterentwicklungsbedarf. Dies ist vor allem an der Tatsache erkennbar, dass trotz des Einsatzes hochmoderner Aufzeichnungs- und Modellierungstechniken die Messung und Verarbeitung großer geoelektrischer (3D) Datensätze immer noch sehr anspruchsvoll und aufwendig ist.

Parallele Datenakquisitionen, bei denen zwei Elektroden als Stromquelle beziehungsweise -senke dienen und alle übrigen Elektroden Potentialdifferenzen bezüglich einer Referenzelektrode messen, haben sich als sehr erfolgreiche Option zur Beschleunigung geoelektrischer Messungen erwiesen. Aufbauend auf einem zuvor am Institut für Geophysik an der ETH Zürich entwickelten und konstruierten experimentellen Meßsystem (*ETH-DCMES*) wurde im Rahmen dieser Doktorarbeit ein neues intelligentes Multielektroden-Meßsystem entwickelt. Dieses ermöglicht im Vergleich zur vorhergehenden Apperatur die parallele Aufzeichnung geoelektrischer Meßdaten in einer sehr viel effizienteren Art und Weise. Die dazu notwendigen Modifikationen und Neuentwicklungen betrafen in der Hauptsache die verwendeten Datenlogger (im Folgenden als "DAUs" bezeichnet). Diese wurden so modifiziert, dass aufgezeichnete Potenzial-Wellenformen direkt auf ihnen analysiert werden können. Damit entfällt das zeitaufwendige Übertragen der Wellenformen von den DAUs über den digitalen Datenbus auf den Feldcomputer. Um den Einsatz des Meßsystems in schwer zugänglichen Gebieten zu ermöglichen, wurde die zuvor verwendete sperrige und schwere Stromquelle (einschliesslich der von ihr benötigten Spannungsversorgung) durch eine neu entwickelte, kompakte und batteriegespeiste Stromquelle ersetzt. Zusätzlich wurden zur allgemeinen Verbesserung der Robustheit und Flexibilität der Meßapparatur weitere technische Modifikationen umgesetzt. Neben den Verbesserungen an der Hardware wurden die verwendeten Meßprozeduren optimiert sowie eine flexible und einfach zu verwendende Meßsoftware implementiert. Letztere ermöglicht das

Ansteuern der Meßapperatur auch von Nicht-Fachleuten.

Innerhalb dieser Arbeit wurde ein neues 2.5D/3D Tomographieprogramm entwickelt, das im Vergleich zu den in der geoelektrischen Literatur publizierten Algorithmen einige Neuentwicklungen beinhaltet. Der eingesetzte Vorwärts-Löser basiert auf der Finite-Element-Technik und verwendet unstrukturierte Gitter, die es erlauben, beliebige Topographien in der Modellierung zu berücksichtigen. Eine neuartige Technik zur Beseitigung der in den geoelektrischen Lösungen auftauchenden Singularitäten wurde entwickelt. Diese basiert auf einer schnellen Multipol-Randelementmethode und ermöglicht die Beseitigung der Singularitäten für Modellgeometrien mit signifikanter Topographie. Um die Unzulänglichkeiten klassischer Randbedingungen zu umgehen und gleichzeitig Artefakte, die durch die künstlichen Ränder des Rechengebietes entstehen, zu vermeiden, kamen sogenannte Infinite Elemente zum Einsatz. Diese erlauben effektiv eine Verschiebung der Ränder des Rechengebietes ins "Unendliche", wo der Betrag des Potentials als verschwindend angenommen werden kann. Die Inversions-Prozeduren wurden im Hinblick auf sehr große Datensätze optimiert. Dies wurde durch eine sequentielle Akkumulierung der Normalengleichung innerhalb der jeweiligen Iterationen des Gauss-Newton Lösers realisiert. Der einzig limitierende Faktor bezüglich des Hauptspeichergebrauchs während einer Dateninversion ist damit die Anzahl der verwendeten Modellparameter. Um eine optimierte (d.h. auf die Auflösungsfähigkeit des zu invertierenden Datensatzes angepasste) Modellparametrisierung zu erhalten, werden die finiten Elemente der Vorwärtsdiskretisierung in Cluster gruppiert. Zwei verschiedene Algorithmen, die ein derartiges Clustering auf 2D/3D Diskretisierungen erlauben, wurden entwickelt. Die Performanz des tomographischen Inversionsprogramms wurde erfolgreich anhand von synthetischen und gemessenen 2D und 3D Datensätzen getestet.

Neuere in der geoelektrischen Literatur publizierte Weiterentwicklungen in der sequentiellen Optimierung von Meßstrategien haben vielversprechende Ergebnisse erbracht. Es hat sich jedoch herausgestellt, dass die sequentielle Optimierung von Meßstrategien für geoelektrische Feldstudien mit mehr als 50 Elektroden nicht effizient genug ist. Zudem benötigen die vorgestellten Verfahren a priori Informationen über die Leitfähigkeitsverteilung des Untergrundes und berücksichtigen weder Datenfehler noch die Möglichkeit moderner Meßapparaturen, Daten parallel aufzuzeichnen. Aus diesen Gründen habe ich eine neue Optimierungsstrategie entwickelt, die (bezogen auf die lineare Unabhängigkeit einzelner Meßkonfigurationen zueinander) auf dem Konzept von vollständigen bzw. Basis- Datensätzen beruht. Aus diesen Basisdatensätzen können durch lineare Superposition Meßwerte zu beliebigen Elektrodenkonfigurationen synthetisiert werden. Dies erlaubt die Rekonstruktion sogenannter "umfassender" Datensätze, die verbesserte Tomographieergebnisse liefern. Notwendig für die vorgestellte Strategie ist lediglich die Aufzeichnung von Basisdatensätzen, die in der Regel eine recht kleine Anzahl an Messungen umfassen und daher effizient gemessen werden können. Unter der Annahme einer

rauschfreien Datenaufzeichnung lassen sich diese Datenrekonstruktionen ohne weiteres auf sowohl Vier- ("bipole-bipole") als auch Drei-Punkt ("pole-bipole") Elektrodendatensätze anwenden. Unter Berücksichtigung realistischer Datenfehler führen rekonstruierte Vier-Punkt Messungen jedoch – wie zu erwarten ist – zu instabilen Ergebnissen, hervorgerufen durch den Prozess der Superposition, der in diesem Fall bis zu sechs Einzelmessungen umfasst. Im Gegensatz dazu konnte gezeigt werden, dass die Rekonstruktion von umfassenden Drei-Punkt (pole-bipole) Datensätzen aus verrauschten Drei-Punkt Basisdatensätzen sinnvoll ist, da für eine derartige Rekonstruktion lediglich je zwei Meßwerte des Basisdatensatzes linear kombiniert werden. Die Zweckmäßigkeit dieser polebipole Datenrekonstruktionen konnte anhand von Tomographie-Ergebnissen basierend auf synthetischen und gemessenen Datensätzen erwiesen werden.

Zusammengenommen erlauben die instrumentellen Weiterentwicklungen, die neuartigen Modellierungs- und Inversionsalgorithmen sowie die neue Meßstrategie eine schnelle und effiziente Aufzeichnung und Verarbeitung sehr großer Meßdatensätze. Im Besonderen können die für die Meßstrategie verwendeten vollständigen Datensätze mit voll parallelisierten Meßsystemen (wie die *ETH-DCMES-II* eines darstellt) sehr effizient aufgezeichnet werden. Die aus den Datenrekonstruktionen resultierenden sehr großen Datensätze können mit Hilfe des neuen Tomographieprogramms effektiv invertiert werden. Es ist vor allem die Kombination der hier vorgestellten Weiterentwicklungen, die einen konstruktiven Beitrag hin zur routinemäßigen Anwendung großskaliger geoelektrischer 3D-Feldmessungen leistet.

Abstract

Over the past two decades the geoelectric method has played an increasingly important role in a wide range of engineering and environmental applications related to the characterization of the shallow subsurface. The success of the method can be attributed to the availability of (i) fast multi-electrode data acquisition systems, (ii) efficient 2D and 3D resistivity inversion programs and (iii) recently proposed novel experimental design techniques. Remarkable developments in all these three aspects have been reported, but there is still a need for further improvements – even with state-of-the-art technology it is still a challenging task to acquire and process large-scale 3D data sets.

A powerful option for speeding up geoelectric data acquisition is that of parallel measurements, whereby two electrodes act as current source and sink, another electrode is employed as a reference potential and all the remaining electrodes measure the voltage differences with respect to the reference electrode. Building on an earlier experimental system designed and constructed in the Institute of Geophysics at ETH Zürich (*ETH-DCMES*) a new, smart multi-electrode acquisition system has been developed (*ETH-DCMES-II*) as part of this thesis research. It allows the parallel data collection task to be performed in a superior and more efficient manner. The most important modification concerns the individual data acquisition units ("DAUs"). They were modified such that the voltage waveforms recorded can be analyzed directly on the DAUs, which avoids the time-consuming download of the voltage waveforms over the serial data bus to the central computer. To allow the data acquisition system to be employed in rugged or difficult terrains not accessible by vehicles, the original bulky current source and its power supply were replaced by a newly developed light-weight and battery-driven source. Additionally, several other technical improvements have been realized to increase the overall system robustness and flexibility, as well as to ease the field handling. Besides improving the acquisition hardware, the measurement procedures were optimized. Finally, versatile and easy-to-use controlling-user software was written, that allows non-specialists to operate the system. With all these modifications *ETH-DCMES-II* is now ready to be employed in large-scale 3D surveys including roll-along strategies.

A new 2.5D/3D tomographic inversion program has been developed that includes

several significant improvements over the algorithms presented in the recent literature. My numerical forward modeling scheme is based on a finite element approach using unstructured domain discretizations, which allows arbitrary topography to be easily incorporated. A novel singularity removal scheme, based on a multi-pole boundary element method, was developed that facilitates application of the singularity removal technique also in the presence of significant topography. To suppress artifacts from the artificial ground boundaries at the edge of the finite computational mesh, and overcome the limitations of conventional mixed boundary conditions, an infinite element scheme was implemented. It effectively places the artificial boundaries at infinity where the potential can be taken to be zero. The inversion procedure was optimized to allow very large data sets to be inverted. This was achieved by sequentially accumulating the normal equations during each iteration of the Gauss-Newton inverse solver. The only limiting constraint in terms of computer memory is the number of model parameters. Therefore, two novel clustering algorithms were developed that allow the finite element blocks to be merged (clustered) into larger inversion blocks without degrading the actual resolution capabilities of the data. The overall performance of the tomographic inversion program was successfully tested on synthetic and observed 2D and 3D data sets.

Recent developments reported in the literature of sequential experimental design for identifying optimized sets of electrode configurations have shown promising results, but are inadequate for geoelectric experiments involving more than 50 electrodes. Furthermore, available experimental design procedures rely on an à priori subsurface model and consider neither data errors nor parallelized recording capabilities. I have developed a new experimental design strategy that is based on complete or basis data sets in terms of linear independence, from which all other electrode configurations can be reconstructed by superposition. This yields comprehensive data sets which offer not only some degree of redundancy but also improved inversion capability. The strategy requires only that complete data sets be measured (not the comprehensive data set), which are usually quite small. For noise-free data, this scheme is applicable to both four-point (bipole-bipole) and three-point (pole-bipole) data sets. In the presence of noise, reconstructing four-point configurations leads to unstable results, caused by large errors accumulating during the superposition procedure (involving the algebraic addition of up to 6 basis configurations). By contrast, reconstruction of a comprehensive three-point data set from an error-contaminated three-point complete data set is successful because it involves the addition of only two basis configurations. The usefulness of inverting reconstructed three-point data sets is demonstrated with both synthetic and observed (field) data.

The instrumental developments, the new modeling and inversion procedures and the novel experimental design approach allow very large data sets to be acquired and processed quickly. In particular, the complete data sets required for the new experimental design scheme can be recorded very efficiently with fully parallelized systems such as

ETH-DCMES-II. Furthermore, the very large data sets resulting from the reconstructions can be handled efficiently by the new tomographic inversion program. Combined application of all these developments is judged to be an important step towards routine application of large-scale 3D geoelectric field surveys.

Chapter 1

Introduction

Detailed knowledge of the shallow subsurface is critical in a broad range of areas including mineral exploration, geotechnical, hydrogeological and environmental investigations. Among all the geophysical methods, electrical and electromagnetic (EM) techniques are particularly useful for delineating and characterizing subsurface structures, because the electrical properties of subsurface soils and rocks vary over a broad range.

Suitable geophysical methods for determining the subsurface resistivity distribution can be classified by their frequency of operation and by the nature of the source signal. Active methods utilize controlled sources with frequencies in the range of DC to a few Hz for direct current resistivity methods (hereafter referred as geoelectrical methods) to several kilohertz for inductive EM methods, to hundreds of MHz for ground-penetrating radar. Passive EM methods use fields generated by natural phenomena (e.g. telluric currents, self potentials) or man-made transmitters (e.g., radiomagnetotellurics).

In geoelectrical methods, DC to low-frequency (< 10 Hz) alternating currents are injected into the ground through a pair of point electrodes and potential differences are measured between another pair of electrodes. The resulting potential differences provide information about the subsurface resistivity structures. Bulk resistivities of earth materials relevant to environmental investigations can vary over many decades (Figure 1.1). This is in striking contrast to other physical properties such as seismic velocities, densities, and relative permittivities, which may vary from a few percent to a factor of 10 (e.g. Keller and Frischknecht, 1966).

The main conduction mechanism in earth materials is electrolytic, involving ion transport by dissolved salts distributed through a complex structure of interconnected pores and fractures. Resistivities of igneous and metamorphic rocks are typically high and largely depend on their porosity and permeability (i.e. their degree of fracturing). Sedimentary rocks are usually much more conductive than igneous rocks. Their resistivity is mainly controlled by the amount of water present, the salinity (free ions) of the water, and the degree of interconnections between the pores. Clay content can also contribute by providing an additional surface conductivity mechanism. Though often

ignored in geoelectrical investigations, macroscopic anisotropy of sedimentary rocks may occur due to small-scale petrophysical variations (e.g. variations in grain size and pore space geometry) (Anderson *et al.*, 1994).
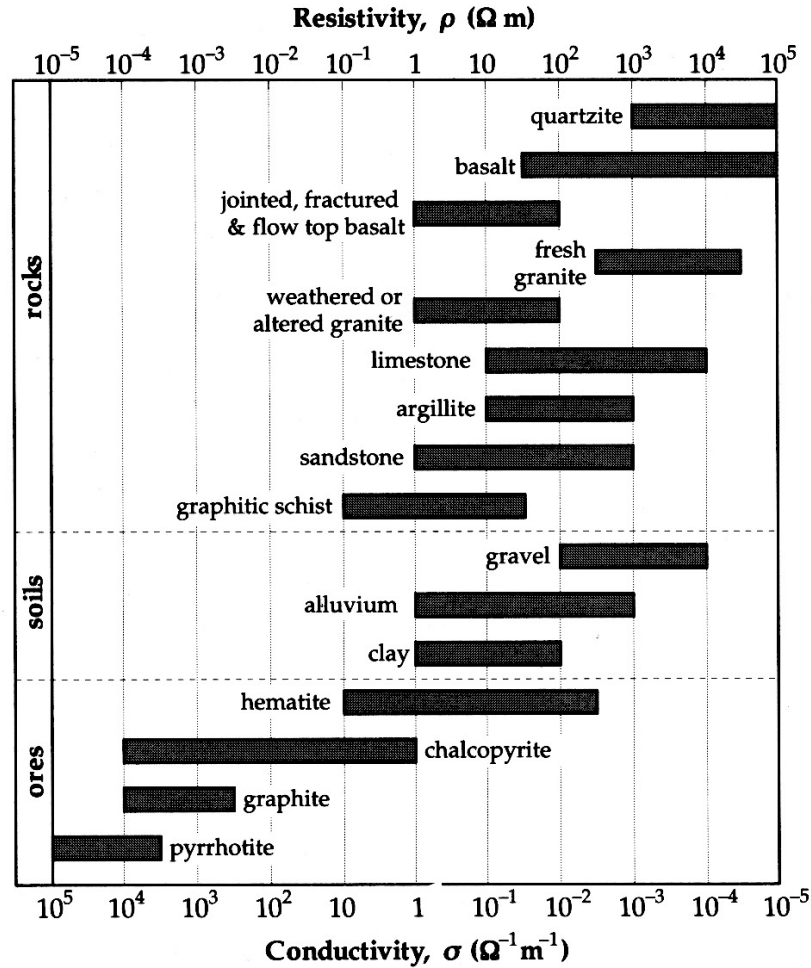
Figure 1.1 – Typical range of electrical resistivities / conductivities of earth materials (after Ward, 1990).

Until the late 1980s, geoelectrical imaging techniques suffered from laborious data collection procedures and highly limited data processing and interpretation schemes. Geoelectrical surveys were either limited to simple 2D profiling (or areal mappings in 3D) or vertical electrical soundings, using standard electrode arrays. For geoelectrical profiling, a fixed configuration of injecting and measuring electrodes was moved over the investigation area. This allowed maps of apparent resistivities to be produced, with which lateral variations within a certain depth range could be delineated (e.g. Knödel *et al.*, 1997). The depth range was determined by the fixed electrode spacing used.

Vertical electrical sounding techniques trace back to the pioneering work by Conrad Schlumberger in 1912 in Europe and, approximately at the same time, by Wenner in the USA (Schlumberger, 1920; Kunetz, 1966). The method exploits the fact that the depth of current penetration into the ground is usually proportional to the source electrode

separation (Gish and Rooney, 1925). Varying the current electrode spacing therefore provides information about changes of resistivities with depth. Interpretation of vertical sounding data results in one-dimensional (1D) subsurface models (Stefanescu *et al.*, 1930; Langer, 1933). Prior to the availability of computer based interpretation techniques in the 1970s (e.g. Gosh, 1971), 1D data interpretations were usually carried out in a trial and error fashion using model curve matching.

Obtaining 2D or 3D subsurface images by combining mapping and vertical electrical sounding techniques is problematic and often impossible, because of the non-linear (model-dependent) current flow patterns. In the past, often a few vertical electric soundings were carried out prior to an areal mapping survey to estimate appropriate electrode spacings (e.g. Zhody *et al.*, 1973), but this did not allow reliable 2D or 3D resistivity models to be established.

With the rapidly emerging 2D and 3D imaging capabilities of the seismic method (e.g. Yilmaz, 2001) and because of the instrumental and interpretational limitations discussed above, the geoelectrical method lost popularity and stagnated until the mid 1980s. This changed drastically with the introduction of two new developments, namely the introduction of multi-electrode arrays (e.g. Griffiths and Turnbull, 1985; Griffiths *et al.*, 1990) and the availability of commercial 2D and 3D tomographic inversion algorithms (e.g. Loke and Barker, 1996b,a). These developments largely eliminated the most severe deficiencies and resulted in a renaissance of the geoelectric method such that it is today the method of choice for many near-surface (uppermost 100 m) applications (e.g. Binley *et al.*, 1997; Van *et al.*, 1991; Olivar *et al.*, 1995; Buselli and Lu, 2001; Yaramanci, 2000; Weller *et al.*, 2000; Slater and Reeve, 2002).

1.1   Multi-electrode data acquisition systems

One of the main advantages of the geoelectrical method is the conceptually simple field equipment required for surveying. Figure 1.2 shows a basic resistivity measurement set-up, as it was commonly employed prior to the introduction of multi-electrode systems. The basic equipment consists of a current source (e.g. a battery pack), a sensitive voltmeter to measure the voltage response of the subsurface, metal stakes (electrodes) and cables to connect the electrodes to the source and the voltmeter. Instead of a pure direct current source, like a battery pack, low-frequency square-wave (commutated DC) or sinusoidal alternating source signals are commonly employed to suppress the effect of electrode polarizations and natural or artificial SP currents fluctuating in the subsurface (Christensen, 1989). Typical frequencies are usually in the few Hz range to avoid electromagnetic coupling of the injecting electrodes with the wires connecting them to the resistivity instrument. Also, the theory of the resistivity method is based on direct current and at frequencies above (say) 10 Hz inductive effects would have to
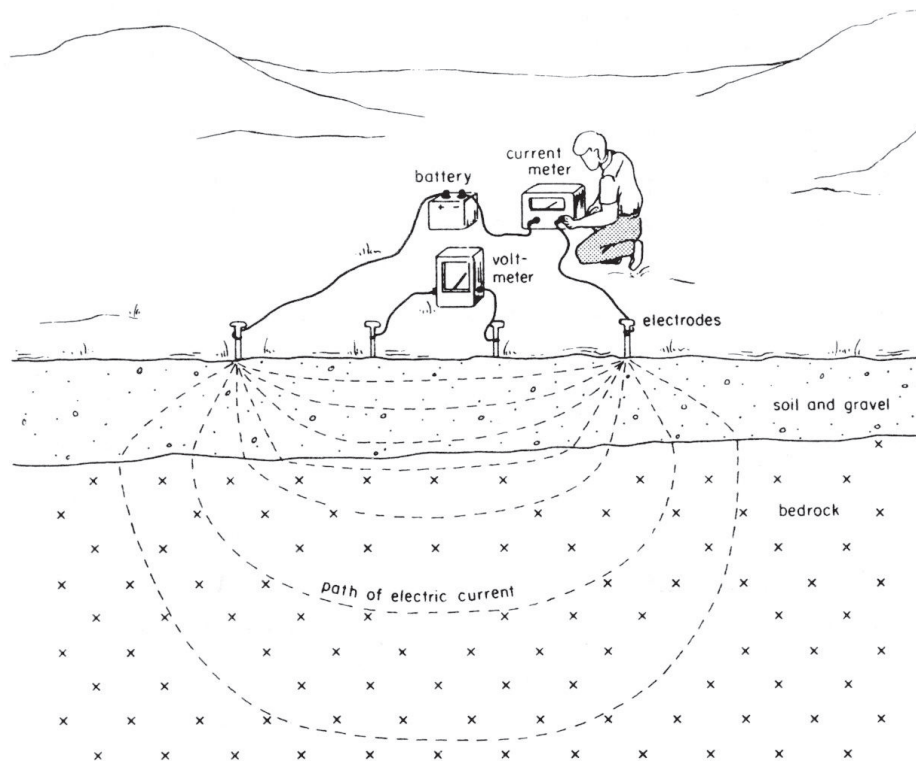
Figure 1.2 – Basic set-up for DC-resistivity measurements using four electrodes (after Robinson and Coruh, 1988).

be taken into account. The voltmeter used to measure the voltage signals must have a high input impedance ($> 10\ M\Omega$) and should be equipped with notch filters for 50Hz power-line rejection (Knödel *et al.*, 1997). To estimate resistance values, it is necessary to precisely measure the amplitudes of the source signal injected into the ground.

Manual data acquisition with four metal stakes, as displayed in Figure 1.2, requires the electrodes to be placed in the ground and moved manually for each consecutive measurement. This time-consuming and thus expensive approach is impractical for 2D and 3D field surveys. This motivated the development of multi-electrode systems, with which many different measurements can be performed in an automated fashion. The first multi-electrode systems, proposed in the early 1980s, required manual switching of the electrode configurations (Barker, 1989). Due to the rapidly evolving electronics industry and inspired by research in medical resistivity imaging, microprocessor-controlled systems with automatic quality control soon became available (e.g. Dahlin, 1989).

The different systems proposed (see Stummer *et al.*, 2002, for a more extensive discussion) can be subdivided into two main categories – centralized and distributed systems. Centralized multi-electrode systems employ a central unit that houses most or all of the system electronics and which may be controlled by an external field computer. Analog voltage signals measured at groups of electrodes (usually 20 or more) are transmitted through multi-core cables to the central unit where analog-to-digital conversion takes

place. The central unit contains a multiplexer and a relay switching component that allows arbitrary electrode configurations to be measured.

Centralized multi-electrode systems are usually low-cost, robust and easy to handle in the field. However, their heavy and expensive multicore-cables carry source and measured signals at the same time, which may lead to cross-talk (EM pickup) along the wires unless adequate shielding is provided. Furthermore, the system is susceptible to ambient electromagnetic noise due to the overall length of the cables employed. Though centralized multi-electrode systems are in principle capable of acquiring arbitrary electrode-configurations, most systems (and their controlling software) continue to be based on classical electrode configurations (e.g., Wenner, Schlumberger, etc.). Finally, the number of channels of centralized systems is generally limited to a few tens, thereby limiting the acquisition speed in parallel recording mode.

Popular commercial instruments that follow the centralized system design are the Syscal Switch-24/Switch-48 (Iris Instruments, France), the *GeoTom Res/IP* (GeoLog-2000, Germany) and the *GMS 125A/150* (GeoSys, Germany). Some systems, for example the *SAS 4000 Lund* (ABEM Instrument AB, Sweden) and the *Tomoplex* (Campus Ltd., United Kingdom), provide parallel measurement capabilities through an analog multiplexer in combination with a single or by a number of parallel A/D converters. Recently, *FlashRes*, a fully parallel system that allows swift data acquisition on up to 64 independent channels, was presented by Zhe *et al.* (2007). It is now being daisy-chained into several hundred channels.

Distributed systems employ "smart" or active electrodes (see Figure 1.3). These electrodes are equipped with data acquisition units ("DAUs") that contain switching relays and may also contain an A/D converter and a microprocessor. Communication between the field computer and the DAUs is implemented using a digital data bus. Those systems with A/D converters and microprocessors in the DAUs allow the measured voltage signals to be transferred digitally to the central processing unit, thereby reducing noise-pickup along the cables. An advantage of distributed systems is that they can be operated with cables including only a few wires, which are less susceptible to cross-talk (compared with the multi-core cables required for centralized systems). Furthermore, they offer more flexibility in terms of expandability. Disadvantages, compared with centralized systems, include the higher costs and their lack of suitability for use in cross-borehole surveys or borehole-to-surface measurements, because the smart electrodes cannot be placed in the corrosive and restricted confines of a narrow fluid-filled borehole.

An example of a distributed system without A/D converters in the DAUs is the *RESECS* multi-electrode array offered by the German company DMT. A commercially available fully distributed system with A/D converters and microprocessors in the DAUs is the *SIP-256* system from the "Deutsche Arbeitsgemeinschaft für SIP-Anwendungen". It supports up to 256 electrodes and allows acquisition of induced polarization data.
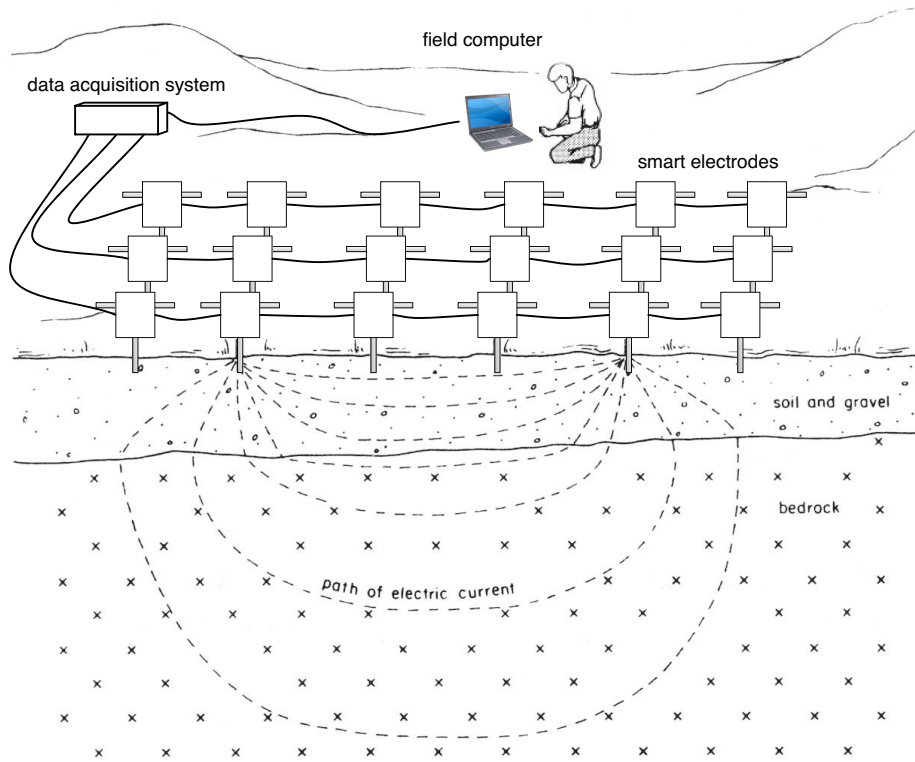
Figure 1.3 – Basic set-up for DC-resistivity measurements using a modern fully distributed data acquisition system (modified after Robinson and Coruh, 1988)

However, it lacks the ability to select separately the operational modes of the individual electrodes. Stummer *et al.* (2002) presented a fully distributed data acquisition system ("*ETH-DCMES*") with arbitrary switching capabilities and support for parallel data acquisitions with a very large number of electrodes. The system was designed for 3D real-time experimental design involving a large number (several hundreds) of surface electrodes.

Conceptually, the *ETH-DCMES* system, proposed by Stummer *et al.* (2002), included all the necessary features for efficient 3D data acquisition, but field tests revealed a number of shortcomings that limited the practicality of the system. In particular, the serial transfer from the individual DAUs to the central computer slowed down the data acquisition significantly. Furthermore, the entire system was very bulky and heavy, such that it was not usable in remote areas. Finally, the system suffered from several minor technical problems that precluded smooth data acquisition.

1.2   2D and 3D modeling and inversion techniques

The multi-electrode systems proposed in the early 1980s allowed efficient acquisition of geoelectrical data sets that could be suitable for constraining 2D or even 3D subsurface structures. This required new data analysis tools that went beyond the qualitative inter-
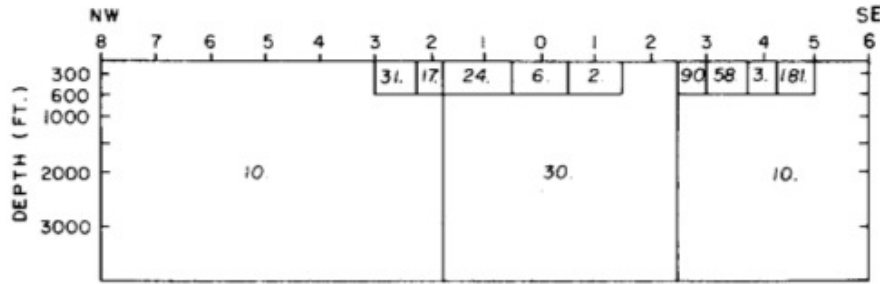
Figure 1.4 – Example tomogram result obtained by the first 2D geoelectric inversion approach reported in the literature (Tripp *et al.*, 1984). The inversion procedure required a pre-defined model geometry with a few model cells whose resistivity values were varied.

pretation of geoelectrical mapping and curve matching approaches employed for vertical electrical soundings. For data sets collected along profiles, pseudo-sections (e.g. Hallof, 1957) offered limited 2D interpretation opportunities, but they were clearly inadequate for investigating complex subsurface structures, as typically found in the uppermost 100m.

With the increasing popularity of digital computers, interactive modeling to fit, by trial and error, the observed resistivity profiles and soundings were first attempted with only limited success. What was needed were automatic methods for adjusting the model parameters. Tomographic inversions were considered as a possible tool for this purpose. Tripp *et al.* (1984) developed one of the first non-linear 2D inversion techniques based on a transmission surface analogy for the forward response (Pelton *et al.*, 1978). Their inversion procedure required a pre-determined model geometry with a few cells whose resistivity values were varied during the inversion process to match the measured and predicted data. The resulting tomograms represented very crude approximations to the true subsurface resistivity structure (Figure 1.4). Furthermore, a trial-and-error process was required to find appropriate model geometries. These procedures were time-consuming, difficult to implement and to apply, and were likely influenced by subjective judgments.

The first three-dimensional inversion schemes were published by Park and Van (1991); Ellis and Oldenburg (1994); Zhang *et al.* (1995). These algorithms received a lot of attention among the specialists, but it was the commercial software packages RES2DINV/ RES3DINV (Loke and Barker, 1996b,a) that made tomographic inversions popular to a wider audience. To date, there exist several commercial and non-commercial tomographic inversion codes which allow non-specialists to perform 2D and 3D inversions. The most recent example is the open source package presented in (Günther *et al.*, 2006) (see also Figure 1.5).

Since the publication of the early tomographic inversion programs, many significant technical improvements have been achieved. Most of them are concerned with the nu-
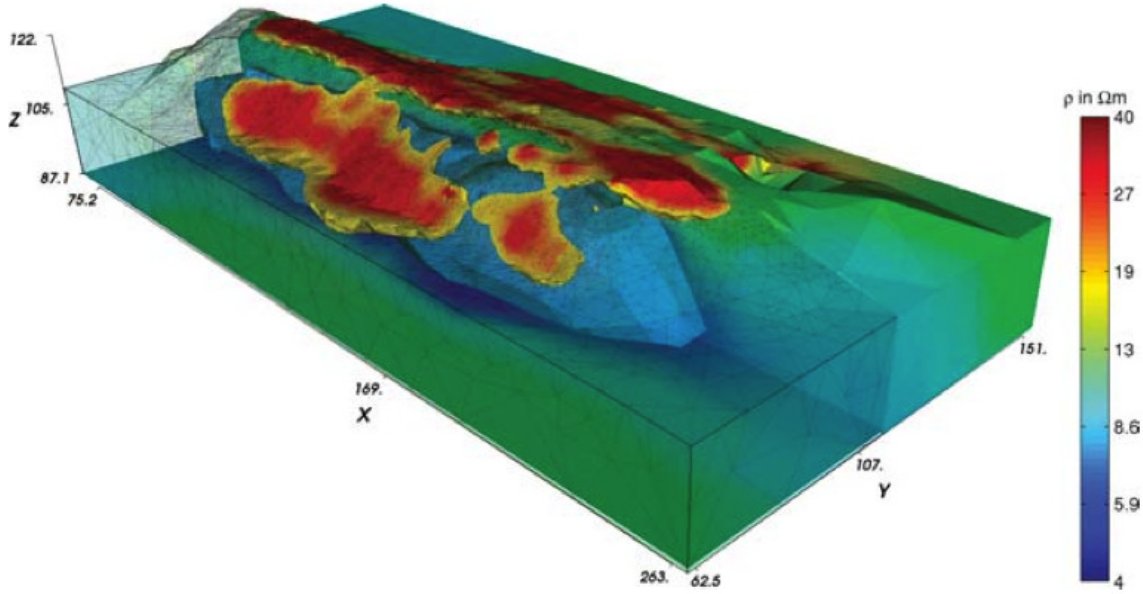
Figure 1.5 – 3D inversion result from a buried waste site including slag material from steel production (from Günther *et al.*, 2006). The dump material is characterized by low resistivities (blue) and the more resistive material (red) may be indicative for hardpan development.

merical modeling algorithms that are required to predict the geoelectrical response for a given resistivity model. The majority of the early inversion codes were based on finite difference modeling algorithms (Dey and Morrison, 1979b,a; Spitzer, 1995; Weller *et al.*, 1996). These techniques relied on structured grids, which could be computationally wasteful and made implementation for an arbitrary surface topography very difficult. Moreover the grid had to be very dense surrounding the source. These disadvantages could be largely overcome with finite element algorithms as proposed by Coggon (1971); Pridmore *et al.* (1981); Sasaki (1994); Zhou and Greenhalgh (2001); Li and Spitzer (2002); Pain *et al.* (2002); Günther *et al.* (2006). Another technique proposed is the boundary element method that is suitable for a modeling domain with arbitrary topography, but with a very simple structure within the domain (Hvozdara and Kaikkonen, 1998; Xu *et al.*, 1998; Ma, 2002; Xu *et al.*, 1998).

Recently, Zhou *et al.* (2009) presented a novel 2.5D/3D forward solver based on Gaussian quadrature grids. The method is similar to the spectral element method (Patera, 1984) but does not require an element mesh. Further, recent developments with regard to numerical forward modeling of geoelectrical data concern the incorporation of anisotropy (Herwanger *et al.*, 2004; Pain *et al.*, 2003; Li and Spitzer, 2005; Zhou *et al.*, 2009; Greenhalgh *et al.*, 2009).

The (numerical) singularity at the current injection point(s) is a problem for which the finite difference method in particular, and to a lesser extent, the finite element method suffer. Lowry *et al.* (1989) and Zhao and Yedlin (1996) proposed singularity removal techniques, with which this problem could be reduced significantly. However,

application of this technique required calculation of the electrical potential for a homogenous subsurface model to be known analytically, which is not possible in the presence of topography.

Another problem that turned out to be problematic concerns the artificial ground boundaries. They have to be applied for keeping the dimension of the numerical model finite. Popular choices include Dirichelet or mixed-boundary conditions (Dey and Morrison, 1979a), but their performance has proven to be not optimal when the electrical potentials were still significant near the artificial ground boundaries.

1.3 Experimental design

The developments of efficient multi-electrode arrays together with advances in modeling and inversion techniques have given the geoelectrical method a massive boost in capability and popularity. However, there was a persistent inadequacy in the methodology that prevented the full potential of this geophysical technique from being fully exploited. Although modern multi-electrode arrays allow arbitrary electrode configurations to be measured, the vast majority of the studies found in the literature employ only traditional configurations such as Wenner, dipole-dipole, or Schlumberger. These configurations were originally developed to allow efficient data acquisition with simple four electrode systems, but it remained unclear if these configurations are optimal in the sense of the data information content offered to 2D and/or 3D inversion algorithms.

The initial approaches to quantifying the resolving power of electrode configurations were based on sensitivity studies. Sensitivities describe changes in the geoelectrical data for a given electrode configuration caused by a small perturbation of the resistivity model. If the changes of the data are small, this implies that they do not offer significant information for constraining the perturbed subsurface region. Evjen (1938) studied analytical sensitivities based on 1D layered models to assess the influence of model parameters on individual measurements. His research led to the definition of depth of investigation that was used to judge the vertical resolution of individual electrode configurations (Roy and Apparao, 1971; Roy, 1972, 1978).

With the advent of 2D and 3D investigations, sensitivity computations for arbitrary subsurface structures and arbitrary electrode configurations were required. Barker (1979) made the first attempt with sensitivity studies in 2D, but only in an approximate way (it was based on updating from a homogeneous model). McGillivray and Oldenburg (1990); Spitzer (1998); Zhou and Greenhalgh (1999) and Greenhalgh *et al.* (2009) presented efficient schemes for computing general 2.5D and 3D sensitivities. Examples of sensitivity patterns for different electrode configurations are shown in Figure 1.6.

Large sensitivities are a necessary but not sufficient requirement for obtaining reliable subsurface images. The individual sensitivity patterns obtained for the various electrode
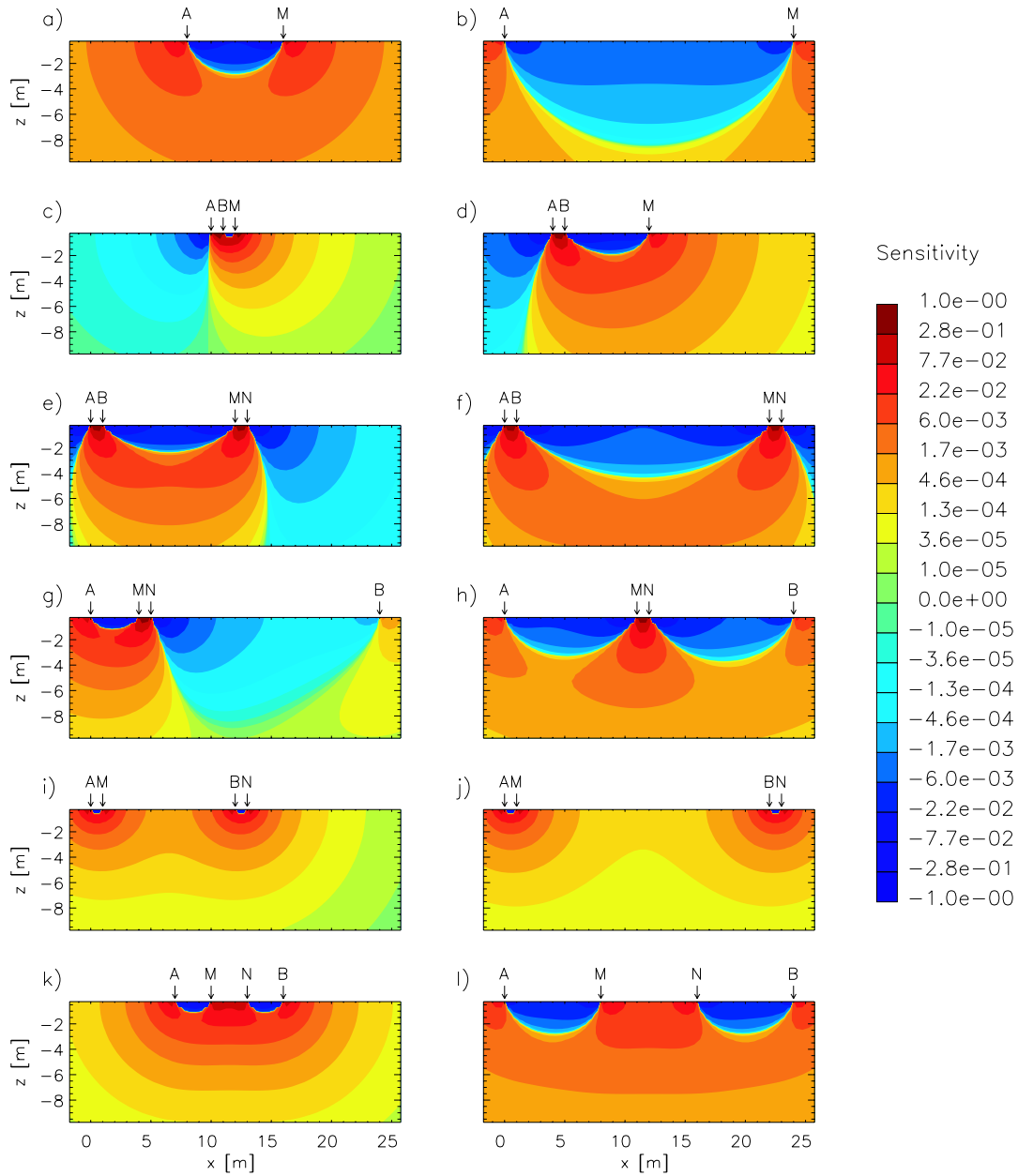
Figure 1.6 – Examples of 2D sensitivity distributions of a homogenous half-space for different arrays: (a,b) pole-pole; (c,d) pole-dipole; (e,f) dipole-dipole ABMN; (g) asymmetric Schlumberger; (h) symmetric Schlumberger; (i,j) dipole-dipole AMBN; (k,l) Wenner (modified after Friedel, 2000)

.

configurations contained in a data set have to complement each other appropriately. This can be quantified using tools from linear inversion theory, for example the model resolution matrix (e.g. Menke, 1984). A related measure that is less expensive to be computed is the depth of investigation index (DOI) as proposed by Oldenburg and Li (1994).

Studying the properties of individual electrode configurations using sensitivities, and appraising the quality of the tomographic images using the model resolution matrix or the DOI provided useful insights into the information content of geoelectrical data, but

it still remained unclear, if the traditional configuration were optimal, or if better survey layouts exist.

The first attempt to tackle this problem in geophysics was made by Cherkaeva and Tripp (1996). They based their approach on earlier work in the biomedical field of impedance tomography (Gisser *et al.*, 1988). They proposed electrode configurations, with which optimized current density patterns could be achieved. Other scientists have made attempts to find optimized survey layouts by only considering the sensitivities (e.g. Furman *et al.*, 2004).

Following earlier ideas from Barth and Wunsch (1990); Maurer and Boerner (1998); Curtis (1999) Maurer *et al.* (2000) proposed statistical experimental design, which provided a more general framework for identifying optimized survey layouts. The early implementations of statistical experimental design were based on global optimization schemes, such as genetic algorithms, but it was realized that this would be computationally prohibitive for realistic geoelectrical applications including several tens of electrodes and several hundreds of model parameters. Therefore, Stummer *et al.* (2004) proposed a sequential design strategy, where suitable electrode configurations were successively added to an initial data set until the desired model resolution was achieved. An example of the performance of this scheme is shown in Figure 1.7. The true resistivity model is displayed in Figure 1.7a. It is assumed that 30 electrodes with 5 m spacing are available at the surface. If all possible electrode configurations would be used for a tomographic inversion (roughly 80,000 measurements), the tomographic image shown in Figure 1.7b would be obtained. If only Wenner (Figure 1.7c), dipole-dipole (Figure 1.7d) or both Wenner and dipole-dipole (Figure 1.7e), would be considered, the tomographic images would be clearly inferior compared with the optimal tomogram in Figure 1.7b. If suitable electrode configurations would be selected using the algorithm of Stummer *et al.* (2004), the tomograms shown in Figures 1.7f to 1.7j would be obtained. Using the same number of optimized measurements as for the combined Wenner/dipole-dipole data set (Figure 1.7f) leads already to a superior image (compared with Figure 1.7e). With roughly 1,000 measurements (Figure 1.7h), the image quality becomes comparable to Figure 1.7b. Adding further data results only in minor improvements (Figures 1.7i and 1.7j).

The method of Stummer *et al.* (2004) received a lot of attention and triggered several other studies. For example, Wilkinson *et al.* (2006) extended and improved the method of Stummer *et al.* (2004), and Coscia *et al.* (2008) adapted the technology for geoelectrical crosshole applications.

Although the performance of sequential experimental design, as proposed by Stummer *et al.* (2004); Wilkinson *et al.* (2006), is impressive, there are several significant limitations that remain to be resolved. The first problem concerns the number of electrodes available and the resulting large number of possible electrode configurations. The
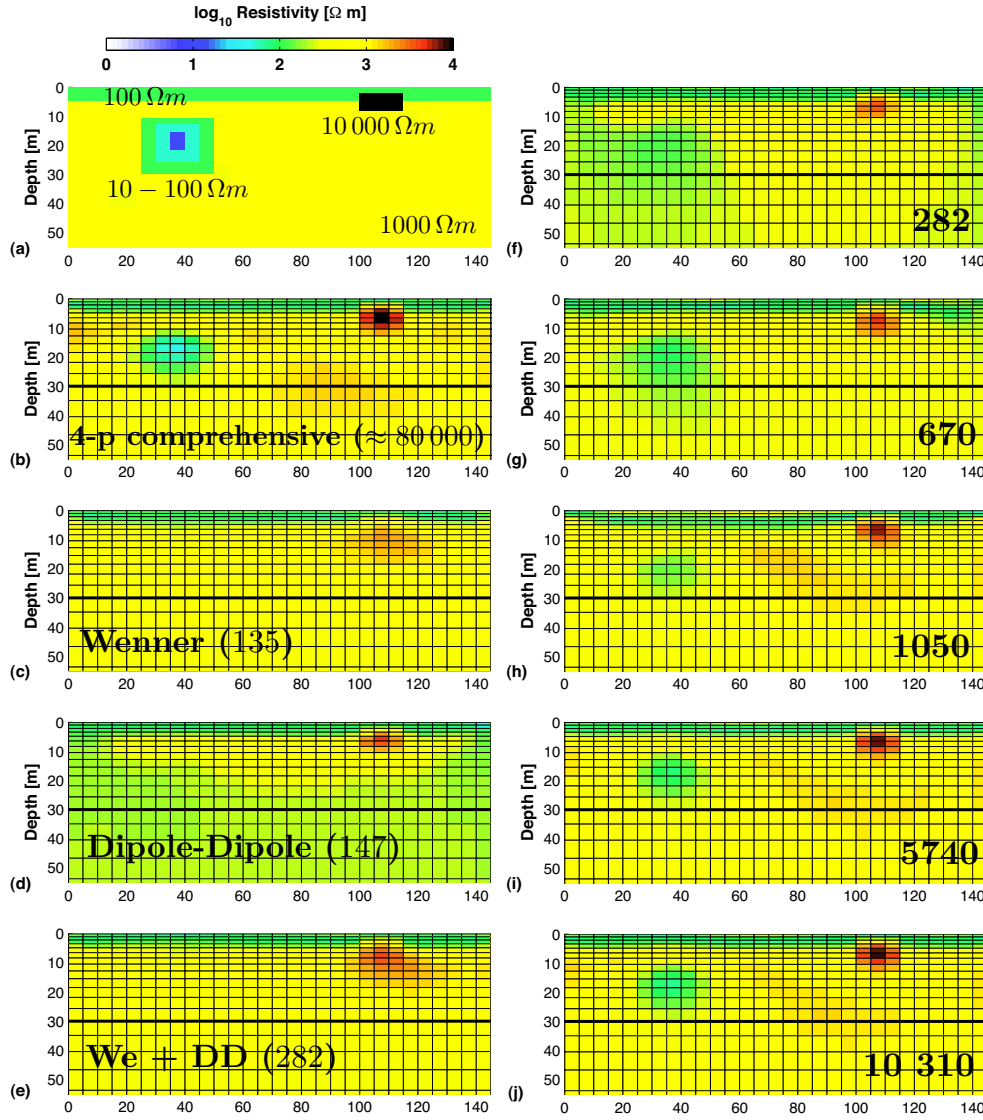
Figure 1.7 – Example of sequential experimental design (modified from Stummer *et al.*, 2004). a) shows the true resistivity model and b) displays the tomogram that would be obtained using all possible configurations. c) to e) show tomograms obtained with Wenner, dipole-dipole and Wenner + dipole-dipole configurations. f) to j) show tomograms for the optimized data sets. Numbers denoted on the tomograms indicate the number of electrode configurations employed.

latter roughly scales with n^4, where n is the number of electrodes (Xu and Noel, 1993). If n exceeds 50, the algorithms of Stummer *et al.* (2004); Wilkinson *et al.* (2006) become impractical.

A second problem that was not fully addressed by Stummer *et al.* (2004); Wilkinson *et al.* (2006) concerns the influence of data noise. In their experimental algorithms they preselected those configurations from the comprehensive data sets, whose geometrical factors were below a given threshold, thus rejecting configurations with likely small voltages (and hence possibly captured by noise). This ensured that only reliable con-

figurations were considered during the design stage, but no individual weighting factors were associated with the different configurations.

Finally, sequential experimental design requires an à priori subsurface resistivity model for which the model parameter sensitivities are computed. If the true subsurface structures deviate from the à priori model, non-linear effects may degrade the quality of experimental design. Stummer *et al.* (2004) and Wilkinson *et al.* (2006) demonstrated for a particular class of models that these non-linear effects are surprisingly small, but it would be nevertheless advantageous to have a design strategy at hand that is independent of our prior subsurface knowledge.

1.4   Motivation and outline of the thesis

As discussed in the preceding subsections, major advances of the geoelectrical method have occurred during the past few years. State-of-the-art instruments allow acquisition of large data sets in an almost automated fashion, forward modeling and inversion algorithms facilitate tomographic inversion analyses of 3D data sets collected in areas with pronounced topography and complex subsurface structures, and experimental design techniques have been developed for identifying data sets that provide maximum subsurface information at minimal costs.

It is the ultimate goal to collect efficiently large 3D data sets that provide maximum subsurface information and which can be analyzed almost in real time. Despite all the progress in the recent past, this goal has not yet been achieved. I have identified 3 critical issues, where further research would be particularly beneficial.

1. Acquiring large 3D data sets requires a multi-electrode array that can handle a large number of electrodes and that is capable of performing fully parallelized measurements. The *ETH-DCMES* system introduced by Stummer *et al.* (2002) has the potential to fulfill these criteria, but it suffers from several technical shortcomings that need to be improved.

2. In the presence of pronounced topography, the finite element method has been identified to be the most suitable option for numerical forward modeling of geo-electrical data. Furthermore, singularity removal has proven to be a very useful technique for improving the numerical accuracy. Combining finite element modeling and singularity removal in the presence of topography has not yet been implemented satisfactorily. Furthermore, the performance of the artificial ground boundary conditions continues to be problematic. Finally, appropriate model parameterization and inversion of large-scale data sets involving several hundred thousand measurements is still an extremely challenging task.

3. Sequential experimental design techniques, as introduced by Stummer *et al.* (2004) and further improved by Wilkinson *et al.* (2006), allowed the information content of geoelectrical data to be exploited in an optimal fashion, but their algorithms become impractical, when the numbers of electrodes becomes large. This requires new strategies to be devised.

In the second chapter of my thesis, I will describe the numerous improvements of the *ETH-DCMES* system that were implemented in the course of my project, followed by a few field examples that demonstrate the superior performance of the new system. Chapter 3 includes the description of a novel numerical forward modeling algorithm that combines unstructured (adaptive) mesh finite element modeling and singularity removal in the presence of topography. Furthermore, I will demonstrate the benefits of infinite elements, a technique that has not yet been applied in geoelectrical modeling but is popular in civil and mechanical engineering. Development and implementation of 2.5D and 3D tomographic inversion algorithms are the topic of chapter 4. I will show by means of synthetic and field data examples that my new algorithm is highly versatile and capable of inverting swiftly very large data sets on a standard workstation. In chapter 5, I will present a novel experimental design concept that takes advantage of the parallel recording capabilities of the improved version of *ETH-DCMES*. Its performance will be demonstrated with synthetic and field examples. In the concluding chapter I will summarize the achievements of my project and I will outline fruitful avenues of future research.

Chapter 2

ETH DCMES II - A new distributed, smart multi-electrode resistivity acquisition system

2.1 Introduction

Implementation of experimental design concepts to geoelectric field surveys demands a sophisticated data acquisition system. Key requirements are (i) software-controlled selection of arbitrary electrode configurations, (ii) fast parallel scans involving up to hundreds of simultaneously recording electrodes and (iii) digital recordings of the full waveform data. The new data acquisition system presented in this chapter is based on the previously developed fully distributed data acquisition system (*"ETH-DCMES"*) by Stummer *et al.* (2002). In the following, I briefly outline the main features of the *ETH-DCMES* and subsequently give details on the technical developments and improvements that have been incorporated into the new system – *ETH-DCMES-II*.

ETH-DCMES

At the time the *ETH-DCMES* was developed, only one of the commercially available systems, the SIP-256 system from the "Deutsche Arbeitsgemeinschaft für SIP-Anwendungen" (Schleifer, 2002), was identified as appropriate for implementing key experimental design aspects. However, it lacked the ability to select separately the operational modes of the individual electrodes. Consequently, it was decided to build a new data acquisition system to satisfy all scientific and technical requirements (Stummer, 2003).

In general, multi-electrode system designs fall into two main categories – centralized
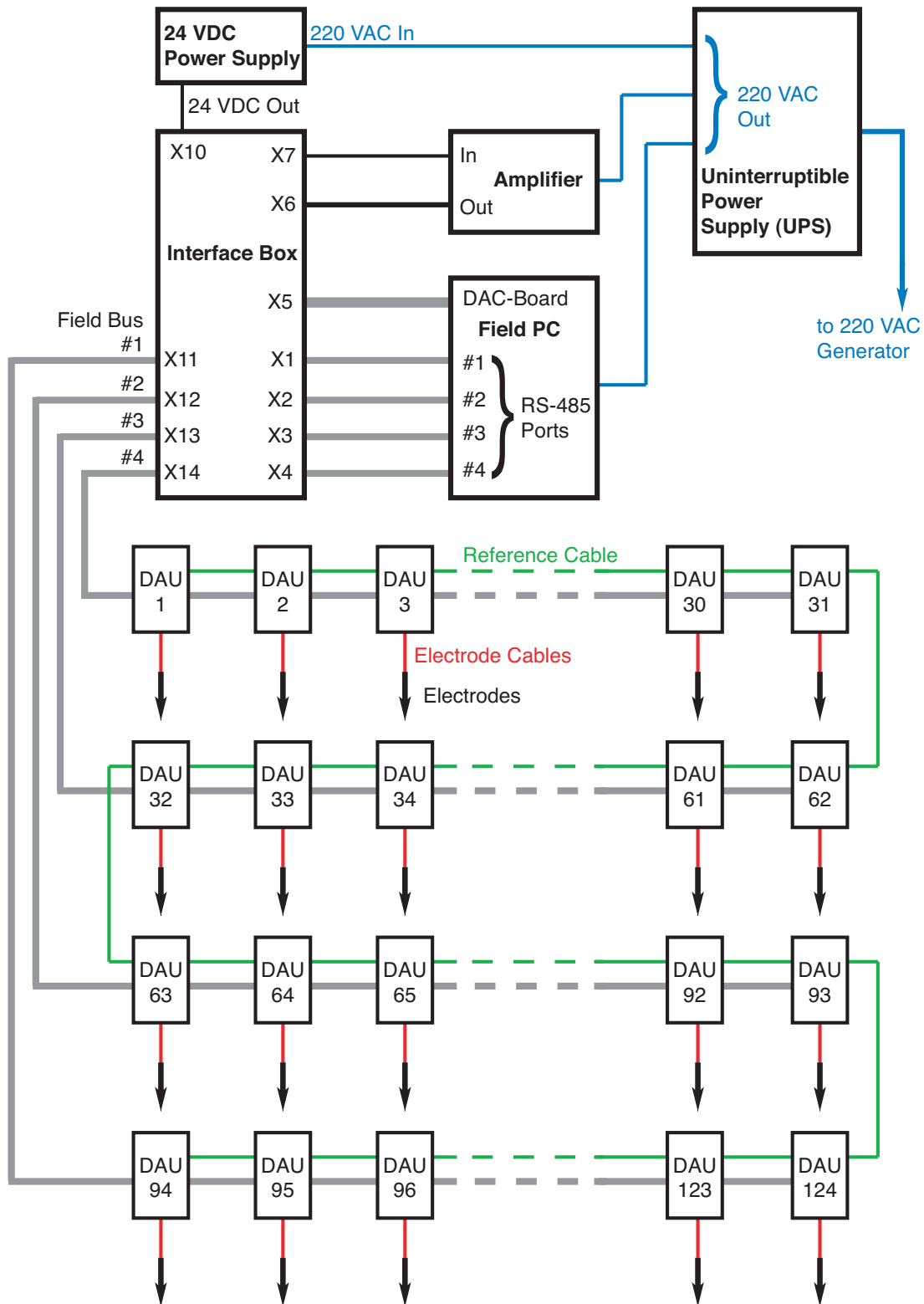
Figure 2.1 – Schematic block-diagram of the fully distributed data acquisition system *ETH-DCMES* (after Stummer, 2003). Communication between the daisy-chained data acquisition units ("DAUs") and a field computer is handled via a bi-directional RS-485 data bus. Arbitrary source signals generated by the field computer, converted to an analogue signal and enhanced through a power amplifier are fed into the electrode array through the interface-box.

and distributed systems. Extensive examination of system designs available at the time
the *ETH-DCMES* was developed (2001) revealed that only distributed systems allow
fast parallel data acquisitions with arbitrary electrode configurations to be carried out
(Stummer, 2003). Consequently, the *ETH-DCMES* was designed to be fully distributed
such that each smart electrode incorporates its own data acquisition unit (DAU, Figure
2.5(a)). An internal switching matrix allows each DAU to be configured either as a
current source, current sink, voltage reference, or measuring device. Signals from the
electrodes are fed into 24 bit AD converters with very high input impedances ($> 1\ G\Omega$).
Initial field tests of the *ETH-DCMES* revealed that the actually achievable resolution
in the presence of ambient electromagnetic noise is about 20 bit. It is primarily limited
by the ambient noise and not by the system itself.

Figure 2.1 shows a schematic layout of the data acquisition system. Communication
between the daisy-chained DAUs and a field notebook computer is handled via a bi-
directional RS-485 data bus and an interface-box (IFB). The RS-485 data bus consists
of four wires within a single cable; a separate coaxial cable carries the reference signal. A
field notebook not only serves as a control unit for the DAUs, but also generates arbitrary
source signals using a digital–to–analog converter. The source signal is enhanced through
a class A power amplifier, routed through the IFB, where a dedicated DAU precisely
determines the input current, which is then fed into the electrode array. The instrument
design of the *ETH-DCMES* allows parallel recordings to be carried out, where one or
two DAUs are used to inject the source current and all remaining DAUs are measuring
with respect to a single DAU that acts as a reference unit. After data acquisition is
completed, the DAUs connect to the data bus to enable transfer of the acquired voltage
time series. A unique feature of the DAUs are their internal rechargeable batteries, that
allow them to operate independently. The batteries are recharged by a 24 V DC source
concurrently while the data transfer to the field notebook takes place (further technical
details of the system are given in Stummer (2003)). Extensive field tests by Stummer
et al. (2002) and Akeret (2003) revealed several deficiencies of the *ETH-DCMES*:

- impractical handling of the components (due to their overal weight and size)

- limited expandibility of the system (limited by the number of available PC extension
  slots in the employed field computer)

- complicated field handling of the DAUs

- insufficient internal battery capacity of the DAUs

- a high failure rate of the DAUs (due to issues with their internal switching matrix)

- the necessity for manual amplifier gain adjustements

- an unsatisfactory performance in the parallel recording mode (due to the long time required to transfer full waveforms back to the field computer)

2.2   Further developments and improvements implemented in the *ETH-DCMES-II*

2.2.1   A lightweight arbitrary waveform adjustable current source

(a)   (b)
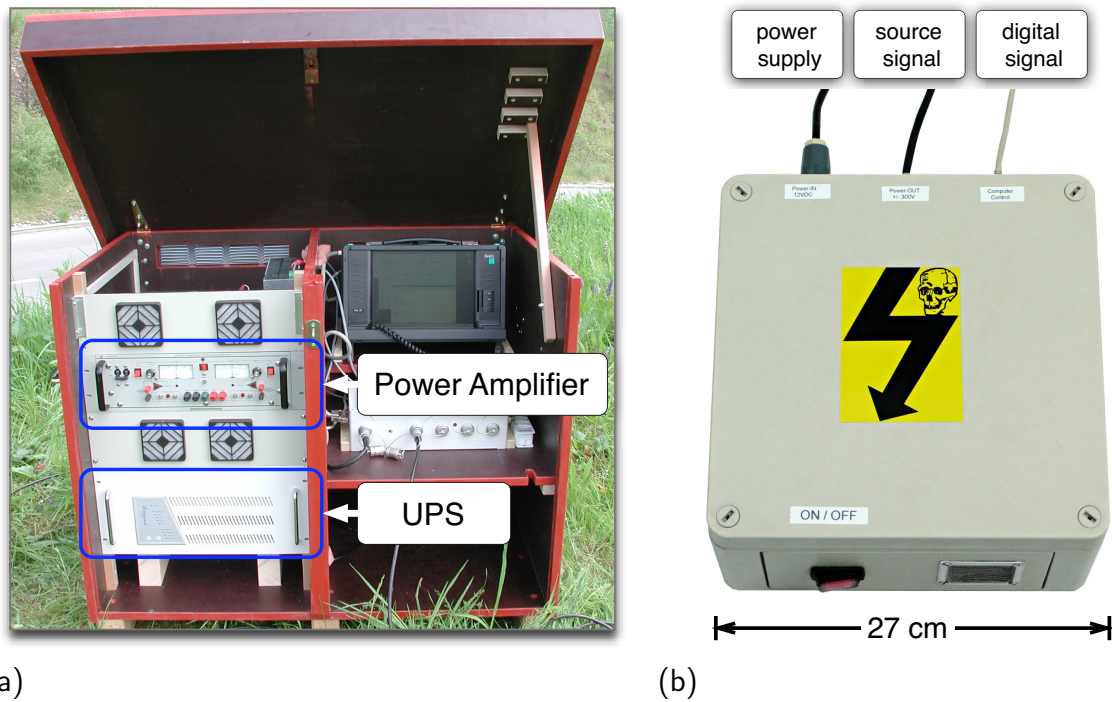
Figure 2.2 – (a) Bulky laboratory amplifier used for the current source in the *ETH-DCMES* and (b) the newly developed lightweight battery-driven current source employed in the *ETH-DCMES-II*. The laboratory amplifier required power from a generator buffered by a weighty uninterruptible power supply (UPS). The new current source reduces the overall weight of the central components from more than 100 kg down to about 15 kg.

Despite an extensive market research effort, no suitable battery-driven current source could be found at the time the *ETH-DCMES* was designed (in 1998). Therefore, a bulky laboratory-standard power amplifier had to be used to amplify the computer-generated current waveform. The amplifier required power from a 220 V generator supported by a heavy uninterruptible power supply (see Figure 2.2(a)). The combined weight and size of these components hindered routine resistivity surveying with the *ETH-DCMES*. Furthermore, field surveys in areas not accessible by vehicles where not feasible.

To improve the mobility of the *ETH-DCMES*, the amplifier was replaced by a newly developed lightweight, battery-driven source thereby removing the need for the field

generator and the uninterruptible power supply. As a beneficial side-effect, possible electromagnetic noise pickup emitted by the field generator is avoided. The new current source reduces the overall weight of the central components from more than 100 kg down to about 15 kg (without the batteries).

Figure 2.2(b) shows a picture of the new current source. It consists of a data acquisition board and a power amplifier. The digital source signal generated on the field notebook is fed via a USB connection into the data acquisition board where digital-to-analog conversion takes place. A power amplifier located in the source enhances the signal by a fixed factor of 30. The signal is routed through the interface box into the electrode array, and applied to the selected current pair (source and sink).
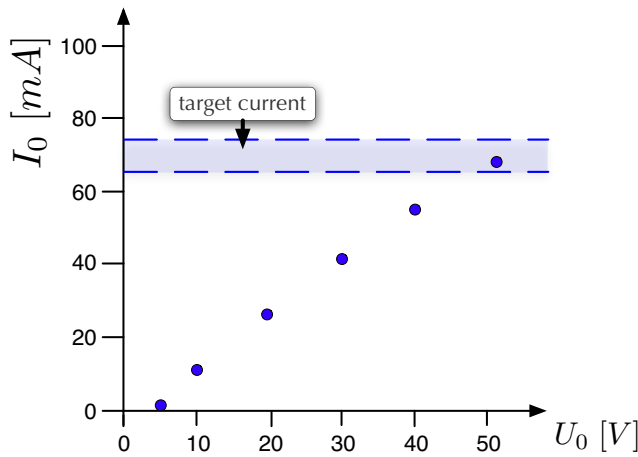
Figure 2.3 – Sketch of the principle used to adjust the source signal voltage amplitude to a given target current strength (e.g. 70 mA) prior to any data acquisition.

The previous laboratory-standard power amplifier offered a precise control over the current strength injected into the ground. By contrast, the power amplifier employed in the new current source amplifies a given waveform by a constant factor (30). Therefore, only the voltage amplitude but not the current strength of the source signal can be specified. Depending on the earth resistance and the contact resistances at the source electrodes, current strengths injected into the ground might be difficult to predict. Furthermore, the employed amplifier offers a maximum output current strength of 100 mA. Inadequate selection of the waveform voltage amplitude might easily lead to clipped waveform signals, or in very conductive ground, the voltages measured might be too small. Both situations would render the data acquisition as being unreliable and not properly exploiting the available dynamic range of the system. Therefore, the optimum level of the source signal voltage amplitude is estimated prior to any data acquisition (Figure 2.3). This is done by injecting a gradually increasing DC voltage signal (V_0) through the source electrodes (A and B in Figure 2.3) and simultaneously measuring the source current strength I_0 via the data acquisition board built into the current source. Once I_0 reaches a predefined target value (e.g. 100 mA), the process is stopped and the obtained voltage amplitude V_0 is used as the amplitude for the source waveform in the

following measurement. This process has been optimized such that the time required to make this selection (less than 150 ms) is insignificant compared to the time needed for the subsequent data acquisition.

2.2.2   Improved system expandability
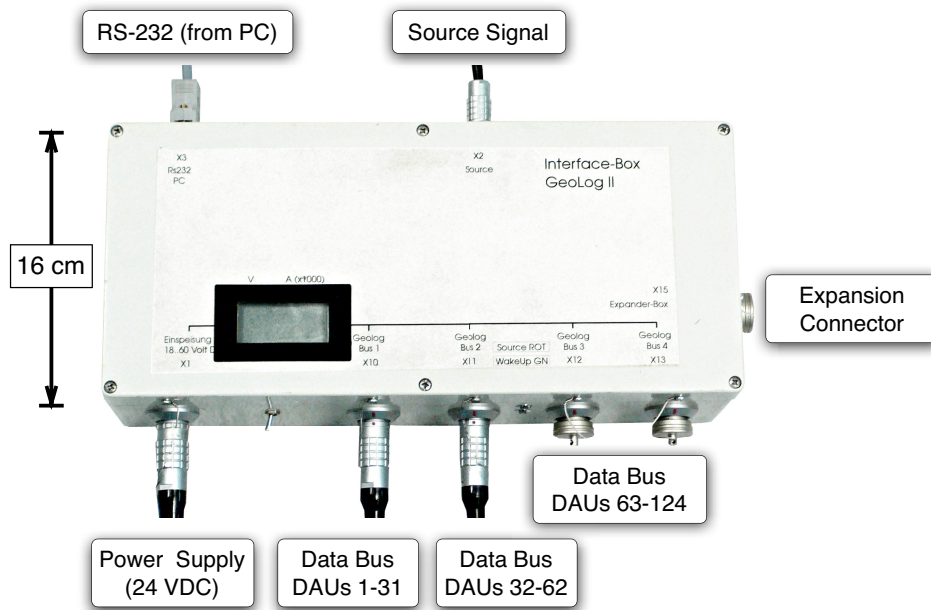
Figure 2.4 – Modified interface-box ("IFB") of the *ETH-DCMES-II*. Data transfer from the daisy-chained DAUs is routed via a bi-directional serial data bus (RS-485) through the IFB to the operating field computer. The amplified source signal from the current source (Figure 2.2(b)) is send through a dedicated DAU located inside the IFB that precisely determines the input current before being fed into the electrode array.

Each of the four field data buses connected to the interface-box (Figure 2.1) can handle a maximum of 31 DAUs for a total of 124 data loggers. The number of deployable DAUs can be increased by adding additional interface-boxes to the system. However, the original *ETH-DCMES* was designed such that for each additional interface-box one additional multichannel RS-485 interface card needs to be added to the field computer. Thus the expandability of the *ETH-DCMES* was effectively limited by the number of available PC extension slots.

To circumvent this limitation, the interface-box was modified. It now includes a single RS-232-to–RS-485 converter, that allows the field notebook to communicate via a single commercial serial port to all four RS-485 channels (see Figure 2.4). Additional RS-485 channels can simply be added to the system through "expander boxes" (connected to the expansion connector, Figure 2.4). Applied source signals and the data transfer from the field notebook are automatically routed through to the additional RS-485 channels.

Besides improving on the expandability of the *ETH-DCMES*, the new interface-box

allows the previously used bulky laboratory computer to be replaced by a mobile field-rugged PC that does not require a 220V power supply. Only a standard USB (for the current source) and serial RS-232 interfaces are required for the field computer to fully operate the *ETH-DCMES-II*.

2.2.3 Redesign of the data acquisition units
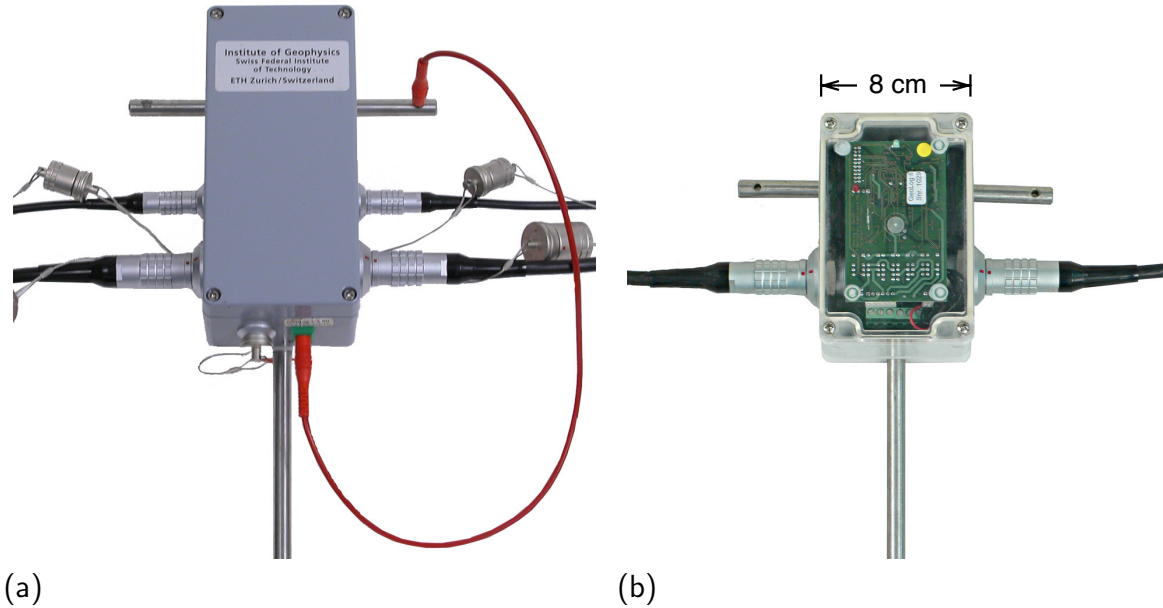
Figure 2.5 – Previous (a) and redesigned (b) version of data acquisition units ("DAUs"). The DAUs were updated to facilitate processing of the measured voltage time-series directly on the loggers. Additionally, their field handling was optimized by (i) reducing their overall weight and size, (ii) combining the reference and data bus cables and (iii) providing a simple "clip"-mechanism that allows them to be connected to the metal electrodes easily.

The DAUs of the ETH-DCMES have been redesigned – Figure 2.5 shows the previous (a) and the updated DAU (b) for comparison – mainly to facilitate on-board processing of the acquired voltage waveforms (see also section 2.2.5). This required upgrading the internal central processing unit and increasing the amount of random access memory available on the DAUs (from 32 to 256 kb). Furthermore, the operating software on the DAU has been extended such that exchangeable processing-software modules can be uploaded and executed during the course of a field campaign.

Extensive field tests of the *ETH-DCMES* conducted by Akeret (2003) revealed two main weaknesses of the DAUs, both of which hindered failure-free data acquisitions over long periods of time: (i) generally inadequate capacity of the internal batteries, and (ii) unreliable working relays inside the switching matrix of the DAUs. Therefore, the revised DAUs are equipped with batteries featuring largely increased capacity (600 mAh) and the relays are replaced by bi-stable relays that behave in a much more robust

fashion under harsh weather and weak power conditions. Field tests proved the fail-safe operation of the new relays under cold ambient temperatures (a few degrees celsius above zero) even for long data acquisition times. The capacity of the batteries is sufficient for at least 9 hours of common field operation, such that recharging can be performed during the night at the end of each days recording.

Besides these modifications, attention has been paid to simplify the overall field handling of the DAUs. Their overall size and weight have been reduced and the reference and data bus cables have been combined into a single four-wire cable. Furthermore, the updated DAUs feature a "clip-on" mechanism that allows them to be attached to the metal electrodes easily without the need for an additional cable (Figure 2.5(b)). Each DAU now features status LEDs that allow the field crew to easily check their status.

2.2.4   Automatic gain control

HV	no HV
± 1278 V	± 2.5 V
± 638 V	± 1.25 V
± 319 V	± 625 mV
± 159 V	± 312.5 mV
± 79 V	± 156.25 mV
± 39.92 V	± 78.12 mV
± 19.96 V	± 39.06 mV
± 9.98 V	± 19.53 mV

(a)   (b)
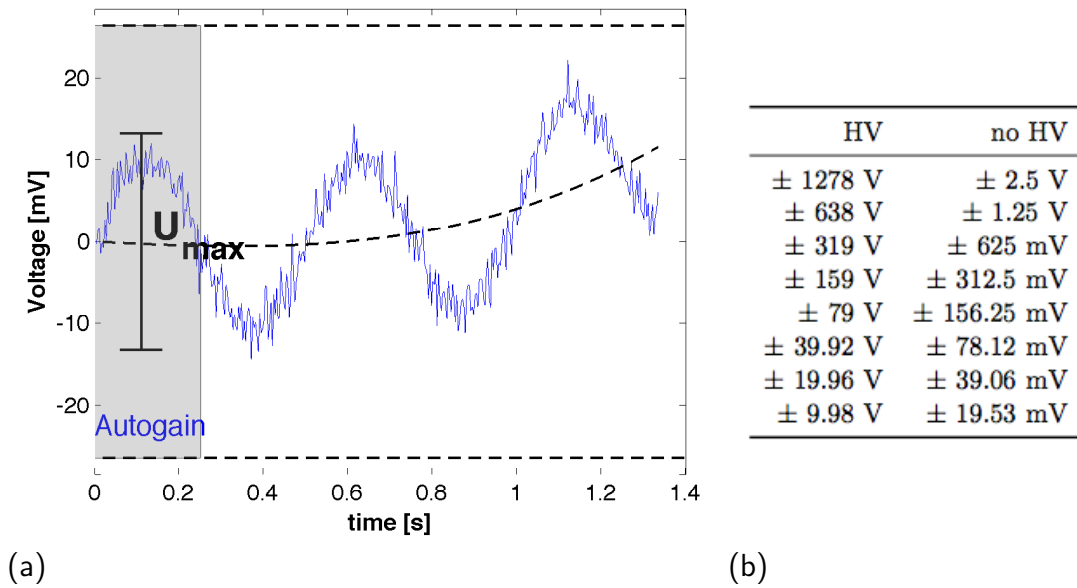
Figure 2.6 – (a) Sketch of the automatic gain control employed in the new DAUs. (b) Possible gain settings for the programmable gain amplifier build into the DAUs' analog–to–digital converter. During automatic gain control, the first few samples of the acquired voltage time-series are scanned in order to properly adjust the gain.

The 24-bit analog–to–digital converter employed in the DAUs of the *ETH-DCMES* includes a programmable gain amplifier that allows the selection of one of eight different amplification settings ($f_n = 2^n$ for $n = 0 \ldots 7$) such that for a gain of "1" the maximum input voltage range of a DAU is $\pm$ 2.5 V and for a gain of "128" the maximum input voltage range is $\pm$ 19.5 mV, otherwise clipping occurs. Optionally, a voltage divider (511 to 1) can be placed in front of the ADC input for high voltage signals. Resulting gain ranges with and without the voltage divider ("HV") applied are displayed in figure

2.6(b).

The *ETH-DCMES* required separate gain measurements that were used to detect appropriate gain amplification factors for subsequent data acquisition. Besides the long time required by this, the time gaps between the gain measurements and the actual data acquisitions can be problematic (Akeret, 2003). A drift in the ground potential due to ambient electromagnetic noise and capacitive effects can easily lead to inappropriate gain settings. A too small gain leads to a low effective resolution during the analog–to–digital conversion, whereas a too large gain may lead to clipped time-series that cannot be interpreted reliably.

Therefore, the revised version of the DAUs features an automatic gain control where the first few samples recorded during a data acquisition are scanned to adjust the gain as outlined in Figure 2.6(a). For each subsequent sample, an optimum gain amplification factor is selected. During this process, amplification factors can be reduced but never increased, i.e. the gain is adjusted to the maximum signal strength ($U_{\max}$). To compensate for a possible drift occurring in the ground voltage (see the black dashed line in Figure 2.6(a)), the gain is adjusted to a multiple of the maximum amplitude $U_{\max}$ as shown by the horizontal dashed lines in Figure 2.6(a). It is important that a sufficient number of samples are used during the gain control to assure that the maximum amplitude of the employed waveform has been reached.

2.2.5 Reducing data acquisition time by distributing the data analysis

The *ETH-DCMES* allows full-waveforms to be recorded, which is beneficial for research-related (e.g. induced polarization) studies. However, the required time to transfer the full-waveforms via the RS-485 data bus to the field computer severely limits the overall data acquisition speed of the *ETH-DCMES*. This imposed serious constraints on the applicability of the *ETH-DCMES* to large-scale geoelectric field surveys. For example, the comprehensive data set recorded by Stummer *et al.* (2002) on four lines, each involving 30 electrodes (49 500 measurements in total) required thirteen days of recording with most of the time being spend on transferring the full waveforms to the field computer. Therefore, the DAUs have been redesigned to allow processing of the voltage time series directly on the DAUs. Instead of the full waveforms only a few numbers characterizing the measured voltage waveforms and some error estimates need to be transferred back to the field notebook.

The new design of the DAUs is flexible in that it allows different data processing algorithms to be downloaded from the central computer through the data bus to the individual data loggers. Driver routines have been implemented such that developed software modules can be exchanged even during the course of a field survey. This offers

the possibility of using fast data acquisitions with arbitrary source waveforms.

Stummer (2003) employed spectral divisions of voltage and source current signals within a narrow frequency band around the dominant source frequency to determine voltage amplitudes (out of which apparent resistivities can be deduced) from the recorded full waveforms. While this method proved to be reliable for most of the data acquired by Stummer (2003), it showed severe limitations when applied to data contaminated with ambient electromagnetic noise with a strong low-frequency content. Large low-frequency noise amplitudes may dominate the signal waveform in the frequency domain, such that the correct amplitude at the source signal frequency cannot be properly recovered.

Akeret (2003) therefore developed a robust method that allowed the low-frequency noise content of a measured time series to be approximated by a n-th order polynomial (with n typically between three and five). After the estimated noise content is substracted from the voltage time-series, the correct amplitude at the source signal frequency can be estimated reliably. This method has been adopted by Capiti (2007) for developing algorithms for various source waveforms (sine waves, rectangular waves and linearly swept frequency chirp source signals) ready for deployment on the DAUs. Corresponding software modules have been developed and tested successfully during a field-campaign. In the following, I demonstrate this methodology for sinusoidal and bipolar rectangular source waveforms.

Sinusoidal source waveform

Assuming that a recorded time series y_k sampled at time steps t_k can be approximated by

$$y_k = A_\omega \, cos(\omega t_k - \phi_\omega) + S + Dt_k + Bt_k^2 + Ct_k^3 \tag{2.1}$$

with a known frequency ω and unknown amplitude (A_ω) and phase shift (ϕ_ω). The unknown parameters S, B, C and D are used to approximate the dc-shift and long-periodic higher-order noise terms in the recorded signal. Elimination of the non-linearity due to the unknown phase ϕ_ω leads to

$$y_k = A_\omega \, cos(\omega t_k)cos(\phi_\omega) + A_\omega \, sin(\omega t_k)sin(\phi_\omega) + S + Dt_k + Bt_k^2 + Ct_k^3. \tag{2.2}$$

Estimating the unknown parameters for a given discrete time series of length n requires solving the following system of linear equations

$$\begin{pmatrix} y_1 \\ y_2 \\ \vdots \\ y_n \end{pmatrix} = \begin{bmatrix} cos(\omega t_1) & sin(\omega t_1) & 1 & t_1^3 & t_1^2 & t_1 \\ cos(\omega t_2) & sin(\omega t_2) & 1 & t_2^3 & t_2^2 & t_2 \\ & \vdots & & & & \\ cos(\omega t_n) & sin(\omega t_n) & 1 & t_n^3 & t_n^2 & t_n \end{bmatrix} \begin{pmatrix} x_1 \\ x_2 \\ \vdots \\ x_6 \end{pmatrix}, \tag{2.3}$$

Figure 2.7 – Synthetic (blue) and reconstructed signals (red) for different percentages of added random noise. The black dashed line represents the fitted low-frequency noise contained in the signals. For (d) the synthetic signal has been clipped at 30 mV to simulate a gain-range overflow.

They can be suitably solved by the individual data acquisition units. This is done by accumulating the corresponding normal equations and then subsequently performing a Cholesky decomposition (Schwarz and Waldvogel, 2004). Resolved coefficients $x_1 = A\cos(\phi_\omega)$ and $x_2 = A\sin(\phi_\omega)$ are used to deduce the unknown amplitude and phase of the measured signal:

$$A_\omega = \sqrt{x_1^2 + x_2^2}, \qquad \phi_\omega = arctan\left(\frac{x_2}{x_1}\right). \tag{2.4}$$

The coefficients x_4 to x_6 approximate the long-periodic noise contained in the signal (B, C and D in Equation 2.2), whereas x_3 describes its dc-shift (S). In addition to these coefficients, the DAUs compute a misfit parameter

$$\xi = \frac{1}{A_\omega} \frac{1}{n} \sum_{k=1}^{n} \left(y_k - y_k^{calc}\right)^2, \tag{2.5}$$

which is the quadratic deviation between the measured signal y_k and the fitted signal y_k^{calc}, the sum normalized by the resolved signal amplitude A_ω. A value for ξ larger than one indicates, that the mean amplitude of the high-frequency noise contained in the recorded signal exceeds the signal amplitude A_ω. The parameter ξ proved to be a reliable indicator for the quality of the waveform fit. It can be used in an automated fashion to reject measurements having a too low signal-to-noise ratio.

Figure 2.7 demonstrates the performance of this approach on synthetic sinusoidal waveforms contaminated with different levels of random noise. The synthetic signal was generated using Equation 2.2 with the following parameters:

$$A_\omega = 20\text{mV} \quad \phi_\omega = 0 \quad S = -8.5\text{mV} \quad B = 3\text{mV} \quad C = 1.2\text{mV} \quad D = 0.5\text{mV}$$

Relative errors of the resolved amplitudes (synthetic signal amplitude is 20 mV) for 10 and 30 percent random noise added are 0.05 and 0.35% (Figures 2.7(a) and Figure 2.7(b)). Even for 60 % random noise, the signal amplitude can be recovered reliably with a relative error of just 0.1% (Figure 2.7(c)). To demonstrate the robustness of the data fit, the synthetic signal in Figure 2.7(d) has been clipped at 30 mV in addition to contaminating it with 30% of random noise. The original signal can, nevertheless, be reconstructed with a relative error for the signal amplitude of 4.4%. Clipping of recorded waveform signals may happen during analog-to-digital conversion on the DAUs due to a gain-range overflow.

Rectangular source waveform

A similar algorithm as the one used for sinusoidal source waveforms can be employed for rectangular source waveforms. For this purpose, a Fourier series analysis is used to approximate the recorded time-series y_k (sampled at discrete time steps t_k) by a series of sine and cosine functions. As for the sinusoidal waveforms, a polynomial of degree three is used to approximate the long-periodic noise content in the time-series:

$$y_k = \frac{4\,A}{\pi} \sum_{q=0}^{p} \left(\frac{cos((2q-1)l/\omega)}{2q-1} sin\left((2q-1)(\omega t_k - \phi)\right) \right) + S + Bt_k^2 + Ct_k^3 + Dt_k \quad (2.6)$$

Here A and ϕ are the unknown signal amplitude and phase shift, respectively, ω is the known source signal fundamental frequency and l is the length of the waveform. Tests revealed that $p = 20$ terms for the Fourier decomposition are sufficient to approximate the waveform with a good accuracy. Fitting a measured time-series of length n to the
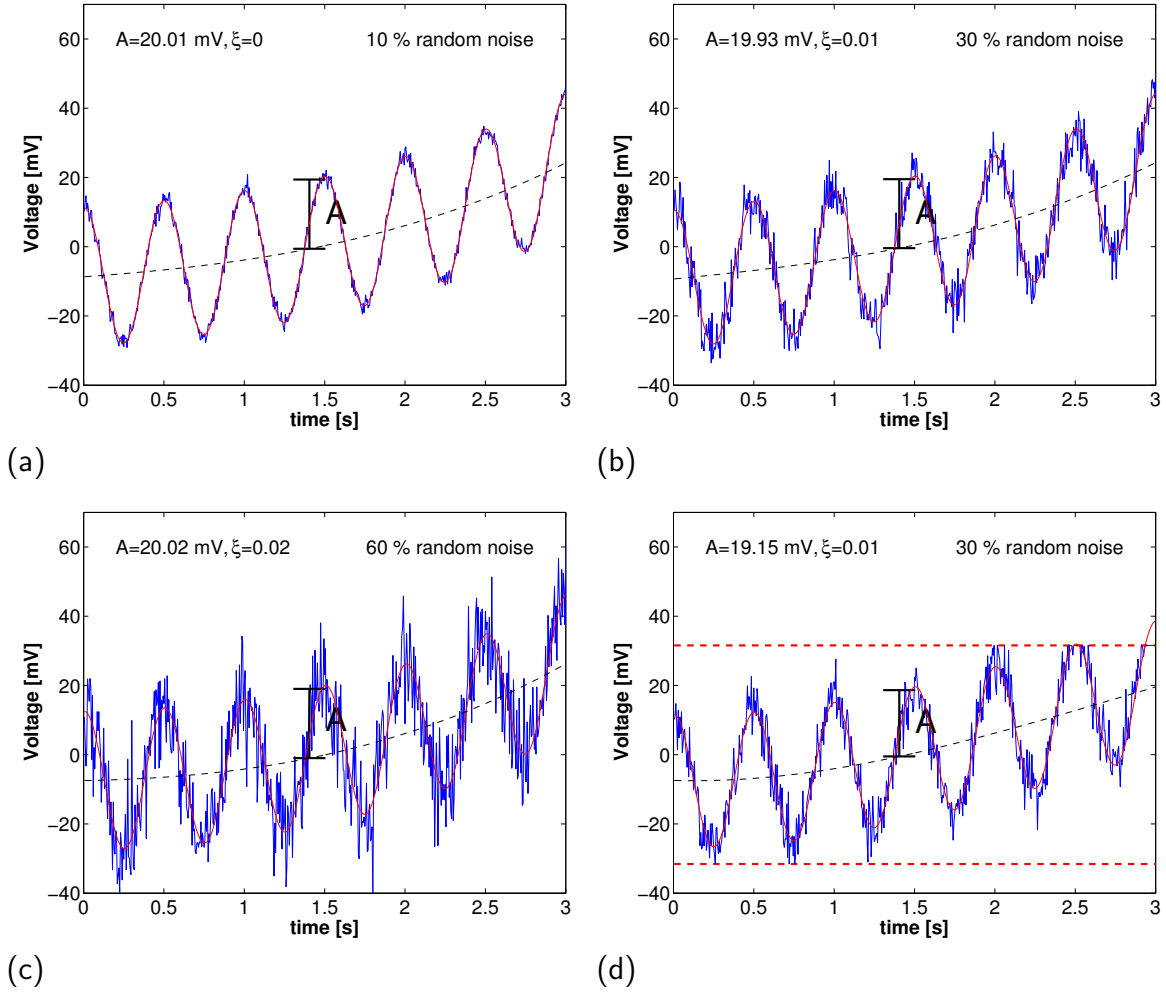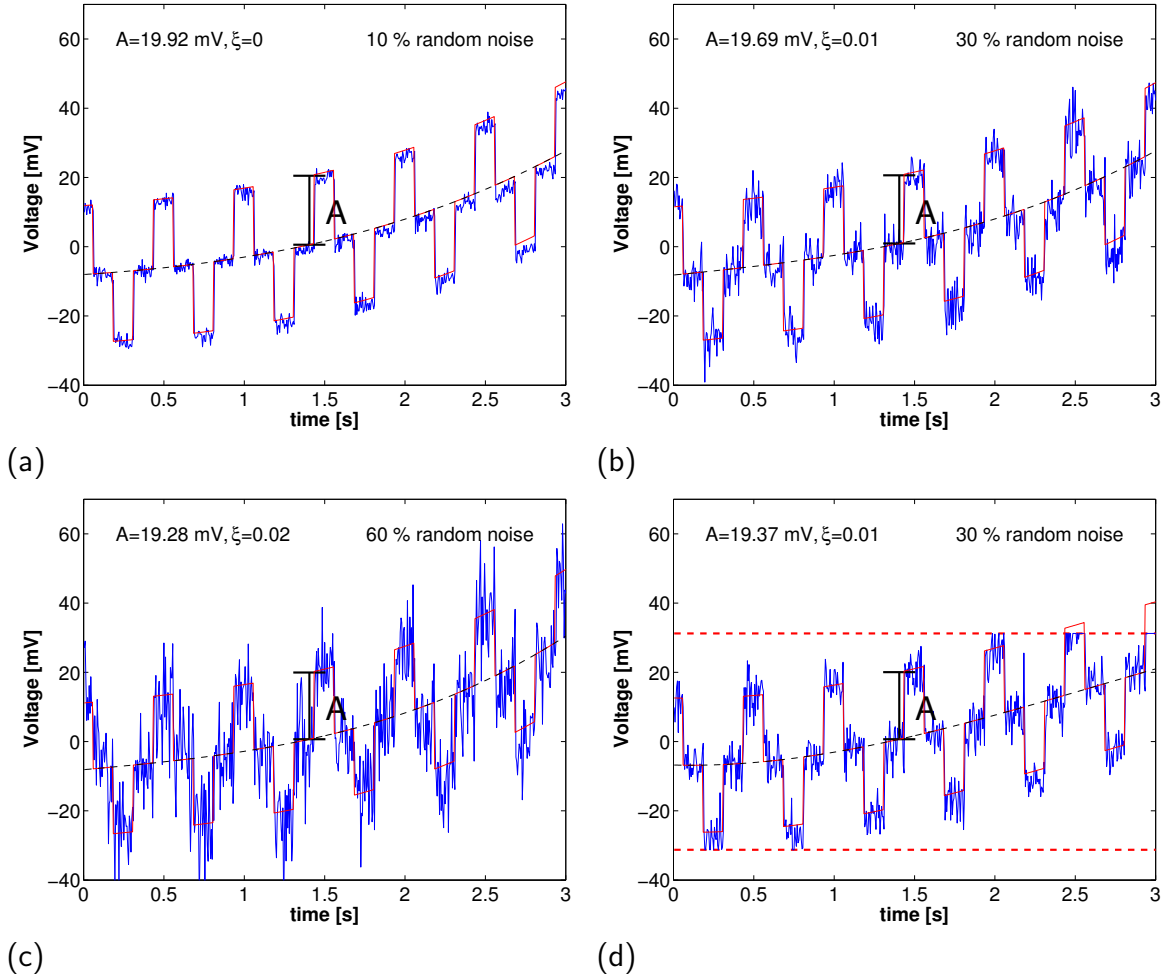
Figure 2.8 – Synthetic (blue) and reconstructed signals (red) for different percentages of added random noise. The black dashed line represents the fitted low-frequency noise contained in the signals. For (d) the synthetic signal has been clipped a 30 mV to simulate a gain-range overflow.

approximation given above requires solving a linear system of equations

$$
\begin{pmatrix} y_1 \\ y_2 \\ \vdots \\ y_n \end{pmatrix} = \begin{bmatrix} f_s(t_1) & 1 & t_1^3 & t_1^2 & t_1 \\ f_s(t_2) & 1 & t_2^3 & t_2^2 & t_2 \\ & \vdots & & \\ f_s(t_n) & 1 & t_n^3 & t_n^2 & t_n \end{bmatrix} \begin{pmatrix} x_1 \\ x_2 \\ \vdots \\ x_5 \end{pmatrix}
$$

$$
\text{with} \quad f_s(t_k) = \frac{4\,A}{\pi} \sum_{q=0}^{p} \left(\frac{cos((2q-1)l/\omega)}{2q-1}\, sin\left((2q-1)(\omega t_k)\right) \right), \qquad (2.7)
$$

whose solution is the unknown amplitude (x_1), the dc-shift (x_2) and the coefficients of the polynomial characterizing the long-periodic noise content $(x_3$ to $x_5)$. Prior to setting up the system of linear equations, the acquired time-series is shifted such that the phase

lag ϕ vanishes.

Figure 2.8 shows the performance of this algorithm on a synthetic rectangular wave-form (with an amplitude of 20 mV) contaminated with 10, 30 and 60% random noise, respectively. The parameters used to generate the synthetic signals are the same as those used for the sinusoidal signals. In all three cases the long-periodic trend of the signal (black dashed line in Figures 2.8(a) to 2.8(c)) is accurately reproduced. Relative solution errors for the resolved signal amplitudes are within reasonable bounds (0.4, 1.5 and 3.6%, respectively) but slightly larger than for the sinusoidal waveforms depicted in Figure 2.7. The steep (non-smooth) voltage jumps in the rectangular signal impedes the data fitting process, especially for low signal sampling rates (200 samples per second have been used here).

2.3   Measurement procedure

The *ETH-DCMES-II* is highly flexible in that it allows arbitrary serial and parallel four-, three- or two-point geoelectric data sets to be recorded viz. bipole-bipole, pole-bipole/bipole-pole and pole-pole electrode configurations. In all cases either the full waveforms, only a few numbers characterizing the waveforms (see section 2.2.5) or both are transferred back to the field computer. Within the framework of this thesis, sophisticated measurement software has been developed to automate the acquisition of geoelectric data sets with the *ETH-DCMES-II* without limiting its versatility. The measurement software has been optimized for fast data acquisition especially in the parallel recording mode. Furthermore, it allows $3D$ field surveys with roll-along schemes to be carried out efficiently. Details on the measurement software can be found in Appendix C.2. In the following, I outline the steps required to perform parallel measurements and provide details on the performance of the *ETH-DCMES-II* regarding data acquisition speed.

Figure 2.9(a) shows a timeline of the measurement procedure for a single parallel recording (200 samples recorded at a 100 Hz sampling rate). Initially, all DAUs are configured for the subsequent data acquisition by a broadcast command sent through the RS-485 data bus. The command contains all required settings, such as the number of samples to be recorded by each DAU, the sampling frequency and the gain settings for the analog—to–digital–conversion, to name just a few of the most important parameters. Subsequently, the DAUs that act as current source/sink and voltage reference electrodes, respectively, are individually configured for their particular tasks.

At this stage, all DAUs are ready to acquire data. A broadcast command is used to synchronously trigger the measurement process on all DAUs. Thereupon the DAUs disconnect from the data bus and set their internal switch-matrix according to their operational modes. Previous to the actual data acquisition, the source voltage amplitude
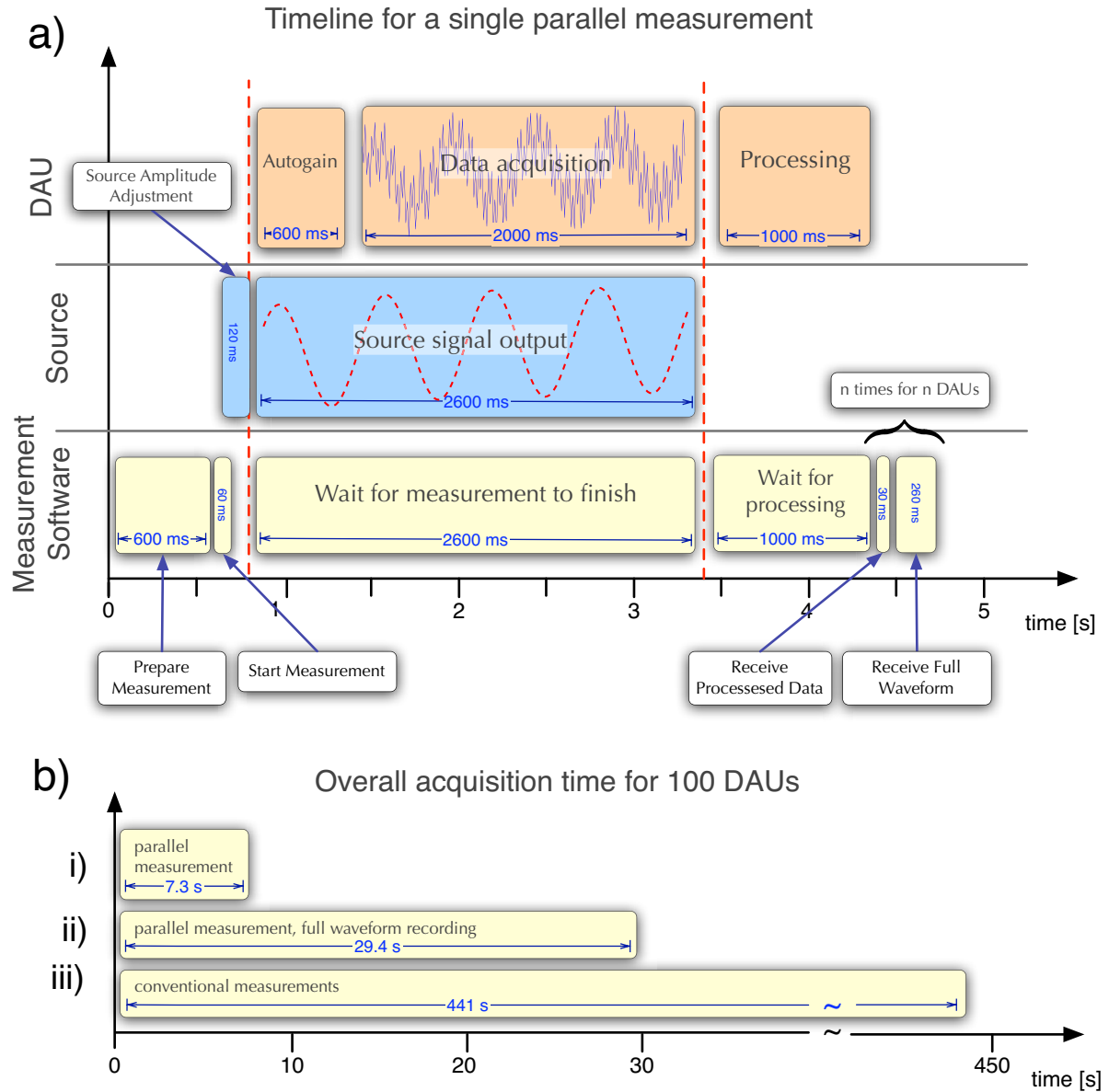
Figure 2.9 – (a) Timeline of the individual steps required for a single parallel recording with the *ETH-DCMES-II*. (b) compares the time needed for a single parallel scan with 100 DAUs in the parallel recording mode with either transferring the full waveforms (i) or only the pre-processed data (ii) back to the central computer. Case (iii) displays the corresponding time required for serial data acquisitions (with the *ETH-DCMES-II*, without full waveform transfer).

is adjusted (section 2.2.1). Output of the source current waveform is initiated exactly at the time the DAUs start to acquire data. The first samples acquired by the DAUs are used to adjust their analog–to–digital converter's gain as described in section 2.2.4.

After the data acquisition is finished, preprocessing of the measured voltage time-series is carried out on the DAUs as described in section 2.2.5 and subsequently all DAUs reconnect to the data bus to enable transfer of the measured data and the preprocessing results back to the field computer. The time required for the data processing depends on the number of samples taken. Field tests revealed that for time-series with up to 500

samples, the data processing takes less than one second.

The data transfer to the central computer takes roughly 260 ms for a single full waveform of typical length (200 samples in this case). In contrast, only 30 ms are required to send back the key waveform parameter results of a pre-processed time-series. The time savings achieved in doing so (230 ms) is rather small compared to the time required for the complete acquisition process ($\approx 4.5s$, see Figure 2.9). However, this time difference becomes crucial for large field surveys entailing parallel data acquisition of up to several hundred DAUs as illustrated in Figure 2.9(b). It shows the time required for a single parallel scan with 100 DAUs. Due to the serial RS-485 data bus employed, measurement results from the individual DAUs need to be transferred back to the central computer, one at a time. In the case where the full waveforms from all DAUs are transferred back to the field notebook (which was required by the original *ETH-DCMES*), the acquisition time would be 29.4 s. This time is reduced down to merely 7.3 s when only the summary parameters characterising the waveform after pre-processing are sent back. Hence, by distributing the data analysis, acquisition times with the *ETH-DCMES-II* could be reduced to a quarter of the times required previously. It is instructive to compare these data acquisition times to the time it would take for a series of 100 serial measurements (i.e. not using the parallel recording mode) – almost seven and a half minutes (Figure 2.9(b)).

	Samples	*ETH-DCMES-II*	*ETH-DCMES*	Geotom
2D survey	≈ 118.000	≈ 5.5 hours	≈ 14 hours	≈ 32 hours
3D survey	≈ 250.000	≈ 7.5 hours	≈ 25 hours	≈ 70 hours

Table 2.1 – Comparison of the recording times actually needed using the *ETH-DCMES-II* with the ones that would have been required with the *ETH-DCMES* and the commercial data acquisition system *Geotom*, respectively.

2.4   Field examples

The *ETH-DCMES-II* has been employed successfully in 2D and 3D resistivity field surveys conducted across a sealed waste-deposit site located approximately 25 km west of Zürich close to the village of Stetten (Switzerland). The resistivity investigations involved a pole-bipole comprehensive data set acquired along a 2D line (50 electrodes) and pole-bipole data acquired using a 3D roll-along scheme with a total of about 250 000 measurements (462 electrode locations). Tomgragraphic inversions of these data sets are dealt with in chapter 4. The *ETH-DCMES-II* system proved to be very reliable during the field operations despite harsh weather conditions. Continuous resistivity

recordings during the day were possible without the need for recharging the DAUs' internal batteries (which was done during the night).

Due to the fast parallel scans offered by the *ETH-DCMES-II* in combination with the distributed data analysis, recording of the $3D$ data set took only ≈ 7.5 hours (excluding the time required to reposition the electrodes for the employed roll-along scheme). Recording the same data set with the *ETH-DCMES* would have taken more than three times as long (≈ 25 hours, see table 2.1). The gain in acquisition speed due to the parallel recording mode of the *ETH-DCMES-II* becomes obvious if we compare these times to the ≈ 70 hours of recording that would have been necessary for acquiring the same data set with the commercial *Geotom* data acquisition system – arguably one of the best systems available on the market. Table 2.1 also shows the same comparison for the comprehensive $2D$ data set comprising $\approx 118{,}000$ measurements. The improvements in acquisition speed due to the parallel recording mode and the distributed data analysis are comparable to those for the $3D$ data set but not as pronounced due to the smaller number of electrodes employed (48 compared to 82 electrodes).

During the $3D$ field campaign at the Stetten waste-deposit site, a few parallel scans have been performed with the full waveforms transferred back to the central computer to assess the ambient noise conditions and to verify the processing of the time-series performed by the DAUs. Figure 6.1 shows typical examples of these waveforms. The recorded time-series are displayed by the blue lines, the red dashed lines are the data fit that would be performed by the corresponding DAUs and the black lines indicate the long-periodic voltage drift of the signals (as revealed by the data fit). Time-series displayed in Figure 6.1 (a), (c)-(d) are typical examples of the waveforms recorded at the Stetten field site. All waveforms displayed exhibit a large dc-shift and a rather mild long-periodic drift. The fraction of the high frequency noise which modulates the signal time-series generally decreases for larger voltage amplitudes (smaller geometry factors) (compare Figures 6.1 (c), (d) and (e)).

The signal displayed in Figure 6.1(a) possesses a spike-like feature. These spikes or glitches regularly appear in the waveforms recorded at the Stetten field site. Furthermore, they always appear synchronously in all the waveforms that belong to the same parallel data scan. Most likely, the noise spikes represent cultural noise in the form of EM pickup from a sorting machine operating at a gravel pit close to the field location.

Figure 6.1(b) shows the frequency spectrum corresponding to the time-series displayed in Figure 6.1(a). As expected, three dominant peaks (indicated by red dashed lines) are clearly visible at the source signal frequency of 2 Hz, the 16.67 Hz frequency used for the Swiss railway system and the powerline frequency of 50 Hz, respectively. The strong signal content in the frequency range between 0 and 2 Hz corresponds to the strong dc-shift and the voltage drift contained in the signal.

Figures 6.1(e) and (f) show examples of problematic signals. The signal in Figure
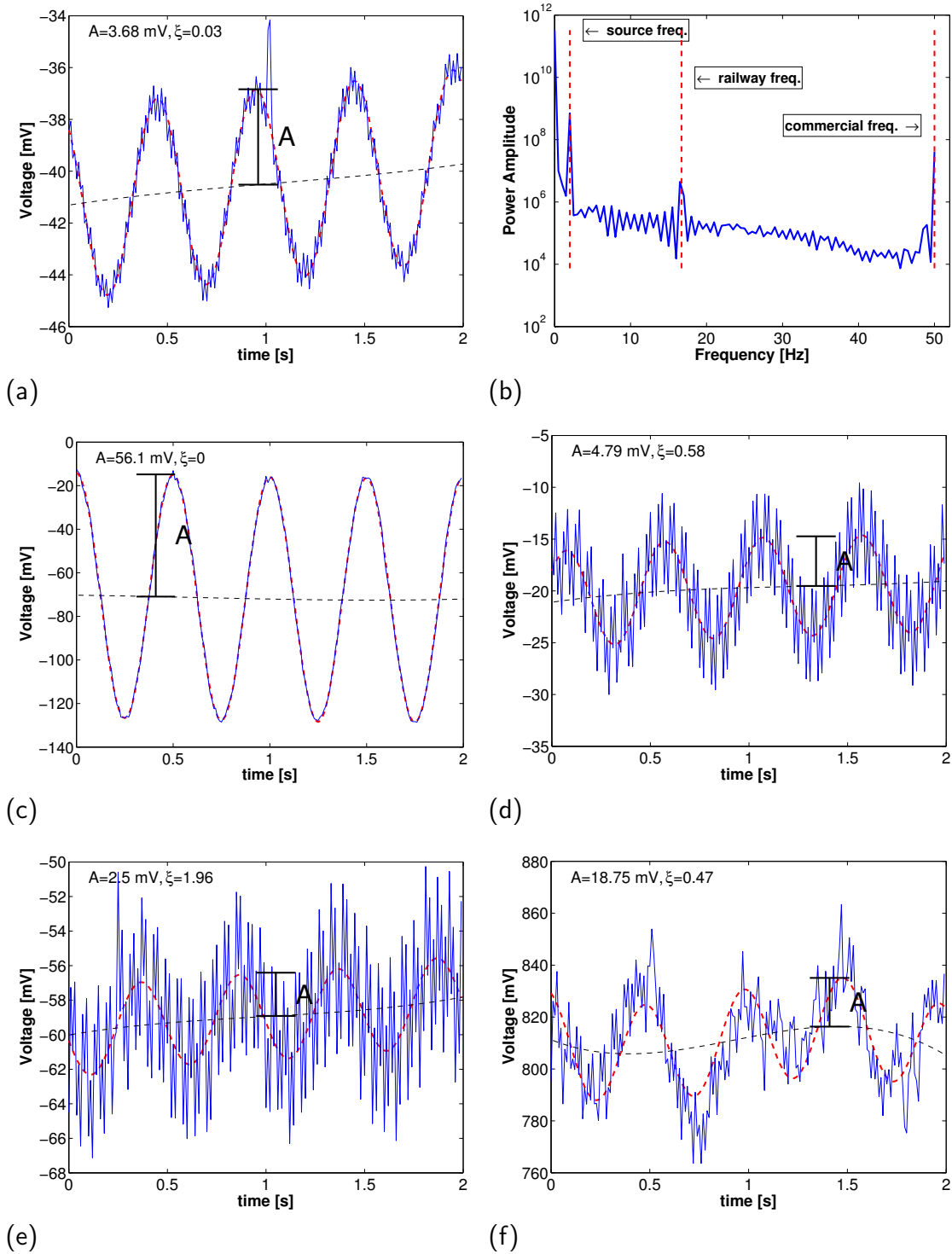
Figure 2.10 – Sample waveforms recorded during the $3D$ field survey at the Stetten waste-deposit site (a, c-f) and a typical frequency spectrum (b). The red dashed lines are the fit estimated by the corresponding DAUs and the black dashed line represents the long-periodic noise trend. Most of the waveforms recorded are similar to the ones shown in (a), (c) and (d). (e) and (f) show problematic signals probably related to a too large geometry factor and a mal-functioning DAU, respectively.

6.1(e)), which is quite small because of the large geometry factor associated with the electrode configuration used, is overshadowed by strong high frequency noise. Nevertheless the data fit (red dashed line) performed by the DAU that recorded the signal seems to resolve the true voltage amplitude with an acceptable accuracy. However, this waveform would be automatically excluded from the data set due to the large data misfit parameter $\xi = 1.96$ returned by the DAU. In contrast, the misfit parameter ξ for the waveform displayed in Figure 6.1(f) indicates a rather good quality signal. In this case, a visual inspection of the recorded waveform reveals that the quality of the signal is rather poor and the corresponding amplitude estimate likely contains a large relative error. The bad signal quality in this case is probably caused by a poor contact between the DAU and the metal electrode. Only a few waveforms of this kind were recorded at the Stetten field site. All of them could be identified by visually comparing the voltage amplitudes of all measurements of the same parallel scan. This can be done conveniently with the data acquisition software developed for the *ETH-DCMES-II* as demonstrated in Appendix C.2. Based on the recorded full waveforms, we conclude that judging the quality of voltage recordings based on the data misfit parameter ξ alone has a serious shortcoming. Potentially too many measurements might be filtered out. Visual inspection of the data set is required to identify questionable or noisy measurements due to technical issues with the DAUs. Further improvements on the time-series fitting algorithm might resolve this issue, for example by taking information from all DAUs involved in a parallel scan into account. Such correlation gain techniques are widely exploited in multichannel seismic recording.

Chapter 3

Advances in 3D geoelectric forward solver techniques

Mark Blome, Hansruedi Maurer, and Kersten Schmidt

Geophysical Journal International, published [1]

3.1 Abstract

Modern geoelectrical data acquisition systems allow large amounts of data to be collected in a short time. Inversions of such data sets require powerful forward solvers for predicting the electrical potentials. State-of-the-art solvers are typically based on finite elements. Recent developments in numerical mathematics led to direct matrix solvers that allow the equation systems arising from such finite element problems to be solved very efficiently. They are particularly useful for 3D geoelectrical problems, where many electrodes are involved. Although modern direct matrix solvers include optimized memory saving strategies, their application to realistic, large-scale 3D problems is still somewhat limited. Therefore, we present two novel techniques that allow the number of grid points to be reduced considerably, while maintaining a high solution accuracy. In the areas surrounding an electrode array we attach infinite elements that continue the electrical potentials to infinity. This does not only reduce the number of grid points, but also avoids the artificial Dirichlet or mixed boundary conditions that are well known to be the cause of numerical inaccuracies. Our second development concerns the singularity

---

removal in the presence of significant surface topography. We employ a fast multipole boundary element method for computing the singular potentials. This renders unnecessary mesh refinements near the electrodes, which results in substantial savings of grid points of up to more than 50%. By means of extensive numerical tests we demonstrate that combined application of infinite elements and singularity removal allows the number of grid points to be reduced by a factor of $\approx 6 - 10$ compared with traditional finite element methods. This will be key for applying finite elements and direct matrix solver techniques to realistic 3D inversion problems.

3.2   Introduction
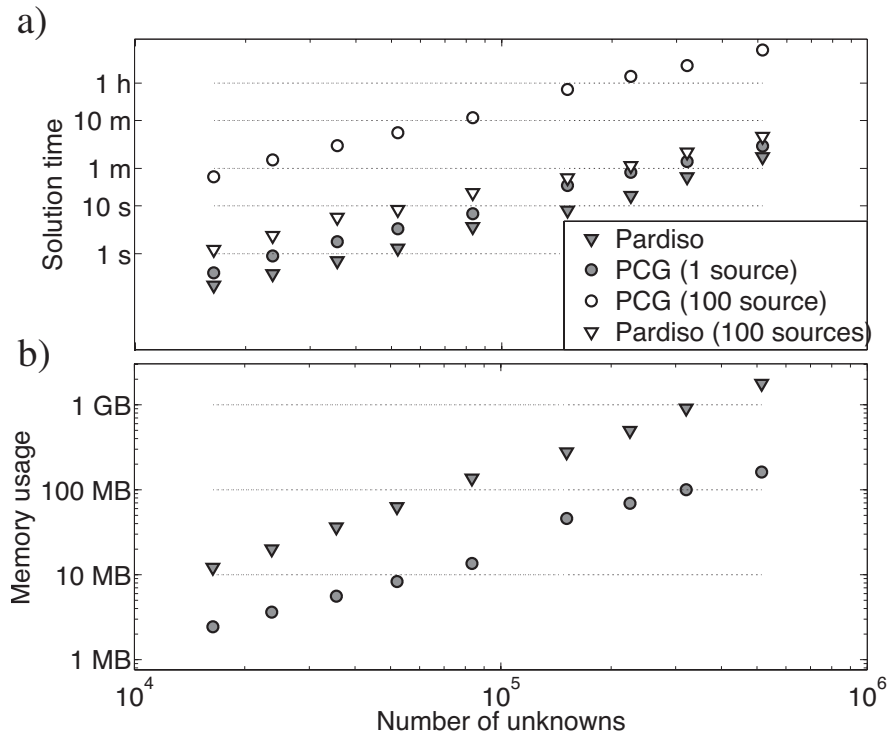
Figure 3.1 – Comparison of the solution time (a) and memory consumption (b) of a preconditioned conjugate gradient solver (PCG, solver tolerance: $1 \cdot 10^{-8}$) and a direct matrix solver (Pardiso). For the tests the geoelectric problem has been solved with the FEM on a series of meshes.

The introduction of multi-electrode data acquisition systems during the 1980's and 1990's has simplified significantly geoelectrical surveying, such that relatively large data sets can now be collected with a moderate field effort (Griffiths and Turnbull, 1985; Stummer *et al.*, 2002). This is certainly an important step towards routine application of 3D surveys, but despite the ever increasing power of computers, realistic 3-D geoelectrical inversions remain challenging. In particular, the solution of the forward problem, i.e. predicting electrical potentials using a particular conductivity model, can be a very

time-consuming task.

During the past few decades much effort has been put into the development of numerical forward solvers. Among the methods used, the finite difference method (FDM) (Mufti, 1976; Dey and Morrison, 1979a; Wang *et al.*, 2000; Zhao and Yedlin, 1996; Spitzer, 1995), the finite element method (FEM) (Coggon, 1971; Pridmore *et al.*, 1981; Li and Spitzer, 2002; Pain *et al.*, 2002; Sasaki, 1994; Zhou and Greenhalgh, 2001) are the most popular. Other methods proposed include the boundary element method (BEM) (Hvozdara and Kaikkonen, 1998; Xu *et al.*, 1998; Ma, 2002) and the integral equation method (IEM) (Lee, 1975; Dieter *et al.*, 1969).

The FDM, first employed for geoelectrics by Mufti (1976) for 2D and by Dey and Morrison (1979a) for 3D problems, has been the method of choice in the geoelectric community for a long time due to its easy and flexible implementation.

Unfortunately, finite difference calculations are generally restricted to structured, orthogonal grids that do not allow local mesh refinements. Only global refinements with respect to a single spatial coordinate can be implemented. This results in an unnecessarily large number of grid points. Furthermore, complicated topography cannot be handled by orthogonal grids, although attempts have been made to circumvent this limitation (e.g. Loke and Barker, 1996a).

The FEM allows unstructured meshes to be used and is therefore much more flexible. In particular, complicated topographies can be implemented and the meshes can be almost arbitrarily coarsened or densified in regions where necessary. For example, Rücker *et al.* (2006) presented a 3D geoelectric forward solver based on tetrahedral unstructured elements that clearly show the advantages of unstructured domain discretizations.

FDM and FEM are attractive options when the subsurface conductivity distributions are highly heterogeneous. For less complicated subsurface structures, for example, a layered halfspace with a few simply-shaped inclusions, application of the BEM or IEM can be advantageous. For example Ma (2002) provided BEM solutions for 3-D inhomogeneous bodies buried in a layered earth and Hvozdara and Kaikkonen (1998) used the BEM to calculate the response of a rectangular prism embedded in a homogeneous subsurface.

Due to its flexibility with regard to domain discretization and model complexity, the FEM is in our view currently the most appropriate method for 3D geoelectrical inversion problems. Its implementation results in a system of equations of the form

$$\mathbf{A}\mathbf{x} = \mathbf{b}, \qquad (3.1)$$

where matrix $\mathbf{A}$ represents the domain discretization and the conductivity model, vector $\mathbf{x}$ includes the unknown potentials or potential differences and vector $\mathbf{b}$ characterizes the geoelectrical sources. Matrix $\mathbf{A}$ is of the size $n \times n$, where n is the number of grid

points in the finite element mesh. It can be very large (n is typically of the order 10^4 to 10^6 or even larger), but it is also extremely sparse.

Such systems of equations can be solved most efficiently with iterative solvers such as the preconditioned conjugate gradient method (Hestenes, 1952; Spitzer, 1995). During geoelectrical inversions the forward problem needs to be solved at least n_e times, where n_e is the number of electrodes employed. Typical 3D surveys may include several hundred electrode positions. It is important to note that the finite element equations can easily be formulated such that only the right hand side **b** of Equation 3.1 changes for the individual electrode positions. This motivates application of direct matrix solvers. Here, the matrix **A** is factorized in a lower and upper triangular matrix using LU decomposition. Once the factorization is performed, solutions for multiple right hand side arguments **b** can be obtained swiftly by simple back substitutions. Despite this very attractive property, direct matrix solvers have been applied so far rarely for the solution of FEM problems. Main reasons for that include the expensive matrix factorization and, more importantly, the fact that the resulting triangular matrices are generally full, which is prohibitive in terms of memory requirements for typical FEM problems.

During the past few years, significant new developments in sparse direct matrix solver techniques emerged (Schenk *et al.*, 2003). Modern implementations are based on matrix reordering strategies that drastically reduce the memory consumption of the matrix factors. Still, for large 3D forward problems the memory requirements of direct matrix solvers can be excessive. Figure 3.1 illustrates advantages and limitations of direct matrix solvers. We employed the state-of-the-art *PARDISO* solver (Schenk *et al.*, 2001) for computing FEM solutions for different grid sizes. A nested dissection reordering strategy (Karypis and Kumar, 1995) was chosen, which proved to be most efficient for our purposes. For comparison, we recomputed the solutions with an iterative preconditioned conjugate gradient solver.

For a single forward solution the direct and iterative solvers show comparable performance, but for the solution including multiple electrode positions, the direct matrix solver clearly outperforms the iterative algorithm (Figure 3.1(a)).

The superiority of the direct matrix solver comes at the expense of memory usage. Despite the application of sophisticated matrix reordering strategies, its memory consumption is still about a factor of 10 higher compared with the iterative solver (Figure 3.1(b)). Solutions of 3D FEM problems including more than 10^6 nodes may thus require excessive amounts of memory.

In this paper, we present two novel techniques that allow the number of grid points of FEM meshes to be reduced significantly. These developments thus allow very large 3D geoelectrical forward problems to be solved with direct matrix solvers, which results in a considerable efficiency improvement of the corresponding inverse problem. The first technique is devoted to the reduction of nodes that are introduced to move the mesh

boundaries (open boundaries within the subsurface) sufficiently far away from the model region of interest. This is achieved with the application of so-called infinite elements (Astley *et al.*, 1998a). Our second development concerns the mesh refinements near the electrode positions. Refinements are required to achieve a high solution accuracy near the singularities of the electrical potentials. Lowry *et al.* (1989) showed that the singularities at the electrodes can be removed by splitting the electrical potential in a singular part that can be computed analytically and a non-singular part that needs to be determined numerically. Unfortunately, analytical solutions for the singular potential exist only for special cases such as homogeneous or layered halfspaces without surface topography. We employ a fast multipole BEM technique (Hackbusch and Nowak, 1989) that allows the singular potential for a homogeneous halfspace with arbitrary topography to be computed efficiently.

In the first part of the paper, we briefly review the fundamentals of the geoelectrical forward problem, the singularity removal technique and the finite element approximation to the governing partial differential equations. Then, we present the open boundary handling with infinite elements followed by a description of the fast multipole BEM technique that we employ for the singularity removal. The performance of these new developments is demonstrated with a series of numerical experiments. In particular, we show that the number of grid points can be reduced significantly without degrading the solution accuracy.

3.3   3D geoelectric forward modelling

3.3.1   Boundary value problem

The geoelectric forward problem is governed by the Poisson equation

$$\nabla \cdot (\sigma \nabla U) = -I_0 \delta(|\mathbf{r} - \mathbf{r_s}|) \qquad \text{in } \Omega \tag{3.2}$$

which results from the equation of continuity for a current strength I_0 injected at a source position r_s into a domain Ω with an arbitrary conductivity distribution σ. Here, we restrict the discussion to single current injection electrodes (pole-pole configuration). Commonly used 4-point electrode configurations can be obtained by superposition of pole-pole potentials.

The domain boundary Γ of Ω can be subdivided into a surface part Γ_s and a subsurface part Γ_g. Since no current can flow into the air, the Neumann boundary condition

$$\frac{\partial U}{\partial \mathbf{n}} = 0 \text{ on } \Gamma_s, \tag{3.3}$$

has to be applied on Γ_s ($\mathbf{n}$ is the outward pointing normal vector on Γ_s). The ground

boundary Γ_g is introduced only for numerical purposes to keep Ω finite. No exact boundary conditions along Γ_g exist. Mixed boundary conditions

$$\frac{\partial U}{\partial \mathbf{n}} + \beta U = 0 \text{ on } \Gamma_g \tag{3.4}$$

have proved to be a reasonable option for Γ_g, whereby the factor β has to be chosen to be $\beta = \mathbf{n} \cdot \mathbf{r}/|\mathbf{r}|^2$ for electrodes placed on Γ_s. Vector $\mathbf{r}$ represents the distance between the source electrode and the boundary Γ_g.

3.3.2 Singularity removal

The solutions of the geoelectric forward problem contain singularities at the source electrode positions due to the δ-function on the right hand side of Equation 3.2. Near these singularities the electrical potential U varies rapidly. To obtain a numerically stable solution of Equation 3.2, a very fine spatial sampling around the electrodes is required, which is computationally inefficient. Lowry *et al.* (1989) presented an alternative approach in which the singularities are removed prior to the numerical solution. This is achieved by splitting the electrical potential U into a singular part U^s and a non-singular part U^n: In the absence of significant topography the singular potential can be expressed by an analytical homogeneous halfspace solution (for surface electrodes)

$$U_h^s = \frac{I_0}{2\pi\sigma_0} \frac{1}{|\mathbf{r} - \mathbf{r}_s|} \tag{3.5}$$

with σ_0 equal to the mean subsurface conductivity, as originally proposed by Lowry *et al.* (1989), or, for a more accurate singularity removal, equal to the conductivity at the source electrode position (Zhao and Yedlin, 1996).

Conceptually, more complex background conductivity models $\sigma_0(x, y, z)$, for which analytical or numerical solutions to Equation 3.2 exists, may be considered. For example, Li and Spitzer (2002) employed horizontally layered earth and vertical contact conductivity models for evaluating the singular potentials U^s.

Formally, the singularity removal is achieved by substituting $U = U^s + U^n$ on the left hand side of Equation 3.2, and substituting

$$\nabla \cdot (\sigma_0 \nabla U^s) = -I_0 \delta(|\mathbf{r} - \mathbf{r}_s|) \tag{3.6}$$

on the right hand side of Equation 3.2. Rearranging terms leads to a modified Poisson equation

$$\nabla \cdot (\sigma(\mathbf{r})\nabla U^n) = -\nabla \cdot ((\sigma(\mathbf{r}) - \sigma_0)\nabla U^s), \tag{3.7}$$

where the δ-function in the right hand side has vanished. The problem is reduced to

determining only the non-singular potential field that results from subsurface conductivities not equal to the background conductivity σ_0. Once the non-singular potential U^n is found, U^s is added to obtain the total electrical potential U.

When the singularity removal technique is applied, mixed type boundary conditions for U^n are not beneficial, because an approximate expression of the non-singular potential field is not known along the ground boundaries. Zhao and Yedlin (1996) suggest application of Dirichlet boundary conditions, i.e. U^n should be forced to be zero along Γ_g.

3.3.3   Finite element equations

In the finite element method, the domain Ω is subdivided in small subregions, which are referred to as finite elements. Within each element the unknown potential U^n (Equation 3.7) is approximated by a linear combination of so called shape functions α_k

$$U^n(x, y, z) = \sum_{k=1}^{p} \alpha_k(x, y, z) u_k^n, \tag{3.8}$$

where P denotes the number of nodes associated with a single element and u_k^n the unknown potential values at the nodes. Appropriate approximations for U^n should minimize the integral

$$\int_{\Omega} [\nabla \cdot (\sigma(\mathbf{r}) \nabla U^n) + \nabla \cdot ((\sigma(\mathbf{r}) - \sigma_0) \nabla U^s)] \omega d\Omega, \tag{3.9}$$

where ω is a weighting function. If the weighting functions are chosen to be equal to the shape functions α_k, the Galerkin solution is obtained (Zienkiewicz, 1977). In order to employ linear shape functions, it is necessary to remove the second derivatives with respect to the potential U^n. This is achieved by applying Green's first identity to Equation 3.9, which results in the weak or variational form

$$\int_{\Omega} \sigma \nabla U^n \cdot \nabla \omega d\Omega - \int_{\Gamma} \sigma \omega \frac{\partial U^n}{\partial \mathbf{n}} d\Gamma$$
$$= -\int_{\Omega} \nabla \cdot ((\sigma(\mathbf{r}) - \sigma_0) \nabla U^s) \omega d\Omega. \tag{3.10}$$

Note that the corresponding expression for the total potential U (Equation 3.2) takes a similar form, but contains the δ-function under the volume integral on the right side. After discretization by finite elements, Equation 3.10 leads to a linear system of equations. Since only the right-hand side of Equation 3.10 includes source electrode dependent terms, the system(s) of linear equations can be suitably solved with direct matrix solvers.

3.3.4   Domain discretization

(a)   (b)
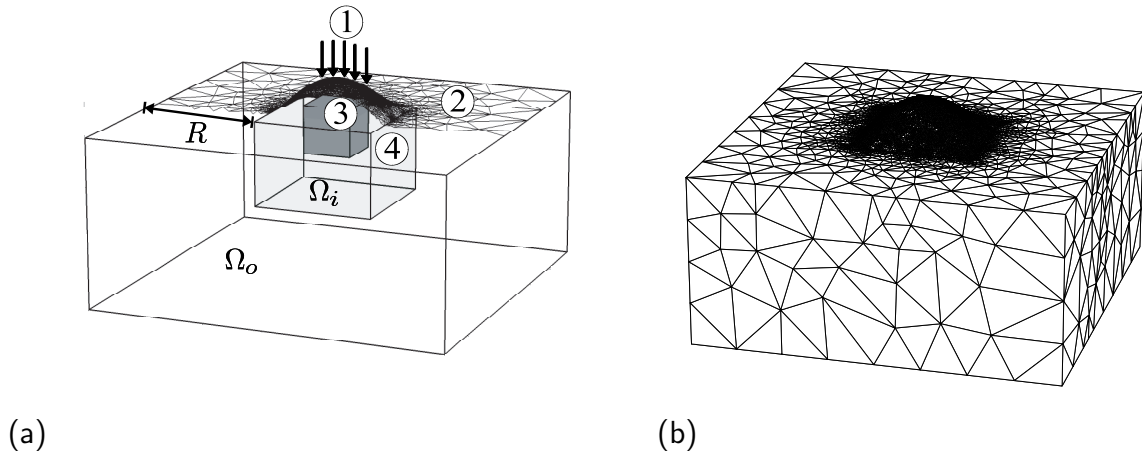
Figure 3.2 – (a) Model description: 1: Electrode positions, 2: discretized surface topography,
3: optional internal boundaries, 4: inversion region (domain Ω_i). (b) The resulting finite
element mesh.

We employ unstructured finite element meshes, which provide an enormous flexibility
with regard to the mesh density inside Ω and the shape of the boundary Γ. In partic-
ular, this facilitates local mesh refinements in critical areas and allows straightforward
implementation of arbitrary complicated surface topography. Figure 3.2 illustrates our
meshing procedure. At first, the mesher is enforced to include nodes at the electrode
positions (see label (1) in Figure 3.2(a)). The surface topography (e.g. measured via
GPS in the field) is then discretized by a triangular mesh (2). Internal boundaries, for
example to represent boreholes, geological layers or conductivity model boundaries can
optionally be defined (3). Inside the computational domain, we choose a tetrahedron-
based discretization. To ensure solution accuracy, a maximum size constraint for all
tetrahedrons is specified in the region Ω_i below the electrode array (4). The inner region
Ω_i is surrounded by an outer region Ω_o, whose extent is defined by the distance R. In our
experience (and in accordance to Rücker *et al.* (2006)), R should be approximately $5-10$
times the size of the largest electrode spacing. Within Ω_o the mesh density decreases
towards the model boundaries, whereby the growth rate of the finite elements is con-
trolled by the maximum element aspect-ratio. The larger the ratio, the more elongated
the elements may be, hence the faster the element size can grow towards the boundary.
Besides defining the element growth rate, the aspect-ratio constraint ensures reasonably
well-shaped mesh elements. Badly shaped elements, i.e. having a too large aspect-ratio,
may degrade the solution accuracy (Wang *et al.*, 2000). Figure 3.2(b) shows an example
of a suitably designed mesh.

Once the initial meshing is completed, local refinements can be applied (e.g. close to
the source electrodes) by inserting additional nodes into the mesh. During the remeshing
procedure the maximum aspect-ratio constraint is re-enforced, which automatically leads

to a local refinement around the additional nodes. Optionally the finite element mesh can be converted to a second order finite element mesh. This is achieved by adding one additional node in the middle of each element edge. For our tetrahedron discretization, this results in ten instead of four nodes per element. Quadratic shape functions are used to approximate the solution on second order finite elements (see equation 3.38).

3.3.5 Open source FEM libraries

Our modelling algorithms are based on several public domain libraries that we modified for our purposes. In particular, we employed *Triangle* (Shewchuk, 1996) for discretizing the surface topography and the quality mesher *Tetgen* (Si and Gaertner, 2005) for performing the volume discretization. The matrix equation assembly routines rely on the finite element library *Libmesh* (Kirk *et al.*, 2006) and the resulting equations were solved with the direct matrix solver *Pardiso* (Schenk *et al.*, 2001). Furthermore, we used the FM-BEM classes in the numerical library *Concepts* (Frauenfelder and Lage, 2002) for the singularity removal.

3.4 Open boundary handling via infinite elements

(a)   (b)
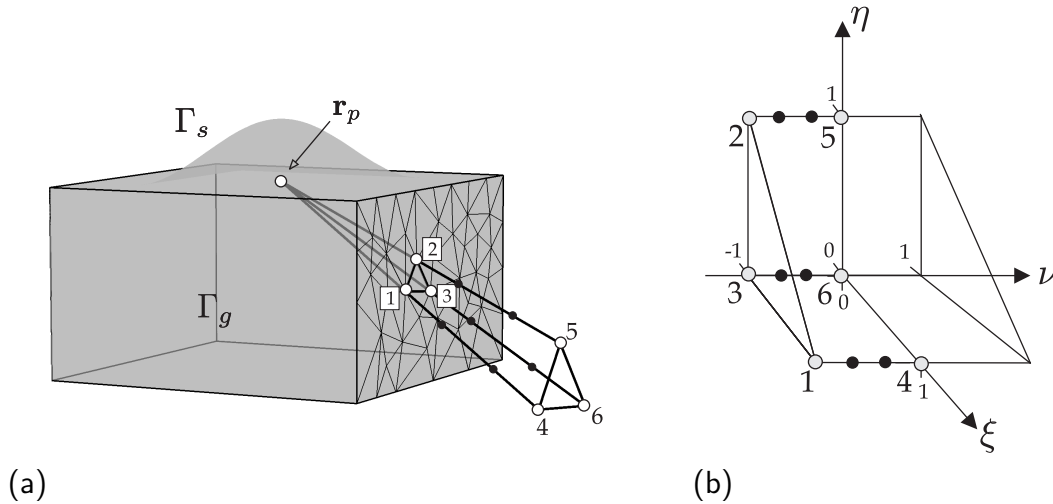
Figure 3.3 – (a) A sample infinite element attached at the ground boundary Γ_g of a FE mesh. The infinite elements are constructed by choosing a common pole that defines their radial direction. The geometry of the infinite elements is defined by projecting rays from the pole through the triangular boundary faces outwards. The outermost three nodes that lie at infinity, are not displayed in this figure. (b) In local coordinates the infinite elements are mapped to a finite extent, where the numerical integration is carried out.

The artificial ground boundaries Γ_g that appear in the finite element formulation to the Poisson equation are introduced only to keep the computational domain Ω finite. This inherently introduces errors in the numerical solution of Equation 3.2. To alleviate

the problem, the outer domain Ω_o must be made very large, but this requires a significant number of additional elements and nodes, which would increase the computational costs unnecessarily.

Infinite elements, originally developed in the field of acoustic radiation (Bettes, 1987), provide a cost-effective and elegant alternative to deal with open boundary problems. Instead of truncating the domain at a certain distance away from the electrode array, the outer domain is modelled by infinite elements. We employ the so-called *Astley-Leys* elements, originally developed by Astley *et al.* (1998a) and later refined for an improved conditioning of the resulting linear system of equations by Dreyer and von Estorff (2003).

The infinite elements are attached to the subsurface boundary Γ_g as shown in Figure 3.3(a). In contrast to the traditional approach using mixed-type or Dirichlet boundary conditions, the extent of Ω_o can be much smaller, i.e., the distance R in Figure 3.2(a) needs to be equal to only about half the largest electrodes spacing (compared to a factor of 5 to 10 for the traditional approach). A single pole inside the FE mesh is chosen at point $\mathbf{r_p}$ for all infinite elements to define the infinite elements radial directions (Figure 3.3(a)). We choose $\mathbf{r}_p$ in the horizontal directions to coincide with the geometric mean of all source electrode positions because the potential fields decrease radially outwards from the source electrodes. The vertical location of $\mathbf{r_p}$ is given by the zero level of the topography to assure a well-shaped continuation of the finite element domain by the infinite elements.

The prismatic-shaped infinite elements are made-up of 9 nodes. The first three nodes coincide with the triangular faces on the boundary Γ_g (nodes 1,2 and 3 located at $\mathbf{r}_1^i$ ($i = 1..3$)) and the outer three nodes (4,5 and 6) are located at positions $\mathbf{r}_2^i = \mathbf{r}_1^i + (\mathbf{r}_1^i - \mathbf{r}_p)$ as shown in Figure 3.3(a). The last three nodes $\mathbf{r}_3^i$ are located at an infinite distance away from $\mathbf{r_p}$ in direction of $\mathbf{n}^i = \mathbf{r}_2^i - \mathbf{r}_1^i$ and are thus not displayed in Figure 3.3(a). The infinite extend of the infinite elements in the radial direction allows the potential field to be approximated up to infinity instead of truncating it at the domain boundaries Γ_g.

A coordinate transformation from the global (x, y, z)-coordinate system to the local (ξ, η, ν)-coordinate system is used to perform the integration necessary to set up the FEM equations:

$$\mathbf{r}^i(\nu) = \frac{-2\nu}{1-\nu}\mathbf{r}_1^i + \frac{1+\nu}{1-\nu}\mathbf{r}_2^i. \tag{3.11}$$

As shown in Figure 3.3, this transformation maps the nodes located at $\mathbf{r}^i = \{\mathbf{r}_1^i, \mathbf{r}_2^i, \infty \cdot \mathbf{n}^i\}$ to the coordinates $\nu = \{-1, 0, 1\}$ in the local (ξ, η, ν)-coordinate system, where the integration can be carried out efficiently with standard Gaussian quadrature rules.

The infinite elements are endowed with standard finite element linear or second order shape functions S_i in the ξ, η-plane and with special shape functions in the radial direction (ν) that are based on Jacobi polynomials $P_i^{(2,0)}$. The order of the Jacobi
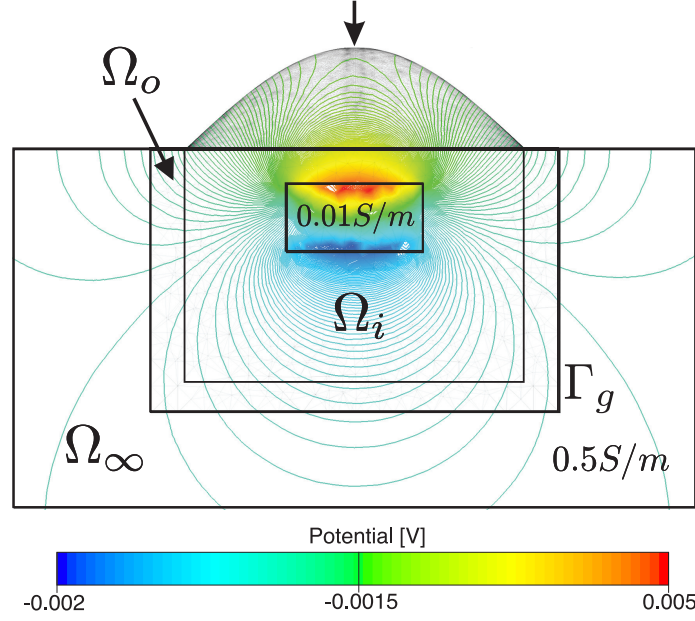
Figure 3.4 – Non-singular potential field for a prismatic-shaped anomaly embedded in a homogeneous background. The potential field is accurately continued beyond the boundaries of the finite element mesh (region Ω_o).

polynomials can be chosen between 3 and 14, where higher radial orders will give rise to additional degrees of freedoms (indicated by the small black dots in Figure 3.3). In our experience a radial order of 5 yields sufficiently accurate results. Finally, the approximation of the potential U inside the infinite elements is given by:

$$U = \sum_i U_i \widetilde{\phi}_i \text{ with } \widetilde{\phi}_i = 1/2 S_i(\xi, \eta)(1 - \nu) P_i^{(2,0)}(\nu). \tag{3.12}$$

Modified test functions are chosen to improve the conditioning of the resulting equations (Dreyer and von Estorff, 2003). The resulting element matrices are slightly different to the ones obtained for conventional finite elements (compare to Equation 3.10):

$$\mathbf{A}_{i,j}^n = \int_{\Omega_n} \sigma_n \nabla \widetilde{\phi}_i \cdot (\widetilde{\phi}_j \nabla D_j + D_j \nabla \widetilde{\phi}_j) d\Omega_n. \tag{3.13}$$

Here $\widetilde{\phi}_i$ are the infinite elements shape functions as defined in Equation 3.12 and $D(\nu) = ((1 - \nu)/2)^2$ are additional radial weights.

In contrast to conventional finite element matrices, the matrices $\mathbf{A}^n$ are asymmetric (due to the radial weight functions D). Therefore, infinite elements lead to slightly asymmetric system matrices. Consequently, we choose either a preconditioned *quadratic minimum residual* iterative solver or the *LU* direct solver implemented in *Pardiso* to solve the resulting system of equations.

Performance of infinite elements is demonstrated in Figure 3.4, which shows the non-singular potential field caused by a cuboid-shaped anomaly. The singularity re-

moval technique leads to sources inside the conductivity anomaly that can physically be interpreted as charges accumulating along the conductivity contrasts (Mendonca, 2003). These charges create a potential field with a dipolar character. As shown in Figure 3.4, the dipolar field is continued properly into the area of the infinite elements. If Dirichlet boundary conditions would have been applied, the potential lines at Γ_g would have been forced to be parallel to the domain boundaries. This unphysical constraint would certainly have led to errors in the potential field computations.

3.5 Singular potential evaluation using a fast multipole BEM

(a)   (b)
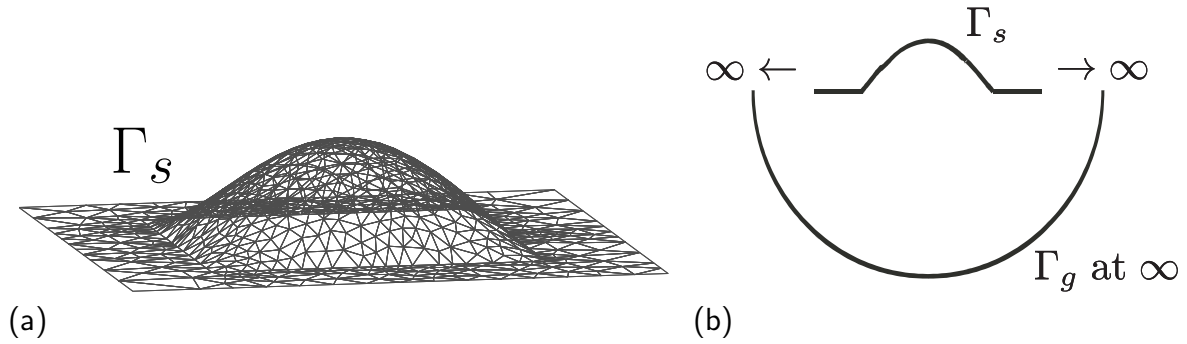
Figure 3.5 – (a) A typical surface mesh used in the BEM (only the inner, i.e. topographic part is shown here). (b) By moving the ground boundaries to ∞, only the inner part of the surface Γ_s needs to be discretized.

As discussed in section 3.3.2, the singularity removal technique allows computation of electrical potentials without excessive grid refinements around the electrodes, but it requires the singular potential to be calculated separately. Unfortunately, no analytical solution exists for homogeneous halfspaces with significant surface topography, but the principal features of the BEM (Xu *et al.*, 1998; Ma, 2002) make this method very suitable for this purpose. In the following, we restrict ourselves to surface electrodes, but the same formulation with minor modifications is applicable to buried electrodes.

3.5.1 Boundary integral equation

When solving the singular potentials with the BEM, the Poisson equation

$$\begin{cases} \sigma_0 \nabla^2 U^s = -I_0 \delta(\mathbf{r} - \mathbf{r}_0) & \text{in } \Omega \\ \partial U^s / \partial \mathbf{n} = 0 & \text{on } \Gamma_s \\ \quad U^s = 0 & \text{on } \Gamma_g \end{cases} \qquad (3.14)$$

needs to be transformed into a Laplace equation with modified boundary conditions. Note that the choice of the ground boundary conditions in Equation 3.14 (Dirichlet type

in this case) is arbitrary, because the BEM allows the artificial ground boundaries to be eliminated anyway. The transformation to the Laplace equation is achieved by splitting the singular potential solution U^s into a homogeneous part U_h^s and an inhomogeneous part U_i^s:

$$U^s = U_i^s + U_h^s \quad \text{with} \quad U_i^s(\mathbf{r}) = \frac{I_0}{2\pi\sigma_0} \frac{1}{|\mathbf{r} - \mathbf{r}_0|} \tag{3.15}$$

and solving only for the homogeneous part of the solution under modified boundary conditions

$$\begin{cases} \sigma_0 \nabla^2 U_h^s = 0 & \text{in } \Omega \\ \partial U_h^s/\partial\mathbf{n} = -\partial U_i^s/\partial\mathbf{n} & \text{on } \Gamma_s \\ U_h^s = -U_i^s & \text{on } \Gamma_g. \end{cases} \tag{3.16}$$

After the solution U_h^s has been found with the BEM, the inhomogeneous solution is added to yield the total singular potential U^s. Due to the linearity of Equation 3.16 with respect to σ_0, U^s can be estimated for an arbitrary value of σ_0 and later scaled to meet the true conductivity at the source electrode. In this way, the singular potentials need to be estimated only once prior to an inversion process. In the following discussion we assume $\sigma_0 = 1$.

As for the finite element equations we use Galerkin's criterion to derive the boundary integral equation corresponding to Equation 3.16:

$$\int_\Omega \nabla^2 U_h^s(\mathbf{r}) G(\mathbf{r}, \mathbf{r}') \, d\Omega = 0 \tag{3.17}$$

Here $G(\mathbf{r}, \mathbf{r}')$ denotes the Green's function to the Laplace operator ∇^2. Applying Green's first identity twice yields the boundary integral equation:

$$\underbrace{\int_\Omega U_h^s(\mathbf{r})\nabla^2 G(\mathbf{r}, \mathbf{r}') \, d\Omega}_{k\,U_h^s(\mathbf{r}')} + \int_\Gamma U_h^s(\mathbf{r})\frac{\partial G(\mathbf{r}, \mathbf{r}')}{\partial\mathbf{n}} \, dS_\mathbf{r}$$

$$= \int_\Gamma \frac{\partial U_h^s(\mathbf{r})}{\partial\mathbf{n}} G(\mathbf{r}, \mathbf{r}') \, dS_\mathbf{r}, \quad \begin{cases} k = 1 & \text{for } \mathbf{r}' \text{ in } \Omega \\ k = 1/2 & \text{for } \mathbf{r}' \text{ on } \Gamma. \end{cases} \tag{3.18}$$

In contrast to the FEM approach, where local basis functions are chosen as the weighting function, full space Green's functions $G(\mathbf{r}, \mathbf{r}')$ are employed in the BEM. Usually homogeneous subsurface solutions are used, but in general Green's functions for arbitrary background conductivity models may be employed, though expressions for these functions can be hard to find or may not exist at all. Ma (2002), for instance, demonstrated the use of layered background conductivity models in BEM calculations. The Green's functions are fundamental solutions to the Laplace operator, therefore the

volume integral in Equation 3.18 reduces to simple function evaluations. Only boundary integrals remain to be evaluated and consequently only the boundary of the domain Ω needs to be discretized. The dimensionality of the problem is reduced from 3D to 2D, resulting in a substantial reduction of the number of unknowns in the equations to be solved. For evaluation points $\mathbf{r}'$ on Γ Equation 3.18 leads to an integral equation that relates U_h^s on Γ to integral expressions over Γ and therefore can be used to solve for the singular potentials along the boundary of the domain. Subsequently, by choosing evaluation points $\mathbf{r}'$ in Ω, Equation 3.18 can be used to evaluate the singular potentials inside the domain. Mathematical analysis (e.g. Sauter and Schwab, 2004) shows that in the first case Equation 3.18 is valid for $k = 1/2$ whereas in the latter case $k = 1$ results.

The absence of volume integrals in the BEM allows for a very natural handling of the unbounded domain that occurs during the computation of the singular potentials. Figure 3.5(b) depicts a sketch of the integration principle. Instead of truncating the domain at a certain distance away from the source electrodes the ground boundaries Γ_g are moved to infinity. As U_i^s and therefore U_h^s approaches 0 at an infinite distance away from the source electrode, the boundary integrals along Γ_g vanish. Along Γ_s the integration can be truncated after a certain distance away from the source ($\approx 5 - 10$ times the largest electrode distance) when $\partial U_h^s/\partial \mathbf{n} = -\partial U_i^s/\partial \mathbf{n} \approx 0$ and thus only an inner part of Γ_s needs to be discretized. Figure 3.5(a) shows an example triangular mesh used for the BEM (for clarity, the outer part of the mesh is not shown).

To obtain accuracy and stability of the solution we employ a weak formulation of the boundary integral Equation 3.18:

$$
\frac{1}{2} \int_{\Gamma_s} U_h^s(\mathbf{r}') \phi(\mathbf{r}') \, dS_{\mathbf{r}'} + \int_{\Gamma_s} \int_{\Gamma_s} U_h^s(\mathbf{r}) \frac{\partial G(\mathbf{r}, \mathbf{r}')}{\partial \mathbf{n}} \phi(\mathbf{r}') \, dS_{\mathbf{r}} \, dS_{\mathbf{r}'}
$$
$$
= \int_{\Gamma_s} \int_{\Gamma_s} \frac{\partial U_h^s(\mathbf{r}')}{\partial \mathbf{n}} G(\mathbf{r}, \mathbf{r}') \phi(\mathbf{r}') \, dS_{\mathbf{r}} \, dS_{\mathbf{r}'}. \tag{3.19}
$$

After discretization by unstructured triangular elements with linear shape functions ϕ_i, Equation 3.19 leads to a linear system of equations

$$
\mathbf{A} \mathbf{u}_h^s = \mathbf{B} \mathbf{q} \tag{3.20}
$$

with the matrix entries given by

$$
\mathbf{A}_{ij} = 1/2 \int_{\Gamma_s} \phi_i(\mathbf{r}) \phi_j(\mathbf{r}') \, dS_{\mathbf{r}'}
$$
$$
+ \int_{\Gamma_s} \int_{\Gamma_s} \phi_i(\mathbf{r}) \frac{\partial G(\mathbf{r}, \mathbf{r}')}{\partial \mathbf{n}} \phi_j(\mathbf{r}') \, dS_{\mathbf{r}} \, dS_{\mathbf{r}'} \tag{3.21}
$$
$$
\mathbf{B}_{ij} = \int_{\Gamma_s} \int_{\Gamma_s} \phi_i(\mathbf{r}) G(\mathbf{r}, \mathbf{r}') \phi_j(\mathbf{r}') \, dS_{\mathbf{r}} \, dS_{\mathbf{r}'}, \tag{3.22}
$$

and the Neumann boundary condition values

$$\mathbf{q}_i = \partial U_{h,i}^s / \partial \mathbf{n}_i. \tag{3.23}$$

Equation 3.20 yields the unknown potential values $\mathbf{u}_h^s$ on the nodes of the surface mesh. Subsequently, Equation 3.18 needs to be re-evaluated in a second step to obtain the potential solution inside the volume (i.e. at all nodes of the corresponding FE mesh).

3.5.2   The fast multipole BEM

The BEM matrices $\mathbf{A}$ and $\mathbf{B}$ in equations 3.21 and 3.22 are fully populated due to the coupling of the Green's function $G(\mathbf{r}, \mathbf{r}')$. Consequently the computational costs, memory consumption and solution time, scale as $\sim \mathcal{O}(N^2)$ for the BEM while they scale as $\sim \mathcal{O}(M)$ for the FEM, for which system matrices are usually extremely sparse (here N and M denote the number of unknowns in the BEM respectively the FEM equations). This imposes a serious limitation on the applicability of the BEM, because especially the unfavorable memory consumption may easily render the BEM inefficient compared to the FEM.

To account for this major drawback of the standard BEM, fast multipole boundary element methods (FM-BEM) were introduced (Hackbusch and Nowak, 1989). These methods employ the fast multipole method originally developed by Greengard and Rokhlin (1987) by expanding the Green's function $G(\mathbf{r}, \mathbf{r}')$ in the far field by a function series such that the variables $\mathbf{r}$ and $\mathbf{r}'$ are separated. With this kernel expansion the matrix assembly and the solution times are considerably reduced by combining the effects of Green's function evaluation points in the far field to so-called multipole moments. In the near field, i.e. where $\mathbf{r}$ and $\mathbf{r}'$ are close-by, standard Green's function evaluations are used. Effectively, this scheme leads to an approximation of the fully populated BEM matrix by a sparse near field matrix and a sum of low-rank far field approximation matrices. The FM-BEM employs a multilevel scheme to exploit the use of multipole moments as efficiently as possible. The computational costs for matrix vector products needed when solving the resulting system of equations with iterative solvers is reduced from $\sim \mathcal{O}(N^2)$ to $\sim \mathcal{O}(N log^\alpha(N))$. We employ a variant of the FM-BEM called *Panel Clustering Method* implemented by Lage (1995) to solve for the singular potentials efficiently. Details about the method used can be found in Appendix 3.9.1.
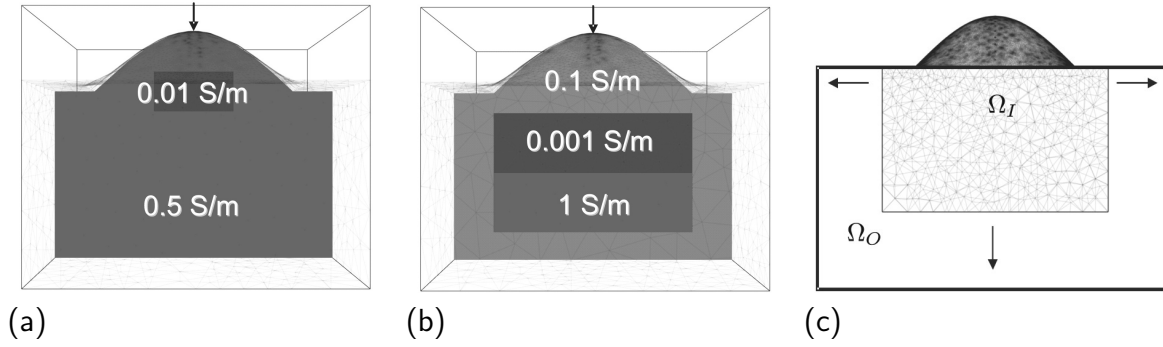
Figure 3.6 – (a) Cuboid model (b) Layered block model (c) The mesh size is increased by moving the subsurface boundaries outwards and increasing the mesh density in the inner part Ω_i

3.6 Numerical tests

3.6.1 Test models

Numerical simulations were carried out for 3 different conductivity models: (i) a homogeneous conductivity model, (ii) a model including a single prismatic anomaly within the homogeneous host rock (Figure 3.6(a)), and (iii) an embedded stack of three layers (Figure 3.6(b)). All three models included a mound-shaped topography on which 50 electrodes were placed. For each model, we performed calculations on a series of 18 meshes with increasing numbers of unknowns. The mesh size was increased by moving the ground boundaries outwards and at the same time increasing the mesh density in the inner part Ω_i (Figure 3.6(c)). In the outer part of the mesh Ω_o, the increasing mesh size towards the boundaries was controlled by a maximum aspect ratio constraint as described in section 3.3.4. The meshes were chosen such that the numbers of unknowns were roughly equidistant on a logarithmic scale to cover a wide range of problem sizes. Meshing was performed such that all mesh elements lay entirely within a region of constant conductivity to avoid model discretization errors.

3.6.2 Potential field calculations

Computations were carried out for each conductivity model, electrode position and mesh size. Moreover, all computations were performed with both, first and second order finite elements. The entire suite of these simulations were repeated using (i) standard FEM with mixed-boundary conditions, (ii) infinite elements, (iii) numerical singularity removal using FM-BEM and (iv) combined application of infinite elements and numerical singularity removal. Computations with infinite elements did not require the outer space Ω_o to be meshed ($R = 0.2$ was chosen such that its boundaries were sufficiently far away from the conductivity anomalies and the outermost electrodes). Since the quality mesher employed created already a very efficient grid in Ω_o, this saved
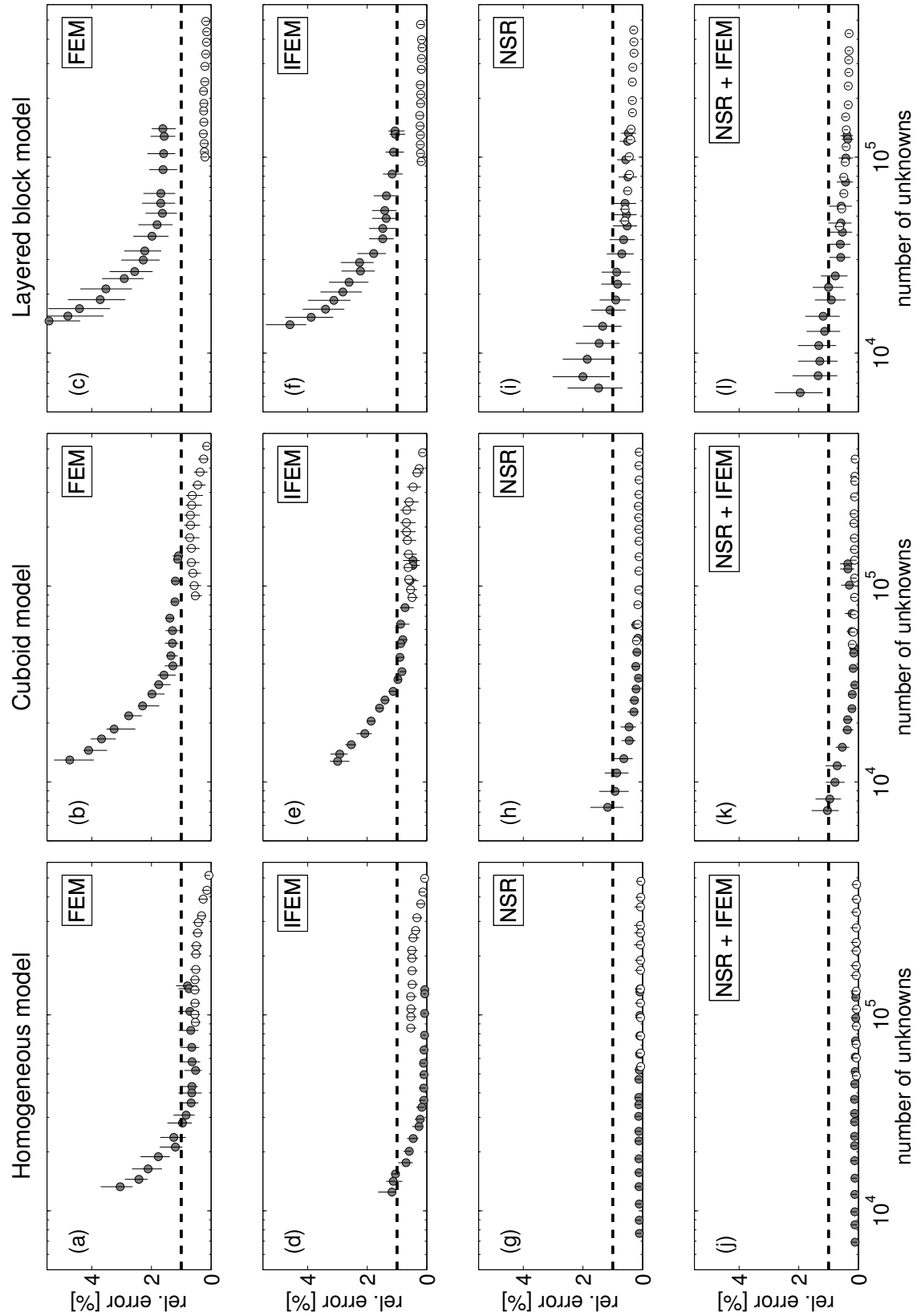
Figure 3.7 – Numerical results of the forward solver for three different conductivity models and the new forward solver techniques. Each subplot shows the median relative solution errors (in%) together with the 25 and 75 percentiles (error bars) estimated for a series of meshes with increasing number of unknowns. Results are displayed for first order (filled dots) and second order finite element approximations (blank dots). Labels: *FEM*: std. FEM calculations, *IFEM*: std. FEM with infinite elements, *NSR*: Numerical singularity removal.

only 5 to 10% of the unknowns, but it was expected that the properties of the infinite elements would generally lead to improved accuracy. Computations involving numerical singularity removal did not require mesh refinements near the electrodes, which led to a 10 to 65% reduction of the unknowns. Finally, combined application of infinite elements and numerical singularity removal was expected to provide the best ratio of accuracy and number of unknowns.

Unfortunately, no analytical solution exists for estimating the accuracy of the different simulations. Therefore, we compared our results with reference solutions that were obtained by the finite element forward solver described in Rücker *et al.* (2006). These reference solutions were calculated on extremely dense meshes equipped with second-order shape functions (each including more than 1 million unknowns). Mixed boundary conditions were applied and a preconditioned conjugate gradient solver with a solver tolerance of $1 \cdot 10^{-9}$ was used.

Initial inspection of the simulation results revealed that the solution accuracy was comparable for all electrode positions. For the sake of simplicity we therefore restricted our further analysis to the results obtained with an injection electrode at the top of the mound shaped topography (vertical arrows in Figure 3.6). Simulation results are summarized in Figure 3.7. It displays the median errors of all grid points relative to the corresponding reference solutions as a function of the mesh sizes. Additionally, the 25 and 75 percentiles (error bars) are shown for a robust estimate of the error variability. We have chosen a target median relative error of 1% as an acceptable solution. This target value is marked with a solid horizontal line in the panels of Figure 3.7.

Using the standard FEM with mixed boundary condition and the coarsest mesh (with the least number of unknowns) provided solution accuracies of about 4% (Figures 3.7a to 3.7c), but it required 28 000 grid points for the homogeneous model and a much larger number of unknowns for the single prism model to approach the target accuracy of 1%. Only solutions involving second order elements yielded acceptable solutions for the layered block model (Figure 3.7c). Unfortunately, even the coarsest second order mesh includes already $\approx 100\,000$ grid points. Further coarsening by reducing the number of elements would have resulted in discretization errors above the 1% line of acceptance.

Enhanced solutions could be obtained, when the mixed-boundary conditions are replaced by infinite elements. The target accuracy could be reached with only 17 000 grid points for the homogeneous model (Figure 3.7d) and with 29 000 points for the single prism model (Figure 3.7e). As for the standard FEM, the first order element solutions performed unsatisfactorily for the layered block model (Figure 3.7f), and the computationally more expensive second order elements had to be used for achieving the accuracy required.

Substantial improvements were observed, when the FM-BEM numerical singularity removal was applied. For the homogeneous case (Figure 3.7g), the errors were almost

zero, but it should be noted that this represents only the accuracy of the singular potential computed with the FM-BEM method (the right hand side of Equation 3.7 is zero for homogeneous models). Numerical singularity removal led to marked improvements for the single prism and layered block models. Only 8 900 and 16 500 grid points, respectively, were required to achieve the target accuracy (Figures 3.7h and 3.7i). As expected, combined application of infinite elements and numerical singularity removal led to further slight improvements of the results (Figure 3.7j to 3.7l).
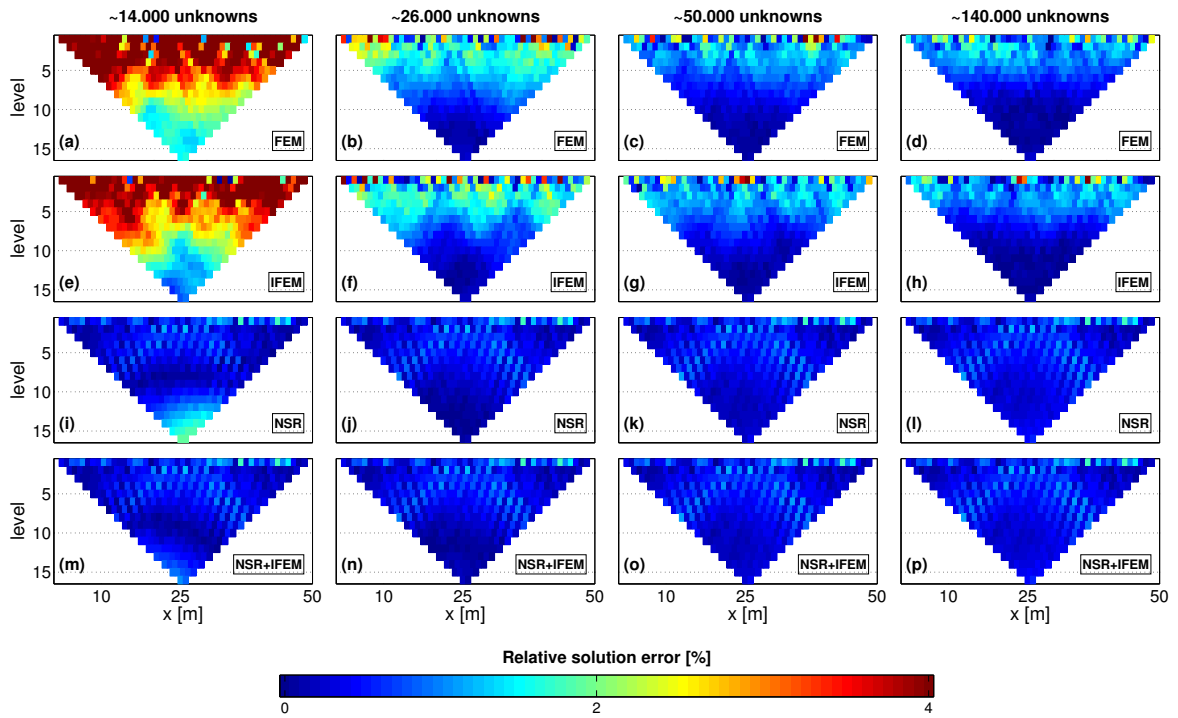
3.6.3   Pseudosections

Figure 3.8 – Synthetic Wenner electrode data calculated for the layered block conductivity model with our new forward solver techniques applied. Each subplot shows the relative solution error (in %) displayed in the form of the Wenner pseudosections. Results are shown for four different mesh sizes (column-wise) and our new forward solver techniques applied (row-wise). Labels: *FEM*: std. FEM calculations, *IFEM*: std. FEM with infinite elements, *NSR*: Numerical singularity removal.

Electrical potentials computed along the surface are particularly important, because they are required for predicting measurements with surface electrodes. Therefore, we inspect the accuracy of these potentials in more detail. For that purpose we construct Wenner pseudosections by superposing the pole-pole type simulation results discussed in the previous subsection. From the resulting apparent resistivities, we subtract the

corresponding values from the reference solutions and compute relative errors. Only first order finite elements are considered.

Figure 3.8 shows the relative error pseudosections for the different computational methods and some selected mesh sizes. Only the results for the most challenging layered block model are displayed. For the conventional FEM calculations (Figures 3.8a-d), large relative errors occur especially in the first 5 levels of the pseudosection. As the first levels correspond to short source-receiver distances, these errors are most likely related to the singularities in the potential solutions. Although a local mesh refinement close to all source electrodes has been applied, the mesh density is apparently still too coarse for approximating the electrical potentials with sufficient accuracy. As expected, the errors decrease for larger meshes (see also Figure 3.7).

Similar error distributions are obtained for the calculations involving infinite elements (Figures 3.8e to 3.8h), though the errors are slightly smaller for the calculations on the smallest and the medium sized meshes (Figures 3.8e and 3.8f).

When the singularity removal is applied (Figures 3.8i to 3.8l), the overall error decreases noticeably, such that the calculation with $14\,000$ unknowns (Figure 3.8i) may be already sufficiently accurate to be used within an inversion algorithm. Note that for the conventional FEM calculations (with or without infinite elements) the same accuracy level is not even reached with the largest mesh size ($140\,000$ unknowns). Only minor improvements (compared with the numerical singularity removal) are observed, when both infinite elements and numerical singularity removal are applied (Figures 3.8m to 3.8p).

3.7 Conclusions

Efficient inversion procedures for the large amount of data produced by modern geoelectrical multi-electrode arrays require appropriate 3D geoelectrical forward solvers. Finite element techniques are currently the most powerful option. They allow straightforward implementations of arbitrarily complicated topographies, and they enable application of unstructured meshes. The latter is in our view the key element for achieving computational efficiency. It has to be made sure that an optimized meshing algorithm is employed before any other refinements, such as those presented in this contribution, are envisaged. The literature on meshing algorithms is vast and excellent open source algorithms are available.

The computationally most expensive part of any finite element solver includes the solution of a large and sparse system of equations. Recent developments in mathematical research resulted in direct matrix solvers that allow relatively sizeable systems of equations to be solved. Direct matrix solvers are particularly useful when equation systems with many right hand side arguments are involved, which is the case for 3D geo-

electrical inversion problems. Despite substantial improvements in direct matrix solver techniques, computer memory requirements for realistic 3D problems remain a problematic issue. Therefore, it is important to minimize the number of unknowns within a finite element mesh, while maintaining a high solution accuracy.

Replacing the traditional Dirichlet or mixed boundary conditions with infinite elements is an attractive option to simultaneously improve the solution accuracy and reduce the number of grid points in a finite element mesh. Truncating or fixing the electrical potential at the computational boundaries is well known as a significant source of numerical inaccuracies. Infinite elements provide a more physical and thus more accurate alternative by continuing the electrical potentials to infinity. The subsurface volume surrounding an electrode layout does not need to be meshed with finite elements, which additionally results in savings of grid points.

Besides the artificial boundary conditions the surface and subsurface areas near the electrodes represent the second major cause of numerical problems. Since the electrical potentials vary rapidly near the current injection points, the finite elements meshes need to be very dense in these areas, which results in a large number of grid points. Singularity removal techniques proposed by Lowry *et al.* (1989) are a powerful option to alleviate the problem, but they require the singular potential to be computed separately. So far, this was achieved by considering analytical solutions, but in the presence of topography this is not possible. We propose application of a fast multipole boundary element method for computing the singular potentials. This technique includes the principal advantages of the traditional boundary element method and overcomes some of their disadvantages, such as their fully populated system matrix. To our knowledge, this is the first application of the fast multipole boundary element method in geophysics, and we believe that this technique may be an attractive option for other numerical modeling problems.

Extensive numerical tests proved the usefulness of infinite elements and numerical singularity removal using the fast multipole boundary element method. Combined application of both techniques allowed the number of grid points to be reduced by a factor of $\approx 6 - 10$ compared with standard finite element techniques. This enables application of direct matrix solvers for realistic 3D geoelectrical inversion problems, which will improve the computational efficiency dramatically. We hope that these new developments will facilitate 3D inversion problems to be carried out directly in the field in the near future.

3.8 Acknowledgments

3.9   Appendix

3.9.1   Panel clustering method

Figure 3.9 – Example of two cluster σ and s on a typical 3D surface mesh used for the BEM. diam(s) or diam(σ) denote the cluster diameters and $dist(x, y)$ denotes the distance of two clusters towards each other.

As described in section 3.5.1, the boundary integral equation employed for calculating the singular potentials leads to a linear system of equations $\mathbf{A}\mathbf{u_h^s} = \mathbf{B}\mathbf{q}$ with the element integrals

$$\mathbf{A}_{ij} = 1/2 \int_{\Gamma_s} \phi_i(\mathbf{r})\phi_j(\mathbf{r}') \, dS_{\mathbf{r}'}$$

$$+ \int_{\Gamma_s} \int_{\Gamma_s} \phi_i(\mathbf{r})\frac{\partial G(\mathbf{r}, \mathbf{r}')}{\partial \mathbf{n}}\phi_j(\mathbf{r}') \, dS_{\mathbf{r}} \, dS_{\mathbf{r}'} \tag{3.24a}$$

$$\mathbf{B}_{ij} = \int_{\Gamma_s} \int_{\Gamma_s} \phi_i(\mathbf{r})G(\mathbf{r}, \mathbf{r}')\phi_j(\mathbf{r}') \, dS_{\mathbf{r}} \, dS_{\mathbf{r}'}. \tag{3.24b}$$

The Green's function respectively its normal derivative in the double integrals in Equation 3.24a and 3.24b couple each degree of freedom on the surface mesh located at node i (position $\mathbf{r}$) to all other degrees of freedoms at nodes j (positions $\mathbf{r}'$) and thereby lead

to fully populated matrices $\mathbf{A}$ and $\mathbf{B}$. This is in contrast to finite element formulations for which only locally defined shape functions respectively their gradients appear in the element integrals and hence very sparse system matrices result. As a consequence, the computational costs, memory consumption and solution time, for conventional BEM formulations exhibit an unfavorable scaling behavior proportional to $\sim \mathcal{O}(N^2)$ where N is the number of unknowns. In the *Panel Clustering Method*, whose basic principles are explained in the following, an approximation of the Green's function and its normal derivative is employed to account for this major drawback.

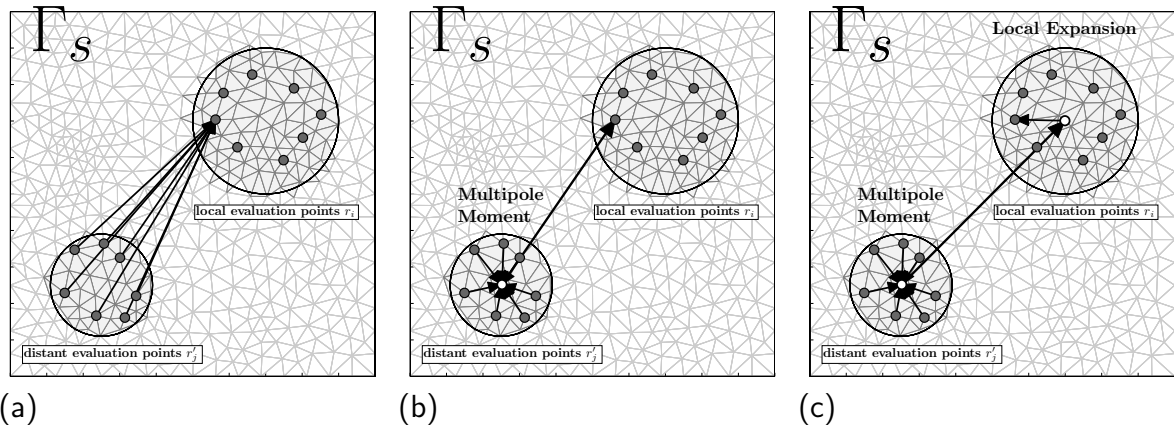### Green's function approximation on cluster-pairs

Figure 3.10 – Sketch of the basic idea of the multipole method. Three different approaches of evaluating the Green's function $G(\mathbf{r}, \mathbf{r}')$ for a set of evaluation points $\mathbf{r}_i$ and $\mathbf{r}'_j$ on a BEM surface mesh are shown. (a) leads to an algorithm with computational costs $\sim \mathcal{O}(N^2)$ whereas (c) results to an algorithm whose computational costs scale as $\sim \mathcal{O}(N)$.

The Green's function that is needed when solving the 3D Poisson equation for the singular potentials takes the form

$$G(\mathbf{r}, \mathbf{r}') = \frac{1}{4\pi\sigma_0 \, |\mathbf{r} - \mathbf{r}'|}. \tag{3.25}$$

It varies rapidly for short $\mathbf{r}$ to $\mathbf{r}'$ distances but shows only slight variations for larger $\mathbf{r}$ to $\mathbf{r}'$ distances. Therefore it is beneficial to distinguish between a near field, where the double integrals in equations 3.24a and 3.24b are evaluated exactly and a far field where these integrals are approximated. The far field-approximation employed in the panel clustering method relies on the idea of *multipole moments* originally developed by Greengard and Rokhlin (1987). Figure 3.10 depicts a sketch of the underlying basic idea. In the conventional BEM for each Green's function source point $\mathbf{r}$ the coupling to all other Green's function points $\mathbf{r}'$ are evaluated exactly when calculating the double integrals which yields numerical costs of the order $\sim \mathcal{O}(N^2)$ (Figure 3.10(a)). In the panel clustering method Greens function evaluation points are grouped in the far field

into clusters such that the combined effect of all Green's function points $\mathbf{r}'$ belonging to one cluster are subsumed into multipole moments. Subsequently only the coupling of the Green's function source point $\mathbf{r}$ to the multipole moment needs to be evaluated (Figure 3.10(b)). The same approximation can be applied locally around the Green's function source points to yield an algorithm with numerical costs that scale as $\sim \mathcal{O}(N \log^{\alpha}(N))$ (Figure 3.10(c)). This scheme requires an approximation of the Green's function on cluster pairs (s, σ) where the variables $\mathbf{r}$ and $\mathbf{r}'$ are separated:

$$G(\mathbf{r}, \mathbf{r}') \approx \tilde{G}(\mathbf{r}, \mathbf{r}') = \sum_{(\vec{\mu}, \vec{\nu})} \mathbf{K}_{\vec{\mu}, \vec{\nu}} \, \Phi_{\sigma}(\mathbf{r}) \Psi_s(\mathbf{r}'). \tag{3.26}$$

Here $\mathbf{K}_{\vec{\mu}, \vec{\nu}}$ is a $k \times k$-matrix of expansion coefficients defined for the cluster pair (s, σ). Φ_{σ} and Ψ_s are the expansion functions defined on cluster s respectively cluster σ. Different Green's function expansions can be employed, e.g. an expansion into the three spatial coordinates by Taylor series, or, as is used within this work, a multipole expansion based on spherical harmonics (see Sauter and Schwab, 2004, for more details).

Whether a pair of basis functions belongs to the far field or to the near field and hence the degree to which the BEM system matrices are approximated is controlled by a parameter η:

$$\eta \, \text{dist}(\sigma, s) \geq \max(\text{diam}\,\sigma, \text{diam}\,s). \tag{3.27}$$

Here $\text{diam}\,\sigma$ and $\text{diam}\,s$ are the diameters of the two clusters and $\text{dist}(\sigma, s)$ is their distance towards each other. For each possible cluster pair (s, σ) a Green's function approximation according to Equation 3.26 is employed if Equation 3.27 is valid, otherwise all pairs of basis functions (ϕ_i, ϕ_j) with $\phi_i \in \sigma$ and $\phi_j \in s$ are part of the near field, i.e. the corresponding matrix entries $\mathbf{A}_{ij}$ are calculated exactly. The scheme by which potential cluster pairs are constructed is outlined in section 3.9.1. By choosing η carefully the error introduced due to the panel-clustering method can be limited to a range which is in the order or smaller than the discretization error due to the surface triangulation. Within this work we use $\eta = 0.5$.

Matrix representation and matrix vector multiplication

The Green's function approximation (Equation 3.26) does not only reduce the computational costs, but also allows the system matrices $\mathbf{A}$ and $\mathbf{B}$ to be approximated. This results in a significant reduction of the overall memory requirements. In the following we denote all nodes belonging to cluster s with I_s and similarly all nodes belonging to cluster σ with I_{σ}. While the matrix entries for all elements belonging to the near field are calculated exactly, all matrix entries A_{ij} for $i \in I_s$ and $j \in I_{\sigma}$ can be approximated
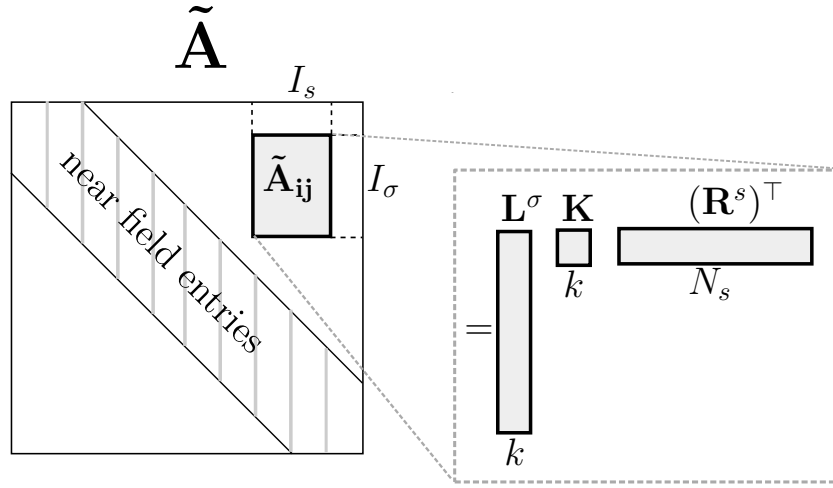
Figure 3.11 – Sketch of the structure of the approximated system matrix $\tilde{\mathbf{A}}$. For all pairs of basis functions (ϕ_i, ϕ_j) in the far field, exact near field entries result into $\tilde{\mathbf{A}}$ whereas for all pairs of basis functions that are in the far field an approximation is performed on pairs of clusters. For each cluster pair the corresponding matrix entries $\tilde{\mathbf{A}}_{ij}$ are given by a product of three matrices $\mathbf{L}^\sigma$, $\mathbf{K}$ and $\mathbf{R}^s$.

by a product of three matrices $\mathbf{L}^\sigma$, $\mathbf{K}$ and $(\mathbf{R}^s)^\top$:

$$\mathbf{A}_{ij} \approx \tilde{\mathbf{A}}_{ij} := \int_\Gamma \int_\Gamma \phi_i(\mathbf{r})\, \tilde{G}(\mathbf{r}, \mathbf{r}')\, \phi_j(\mathbf{r}')\, \mathrm{d}S_\mathbf{r} \mathrm{d}S_\mathbf{r}'$$
$$= \sum_{(\vec{\mu}, \vec{\nu})} \mathbf{L}^\sigma_{i,\vec{\nu}} \mathbf{K}_{\vec{\nu}, \vec{\mu}} \mathbf{R}^s_{j,\vec{\mu}} = \left(\mathbf{L}^\sigma \cdot \mathbf{K} \cdot (\mathbf{R}^s)^\top \right)_{ij} \tag{3.28}$$

with

$$\mathbf{L}^\sigma_{i,\vec{\nu}} := \int_\Gamma \phi_i(\mathbf{r})\, \Psi_s(\mathbf{r}')\, \mathrm{d}S_{\mathbf{r}'}, \qquad\qquad \mathbf{R}^s_{j,\vec{\mu}} := \int_\Gamma \phi_j(\mathbf{r})\, \Phi_\sigma(\mathbf{r}')\, \mathrm{d}S_\mathbf{r}.$$

For simplicity the approximation is demonstrated here only for matrix $\mathbf{A}$. Figure 3.11 shows a sketch of the structure of $\tilde{\mathbf{A}}$: The exact near field matrix entries close to the diagonal of $\tilde{\mathbf{A}}$ are highlighted together with one matrix block that is approximated by a Green's function expansion on a pair of clusters. Note that the nodes indices I_σ and I_s for a cluster pair (σ, s) are in general distributed across the matrix but for simplicity they are shown in the form of a rectangular block. Each of the approximated matrix blocks consists of a multiplication of three matrices as in Equation 3.28. If we denote the number of nodes in the clusters s and σ by N_s respectively N_σ, then the three matrices have the dimensions $N_\sigma \times k$, $k \times k$ and $k \times N_s$, as shown in Figure 3.11. Here k denotes the number of expansion coefficients, which are significantly smaller than N_σ and N_s.

The system matrices $\mathbf{A}$ and $\mathbf{B}$ are not given explicitly in the panel-clustering method but are defined in terms of the approximation scheme as outlined above. When solving the BEM equations with iterative matrix solvers, only matrix times vector products are needed. The panel-clustering method provides a fast way of evaluating these products. The computational savings become obvious if we look at the matrix-vector multiplication

of the matrix block $\tilde{\mathbf{A}}_{ij}$ with a vector $\mathbf{u}$:

$$(\tilde{\mathbf{A}}\mathbf{u})_i = \sum_{j \in I_s} \tilde{\mathbf{A}}_{ij}\mathbf{u}_j = \sum_{\vec{\nu}} \mathbf{L}_{i,\vec{\nu}}^{\sigma} \sum_{\vec{\mu}} \mathbf{K}_{\vec{\nu},\vec{\mu}}^{b} \sum_{j \in I_s} \mathbf{u}_j \mathbf{R}_{j,\vec{\mu}}^{s}, \qquad (3.29)$$

Clearly this product needs considerably less floating point operations than a full matrix vector multiplication with the matrix block $\mathbf{A}_{ij}$.

Multilevel scheme

In the previous sections the Green's function approximation on a single cluster pair was described and it was outlined that such an approximation results in a significant improvement on the performance of the BEM. The question remains, how the set of cluster pairs can be constructed in an optimal fashion. The panel-clustering method employs a multilevel scheme in which a hierarchic tree structure of clusters $\mathcal{T}$ is generated.

The root of the cluster tree $\mathcal{T}$ is constructed by a minimal axis-parallel cuboid that encloses the entire surface mesh Γ_s. The root of $\mathcal{T}$ consists of all basis functions or nodes in Γ_s. Subsequently the cuboid is subdivided in eight congruent cuboids. The nodes of the surface mesh that are contained in these cuboids form the eight children of the root of $\mathcal{T}$. This subdivision is repeated recursively for all children until the smallest cluster consists of a predefined minimum number of nodes.

The resulting cluster tree $\mathcal{T}$ is used to construct a set of cluster pairs P^{far} for which the Green's function approximation (Equation 3.26) is applied, and a set of cluster pairs P^{near} for which exact evaluations are used. Equation 3.27 is used to decide whether a cluster pair belongs to P^{near} or P^{far}.

The process starts with a cluster pair (σ, s) where σ and s are both the root of $\mathcal{T}$, i.e. both contain all nodes of Γ_s. If Equation 3.27 is true for (σ, s), which is obviously not the case for the root clusters, then (σ, s) belongs to P^{far}, otherwise the process is continued recursively for the children cluster pairs. Thereby, the children cluster pairs of (σ, s) are all combinations (σ', s'), where σ' is one of the children of σ in $\mathcal{T}$ and correspondingly s' is one of the children of s in $\mathcal{T}$. Cluster pairs (σ, s), for which Equation 3.27 is not true, will only be appended to P^{near} if they have no children, i.e. if both clusters σ and s are not further subdivided in $\mathcal{T}$.

Finally each pair of basis functions (ϕ_i, ϕ_j) (corresponding to a pair of surface mesh nodes (i, j)) belongs either to the far field P^{far} or to the near field P^{near}. For all $(\phi_i, \phi_j) \in P^{near}$ exact calculations are performed resulting into near field entries $\mathbf{A}_{ij}$ as sketched in Figure 3.11 whereas for all pairs of basis functions $(\phi_i, \phi_j) \in P^{far}$ approximations on cluster pairs are performed as outlined above. Since the expansion functions Φ_σ, Ψ_s in any cluster pair (σ, s) can be written as a combination of functions on the cells, all operations are performed on triangles and then "raised" to higher levels in

the cluster tree. Altogether, the panel-clustering method results to a boundary element implementation for which the computational costs scale as $\sim \mathcal{O}(N \, log^5(N))$ instead of the $\sim \mathcal{O}(N^2)$ scaling for conventional BEM implementations.

For the singularity removal technique described in section 3.3.2 the singular potentials may be required not only along the surface Γ_s, but also inside the volume at all nodes of the finite element mesh. Once the surface solution is found with the panel-clustering method, the same technique can be employed for evaluating the volume solution values. For this purpose, an additional cluster tree $\mathcal{T}_{vol}$ is constructed for the finite element mesh and the clustering algorithm described above is applied to pairs of clusters (σ, s) with $\sigma \in \mathcal{T}$ and $s \in \mathcal{T}_{vol}$.

3.9.2   2.5D forward approximation

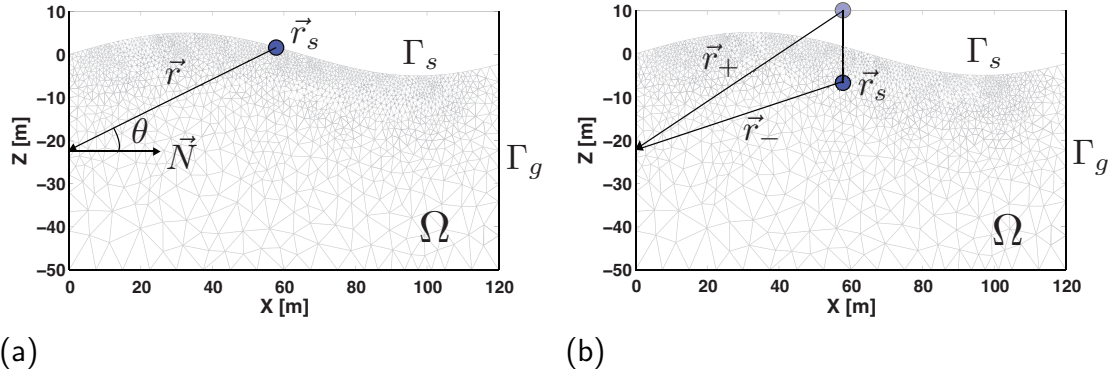

(a)   (b)

Figure 3.12 – (a) Implementation of the mixed boundary condition for surface electrodes (located at $\vec{r}_s$), requires the angle θ between the ground boundaries normal vector $\vec{N}$ and the vector $\vec{r}$, that connects the source location to nodes on the boundary Γ_g, to be known. (b) For subsurface (i.e. borehole) electrodes an image source located above the surface is employed for the analytic solution. $\vec{r}_-$ and $\vec{r}_+$ denote the vectors connecting points on Γ_g to the source and its image source location, respectively.

Even though most subsurface conductivity distributions are $3D$ in nature, in certain geological settings a $2D$ model is a sufficiently good approximation of the true subsurface. In these cases the much lower computational costs of a $2D$ compared to a full $3D$ data inversion is highly beneficial. Therefore, a so-called $2.5D$ forward approximation based on triangular domain discretizations has been implemented.

Even though the conductivity distribution $\sigma(x, z)$ is assumed to be two-dimensional, the potential field $\phi(x, y, z)$ exhibits $3D$ characteristics caused by the point source. A pure $2D$ modelling of the potential field would require $2D$ line sources in the strike direction, which is impossible to realize in field measurements. To account for the $3D$ source characteristic, a spatial Fourier transformation of the potential $U(x, y, z)$ is

performed along the strike direction (y):

$$\widehat{U}(x, k, z) = 2 \int_0^\infty U(x, y, z) \, cos(ky) \, dy \tag{3.30}$$

As the potential $U(x, y, z)$ is an even function with respect to the strike direction, we employ a Fourier-Cosine transformation. Applying this transformation to the $3D$ Poisson equation (equation 3.2) results into a $2D$ Helmholtz equation

$$\begin{cases} \nabla \cdot (\sigma \nabla U_k) + k^2 \sigma U_k = -I\delta(|\vec{r} - \vec{r}_s|) & \text{in } \Omega \\ \partial U_k/\partial \mathbf{n} = 0 & \text{on } \Gamma_s \ , \\ \partial U_k/\partial \mathbf{n} + \beta U_k = 0 \text{ on } \Gamma_g & \text{on } \Gamma_g \end{cases} \tag{3.31}$$

which is solved for a $2D$ domain Ω limited by a boundary Γ that is subdivided into a surface (Γ_s) and a subsurface part (Γ_g). As for the $3D$ Poisson equation (section 3.3.1) we apply a Neumann boundary condition along Γ_s (no current-flow perpendicular to the surface boundary is allowed) and a mixed boundary condition along the ground boundary Γ_g. For the mixed boundary conditions, the potential field along Γ_g is assumed to asymptotically behave like the homogeneous half-space solution $U^h(k)$ given in terms of the modified, zeroth order bessel functions $\mathcal{K}_0$:

$$\begin{cases} \widehat{U}_h(k) = \dfrac{I}{2\pi\sigma_0} \mathcal{K}_0(kr) & (\vec{r}_s \text{ on } \Gamma_s) \\ \widehat{U}_h(k) = \dfrac{I}{2\pi\sigma_0} \left(\mathcal{K}_0(kr_-) + \mathcal{K}_0(kr_+) \right) & (\vec{r}_s \text{ in } \Omega) \end{cases} \tag{3.32}$$

Here σ_0 is the homogeneous domain conductivity, k the spatial wavenumber and I the current source strength for a source located at $\vec{r}_s$. For sources located inside the domain (e.g. borehole electrodes), an image source located above the surface (see Figure 3.12(b)) is employed for the analytic solution. $r_- = \sqrt{(x - x_s)^2 + (z - z_s)^2}$ and $r_+ = \sqrt{(x - x_s)^2 + (z + z_s)^2}$ denote the distance of points $\vec{r}_g = (x, y)$ on the ground boundary to the source and its image source, respectively. Inserting the homogeneous subsurface solution (Equation 3.32) into the expression for the mixed boundary condition (Equation 3.31) yields an expression for the factor β

$$\begin{cases} \beta = \sigma_0 \, cos(\theta) \, \dfrac{k\mathcal{K}_1(kr)}{\mathcal{K}_0(kr)} & (\vec{r}_s \text{ on } \Gamma_s) \\ \beta = \sigma_0 \dfrac{k \left[\mathcal{K}_1(kr_-) + \mathcal{K}_1(kr_+) \right]}{\mathcal{K}_0(kr_-) + \mathcal{K}_0(kr_+)} & (\vec{r}_s \text{ in } \Omega) \end{cases}, \tag{3.33}$$

that is used to implement the mixed boundary conditions for surface and subsurface electrodes. Here $\mathcal{K}_1$ denotes the modified bessel functions of first order. When a direct matrix solver is used to solve the finite element equations (see section 3.3.3), a geometric

mean of all source and mirror source electrode positions is used to approximate the mixed boundary conditions. In this way the system matrix becomes independent of the source electrode position and therefore only a single matrix decomposition needs to be performed to compute the solutions for all source electrodes efficiently. After computing the Fourier transformed solutions for a sufficiently large number of discrete wavenumbers k, an inverse Fourier transformation is applied to obtain the potential solutions in the spatial domain:

$$U(x, 0, z) = \frac{1}{\pi} \int_0^\infty \widehat{U}(x, k, z) dk \tag{3.34}$$

The transformed potentials $\widehat{U}(x, k, z)$, which are proportional to $\mathcal{K}_0(kr)$ (see Equation 3.32), behave as $\sim -ln(kr)$ for $(kr) \to 0$ and $\sim e^{-kr}/\sqrt{kr}$ for $(kr) \to \infty$. Therefore, following the approach of Kemna (2000) and LaBrecque *et al.* (1996), we split up the integral into two parts

$$\frac{1}{\pi} \int_0^\infty \widehat{U}(x, k, z) dk = \underbrace{\frac{1}{\pi} \int_0^{k0} \widehat{U}(x, k, z) dk}_{I_1} + \underbrace{\frac{1}{\pi} \int_{k0}^\infty \widehat{U}(x, k, z) dk}_{I_2}, \tag{3.35}$$

and evaluate integral I_1 (small wavenumbers) by a Gauss-Legendre quadrature rule and integral I_2 (large wavenumbers) by a Gauss-Laguerre quadrature rule. For I_1 the integral variable is substituted by $k' = \sqrt{k/k_0}$ to overcome the singularity in the integrand for $(kr) \to 0$; the resulting integral is solved by N_G Gaussian quadrature points with abscissa k_i' and corresponding weights w_i':

$$I_1 = \int_0^1 F(k') dk' \approx \sum_{i=1}^{N_G} w_i' F(k_i') \tag{3.36}$$

$$= \pi \sum_{i=1}^{N_G} w_i \widehat{U}(x, k_i, z) \quad \begin{cases} k_i = k_0 k_i'^2 \\ w_i = 2 k_0 k_i' w_i'/\pi. \end{cases}$$

Due to the integral range $[0, \infty)$ and the $\sim e^{-kr}/\sqrt{kr}$ functional behaviour of the integrand in Integral I_2, an N_L-point Gauss-Laguerre quadrature rule with abscissa k_i' and corresponding weights w_i' is used to solve this integral efficiently:

$$I_2 = \int_0^\infty e^{-k'} F(k') dk' \approx \sum_{i=1}^{N_L} w_i' F(k_i') \tag{3.37}$$

$$= \pi \sum_{i=1}^{N_L} w_i \widehat{U}(x, k_i, z) \quad \begin{cases} k_i = k_0 (k_i' + 1) \\ w_i = k_0 e^{k_i'} w_i'/\pi \end{cases}$$

The critical wavenumber k_0 used to split up the inverse Fourier integral is estimated as $k_0 = 1/r_{min}$, where r_{min} is the minimum distance between any of the employed

electrode locations. We found that choosing $N_G = 8$ Gauss-Legendre and $N_L = 4$ Gauss-Laguerre quadrature points yields sufficiently accurate results. Comparisons with a $3D$ homogeneous half-space solution for a single surface source electrode and the mixed boundary conditions applied revealed relative solution accuracies well below 0.1 percent across the domain.

The same inverse Fourier sampling scheme as outlined here is used to compute the $2.5D$ sensitivity kernels needed for the inverse algorithm. Note that for this purpose the Fourier transformed potentials $\widehat{U}(x, k, z)$ for all employed discrete wavenumbers k_i are required and hence need to be kept in main memory.
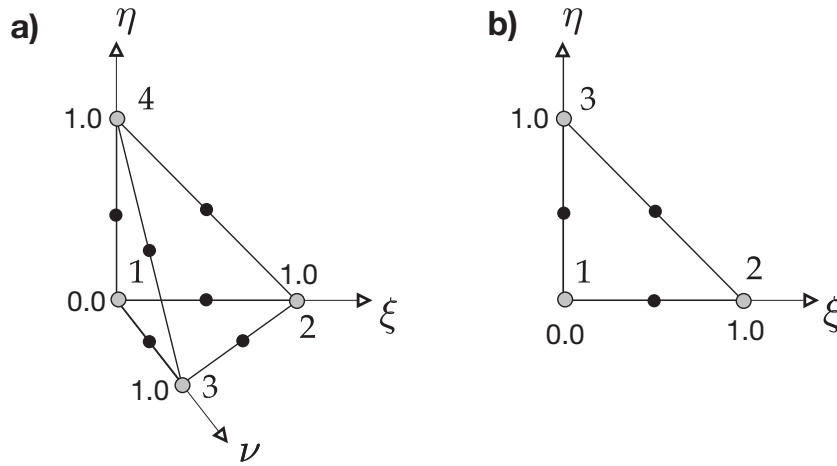
3.9.3 Finite-element modeling

Figure 3.13 – Sketch of the local coordinate systems employed during integration of the finite element equations for a) tetrahedral and b) triangular elements. Gray dots indicate the locations of the degree of freedoms associated to the individual elements. For second order approximations, additional degrees of freedom are used (black dots).

The solution to the $2D$ Helmholtz equation (section 3.9.2) and the $3D$ Poisson equation (section 3.3.1), respectively, is approximated using the finite-element method. It requires subdividing the domain (Ω) and the boundary (Γ) in small sub-domains Ω_e and boundary elements Γ_e, such that $\Omega = \{\Omega_1 \cdots \Omega_{N_e}\}$ and $\Gamma = \Gamma_g \cup \Gamma_s = \{\Gamma_1 \cdots \Gamma_{N_g}\}$. Triangular elements are used to discretize the $2D$ Helmholtz equation and tetrahedral elements are used for the $3D$ Poisson equation. Within each element the unknown potential U^n is approximated by a linear combination of first or second order shape functions ϕ_k

$$U^n(x, y, z) = \sum_{k=1}^{p} \phi_k(x, y, z) u_k^n, \tag{3.38}$$

where p denotes the number of nodes associated with a single element and u_k^n the unknown potential values at the nodes. For simplicity, I demonstrate the finite-element discretization for the $3D$ modified Poisson equation (Equation 3.7 in section 3.3.2) –

discretization of the $2D$ Helmholtz equation follows along the same lines. Starting from the weak or variational form (see section 3.3.3)

$$\underbrace{\int_\Omega \sigma \nabla U^n \cdot \nabla \omega \, d\Omega}_{I_1} + \underbrace{\int_\Gamma \sigma \omega \, \beta(\mathbf{r}) U^n d\Gamma}_{I_2} = \underbrace{- \int_\Omega \nabla \cdot ((\sigma(\mathbf{r}) - \sigma_0) \nabla U^s) \omega d\Omega}_{I_3}, \qquad (3.39)$$

the finite element equations are assembled element-wise into local element matrices $\mathbf{K}^e$ and forcing vectors $\mathbf{F}^e$, which are subsequently inserted into the main equation system. For finite element e the resulting local element matrix takes the form

$$\mathbf{K}_{i,j}^e = \sum_{i,j=1}^{N_s} \left(\sigma_e \int_{\Omega_e} \nabla \phi_i \cdot \nabla \phi_j \, d\Omega_e \right) + \sum_{i,j=1}^{N_s'} \left(\sigma_e \int_{\Gamma_e^g} \beta \, \phi_i' \phi_j' \, d\Omega_e \right), \qquad (3.40)$$

where the first sum corresponds to the main finite element volume integral (I_1 in Equation 3.39) and the second sum results from the boundary integral I_2 that formulates the mixed boundary conditions. Note that the latter is evaluated only for elements e that share one or more sides with the ground boundary Γ_g. N_s and N_s' are the number of shape functions ϕ_i and ϕ_i' for domain and boundary elements, respectively. σ_e is the constant conductivity of finite element e and β is the mixed boundary condition factor (Equation 3.4). The element integration in Equation 3.40 is carried out using conventional N_{qp} and N_{qp}' point gaussian quadrature rules with weights w_p and the quadrature point locations q_p resulting into the explicit expression for the element matrix $\mathbf{K}_e$:

$$\begin{aligned}
\mathbf{K}_{i,j}^e &= \sum_{i,j=1}^{N_s} \left(\sigma_e \sum_{p=1}^{N_{qp}} J_p \, w_p \, \nabla \phi_i(\vec{q}_p) \cdot \nabla \phi_j(\vec{q}_p) \right) \\
&+ \sum_{i,j=1}^{N_s'} \left(\sigma_e \sum_{p=1}^{N_{qp}'} J_p \, w_p \, \beta(\vec{q}_p, \vec{n}_p) \, \phi_i'(\vec{q}_p) \phi_j'(\vec{q}_p) \right) \qquad (3.41)
\end{aligned}$$

Numerical integrations are carried out in local coordinate systems on so-called *unit elements*. This is common practice in finite element methods because it allows tabulated quadrature points ($\vec{q}_p$) and weights (ω_p) to be used irrespective of the individual shape of the finite elements, thereby greatly accelerating the necessary computations. Analytic expressions could be employed for the finite element integrals (Kost, 1994). However, using gaussian quadrature rules allows them to be dicretized in a more general fashion without a loss in numerical accuracy (Zienkiewicz, 1977). This largely simplifies discretization of the finite element equations for different cell geometries (e.g. triangular, tetrahedral and prismatic-shaped cells). Figure 3.13 depicts a sketch of the local coordinate systems used for triangular and tetrahedral elements, respectively. The coordinate

transformations from the local to the global coordinate system are given by

$$
\begin{cases}
x = x_1 + (x_2 - x_1)\xi + (x_3 - x_1)\eta \\
y = y_1 + (y_2 - y_1)\xi + (y_3 - y_1)\eta
\end{cases}
\tag{3.42}
$$

for triangular and

$$
\begin{cases}
x = x_1\xi + x_2\eta + x_3\nu + x_4(1 - \xi - \eta - \nu) \\
y = y_1\xi + y_2\eta + y_3\nu + y_4(1 - \xi - \eta - \nu) \\
z = z_1\xi + z_2\eta + z_3\nu + z_4(1 - \xi - \eta - \nu)
\end{cases}
\tag{3.43}
$$

for tetrahedral elements.

The discretized expression for the right hand side in Equation 3.39 (I_3) takes the form

$$
\vec{F}_i^e = \sum_{i,j=1}^{N_s} \left((\sigma_e - \sigma_0) \sum_{p=1}^{N_{qp}} J_p \, w_p \, U^s(\vec{p}_j) \, \nabla\phi_i(\vec{q}_p) \cdot \nabla\phi_j(\vec{q}_p) \right)
\tag{3.44}
$$

where $U^s(\vec{p}_j)$ are the pre-calculated singular potentials (estimated either by the boundary element method (section 3.5) or, in the case of flat surface domains, by analytical homogeneous half-space solutions), that are required at all nodes of each finite element. σ_0 is the conductivity at the source electrode according to the singularity removal technique. Note that gradients of the singular potentials as they appear in Equation 3.39 are approximated by the gradients of the employed shape functions.
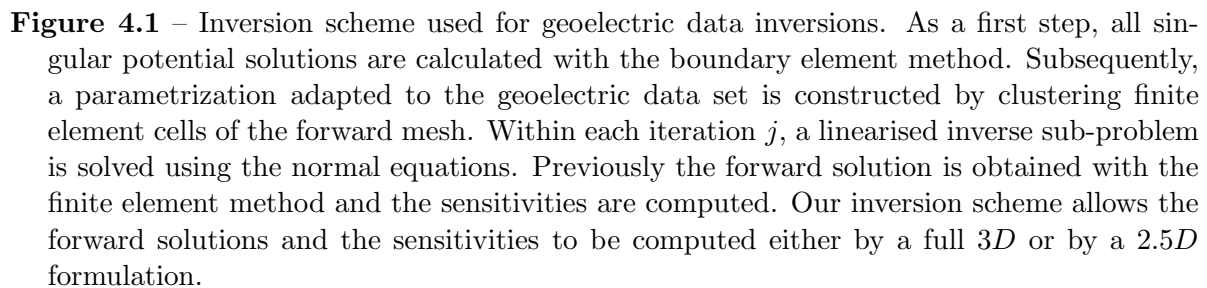
Chapter 4

Inversion of Large-Scale Geoelectric Data Sets

4.1 Introduction

Modern geoelectrical data acquisition systems, such as the multi-channel measurement system *ETH-DCMES-II* described in Chapter 2, allow large amounts of data to be collected in a short time. This enables large-scale $3D$ geoelectric field surveys to be carried out efficiently. Resulting data sets may easily comprise up to several hundred thousand measurements. Despite the seemingly ever-increasing power of computers, full $3D$ inversions of these data sets remain challenging and time-consuming tasks. Therefore, optimized inversion procedures have been developed in the framework of this PhD project with the following main features:

Large data sets: In many inversion approaches, the size of the data set that can be inverted is seriously limited by the available main memory. Our inversion approach allows arbitrarily large data sets to be inverted with the number of employed model parameter cells as the only limiting factor. Attention has been paid to largely decouple the number of necessary floating point operations from the size of the data set, thereby allowing large $3D$ data sets to be inverted economically.

Optimized model parametrization: A flexible parametrization of the inverse problem is of key importance to reduce the general ill-posed character associated with geoelectric data inversions. Conceptually, the parametrization should be adapted to the resolving power of the data set considered. This also helps to avoid unnecessary computations, because the computational costs and memory generally required in inversion algorithms, largely depend on the number of model parameters specified.

Figure 4.1 – Inversion scheme used for geoelectric data inversions. As a first step, all singular potential solutions are calculated with the boundary element method. Subsequently, a parametrization adapted to the geoelectric data set is constructed by clustering finite element cells of the forward mesh. Within each iteration j, a linearised inverse sub-problem is solved using the normal equations. Previously the forward solution is obtained with the finite element method and the sensitivities are computed. Our inversion scheme allows the forward solutions and the sensitivities to be computed either by a full $3D$ or by a $2.5D$ formulation.

2.5D approximation: In certain geological settings a $2D$ model is a sufficiently good approximation of the true subsurface. In these cases, 2.5D modelling can greatly increase the speed of the inversion process. Our inversion scheme allows the sensitivities as well as the forward problem to be solved either on $2D$ triangular meshes (with $3D$ source characteristics) or on $3D$ tetrahedral meshes.

Topography: Many target areas for geoelectric measurements are characterized by pronounced topography. To avoid systematic errors in the forward modeling and sensitivity computations, the surface topography needs to be incorporated in the computations (see also Chapter 3). Likewise, the topography needs to be accounted for during the construction of the parameter mesh.

Unstructured grids: Unstructured computational grids, e.g. based on non-regular triangular or tetrahedral meshes, have proved to be most efficient in discretizing the forward problem (e.g. Rücker *et al.*, 2006).

The main elements of our inverse scheme are outlined in Figure 4.1. Initially, an unstructured domain discretization, comprising either first- or second-order tetrahedral ($3D$ domain) or triangular ($2D$ domain) finite elements, is created. The domain discretization is constructed such that it accomodates the surface topography. Furthermore, it is adapted to the desired accuracy of the forward solution. In the case that a $3D$ forward modeling is required, singular potentials are pre-calculated with the boundary element method such that only the secondary potentials need to be solved for during each iteration of the inverse algorithm (see Chapter 3 for details). A model parametrization optimized to the resolving power of the data set under consideration is created out of the previously generated domain discretization by grouping finite element cells into clusters (section 4.2).

Starting with an initial (usually homogeneous) subsurface model $\vec{m}_0$, the inversion then proceeds in an iterative fashion by locally linearising the forward operator $\mathcal{F}(\vec{m}_j)$ within each iteration j. The resulting linear sub-problem $\vec{m}_{j+1}^{est} = \mathbf{G}^{-g}(\vec{d}_{obs})$ is solved using the normal equations (section 4.5) to obtain an updated model vector $\vec{m}_{j+1}$. Due to the general ill-posedness of geoelectric inverse problems, the normal equations need to be regularized by appropriate à-priori constraints (e.g. smoothing and damping, section 4.4).

Linearizing the forward operator requires knowledge of the partial derivatives $\mathbf{S}_{kl} = \partial \mathcal{F}_k / \partial \vec{m}_l$ referred to as sensitivities, which are previously calculated either based on the forward solution (section 4.3.1) or by the reciprocity theorem (section 4.3.2). Furthermore, the forward solution $\vec{d}_j^{syn} = \mathcal{F}(\vec{m}_j)$ obtained using the finite element method (Chapter 3) is required for estimating the sensitivities and to predict the data residuals $\vec{r}_j = \mathbf{D}(\vec{d}_{obs} - \mathcal{F}(\vec{m}_j))$ (section 4.5). The inversion process stops, once the rms of the data residuals falls below a certain specified threshold.

4.2 Model parametrization

To obtain high quality tomographic images of geoelectric data sets requires not only high quality data and accurate forward and inverse solvers, but also adequate model parametrizations. This is especially important considering the general ill-posed character of geoeletric inverse problems. Appropriate model parametrization should be designed such that (i) grid cell sizes are adequate for the resolving power of the data set to be inverted and (ii) the grid cells are sufficiently dense such that un-aliased tomogram images are obtained.
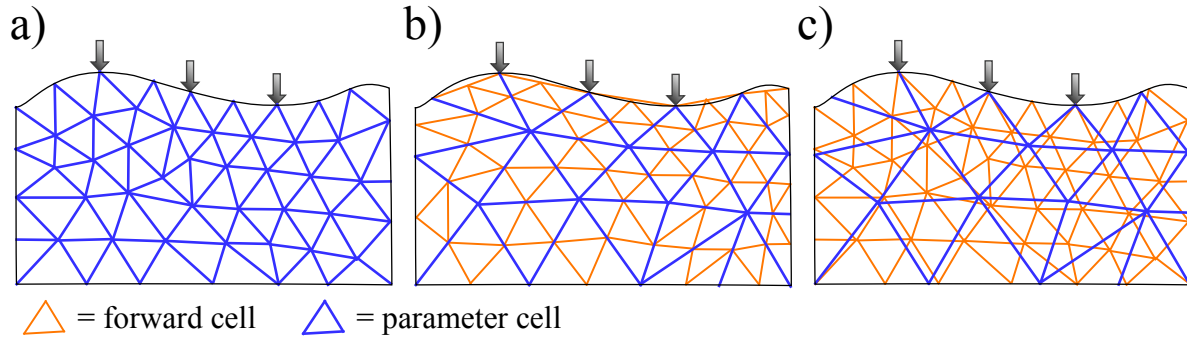
a)   b)   c)

△ = forward cell   △ = parameter cell

Figure 4.2 – Three different approaches to unstructured model parametrisations: In a) the
  forward cells are identical to the parameter cells, whereas in b) the forward mesh is obtained
  by element subdivision on the parameter grid. In c) two independent domain parametriza-
  tions are used. While the approaches in a) and b) offer ease of implementation, they fail
  to meet the (potentially conflicting) demands of adequate forward modeling and parameter
  discretizations. Approach c) offers the most flexibility, but entails complications in (among
  other things) the sensitivity computations.

The literature on geoelectric data inversions reveals three different approaches to
model parametrizations. Figure 4.2 illustrates these approaches for unstructured domain
discretizations. Due to its relative simplicity, the first and most common approach is to
use the same discretization for the forward solver and the model parametrization (Figure
4.2 a)). Clearly, with such an approach the conflicting demands of adequate forward
and parameter discretizations cannot be met. The requirement for an efficient forward
solver and the general ill-posed character of the inverse equations obviously demand two
different computational grids. The forward grid, which is generally much finer, needs to
be adapted to the desired accuracy of the finite element equations. For example, grid
refinements around the source electrodes can largely help improve the overall forward
solution accuracy whereas increasingly coarse grid cells towards the domain boundaries
are important to keep the computational costs within reasonable bounds. On the other
hand, appropriate parametrizations of the inverse problem depend almost exclusively
on the data set to be inverted. For example, exponentially decreasing sensitivities, as
they commonly occur for geoelectric data sets towards the deeper parts of the domain,
usually require the parameter grid cells to increase in size with depth accordingly.

An appealing approach to unstructured model parametrizations is demonstrated
by (Günther *et al.*, 2006). In their approach, an unstructured mesh is used for the
model parametrization, out of which the forward discretization is obtained by element
subdivision (Figure 4.2 b)). In this approach, the element subdivision should ideally be
done in an adaptive fashion, such that element refinements are only carried out in regions
that require a dense discretization to obtain a high forward solution accuracy. Multigrid
equation solvers can be used on the adaptive forward discretization to significantly speed
up the forward solution. In our view, this approach has one important drawback. It
requires generation of an unstructured mesh - used for the model parametrization - with

cell sizes across the domain fine-tuned to the resolving power of the data set that is
to be inverted. In our experience, unstructured mesh generation, especially for three-
dimensional domains with pronounced topography, is a complicated process which allows
only minor to moderate influence on the spatial cell size distribution in the resulting
mesh.

A third and final approach would be to use two completely independent domain dis-
cretizations for the forward solver and the inverse approach, respectively. Clearly, this
approach offers the most flexibility. However, two independent discretizations would
require the forward solutions to be interpolated to the inverse grid for the sensitiv-
ity computations, which can easily lead to numerical errors. Additionally, appropriate
means of projecting the model vector from the inversion grid to the forward grid need
to be implemented, which further complicates the whole inverse approach.

Considering the shortcomings of the three approaches described above, we propose
a new way of forming optimized model parametrization out of the forward discretiza-
tion by grouping the forward cells into clusters. This approach provides a maximum of
flexibility for adequately fine-tuning the model parametrization to the individual data
sets under consideration. Yet, it allows for a straightforward computation of the sen-
sitivities (see section 4.3) and uncomplicated predictions of the forward response for
estimated parameter models. The specific algorithm used to cluster the finite elements
is completely decoupled from the remaining parts of the data inversion and hence can
easily be interchanged for maximal adaptibility. In the following sections, I describe two
clustering algorithms suitable for $2D$ and $3D$ domain discretizations.

4.2.1   Auxiliary staggered grid method

Staggered grid parametrizations are employed in several inverse schemes (e.g. Loke and
Barker, 1996b; Günther, 2004) due to their straight-forward implementation and un-
complicated adaptability to the resolution of the data set that is inverted. Typically,
they are used in conjunction with a regular, cartesian finite-difference discretization of
the forward operator. Layer thicknesses can vary with depth and cell widths gradu-
ally increase towards the bottom of the domain respecting the cell boundaries of the
underlying forward grid. The flexibility stems from the fact that the geometry can be
parameterized by just a few numbers, e.g. by initial cell sizes for the uppermost grid
layer and vertical and horizontal stretching factors, that define cell size growth rates
with depth. These parameters can easily be inferred from e.g. a homogeneous sensi-
tivity distribution of the data set (Günther, 2004) or by an à-priori resolution analysis
(Friedel, 2003). However, staggered grid parametrizations cannot be used in a straight-
forward fashion if the domain exhibits a pronounced topography. Furthermore, they are
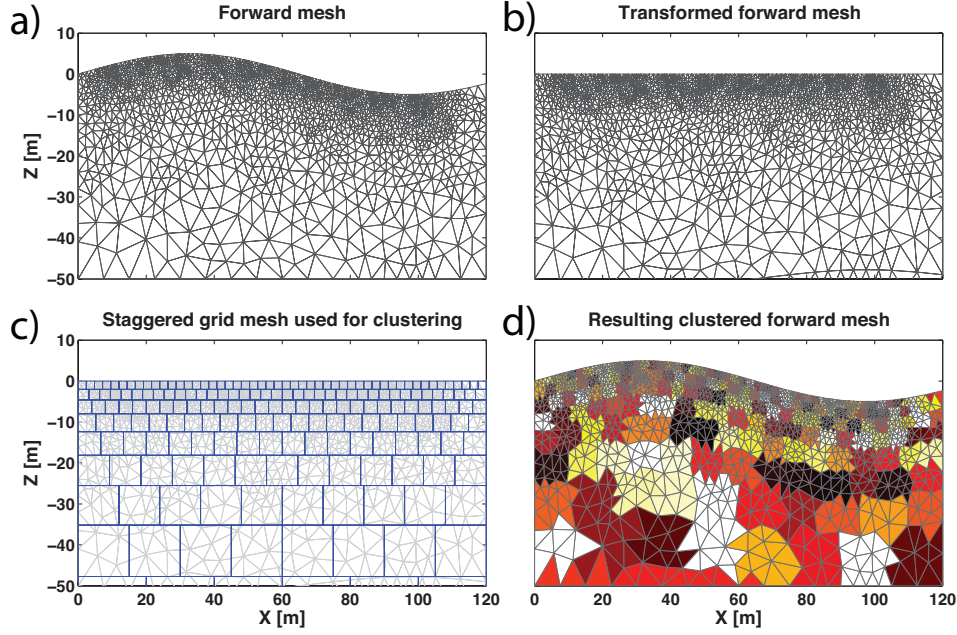not applicable if the underlying forward mesh is not rectangular.

Figure 4.3 – Construction of a parameter mesh by the auxiliary staggered grid method. A coordinate transformation is applied to the original forward mesh (a) in order to obtain a flat surface domain (b). Subsequently, a staggered grid mesh (c) is used to perform the clustering (d). Finite elements in (d) belonging to the same cluster are highlighted with the same colours. A similar algorithm is used for $3D$ tetrahedral forward discretizations.

Therefore, we propose to combine the effectiveness of staggered grid parametrizations with the flexibility and improved performance of unstructured forward discretizations. Figure 4.3 outlines the approach used to construct the parameter mesh. In the first step, the vertical coordinates r_z^p for all forward mesh nodes p (located at $\vec{r}^p$) are linearly transformed by the relation

$$r_z^p = r_z^p - \frac{\mathcal{T}(\vec{r}^p) - z_0}{\mathcal{T}(\vec{r}^p) - z_b} \left(r_z^p - z_b\right) \tag{4.1}$$

such that a flat surface domain is obtained (Figure 4.3 (a)). Here $\mathcal{T}(\vec{r}^p)$ is a function returning the (interpolated) vertical coordinate of the topography above node p, z_b is the vertical coordinate of the bottom domain boundary and z_0 specifies the vertical coordinate of the resulting flat topography (which is usually equal to zero). Subsequently, N_p clusters (with N_p equal to the number of staggered grid cells) are formed, with each cluster i containing all forward cells $\mathcal{P}_i = \{e_i^1, e_i^2, \cdots\}$, whose centroids are located within the boundaries of staggered grid cell i. Thereby, Ω_p, the inner part of the domain Ω, where the inversion takes place, is parameterized as:

$$\Omega \supset \Omega^P = \left\{\Omega_1^P \cup \Omega_2^P \cdots \cup \Omega_{N_p}^P\right\} \quad \text{with} \quad \Omega_i^P = \bigcup_{\forall e \in \mathcal{P}_i} \Omega_e \tag{4.2}$$

In Figure 4.3 (d) a sample parameter grid is visualized by colouring forward cells that

belong to the same cluster in the same colour. The outer space, i.e. the region beyond the domain that is covered by surface electrodes, is not displayed in this figure. Nevertheless, it is included in the parametrization through a couple of large staggered grid cells to account for outer-space sensitivities (Maurer and Friedel, 2006). The same algorithm works seamlessly for $3D$ tetrahedral forward parametrizations. Figure 4.4(a) shows the inner part of a $3D$ auxiliary staggered grid mesh and Figure 4.4(b) shows a cross-section through the resulting parametrization, where tetrahedra belonging to the same cluster are assigned the same colour.

(a)   (b)
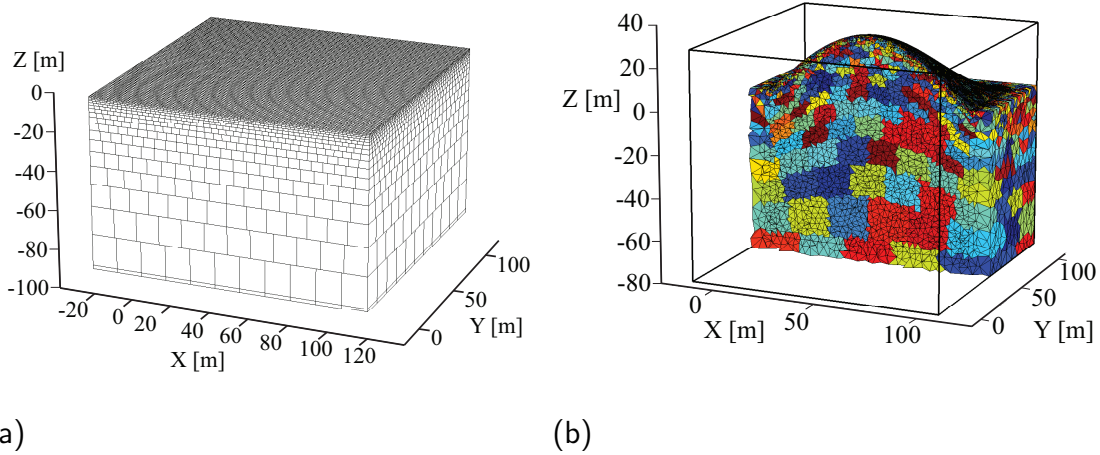
Figure 4.4 – (a) A sample $3D$ auxiliary staggered grid mesh and a vertical cut through the resulting parametrization (only the inner part of the domain is shown for clarity). Finite elements belonging to the same cluster are highlighted with the same colours.

Each parameter may represent either a constant resistivity or conductivity value forming the model vector $\vec{m} = \{m_1 \cdots m_{N_p}\}$. Often, linear parameters with associated resistivity or conductivity values tend to overestimate resistive or conductive subsurface structures during the inversion. Logarithmic parameters are generally preferable, because they eliminate the subjective choice of either conductivity or resistivity parameters and automatically enforce positivity on all parameters.

4.2.2   Advancing front cluster algorithm

The *Advancing Front Method* is a technique commonly used for unstructured mesh generation (see, for example Frey *et al.*, 1996). In this technique, a mesh is constructed by progressively adding mesh elements starting at the boundaries of the domain. During the meshing process, a propagating front - the border between the meshed and the unmeshed region - continuously moves towards the inner part of the domain until the meshing is complete.

We adopt this technique to cluster the forward mesh elements starting at the surface of the domain and progressively continuing downwards towards the bottom of the domain
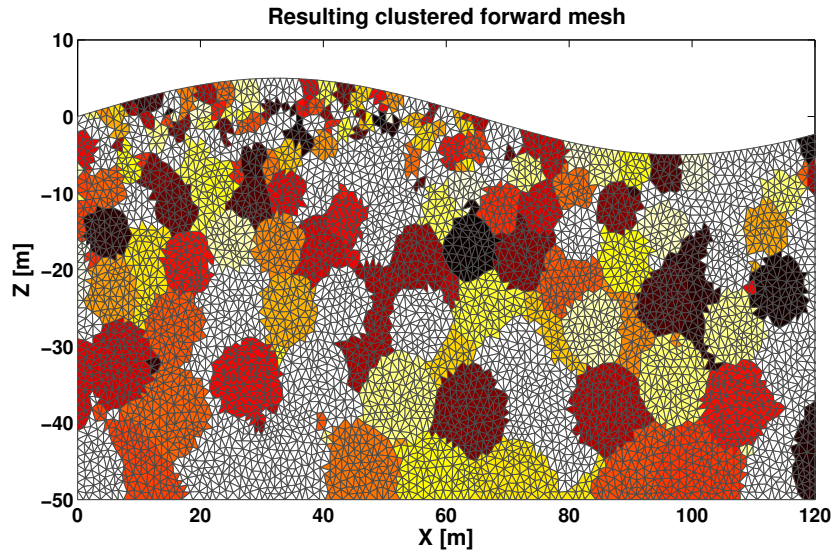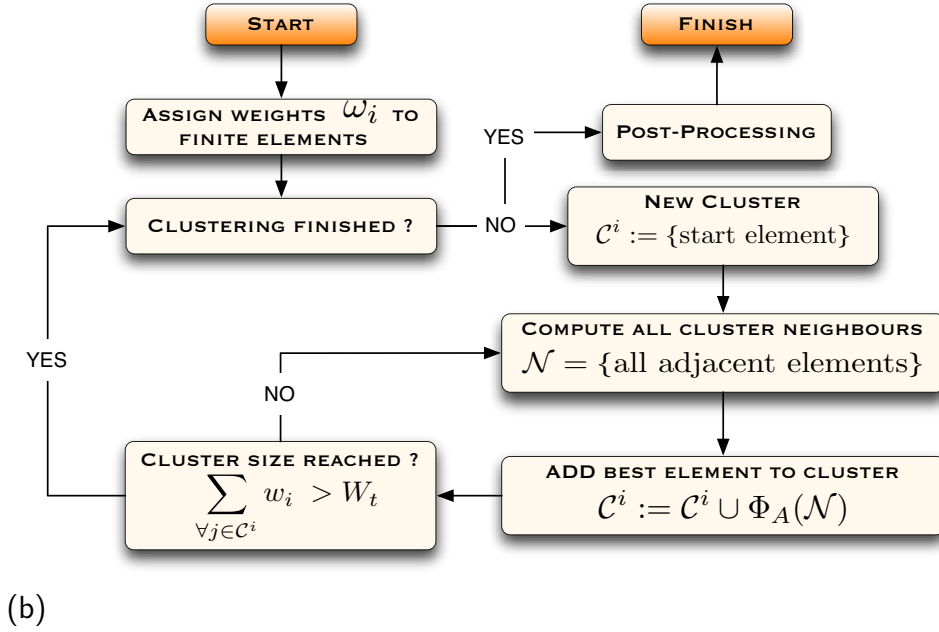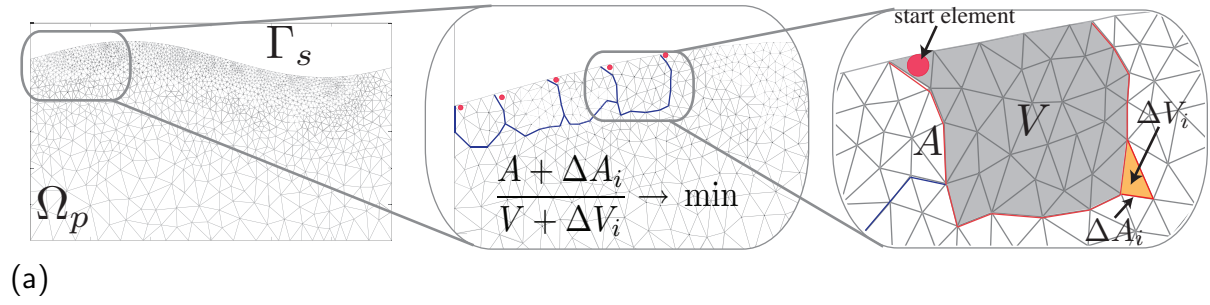
(a)

(b)

(c)

Figure 4.5 – Sketch (a) and algorithm (b) describing the advancing front clustering method to create a parameter mesh by finite element clustering. Clustering begins at the uppermost part of the domain. Clusters are constructed by selecting an initial element to start with (red dots in (a)) and successively adding out of all neighbouring elements $\mathcal{N}$ the one which minimizes the radius to area ratio $\Phi_A = (A + \Delta A_i)/(V + \Delta V_i)$. A target size for a cluster is reached when the sum of element weights w_i within a cluster exceeds a certain threshold W_t. Appropriate element weights can be based on data sensitivity or data resolution to obtain optimized model parametrizations. (c) Shows a sample $2D$ parameter mesh with clusters identified by common colours.

until all finite elements in the domain Ω_p, the inner part of the domain Ω where the inversion takes place, are assigned to one of the parameter cells. Ultimately, this results in a domain parametrization

$$\Omega \supset \Omega^P = \left\{ \Omega_1^P \cup \Omega_2^P \cdots \cup \Omega_{N_p}^P \right\} \;\; \text{with} \;\; \Omega_i^P = \bigcup_{\forall e \in \mathcal{P}_i} \Omega_e, \tag{4.3}$$

where $\mathcal{P}_i$ ($i = 1 \ldots N_p$) are index sets that contain indices for all of the finite elements of which the individual parameter cells are composed. Figure 4.5 b) depicts the algorithm used for the clustering. As a first step, element weights ω_i are assigned to all finite elements. These weights constrain the final size of the individual clusters and thereby largely determine the optimality of the resulting parametrization. Appropriate element weights can be based on data sensitivity or data resolution to obtain adequate model parametrizations.

Each new cluster $\mathcal{C}$ starts with a single finite element, as indicated by the red dots in Figure 4.5 a). As the starting element, we pick the element with the minimum absolute vertical (z) and horizontal (x) coordinates which is not yet included in another cluster. In this way, the clustering automatically progresses in horizontal layers downwards from the surface to the bottom of the domain.

Subsequently, additional finite elements are added to the new cluster until the sum of the element weights exceeds a previously defined threshold value: $\sum_{\forall j \in \mathcal{C}} \omega_j > W_t$. At each step, any of the finite elements adjacent to the boundary of the cluster, to which we refer to as the neighbouring elements $\mathcal{N}(\mathcal{C})$, are potential candidates to be added to the existing cluster. To assure a reasonable shape for the resulting clusters, we select out of all neighbouring elements $i \in \mathcal{N}(\mathcal{C})$ the one which minimizes the radius to area ratio $\Phi_A = (A + \Delta A_i)/(V + \Delta V_i)$. Here V is the area of the cluster $\mathcal{C}$, A denotes its circumference and ΔV_i and ΔA_i are the area and circumference, respectively, of the element that is to be potentially added (see Figure 4.5 a)).

During the clustering process, it may happen that *holes* (i.e. small unclustered regions) remain inside the domain Ω_p. By the end of the clustering process, these *holes* are filled by the algorithm with clusters that are neither well-shaped nor of the correct size according to the element-weights. Therefore, we employ a post-processing step, in which elements are swapped between clusters to improve the overall quality of the parametrization. Figure 4.5 c) shows an example model parametrization for the domain illustrated in Figure 4.5 a). The same algorithm as outlined here has been implemented and tested on $3D$ tetrahedral finite element discretizations.

4.3   Sensitivity calculation

For any non-linear inversion, the partial derivatives of the forward response with respect to the model parameters (the so-called sensitivities or Fréchet derivatives) are required. Besides providing the gradient information for the inversion process, spatial sensitivity distributions provide valuable information about the depth of penetration of certain geoelectric measurement configurations.

Alongside the forward solution, calculation of the sensitivities is required at each iteration of the inverse process; it is the most time-consuming part of geoelectric data inversions. Some authors (e.g. Loke and Barker, 1996a) use an approximate method described by Broyden (1972) to update the sensitivities at each iteration. However, we judge that in order to be able to recover deep subsurface features as well (for which sensitivities can be extremely small) full calculation of the sensitivities during each iteration is indispensable. Spitzer (1998) and McGillivray and Oldenburg (1990) compared different methods for swiftly calculating the $3D$ sensitivities for inhomogeneous subsurface distributions. Two of the presented methods for sensitivity calculations based on (i) finite element forward calculations (called *the matrix method*, Smith and Vozoff, 1984), and (ii) the reciprocity principle (or *adjoint method*, Geselowitz, 1971), have been identified as the most efficient for large geoelectric data sets. The implementation of both methods is outlined in the following section. In both cases we calculate pole-pole sensitivities

$$\mathbf{S}_{i,j}^{PP}(\vec{d}_{PP}) = \frac{\partial \mathcal{F}_i}{\partial m_j}. \tag{4.4}$$

From these sensitivities any three- or four-point electrode configurations can be formed by linear combinations or simple algebraic addition. For example, for a bipole-bipole array:

$$\frac{\partial f_i}{\partial m_j} = \mathbf{S}_{am,j}^{PP} - \mathbf{S}_{bm,j}^{PP} - \mathbf{S}_{an,j}^{PP} + \mathbf{S}_{bn,j}^{PP}. \tag{4.5}$$

This is generally more efficient (especially for large data sets) than computing sensitivities for each electrode configuration separately, because usually the number of possible non-reciprocal pole-pole configurations $N_{pp} = N_e(N_e - 1)/2$ (where N_e is the number of employed electrodes) is much smaller than the number of measured data that are to be inverted.

Computing the sensitivities for inhomogeneous subsurface models requires the numerically estimated voltage solutions for all source electrodes at all the nodes of the computational grid. Close to the source electrode locations, the magnitude of the estimated potentials are usually largely overestimated due to the numerically necessary but physically unrealistic approximation of the injecting electrodes by point (delta function) sources. Therefore, their absolute values need to be limited to prevent unrealistically large sensitivities close to the source electrodes from dominating the inverse equations.

We filter the numerical potentials for each source electrode s using a threshold potential $U_{Max}^s(\vec{r}_{Min})$, which is an estimate of the potential that would result for a homogeneous subsurface at a specified distance $\vec{r}_{Min}$ away from the source.

4.3.1 Sensitivities by DC forward calculation (Matrix Method)

During the inversion process, prior to the computation of the sensitivities, the forward solution is calculated by solving a set of linear equations

$$\mathbf{K} \cdot \vec{U} = \vec{F}. \tag{4.6}$$

Such a linear equation system can arise from a finite element discretization of the Poisson equation. Here $\mathbf{K}$ is the finite element stiffness matrix, $\vec{F}$ the discretized forcing function and $\vec{U}$ contains the unknown potentials. Following the approach by Smith and Vozoff (1984) and Sasaki (1994), differentiation of Equation 4.6 with respect to the cell conductivities σ_e yields

$$\mathbf{K} \cdot \frac{\partial \vec{U}}{\partial \sigma_e} = -\frac{\partial \mathbf{K}}{\partial \sigma_e}\vec{U} \tag{4.7}$$

because both the stiffness matrix $\mathbf{K}$ and the potential vector $\vec{U}$ depend on the conductivities σ_e. Equation 4.7 represents an additional forward solution step with a modified forcing function whose solutions are the unknown sensitivities $\partial \vec{U}/\partial \sigma_e$ for the model parameter e. Because the conductivity within each finite element cell is constant, the modified forcing function $-\partial \mathbf{K}/\partial \sigma_e U$ can be expressed easily by the local element matrices $\mathbf{K}_e$ that are readily available from the forward solution step:

$$\frac{\partial \mathbf{K}^e}{\partial \sigma_e} = \frac{1}{\sigma_e}\mathbf{K}^e. \tag{4.8}$$

As there are N_e sets of finite element equations for N_e source electrodes, $N_e \cdot N_p$ (with N_p being the number of employed model parameters) additional forward calculations are required to obtain all pole-pole sensitivity values, which is impractical in terms of the involved computational costs when traditional equation solvers are employed.

As it was mentioned previously, the finite element equations can easily be formulated in such a way that $\mathbf{K}$ does not depend on the individual source electrode used. In that case, using state-of-the-art direct sparse matrix solvers, $\mathbf{K}$ can be factorized into a lower and upper triangular matrix using LU decomposition: $\mathbf{K} = \mathbf{LU}$. Subsequently, Equation 4.7 can be solved efficiently for all $N \cdot m$ different forcing functions by simple

forward and backward substitutions:

$$y_i = \frac{1}{\mathbf{L}_{ii}} \left(b_i - \sum_{k=1}^{i-1} \mathbf{L}_{i,k}\, y_k \right), \quad x_i = \frac{1}{\mathbf{U}_{ii}} \left(y_i - \sum_{k=i+1}^{n} \mathbf{U}_{i,k}\, x_k \right) \tag{4.9}$$

Here $b_i = -\left(\partial\mathbf{K}/\partial\sigma_e\, \vec{U} \right)_i$ are the entries in the modified forcing function (Equation 4.7) and $x_i = \left(\partial\vec{U}/\partial\sigma_e \right)_i$ are the resulting sensitivity values. Available sparse direct matrix solvers usually assume dense right-hand-side and solution vectors when performing the forward and backward substitutions. Vector $\vec{b}$ could easily include several hundred thousand entries out of which only a few are non-zero. Additionally, we are only interested in a few of the values in the solution vector $\vec{x}$. Re-implementing the forward and backward substitutions in Equation 4.9 taking the sparsity patterns of the potential and the right hand side vectors into account can therefore substantially improve the performance of the sensitivity computations. The necessary optimizations have been implemented in the sparse direct matrix solver *Pardiso* (Schenk *et al.*, 2001) in close collaboration with Dr. Olaf Schenk from the University of Basel.

4.3.2 Sensitivity calculations based on the reciprocity theorem (Adjoint Method)

$3D$ sensitivity computation

An efficient way of calculating the sensitivities for inhomogeneous subsurface models is based on the reciprocity principle or adjoint source method. For electromagnetic inverse problems Geselowitz (1971) derived an analytic expression for the sensitivity of the impedance Z with respect to a conductivity change $\delta\sigma$ within a finite sub-domain Ω_e:

$$\delta Z = -\delta\sigma \int_{\Omega_e} \frac{\nabla U(\vec{r}_s, \vec{r})}{I_s} \cdot \frac{\nabla U(\vec{r}_p, \vec{r})}{I_p}\, d^3\vec{r}, \tag{4.10}$$

where $U(\vec{r}_s, \vec{r})$ is the potential that results from injecting current I_s at electrode location $\vec{r}_s$ and similarly $U(\vec{r}_p, \vec{r})$ is the potential caused by injecting current I_p at $\vec{r}_p$ (the adjoint source). The corresponding expression for geoelectric pole-pole sensitivities for a source electrode located at $\vec{r}_s$ and the measuring electrode located at $\vec{r}_p$ reads (Zhou and Greenhalgh, 1999)

$$\frac{\partial U(\vec{r}_c, \vec{r}_p)}{\partial\sigma_e} = -I_s \sum_{\forall k \in P_e} \left[\int_{\Omega_k} (\nabla G(\vec{r}_s, \vec{r}) \cdot \nabla G(\vec{r}_p, \vec{r}))\, dr \right], \tag{4.11}$$

where σ_e is the conductivity of the model parameter Ω_e^P that is formed out of all forward mesh cells $\{\Omega_k \mid \forall k \in \mathcal{P}_e\}$ (see section 4.2). It is obvious from the above equation that the sensitivities for a certain parameter cell are computed by summing up the calculated

sensitivities of all forward mesh cells which makes up the inversion cell. The gradients of the Green's functions $G(\vec{r}_s, \vec{r})$ and $G(\vec{r}_p, \vec{r})$ are approximated by the gradients of the finite element shape functions, i.e.

$$\nabla G(\vec{r}_s, \vec{r}) = \sum_{i=1}^{N_s} \nabla \phi_i(\vec{r}) \, U(\vec{r}_s, \vec{p}_i)/I_s, \tag{4.12}$$

where ϕ_i $(i = 1..N_s)$ are the finite element shape functions, I_s is the current source strength and $U(\vec{r}_s, \vec{p}_i)$ are the previously computed forward solutions estimated for a source located at $\vec{r}_s$ and evaluated at the finite elements node i.

$2.5D$ sensitivity computation

Computing the pole-pole sensitivities for two-dimensional conductivity distributions $\sigma(x, z)$ taking three-dimensional source characteristics into account, requires estimating the Fourier-transformed Green's functions $\hat{G}(\vec{r}_s, \vec{r})$ and $\hat{G}(\vec{r}_p, \vec{r})$, for the active source and the adjoint source, respectively, based on the governing $2.5D$ Helmholtz equation (see section 3.9.2). The resulting expression for the pole-pole sensitivities takes a similar form to Equation 4.11 (Zhou and Greenhalgh, 1999):

$$\frac{\partial U(\vec{r}_c, \vec{r}_p)}{\partial \sigma_e} = -\frac{I_s}{2} F_c^{-1} \left\{ \sum_{k \epsilon C_e} \left[\int_{\Omega_k} \left(\nabla \hat{G}(\vec{r}_s, \vec{r}) \cdot \nabla \hat{G}(\vec{r}_p, \vec{r}) + k_y^2 \, \hat{G}(\vec{r}_s, \vec{r}) \hat{G}(\vec{r}_p, \vec{r}) \right) d^3 r \right] \right\}. \tag{4.13}$$

Here F_c^{-1} denotes the inverse Fourier transformation with respect to spatial wavenumber k_y required to obtain the sensitivities in the spatial domain. As for the $3D$ pole-pole sensitivities, integrals are carried out by summing over the forward mesh cells (triangular elements in this case) that form the individual inversion parameter cells. Gradients of the Fourier-transformed Green's functions are approximated by the shape functions $\phi_i(\vec{r})$ of the finite elements:

$$\nabla \hat{G}(\vec{r}_s, \vec{r}) = \sum_{i=1}^{N_s} \nabla \phi_i(\vec{r}) \, \hat{U}(\vec{r}_s, \vec{p}_i)/I_s. \tag{4.14}$$

Note that for the inverse Fourier transformation, we use the same discrete wavenumber sampling scheme as for the $2.5D$ forward solution described in section 3.9.2.

4.4   Regularization

Geoelectric inverse problems are usually both non-unique and ill-conditioned, i.e they are over-determined, under-determined or, which is the most common case, over- and under-determined at the same time. This is mainly due to the broad range of sensitivities

spanning several orders of magnitude that typically occur for geoelectric data sets. As a consequence the model domain is often characterized by regions that are well resolved and other regions that are very poorly resolved. Regularization constraints are required to stabilize the solution and to prevent highly oscillatory model fluctuations with unrealistically large parameter contrasts to emerge during the inversion. We globally constrain the model vector $\vec{m}_{i+1}$ at each iteration of the inversion process by imposing (i) damping constraints, and (ii) smoothness constraints. Damping constraints require the model to not deviate too far from the previous (or preferred) model by minimizing the functional

$$\Phi_m^d = |\vec{m}_{i+1} - \vec{m}_i|^2. \tag{4.15}$$

Here $\vec{m}_i$ is the model vector from the previous iteration. Smoothness constraints are applied according to *Occam's Principle* to obtain simple models in the sense of spatially smooth models (deGroot Hedlin and Constable, 1990) by minimizing the functional

$$\Phi_m^c = |\mathbf{C}\vec{m}_{i+1}|^2, \tag{4.16}$$

where $\mathbf{C}$ is a matrix that contains the first or second order spatial model derivatives. The damping and smoothness constraints are weighted by regularization parameters α and β, respectively, that weight the data misfit against the applied constraints for each inverse sub-problem. The corresponding composit misfit function for iteration i of the inverse problem takes the form

$$\Phi^i = \Phi_d^i + \alpha \cdot \Phi_{m_d}^i + \beta \cdot \Phi_{m_c}^i, \tag{4.17}$$

where Φ_d^i is the data misfit (see section 4.5). Careful selection of the regularization parameters is of key importance to obtain reasonable inversion results. Too large values for α and β would lead to simple model vectors that poorly explain the measured data, whereas too small values would result in models with unrealistically high resistivity contrasts, thus potentially over-interpreting noisy data. Conceptually, we seek to find a model that satisfies the regularization constraints and fits the data to within the data uncertainty range. For measurements with an assumed uncorrelated Gaussian noise of zero mean, the expected data misfit is equal to the number of inverted data, i.e $\Phi_d \approx N_d$. Usually, for early iterations in the inversion process the obtained model vectors are too far away from the true model, such that the criterion $\Phi_d \approx N_d$ cannot be met. Therefore, following the approach of Farquharson and Oldenburg (2004) we employ a "cooling scheme" for the regularization parameters. That is, we start with

large values β^1 and α^1 that are subsequently reduced in each iteration i according to

$$\begin{cases} \beta^i = \max(c\,\beta^{i-1}, c_0\,\beta^1) \\ \alpha^i = \max(c\,\alpha^{i-1}, c_0\,\alpha^1) \end{cases}, \tag{4.18}$$

where $0.01 \leq c \leq 0.5$ is a regularization reduction parameter. Reduction of the regularization parameters is continued down to target values $c_0\,\beta^1$ and $c_0\,\alpha^1$, where c_0 is chosen such that the criterion $\Phi_d \approx N_d$ is fulfilled.

(a) $\qquad$ (b)
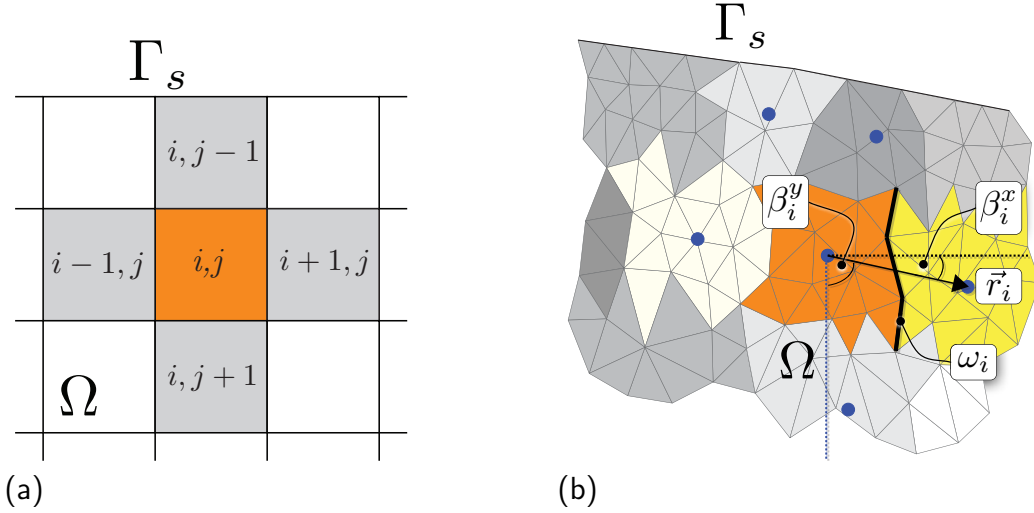
Figure 4.6 – (a) For a simple $2D$ cartesian grid, there are four adjacent cells to each parameter cell that are usually equally weighted when computing smoothness constraints. (b) For $2D$ parameter grids composed of triangular finite element clusters, smoothness strengths are weighted by the cumulative length of all triangular edges that two parameter cells have in common (ω_i). Directional smoothing is implemented considering the angles formed between the vectors $\vec{r}_i$ and the cartesian axes (β_i^x and β_i^y). $\vec{r}_i$ are the vectors connecting the centroids of adjacent clusters. The same methodology is used for $3D$ parameter grids consisting of clustered tetrahedral cells.

The smoothness constraint matrix $\mathbf{C}$ in Equation 4.16 that contains the spatial model derivatives is constructed for a parameter grid made up of a set of finite element clusters (section 4.2). Appropriate means of obtaining $\mathbf{C}$ for such a geometry are required. In the simplest case of $2D$ regular cartesian grids (e.g. those in finite-difference schemes), there are four adjacent cells for each parameter cell (see Figure 4.6(a)). A corresponding first order smoothness matrix takes the simple form (Günther, 2004)

$$\mathbf{C}_{i,j} = \begin{cases} 1 & i = j \\ 0 & i \notin \{N_j^1 \cdots N_j^4\} \\ -1/4 & i \in \{N_j^1 \cdots N_j^4\} \end{cases} \tag{4.19}$$

with entries of 1 on the main diagonal corresponding to individual parameter cell indices j and four additional non-zero entries per row, constraining the parameter cell's

neighbours $N_j^1 \cdots N_j^4$.

Figure 4.6(b) depicts a sketch of the principle used to construct appropriate smoothness constraints for parameter grids formed out of clustered finite elements. As a first step, we compute for each cluster j a list of neighbouring clusters $\mathcal{N}_j$. Neighbours to a cluster j are defined as those clusters that include at least one finite element that has a common side with one of the finite elements in the cluster j. Smoothness constraints for all neighbouring clusters in $\mathcal{N}_j$ are weighted according to the cumulative length (or area) they have in common with the cluster j under consideration. In this way, we avoid applying too strong smoothness constraints for pairs of clusters that only share a small portion of their periphery.

Under certain circumstances, direction dependent smoothness constraints can help to find realistic subsurface models during an inversion process. For example, in many geological settings it is known à-priori that the subsurface exhibits sharp vertical resistivity contrasts. Therefore, we allow the relative strengths of the smoothness constraints to be defined separately for all spatial coordinates via parameters $0 \leq f_x, f_y, f_z \leq 1$, that define the relative strengths of the vertical and horizontal smoothness constraints. This is archived by considering for each pair of neighbouring clusters a vector $\vec{r}_i$ that connects their centroids. Smoothness constraints are then weighted by the angles that $\vec{r}_i$ form with the cartesian axes. The resulting smoothness constraint matrix $\mathbf{C}$ for a $2D$ parametrization takes the form

$$\mathbf{C}_{i,j} = \begin{cases} 1 & i = j \\ 0 & i \notin \mathcal{N}_j \\ -\omega_i \left[f_x cos(\alpha_i^x) + f_y cos(\alpha_i^y) \right] & i \in \mathcal{N}_j. \end{cases} \tag{4.20}$$

4.5   Inversion approach

The forward solver described in Chapter 3 allows the prediction of a corresponding data vector $\vec{d}_{syn}$ for a certain model vector $\vec{m}$:

$$\vec{d}_{syn} = \mathcal{F}(\vec{m}_{true}). \tag{4.21}$$

Obviously, for geoelectric data inversions, we are interested in the inverse relationship – i.e. for a set of measurements $\vec{d}_{obs}$ acquired in the field, we seek to find an approximation of the true subsurface model $(\vec{m}^{est})$ that matches the data: $\vec{m}_{est} = \mathcal{F}^{-1}(\vec{d}_{obs})$. Usually, this is done in an iterative fashion by locally linearising the forward operator around a model vector $\vec{m}_0$:

$$\mathcal{F}(\vec{m}_0 + \Delta\vec{m}) \approx \mathcal{F}(\vec{m}_0) + \frac{\partial\mathcal{F}(\vec{m}_0)}{\partial\vec{m}} \Delta\vec{m} = \mathcal{F}(\vec{m}_0) + \mathbf{G}\, \Delta\vec{m} \tag{4.22}$$

with the matrix $\mathbf{G}$ containing the partial derivatives $\mathbf{G}_{ij}(\vec{m}_0) = \partial \mathcal{F}_i(\vec{m}_0)/\partial \vec{m}_j$, usually referred to as sensitivities. Within each iteration i of the inversion process a linear sub-problem

$$\vec{d}_{obs} - \mathcal{F}(\vec{m}_i) = \mathbf{G}\,\Delta\vec{m} \tag{4.23}$$

needs to be solved in an appropriate sense to minimize the data residuals $\vec{d}_{obs} - \mathcal{F}(\vec{m}_i)$. Adding $\mathbf{G}\vec{m}_{i-1}$ to both sides of Equation 4.23 allows us to solve for the total model vector $\vec{m}_{i+1}$ instead of the model update vector $\Delta\vec{m}$:

$$\vec{d}_{obs} - \mathcal{F}(\vec{m}_i) + \mathbf{G}\vec{m}_i = \mathbf{G}\vec{m}_{i+1}. \tag{4.24}$$

Usually, for each datum d_j in $\vec{d}_{obs}$ a measurement uncertainty δ_j is known either directly from the measurement process (e.g. it is automatically estimated by the measurement system) or by a post-experimental error appraisal based on some reasonable assumptions. These measurement uncertainties are used to weight the data residuals:

$$\mathbf{D}(\vec{d}_{obs} - \mathcal{F}(\vec{m}_i)) \ \text{ with } \ \mathbf{D} = diag\left(\frac{1}{\delta_j}\right) \tag{4.25}$$

Here it is assumed that the noise in the measured data is Gaussian and uncorrelated. Adding damping and smoothing constraints with the regularization parameters α and β (see section 4.4) results in the combined set of equations:

$$\begin{bmatrix} \mathbf{DG} \\ \alpha\mathbf{C} \\ \beta\mathbf{I} \end{bmatrix} \vec{m}_{i+1} = \begin{bmatrix} \mathbf{D}(\vec{d}_{obs} - \mathcal{F}(\vec{m}_i)) + \mathbf{DG}\vec{m}_i \\ 0 \\ \beta\vec{m}_i \end{bmatrix} \tag{4.26}$$

which is solved in a least-square-sense. For linear systems of equations of the form $\mathbf{A}\vec{x} = \vec{b}$ this is usually accomplished by a pre-multiplication with $\mathbf{A}^T$. Applied to Equation 4.26 this results in the normal inverse equation

$$(\underbrace{\mathbf{D}^T\mathbf{G}^T\mathbf{DG}}_{T_2} \ + \ \alpha^2\mathbf{C}^T\mathbf{C} + \beta^2\mathbf{I})\,\vec{m}_{i+1} \tag{4.27}$$

$$= \ \mathbf{D}^T\mathbf{G}^T\left[\mathbf{D}(\vec{d}_{obs} - \mathcal{F}(\vec{m}_i)) + \mathbf{DG}\,\vec{m}_i\right] + \beta^2\,\vec{m}_i$$

$$= \ \underbrace{\mathbf{D}^T\mathbf{G}^T\mathbf{D}\,(\vec{d}_{obs} - \vec{d}_{calc})}_{T_1} + \underbrace{\mathbf{D}^T\mathbf{G}^T\mathbf{DG}}_{T_2}\,\vec{m}_i + \beta^2\,\vec{m}_i$$

which can be efficiently solved e.g. by a LU-decomposition. Solving Equation 4.27 for the model vector $\vec{m}_{j+1}$ is equivalent to minimizing the combined objective function:

$$\begin{aligned} \Phi &= \Phi_d + \alpha \cdot \Phi_{m_d} + \beta \cdot \Phi_{m_c} \\ &= |\mathbf{D}(\vec{d}_{obs} - \mathcal{F}(\vec{m}_i))|^2 + \alpha \cdot |\vec{m}_{i+1} - \vec{m}_i|^2 + \beta \cdot |\mathbf{C}\vec{m}_{i+1}|^2. \end{aligned} \tag{4.28}$$

Figure 4.7 – Simple sketch to outline the method used to assemble the Hessian matrix without explicitly forming the whole sensitivity matrix $\mathbf{G}$, which, for large data sets, could easily exhaust the available computer's main memory.

If the number of data points to be inverted is much larger than the number of parameter cells ($N_d >> N_c$), which is usually the case for large-scale geoelectric surveys, then the amount of memory required to keep the sensitivity matrix $\mathbf{G}$ (which is of dimension $N_d \times N_c$) in the computer's main memory may be excessive. Solving the normal inverse equations instead of Equation 4.26 circumvents this limitation, because the main matrix $\mathbf{D}^T\mathbf{G}^T\mathbf{D}\mathbf{G}$ of the normal equation is of dimension $N_c \times N_c$. However, the numerical expense of assembling the normal equations is relatively large due to the involved matrix-matrix products. Furthermore, due to the aforementioned potential memory limitations, it has to be assured that the sensitivity matrix $\mathbf{G}$ is never formed explicitly during the assembly.

Therefore we employ an efficient technique to assemble the matrix expressions T_1 and T_2 in Equation 4.27. Writing out the matrix-matrix product in expression T_2

$$\left((\mathbf{D}\mathbf{G})^T\mathbf{D}\mathbf{G}\right)_{ij} = \sum_{r=1}^{n} (\mathbf{D}\mathbf{G})_{r,i} (\mathbf{D}\mathbf{G})_{r,j} = \sum_{p=1}^{N_p} \left[\sum_{r \epsilon I_p} (\mathbf{D}\mathbf{G})_{r,i} (\mathbf{D}\mathbf{G})_{r,j} \right], \tag{4.29}$$

reveals that $\mathbf{D}^T\mathbf{G}^T\mathbf{D}\mathbf{G}$ can be evaluated efficiently by subdividing $\mathbf{D}\mathbf{G}$ into N_p sub-matrices $\{\mathbf{D}_1\mathbf{G}_1, \mathbf{D}_2\mathbf{G}_2, ..., \mathbf{D}_{N_p}\mathbf{G}_{N_p}\}$ and summing up the matrix-matrix products of these sub-matrices. Figure 4.7 illustrates this approach. Forming sub-matrices instead

of evaluating the matrix products on a row-by-row basis allows us to greatly speedup the computations by the use of highly efficient *Level-3 BLAS* routines (Dongarra *et al.*, 1990).

A similar technique is used to form the matrix product necessary to evaluate expression T_1 in equation 4.27:

$$\left((\mathbf{DG})^T (\vec{d}_{obs} - \vec{d}_{calc})\right)_i = \sum_{p=1}^{N_p} \left[\sum_{r \epsilon I_p} (\mathbf{DG})_{r,i} \left(\vec{d}_{obs} - \vec{d}_{calc}\right)_r \right] \qquad (4.30)$$

4.6 Synthetic data examples

In this section, we test and verify our inversion procedures on synthetic $2D$ and $3D$ data sets generated with our finite element forward solver on models with a pronounced topography.

2D examples

Figure 4.8 shows the tomogram results (resistivity images) obtained for synthetic Wenner, Schlumberger and Summa data sets. The latter is composed of a Wenner, a Schlumberger and a Dipole-Dipole data set. All synthetic data sets were generated using the discretized subsurface model shown in Figure 4.8(a). It consists of a 2.5 m surface layer with a resistivity of 100 Ωm, a conductive block that grades from 100 Ωm to 10 Ωm in the center and a 10 000 Ωm highly resistive block. Simulations of all synthetic data sets are based on a profile with 100 electrodes at 1.2 m spacings with a total line length of 120 m. Forward solutions were performed on a second order finite element mesh comprising 25 000 finite elements. A mixed boundary condition has been employed and 12 discrete wavenumbers were used for the inverse Fourier sampling.

Inversions were carried out on the model parametrization shown in Figure 4.8(b) with $\approx 1\,600$ cells. The tomogram results in Figure 4.8 (c)-(e) were obtained by noise-free synthetic data whereas the data sets in Figure 4.8 (f)-(h) were contaminated with Gaussian distributed noise of 1% relative voltage noise and 20 mV constant (absolute) noise amplitude. Such a noise model is commonly assumed (e.g. Günther, 2004). An initial regularization parameter of $\alpha = \beta = \nu \approx 0.05$ (equal strength for damping and smoothing) was applied and successively reduced down to a third of its starting value during the first few iterations.

Inversion results obtained for the three noise-free data sets (4.8 (c)-(e)) resemble the main features of the synthetic model quite well. The shape and conductivtiy values of the graded conductive block, the highly resistive block as well as the surface layer are recovered by the inversion process. However, the shape of the graded block is
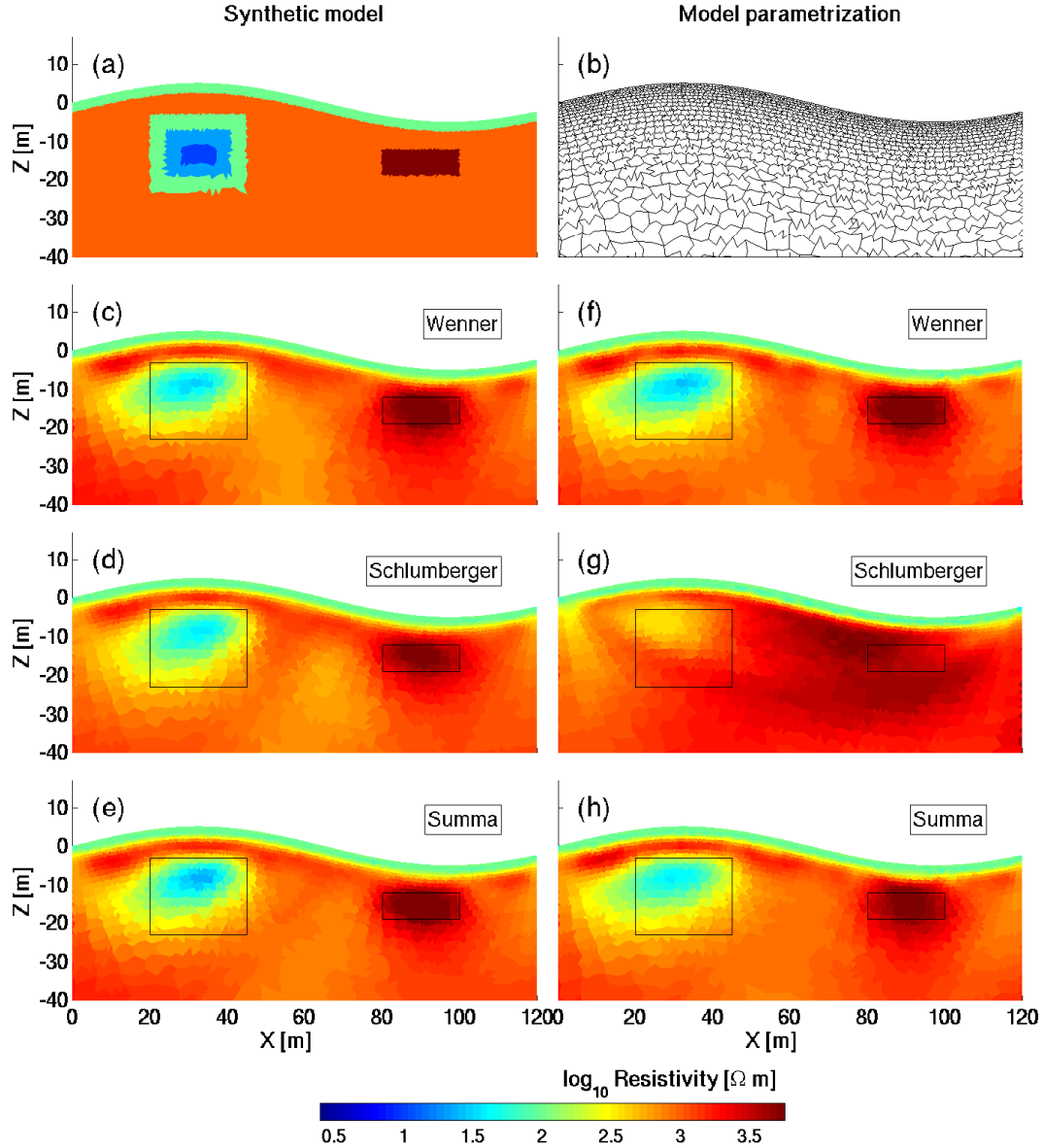
Figure 4.8 – Tomogram results for the subsurface model shown in (a) and synthetic Wenner, Schlumberger and Summa data sets generated for a profile of 100 electrodes placed at the surface of the domain at 1.2 m intervals. Results in (c)-(e) were obtained from noise-free data whereas inverted data sets in (f)-(h) were contaminated with gaussian distributed noise (1% relative and 20 mV absolute noise amplitude).

somewhat smeared out and its $10\,\Omega m$ conductive center is only partially resolved. It is astonishing to see that all three noise-free data sets (Wenner, Schlumberger, Summa) perform almost equally well in resolving the synthetic model. We presume that for deeper conductivity anomalies, more pronounced differences in the tomogram results would be visible especially between the Summa and the Schlumberger data sets.

The tomogram results for the noise-contaminated Wenner and Summa data sets (Figures 4.8(f) and 4.8(h)) resemble the tomogram results for the corresponding noise-free data sets. The Schlumberger data set seems to be much more susceptible to the influence of noise, because its voltages are much smaller, neither the graded conductive

block nor the highly resistive block are recovered.

3D example with topography
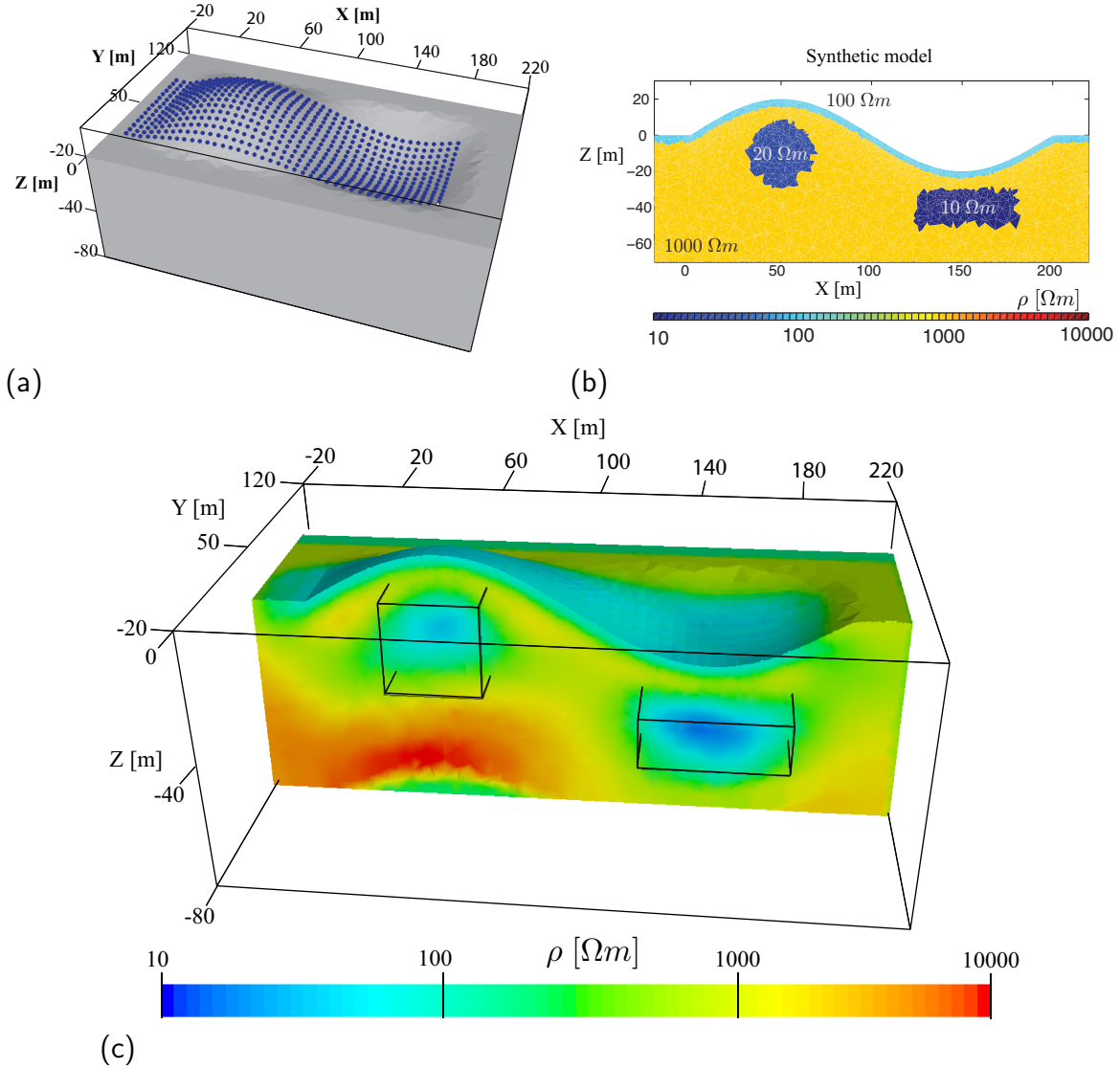

(a)

(b)

(c)

Figure 4.9 – 3D tomogram result (c) obtained from synthetic profiling data generated along 15 electrode spreads each including 40 electrodes at 5 m intervals (a). The synthetic data comprises a combination of Wenner, Schlumberger and a Dipole-Dipole data sets created on each of the individual profiles. The subsurface model employed consists of a 100 Ωm surface layer, a 20 Ωm sphere and a 10 Ωm cuboid, both embedded in a homogeneous 1 000 Ωm medium (b). The tomogram result in (c) is clipped at $Y = 50$ m for visualization purposes. Furthermore, the bounding boxes of the highly conducting cuboid- and sphere-shaped anomalies are highlighted.

We demonstrate the $3D$ capabilities of our inverse approch on a synthetic profiling data set generated on a sequence of 15 electrode parallel lines each including 40 electrodes at 5 m intervals. A combination of Wenner, Schlumberger and Dipole-Dipole array data sets have been constructed on each of the electrode profiles with a total of $\approx$

19 000 measurments for the combined data set. All measurement configurations with a geometry factor larger than 5 000 m have been excluded from the data set. Such high K values normally imply small voltages and so such data can be easily noise-captured. Figure 4.9(a) shows the electrode locations employed (blue points) and the undulating topography of the domain used. A vertical plane cut through the center of the synthetic subsurface model is shown in Figure 4.9(b). It consists of a 100 Ωm surface layer and two conductive bodies, a 20 Ωm sphere and a 10 Ωm cuboid, embedded in a homogeneous 1 000 Ωm medium.

The inversion has been carried out with a finite element forward discretization incorporating roughly 1.2 million finite elements that were clustered with the auxiliary staggered grid method to form a model parametrization with 20 000 parameter cells. Forward solutions were computed with a first order finite element approximation, a mixed boundary condition in combination with a mesh largely extended towards the computational boundaries, and a direct matrix solver. To regularize the inverse equations, regularization parameters $\alpha = \beta = \nu = 0.3$ (with equal strengths for the smoothness and damping constraints) have been used. Both constraints were progressively reduced during the inversion process down to a third of the original value.

Figure 4.9 shows the inversion result obtained at iteration number 6 for which the RMS value of the residuals is $\approx 4.7\%$. The tomogram at $Y = 50$ m shows the conductivity distribution within the two resolved conductive features. Clearly, the resistivity and thickness of the surface layer is accurately reproduced by the inversion process. Also, the two highly conductive bodies are picked -up quite well by the inversion algorithm, though their shapes are somewhat smeared out and, especially for the sphere-shaped anomaly, the resolved resistivity values are slightly over-estimated. The highly resistive anomaly that appears below the conductive sphere with resistivities in excess of 10 000 Ωm clearly indicates the maximum resolution depth of the surface data employed. We judge, that with the synthetic data set used (line length 120 m), resitivity features can only be resolved down to a depth of 30 m (measured below the surface).

4.7 Application to field data

Buried waste deposit site near Stetten (Switzerland)

To further test and evaluate our inversion procedures, we have analysed data recorded with the fully distributed data acquisition system *ETH-DCMES-II* described in Chapter 2. The resistivity data were collected across the well-studied, sealed waste-deposit site located approximately 25 km west of Zürich close to the village of Stetten (Switzerland) (Lanz *et al.*, 1996, 1998, 1999; Green *et al.*, 1999). Figure 4.10 shows the location of the field test site. The resistivity investigations involved the following:
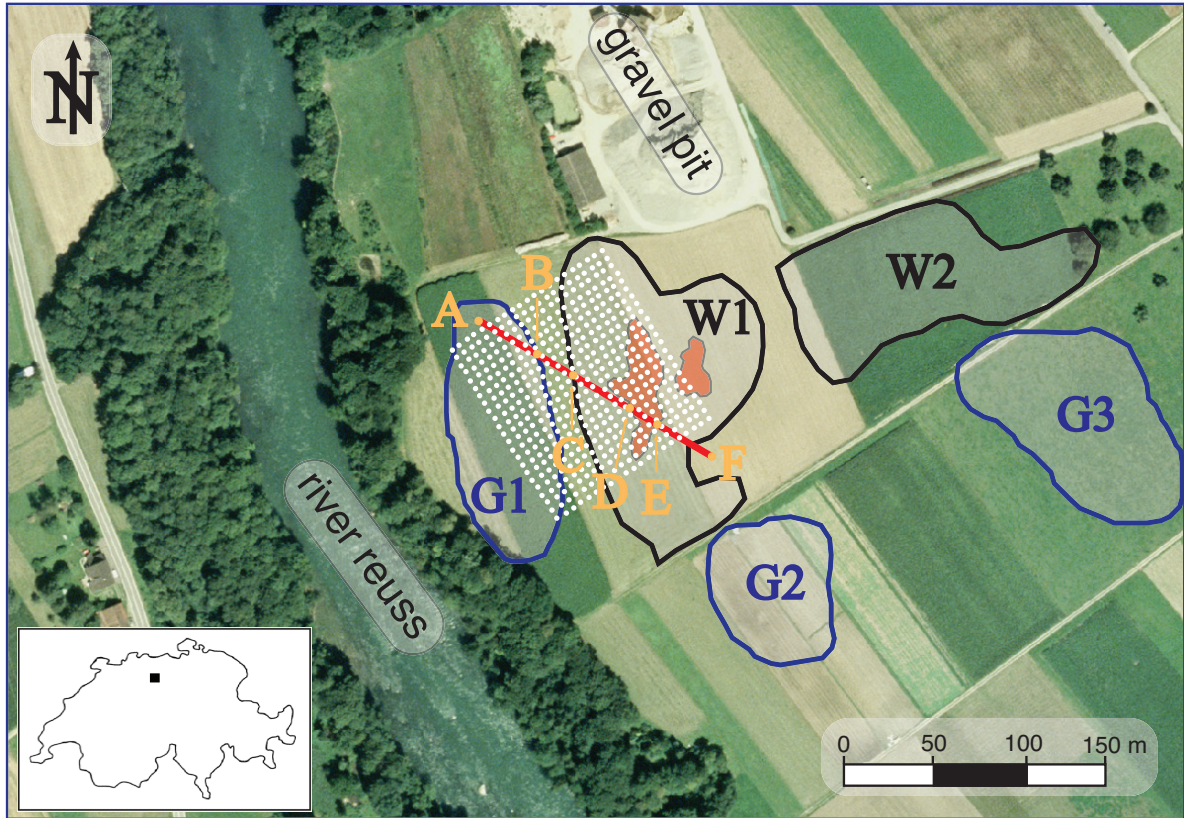
Figure 4.10 – $2D$ and $3D$ geoelectric field surveys have been carried out over a sealed industrial waste deposit site close to the village of Stetten (Switzerland). The red line indicates the location of the $2D$ profile and the white dots mark the electrode positions used during the $3D$ survey. Extensive previous measurements with various geophysical techniques revealed the borders of shallow surface gravel lenses (regions G1, G2 and G3) and two distinct waste deposit bodies (regions W1 and W2). High conductivities in excess of 0.1 S/m have been recorderd with *EM-31* measurements below the zones marked in red.

- a pole-bipole comprehensive data set acquired along a $2D$ line of 50 electrodes with 3m spacing (red line in Figure 4.10)

- pole-bipole data acquired using a $3D$ roll-along scheme with a total of about 250,000 measurements recorded on 462 equispaced ($5m$ distance) electrode locations (white dots in Figure 4.10)

For both data sets, the parallel recording capability of the *ETH-DCMES-II* was employed. That is, each single measurement sequence involved first choosing one source and one reference electrode and then simultaneously acquiring potential readings from all remaining data acquisition units measured with respect to the single reference electrode.

The landfill contains household and industrial waste that was dumped in abandoned gravel/sand pits before being covered by a $0.8m$ thick layer of soil. The lateral boundaries of two distinct waste deposit bodies (region W1 and W2 in Figure 4.10) were recovered through vertical-gradient magnetic and frequency-domain electromagnetic surveying (Lanz *et al.*, 1999). The latter revealed high conductivities in excess of 0.1 S/m

in some parts of the western waste deposit body (zones highlighted in red, region W1). Presumably, the western deposit body is mainly filled with industrial waste, whereas the eastern waste deposit body (region W2) is mainly filled with household garbage and diverse metallic objects (Lanz *et al.*, 1999). The depth extend of the two waste pits determined from high-resolution refraction seismic data was $\approx 11m$ (region W1) and $\approx 8m$ (region W2), respectively (Lanz *et al.*, 1998). Three distinct gravel lenses (regions G1, G2 and G3) were delineated in location and aerial extend by electromagnetic surveys, and the thicknesses delineated by georadar surveys (Lanz, 1998).

Two-dimensional investigation
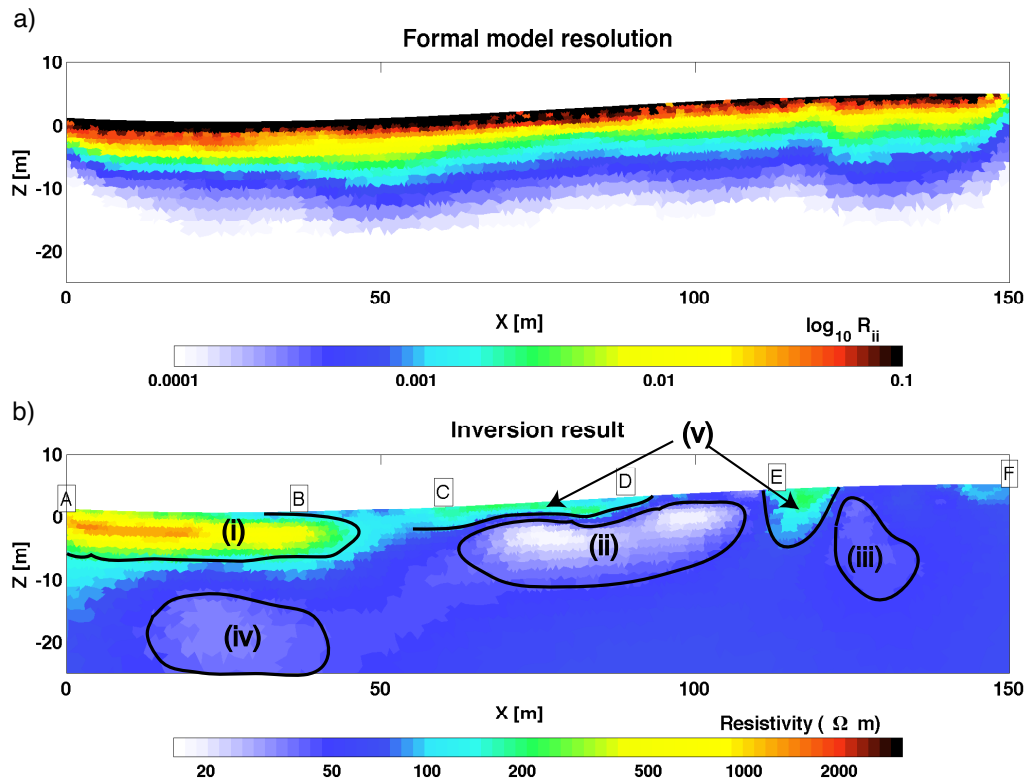
Figure 4.11 – Formal model resolution (a) and tomogram result (b) of the $2D$ comprehensive pole-bipole data set. Resistivity features in (b) correspond to fluvial gravels and coarse sands within a gravel lense (i), highly conducting industrial waste (ii) and (iii) and material originating from the abandoned gravel pit (v). The conductive feature in (iv) most likely represents an inversion artefact.

Figure 4.11 shows the tomogram result of the comprehensive pole-bipole data set acquired along a profile of 50 electrodes at 3 m intervals (red line in Figure 4.10). A homogeneous half-space with resistivity equal to the average of the measured apparent resistivities ($\approx 95\ \Omega m$) was used as the initial input model. For the forward modeling, we employed a second oder finite element mesh ($\approx 30\,000$ cells) in combination with

mixed boundary conditions and a direct matrix solver. Twelve discrete wavenumbers were used for the inverse Fourier sampling.

The parameter mesh used was created by the auxiliary staggered grid method with a total of $\approx 1\,600$ cells. To regularize the inverse equations, we used a damping parameter of $\nu = 0.65$ with equal strengths for the damping and smoothing constraints. The aforementioned cooling scheme has been applied to reduce the regularization strengths during the inversion process.

Reverse electrode configurations were purposely included in the comprehensive data set to asses the overall data quality. Pole-bipole data recordings were performed using a remote source electrode placed at a distance of roughly 800 m in the south-eastern direction from the electrode deployment. The comprehensive data set comprises $N = 50 \cdot 49 \cdot 48 = 117\,600$ measurements (including reciprocal recordings). Four out of the 50 employed electrodes were producing unreliable data when acting as reference electrodes; the corresponding measurements ($9\,600$) were excluded from the data set. Moreover, all measurements ($3\,016$) with geometric factors larger then $10\,000$ m and all measurements with an absolute relative error (computed by the reciprocal measurements) larger than 20 percent ($\approx 37\,000$ readings) were filtered out, resulting in a reduced data set comprising roughly $65\,000$ measurements. The overall data quality, as assessed by the reciprocal recordings, was not as good as expected (judging from previous extensive laboratory tests (Stummer *et al.*, 2002)). Most likely, the observed large deviations in the reverse recordings are due to electromagnetic noise induced by a sorting machine operating at a nearby gravel pit (see Figure 4.10).

As shown in Figure 4.10, the measurement profile crosses a gravel lens (region G1) and the western waste deposit body (region W1). For convenience, corresponding crossing points are labelled in Figure 4.10 and Figure 4.11. The tomogram result resembles the known shape of both the gravel lense as well as the waste deposit body. High resistivities in the range $200 - 800\ \Omega m$ ((i) in Figure 4.11)) correspond to fluvial gravels and coarse sands inside the gravel lense.

The shallow, highly conducting body (ii) below labelling *C-E* most likely corresponds to the industrial waste dumped in the western waste deposit body. Its lateral location is in good agreement with the waste deposit boundaries (see region W1 in Figure 4.10) as they were resolved by previous electromagnetic measurements (Lanz *et al.*, 1999). Furthermore, the depth of the deposit body was delineated to be $\approx 11m$, which is in agreement with our inversion result. Below the labels *D-E*, the high conductivity feature (ii) almost reaches up to the surface. At this location, between labels D and E, the measurement profile crosses the zone highlighted in red in Figure 4.10, where high conductivities ($< 10\ \Omega m$) were revealed by electromagnetic measurements. The employed method (*EM-31* measurements) has a limited penetration depth of 3-6 m (Lanz *et al.*, 1999). The conducting body (iii), with resistivities in the range of $20 -$

$30\ \Omega m$, is probably due to dumped waste within the waste deposit. We interpret the high resistivities at the surface (regions labelled (v)) as remaining material originating from the abandoned gravel/sand pit that was used to seal the waste deposit.

It is unclear whether the conductive feature (iv) below the gravel lense is a true geological feature supported by the measurement data, or whether it is an anomaly generated during the inversion process. Considering the low resolution at this depth range (compare to Figure 4.11 a)) and the high resistivities above this feature, we judge that it is most likely an inversion artefact.

Though the main structures resolved are in good agreement with previous measurements, the $2.5D$ inversion employed is a rather crude approximation. Considering the highly heterogeneous material within the waste deposit body and the $3D$ characteristics of the gravel lense, it is obvious that the implied assumption of homogeneous conductivities perpendicular to the electrode deployment is not justified. Results for the $3D$ field survey, described in the next section, will give further insight into the reliability of the results just described.

Three-dimensional investigation
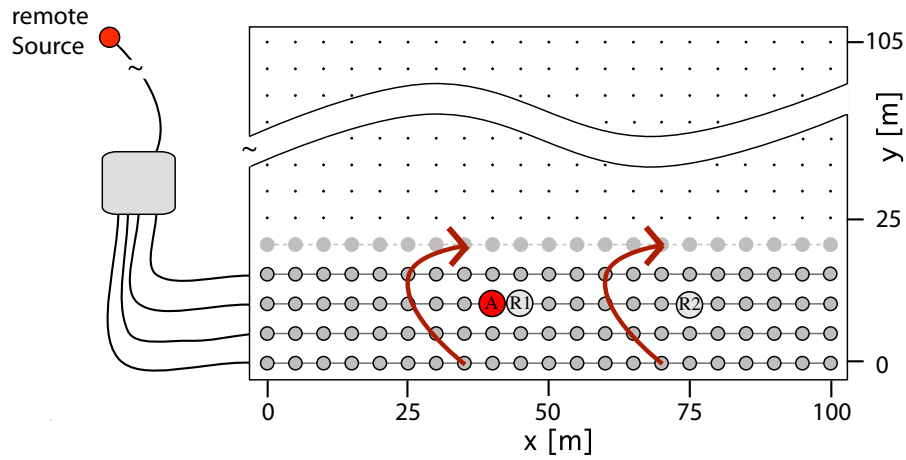
Figure 4.12 – Roll-along scheme employed during the $3D$ field campaign. Within each step of the roll-along procedure one electrode line is moved after a complete set of pole-bipole parallel measurements have been performed. Each sub-deployment includes 4×21 electrodes. The whole survey included 19 roll-along steps with a total of 462 electrode locations spanning a survey area of $100m \times 105m$.

To obtain a $3D$ image of the waste-deposit body, a $3D$ field survey involving 462 equidistantly spaced electrode locations (at $5m$ intervals) covering a survey area of $100 \times 105m$ has been carried out roughly at the same location where the $2D$ data was recorded.

As there is only a limited number of data acquisition units available with the employed *ETH-DCMES-II*, we applied $3D$ roll-along techniques for constructing a series of

20 individual electrode deployments (Figure 4.12). The roll-along strategy is designed such that the effort for moving the electrodes is minimized and sufficient $3D$ coverage is obtained. The employed procedure starts with a $3D$ electrode grid of 21×4 electrodes. After a pre-defined set of pole-bipole parallel measurements are recorded on this deployment, the first electrode line is moved beyond the last electrode line, i.e. electrode line one is moved onto the next free electrode locations (see Figure 4.12). Alternatively, several (e.g. two or three) electrode lines could be moved at once to speed up the data acquisition. However, in moving one line at a time, we could ensure a dense subsurface coverage and a sufficient amount of redundant information in the recordings.

On each of the individual electrode deployments, complete pole-bipole data sets were recorded. These data sets consist of two parallel scans per source electrode A, one with a reference close to A (R_1) and one with a reference at a certain distance away from A (R_2) (see Figure 4.12). The source electrode is successively placed at all N electrode locations. The resulting data sets (see Chapter 5 for further information)

(i) are complete according to the definition of Xu and Noel (1993), and therefore potentially contain the full information offered by all pole-bipole configurations

(ii) are noise-robust due to the combination of two reference electrodes per source A

(iii) can be acquired swiftly with $2N$ parallel scans, thereby fully utilizing the parallel recording capabilities of the *ETH-DCMES-II*

Due to the fast parallel scans offered by the *ETH-DCMES-II*, recording of the individual data sets only took ≈ 22 minutes resulting in a total recording time for the whole $3D$ survey of only ≈ 7.5 hours. Several filtering steps were applied to the recorded data set prior to the data inversion:

(1) In an initial step, the data sets recorded on the individual electrode deployments were merged to form one data set. A few data acquisition units were producing unreasonable results (assessed by visual data inspection); the corresponding measurements were removed from the data set.

(2) For each combination of a source (A) and a measuring electrode (N), there are two measurements contained in the data set – the ones acquired with voltage reference electrode R_1 and R_2, respectively. In each of these cases, the measurement that provided the larger signal-to-noise ratio was retained while the other was rejected from the data set. Roughly 120 000 measurements were removed during this process.

(3) Roughly 4,000 of the measurements having a geometrical factor larger than 10 000 m were filtered out.

(4) All measurements, for which the data acquisition units returned a normalized
misfit parameter $\xi > 1$ were removed from the data set (2,000 data points in total).
The misfit parameter characterizes the quality of the fitting on the individual
voltage waveforms (see Chapter 2 for details).

(5) Due to the employed roll-along procedure, there were $\approx 170{,}000$ recordings in the
data set that were repeated once, and $\approx 12{,}500$ recordings that were repeated
twice. The corresponding measurements were either filtered out, in case their
potential values differed too largely in amplitude, or averaged for increased data
reliability.
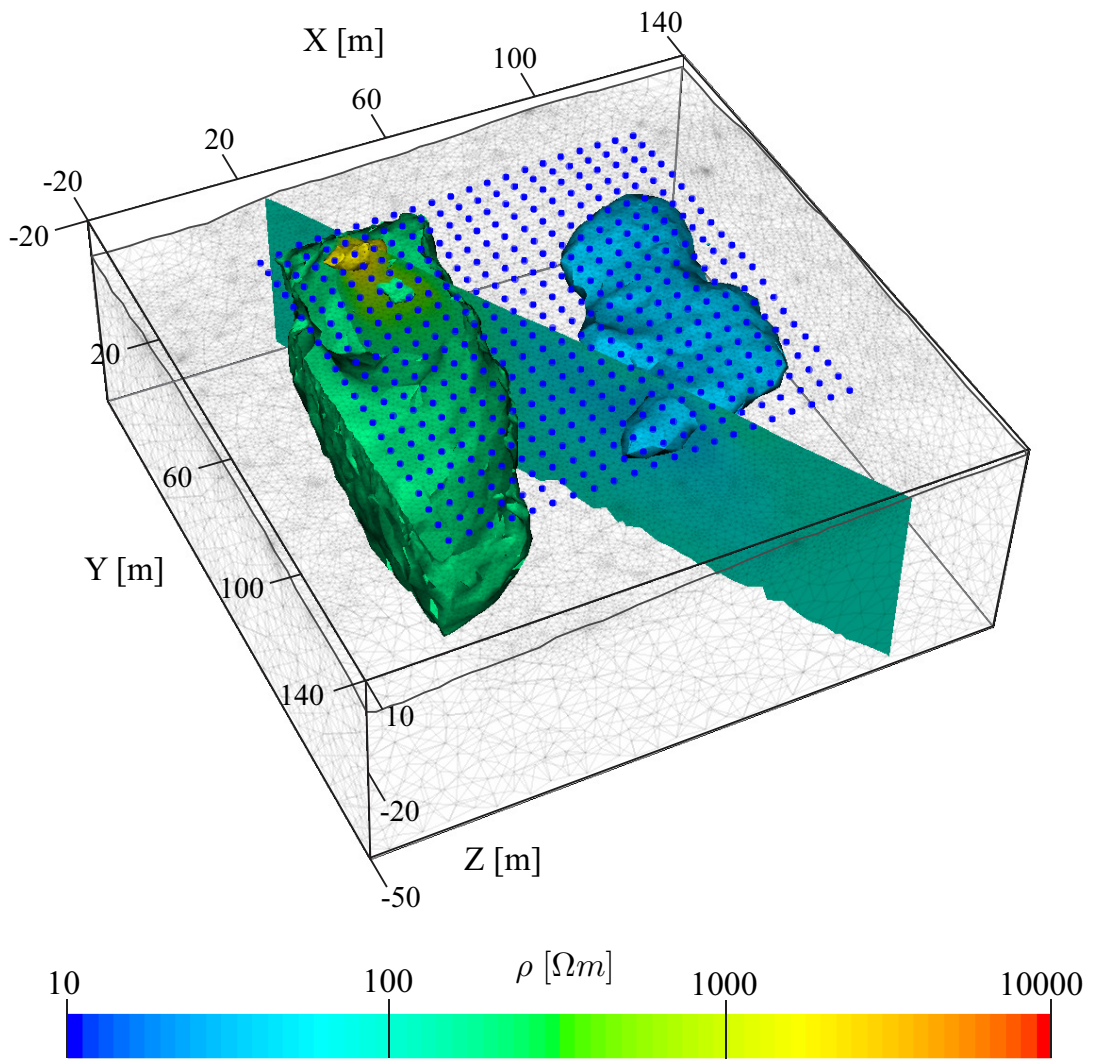
Figure 4.13 – Visualization of the $3D$ inversion result obtained from the data recorded at
the Stetten field site. Isosurfaces of 200 Ωm and 30 Ωm are used to delineate the gravel
lense and the highly conducting features in the western waste deposit body, respectively.
The highly resistive feature outlined by a $2\,000$ Ωm isosurface most likely is caused by an
erratic block. Electrode locations (462 in total) are indicated by blue points and the vertical
cut plane denotes the location, where the comprehensive $2D$ data set has been recorded
(compare to Figure 4.11). The topography slightly dips towards the south-west direction.

The resulting filtered data set contains roughly 76,000 data points. The data inversion was performed on a parameter mesh equiped with $\approx$ 10,000 parameter cells. Appropriate smoothness and damping constraints have been applied with a regularization parameter of $\alpha = \beta = \nu = 1.2$. As for the 2D Stetten data set, the regularization has been reduced down to a fifth of its original values during the first few iterations. Forward calculations were performed by a first order finite element approximation ($\approx$ 350,000 cells) in combination with a mixed boundary condition. The slightly south-west dipping surface topography, as measured by differential GPS during the field campaign, has been included in the modeling process.

The main resitivity features of the inversion result are illustrated in Figure 4.13 by three distinct isosurfaces with resistivities selected based on the 2D tomogram results in Figure 4.11. A 200 Ωm isosurface outlines the boundary of a resistive feature that corresponds to fluvial gravels and coarse sands inside the gravel lense (region G1 in Figure 4.10). Highly conductive features within the waste deposit body (region W1 in Figure 4.10) are clearly resolved by the data inversion as delineated by a 30 Ωm isosurface.

The origin of the very high resistive feature that appears inside the gravel lense (as outlined by a 2 000 Ωm isosurface) is unclear. Most likely, it is caused by an erratic block. Several anomalies interpreted as erratic blocks have been detected at the Stetten field site by seismic reflection measurements (Lanz *et al.*, 1996). It is interesting to note that resistivities as large as 2 000 Ωm are also visible in the 2D inversion result shown in Figure 4.11. The electrode profile on which the 2D data set has been acquired exactly crosses through the high resistive feature as indicated by the vertical slice in Figure 4.13. Clearly, the 2.5D approximation employed for the 2D data set fails to reconstruct this feature – it is strongly smeared out in the horizontal direction – and thereby hinders a correct interpretation.

Figure 4.14 shows further details of the 3D inversion result in the form of horizontal slices at five different depths: 0, 3, 10, 20 and 30 m. For ease of comparison the employed colorbar and the range of resistivities are the same as for the 2D inversion result in Figure 4.11. The lateral boundaries of the gravel lense and the waste deposit body as revealed by previous electrodmagnetic measurements (Lanz *et al.*, 1999) are overprinted on top of the first depth slice. The resolved resistivity features as displayed for $Z = 0$ m are in good agreement on the lateral boundaries.

The limited extent of the highly resistive feature with resistivities of $> 2\,000 \Omega m$ is clearly visible with a maximum elongation at $Z = -3$ m. Some smaller resistive features ($\approx 200 \ \Omega m$) appear within the lateral bounds of the waste deposit for $Z = 0$ m. They probably originate from left-over material taken from the abandoned gravel/sand pit in order to seal the waste deposit. Corresponding resistive features are also visible in the 2D inversion result (zones (i) in Figure 4.11). The highly conducting body with
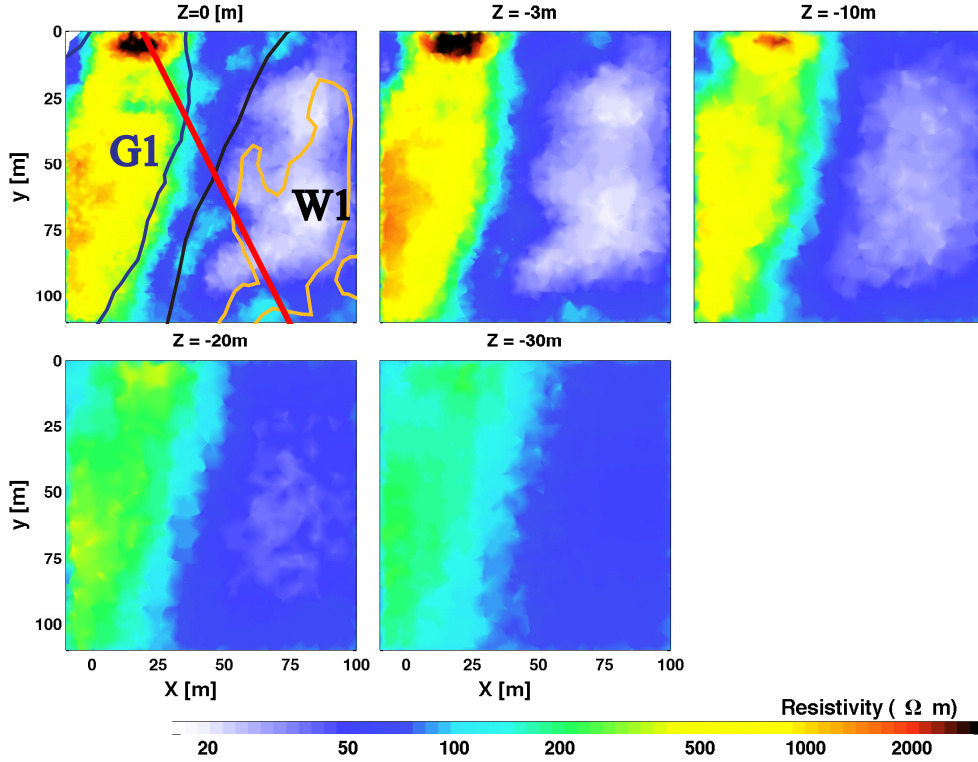
Figure 4.14 – Horizontal slices through the Stetten data inversion result showing the resolved gravel lense and the imaged highly conducting feature within the waste deposit body at different depths. The lateral boundaries of the gravel lense and the waste deposit body as revealed by previous electromagnetic measurements (Lanz *et al.*, 1999) are overprinted on top of the first depth slice for comparison. The red solid line indicates the location of the 2D profile on which the comprehensive data set was acquired.

resistivities in the range of $5 - 30\ \Omega m$, which is most likely caused by industrial waste, is clearly visible down to a depth of $Z = 10$ m. Its lateral extent slightly deviates from the zone where high conductivities ($< 10\ \Omega m$) have been acquired by previous *EM-31* measurements (zone outlined in light red in Figure 4.14, (Lanz *et al.*, 1999)). Considering the 10 years difference between the electromagnetic and the geoelectric measurements, and taking into account the different seasons over which the data were recorded (summer versus winter), these deviations are not surprising. Temporal changes in the conductivity structure of the waste deposit are to be expeted due to the influence of fluids.

Finally, Figure 4.15 provides a direct comparison between the inversion results obtained from the 2D and the 3D data, respectively, by slicing the 3D inversion result exactly along the plane where the 2D data set was recorded. This facilitates further inspection of the validity of the 2.5D approximation employed during inversion of the 2D data set and allows for a rough comparison of the depth resolution of the individual data sets.

In light of the 3D inversion results shown in Figure 4.13 and Figure 4.14, it is clear
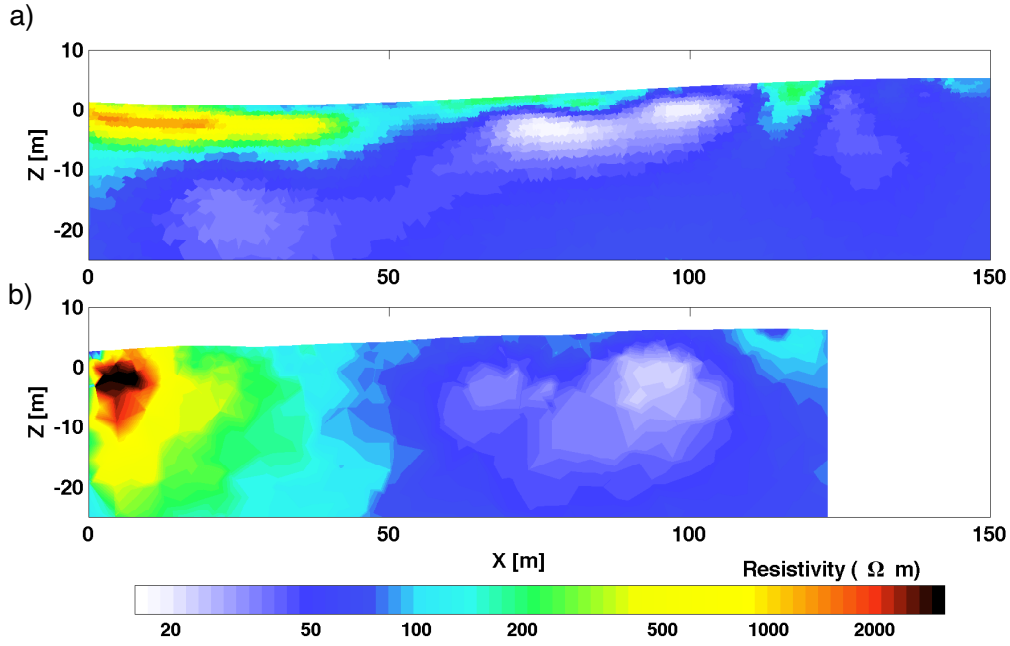
Figure 4.15 – Comparison of the inversion results of (a) the $2D$ comprehensive pole-bipole data set with (b) the $3D$ data set. (b) was generated by slicing the $3D$ inversion result exactly along the plane where the data set in (a) was recorded (see Figure 4.13). The comparison clearly shows the limitations of the $2.5D$ approximation employed in (a).

that the implied assumption of homogeneous conductivities perpendicular to the $2D$ electrode profile is not justified. Though the lateral extent and the resolved resistivities of the $2D$ and $3D$ inversion results are in fair agreement, the limitation of the $2D$ inversion becomes obvious when comparing the features that resemble the gravel lense and the waste deposit body. The highly resistive structure in Figure 4.15(a) that resembles the gravel lense is largely smeared out in the horizontal direction and resistvity values are under-estimated due to the $2.5D$ approximation. Presumably as a consequence, a highly conductive feature appears below it, which most likely is an inversion artefact.

Based on the location where the $2D$ electrode profile crosses the highly conductive features in the waste deposit (Figure 4.13), we judge the $3D$ inversion result to be more reliable and believable. The resolved shape and conductivities in the $3D$ inversion result in 4.15(b) are clearly more trustworthy. The depth of the corresponding feature in Figure 4.15(a) seems to be under-estimated whereas conductivity values seem to be slightly over-estimated.

Chapter 5

Geoelectric experimental design - efficient acquisition and exploitation of complete data sets

Mark Blome, Hansruedi Maurer, Steward Greenhalgh

to be submitted to **Geophysics**

5.1 Abstract

Exploiting the information content offered by geoelectric data in an efficient manner requires careful selection of the electrode configurations to be used. This can be achieved using sequential experimental design techniques proposed over the past few years. However, these techniques become impractical when large-scale 2D or 3D experiments have to be designed. Even if sequential experimental design would be applicable, acquisition of the resulting data sets would require an unreasonably large effort using traditional multi-electrode arrays. We present a new, fully parallelized measuring strategy by which large amounts of data can be acquired swiftly. Furthermore, we introduce a new experimental design concept that is based on complete data sets in terms of linear independence. Complete data sets include a relatively small number of basis electrode configurations, from which any other configuration can be reconstructed by superposition. The totality of possible configurations is referred to as the comprehensive data set. We demonstrate the benefits of such reconstructions using eigenvalue analyses for the

case of noise-free data. In the presence of realistic noise, such reconstructions lead to unstable results when only four-point (bipole-bipole) configurations are considered. In contrast, complete three-point (pole-bipole) data sets allow more stable reconstructions. Moreover, complete pole-bipole data sets can be acquired very efficiently with a fully parallelized system. Resolution properties of complete pole-bipole data sets are illustrated using both noise-free and noisy synthetic data sets. We also show results from a field survey performed over a buried waste disposal site, which further demonstrates the usefulness of our approach. Although this paper is restricted to 2D examples, it is trivial to extend the concept to 3D surveys, where the advantages of parallelized pole-bipole data acquisition become very significant.

5.2   Introduction

Geoelectric tomography is a powerful technique for imaging the shallow subsurface. Its usefulness has been proven in a plethora of applications (e.g. Rubin and Hubbard, 2005; Knödel *et al.*, 1997; Butler, 2005). The success of the method is primarily based on the availability of multi-electrode systems, with which large amounts of data can be collected in an efficient manner (e.g. Griffiths and Turnbull, 1985; Griffiths *et al.*, 1990; Stummer *et al.*, 2002; Zhe *et al.*, 2007). Compared with the competing electromagnetic methods (e.g. Nabighian, 1987), direct current geoelectric measurements are less susceptible to ambient noise, they are less affected by the presence of metallic objects and power lines, and they are superior for resolving resistive targets.

Although electrical resistivity data can be recorded with arbitrary two-point (pole-pole), three-point (pole-bipole or bipole-pole), and four-point (bipole-bipole) electrode configurations, the vast majority of recent model-based studies have been concerned with determining the efficacy of the five standard electrode arrays for use with multi-electrode systems and 2D and 3D inversion schemes, namely Wenner, Schlumberger, Dipole-Dipole, Pole-Pole and Pole-Dipole arrays (e.g. Friedel, 1997; Spitzer, 1998; Dahlin and Loke, 1998; Oldenburg and Li, 1999; Olayinka and Yaramanci, 2000; Dahlin and Zhou, 2001; Zhou and Greenhalgh, 2002). Consequently, most reported field applications of 2D imaging have been based on either one or a combination of these traditional arrays. Note that the term dipole is soemetimes used interchangeably in the literature with the term "bipole", but the strict definition of "dipole" requires that the separation between the electrode pair be small, which is often not the case. So for purposes of generality and to avoid any confusion we prefer to use the term bipole throughout this paper.

During the past decade or so, several techniques have been proposed for better exploiting the information content offered by geoelectrical data. Cherkaeva and Tripp (1996) proposed electrode configurations with which optimized current density patterns can be achieved. They based their approach on earlier developments in biomedical

impedance imaging (Isaacson, 1986). Other scientists have made attempts to find optimized survey layouts by simply considering the sensitivities of individual configurations with respect to small perturbations of the subsurface resistivities (e.g. Furman *et al.*, 2004).

Following earlier ideas introduced by Barth and Wunsch (1990); Maurer and Boerner (1998) and Curtis (1999) Maurer *et al.* (2000) proposed statistical experimental design, which provided a more general framework for identifying optimized survey layouts. The early implementations of statistical experimental design were based on global optimization schemes, such as genetic algorithms, but it was realized that this would be computationally prohibitive for realistic geoelectric applications involving several tens of electrodes and several hundreds of model parameters. Therefore, Stummer *et al.* (2004) proposed a sequential design strategy, in which suitable electrode configurations were successively added to an initial data set until the desired model resolution was achieved. Wilkinson *et al.* (2006) extended and improved the method of (Stummer *et al.*, 2004), whereas Coscia *et al.* (2008) adapted the technology for optimizing electrode placement in crosshole investigations. Although the performance of sequential experimental design as proposed by Stummer *et al.* (2004) and Wilkinson *et al.* (2006) is impressive, there are several significant limitations that remain to be overcome. The first problem concerns the number of electrodes available and the resulting large number of possible electrode configurations. As discussed by Xu and Noel (1993), an n electrode deployment allows implementing

$$n_{\text{compr}}^{4p} = n \cdot (n-1) \cdot (n-2) \cdot (n-3)/8 \qquad (5.1)$$

different and non-reciprocal four-point configurations (two injecting and two measuring electrodes within the array). A data set that includes all 4-point configurations was referred to by Stummer *et al.* (2004) as a comprehensive data set. Of course, many of these configurations are not independent but can be synthesized (constructed) from other basis configurations. Using 50 electrodes, a comprehensive data set would comprise more than 690'000 configurations and with 100 electrodes, there would be more than 11 million configurations. Sequential experimental design would identify a small subset (e.g. 5%) of a comprehensive data set from which most of the subsurface information could be retrieved. However, even such a "small" subset would be time-consuming to collect in the field when the number of electrodes is larger than 50. Moreover, the algorithms proposed by Stummer *et al.* (2004) and Wilkinson *et al.* (2006) would require excessive computing resources for larger electrode arrays. Considering that present and future 3D deployments may include several hundred electrodes, alternative strategies need to be considered.

A second problem that was not fully considered by Stummer *et al.* (2004) and Wilkinson *et al.* (2006) concerns the influence of data noise. In their experimental algorithms

they pre-selected those configurations from the comprehensive data sets whose geometrical factors were below a given threshold. This ensured that only measurable configurations (i.e. those configurations for which the signal levels are sufficiently strong) were considered during the design stage, but no individual weighting factors to reflect the data reliability were associated with the different configurations.

Finally, sequential experimental design requires an à priori subsurface resistivity model for which the model parameter sensitivities are computed. If the true subsurface structures deviate significantly from the à priori model, non-linear effects may degrade the quality of experimental design. Stummer *et al.* (2004) demonstrated with several models that these non-linear effects are surprisingly small, but it would be nevertheless advantageous to have a design strategy that is independent of any prior subsurface knowledge.

In this paper, we describe an approach that addresses the problems mentioned above. Our concept is based on the idea of complete (or basis) data sets as described by Xu and Noel (1993) and Lehmann (1995). A complete data set is defined as a set of electrode configurations from which any other configuration can be reconstructed by superposition. After a brief introduction to the theoretical background, we discuss the resolution properties of complete and comprehensive data sets. Next, we investigate the influence of noise on the reconstruction of comprehensive data sets out of the complete data sets and demonstrate that such an endeavor is generally not practical when the underlying complete data set comprises only four-point configurations. In contrast, we show that complete data sets involving three-point configurations (e.g. pole-bipole) are theoretically more amenable for reconstructing comprehensive data sets; such configurations can be measured very efficiently with state-of-the-art parallel data acquisition systems. We demonstrate that complete pole-bipole data sets can be suitably combined such that, even in the presence of realistic noise, excellent tomographic inversion results can be achieved, which are comparable to those of measured comprehensive data sets. In the final part of the paper, we present a field example acquired across a buried landfill site in Switzerland, which confirms the theoretical results.

5.3   Theory

Forward modeling and inversion

Geoelectric data are typically analyzed using tomographic inversion algorithms. They include a forward solver $\mathcal{F}$ that predicts (computes) the electric potential differences $\vec{d}^{\,\mathrm{pred}}$ for a particular resistivity model $\vec{m}$

$$\vec{d}^{\,\mathrm{pred}} = \mathcal{F}(\vec{m}), \tag{5.2}$$

and a corresponding inverse operator

$$\vec{m}^{\,\mathrm{est}} = \mathcal{F}^{-1}(\vec{d}^{\,\mathrm{obs}} - \vec{d}^{\,\mathrm{pred}}), \tag{5.3}$$

which estimates the subsurface resistivities $\vec{m}^{\,\mathrm{est}}$ from the observed data $\vec{d}^{\,\mathrm{obs}}$. We adopt the common practice in geoelectric tomography of using logarithms of both the data and the model parameters (e.g. Tarantola, 1987) to ensure positivity and allow for a wide range of parameter variations.

Our forward operator $\mathcal{F}$ solves the 3D or 2.5D problem using a finite element algorithm as described in (Blome *et al.*, 2009). The subsurface is discretized with an unstructured mesh of tetrahedrons (3D) or triangles (2.5D). This allows easy incorporation of surface topography and higher density of (smaller) elements close to the source. Our Gauss-Newton type inverse operator $\mathcal{F}^{-1}$ can be written as

$$\vec{m}_{i+1}^{\,\mathrm{est}} = \left(\mathbf{J}^T \mathbf{C}_D^{-1} \mathbf{J} + \mathbf{C}_M^{-1}\right)^{-1} \mathbf{J}^T \mathbf{C}_D^{-1} \left[\left(\vec{d}^{\,\mathrm{obs}} - \vec{d}^{\,\mathrm{pred}}\right) + \mathbf{J}\vec{m}_i^{\,\mathrm{est}}\right], \tag{5.4}$$

where $\mathbf{J}$ is the Jacobian matrix, the elements of which are the sensitivities or Fréchet derivatives, i is the iteration number ($\vec{m}_0^{\,\mathrm{est}}$ is the initial model) and $\mathbf{C}_M^{-1}$ is the à priori model covariance matrix. The latter allows regularization constraints, such as damping and smoothing, to be applied (Maurer *et al.*, 1998). This has the effect of stabilizing the inversion in that it allows the pseudo inverse matrix to be calculated. The quantity $\mathbf{C}_D^{-1}$ is the à priori data covariance matrix. This is usually a diagonal matrix whose entries are the inverses of the squared data error estimates. As such, $\mathbf{C}_D^{-1}$ acts as a data weighting matrix.

An L_2 norm misfit objective function is implicit in equation 5.4. The sensitivities in the Jacobian matrix can be computed rapidly using the explicit expressions published by Zhou and Greenhalgh (1999) and Greenhalgh *et al.* (2009). Furthermore, the matrix $\mathbf{J}^T \mathbf{C}_D^{-1} \mathbf{J}$ and the vector $\mathbf{J}^T \mathbf{C}_D^{-1} \left[\left(\vec{d}^{\,\mathrm{obs}} - \vec{d}^{\,\mathrm{pred}}\right) + \mathbf{J}\vec{m}_i^{\,\mathrm{est}}\right]$ in equation 5.4 can be accumulated sequentially (e.g. Sheen et al., 2006), such that the only limiting factor in terms of computer memory is the number of model parameters in $\vec{m}$, which determines the dimension of $\mathbf{J}^T \mathbf{C}_D^{-1} \mathbf{J}$. This is critical when considering measured or reconstructed comprehensive data sets, which may include a much larger number of data points than the number of model parameters.

Measures of data information

Since our geoelectrical tomography algorithm is based on linearized inverse theory (equations 5.2 to 5.4), we consider corresponding measures for quantifying the benefits (imaging capability) of a particular survey (e.g. Menke, 1984). The choice of a survey layout governs the structure of the Jacobian matrix $\mathbf{J}$, and close inspection of equation 5.4

indicates that the reliability of the parameter estimates $\vec{m}^{\text{est}}$ depends primarily on our ability to invert the matrix $\mathbf{J}^T\mathbf{C}_D^{-1}\mathbf{J} + \mathbf{C}_M^{-1}$. Without the regularization constraints in $\mathbf{C}_M^{-1}$, this matrix would likely be singular, such that its determinant would be zero and its condition number (i.e., ratio of the largest to the smallest eigenvalues) would be infinite. Since the sensitivities in $\mathbf{J}$ represent the information content offered by a particular survey design, and $\mathbf{C}_M^{-1}$ indicates our preconceived ideas on the subsurface structure (e.g., closeness to initial model or smooth variation of the model resistivities), it is certainly advisable to maximize the contribution of $\mathbf{J}^T\mathbf{C}_D^{-1}\mathbf{J}$ and to minimize the influence of $\mathbf{C}_M^{-1}$. This can be achieved by choosing electrode configurations such that the resulting Hessian matrix $\mathbf{H} = \mathbf{J}^T\mathbf{C}_D^{-1}\mathbf{J}$ has as many non-zero eigenvalues as possible.

Besides the eigenvalues of the Hessian matrix $\mathbf{H}$ we also consider the model resolution matrix $\mathbf{R}$ defined as (e.g. Menke, 1984):

$$\mathbf{R} = \left(\mathbf{J}^T\mathbf{C}_D^{-1}\mathbf{J} + \mathbf{C}_M^{-1}\right)^{-1}\mathbf{J}^T\mathbf{C}_D^{-1}\mathbf{J}. \tag{5.5}$$

It relates the estimated model parameters $\vec{m}^{\text{est}}$ to the true model parameters $\vec{m}^{\text{true}}$ ($\vec{m}^{\text{est}} \approx \mathbf{R}\,\vec{m}^{\text{true}}$). Of particular interest are the diagonal elements of $\mathbf{R}$. Values close to zero indicate poorly resolved model parameters, whereas values close to one indicate well resolved model parameters.

5.4 Experimental setup

Our approach will be most beneficial for large-scale 3D surveys, but for the sake of simplicity we demonstrate its performance using a simple 2D setup as shown in Figure 5.1. The true resistivity structure includes two conductive and two resistive blocks. The acquisition geometry comprises 25 electrodes at 2 m spacing along the ground surface. For the solution of the forward problem, the subsurface was parameterized with a fine unstructured triangular mesh. Since our geoelectric data will be unable to resolve such a large number of resistivity parameters, the forward cells were merged to 1450 larger inversion cells displayed in Figure 5.1(b). More details on the construction of the inversion cells can be found in Chapter 4.

5.5 Tomographic inversion of complete and comprehensive four-point (bipole-bipole) data sets

Following Xu and Noel (1993), an $n = 25$ electrode array (Figure 5.1) has at most

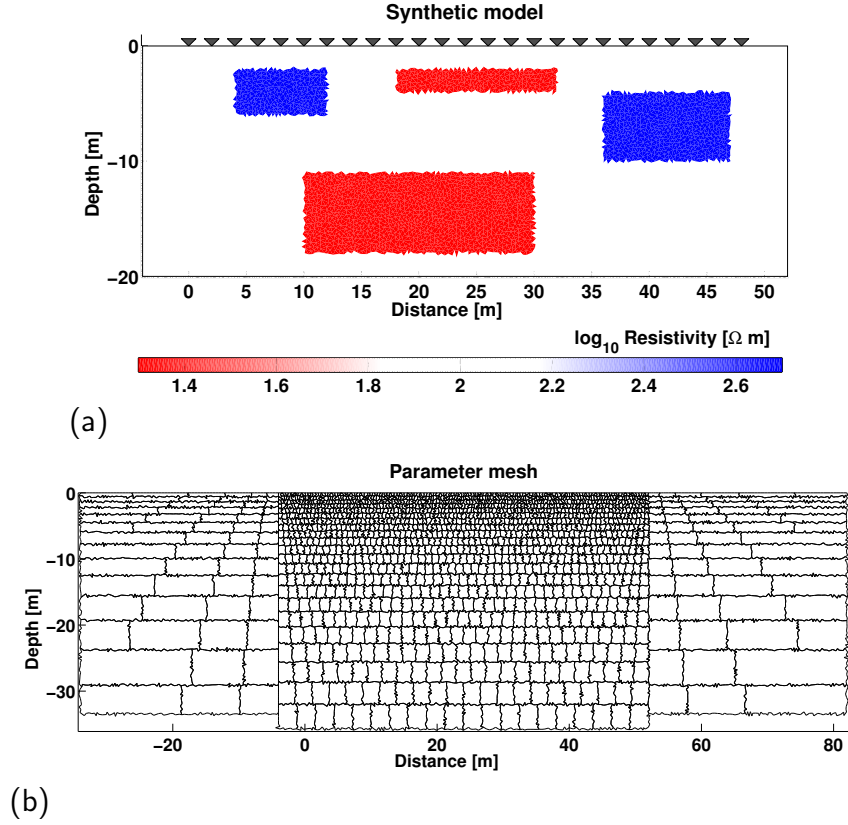$$n_{\text{complete}}^{4p} = n \cdot (n-3)/2 = 275$$

Figure 5.1 – The true synthetic model (a) and model parametrization (b) used to estimate the eigenvalue spectra of the Hessian matrix shown in Figures 5.2 and 5.6, and the tomogram results shown in Figures 5.3 and 5.7.

linearly independent four point configurations, whereas a comprehensive data set (all possibilities) would involve

$$n^{4p}_{\text{compr}} = n \cdot (n-1) \cdot (n-2) \cdot (n-3)/8 = 37\,950$$

four-point configurations. For comparison, a two-point pole-pole data set would comprise

$$n^{pp} = n \cdot (n-1)/2 = 300$$

configurations. Initially, we consider noise-free data sets, such that $\mathbf{C}_D^{-1}$ is the unit matrix. To understand the different characteristics of these data sets, we compute the eigenvalues of the Hessian matrix $\mathbf{J}^T \mathbf{C}_D^{-1} \mathbf{J}$ for the complete and comprehensive data sets. As references, we additionally compute the eigenvalues for the pole-pole and Wenner data sets, which are popular choices in many investigations. The results are displayed in Figure 5.2. The normalized eigenvalue spectra reveal that indeed only 275 eigenvalues are non-zero for both the complete and comprehensive data sets and 300 eigenvalues are non-zero for the pole-pole data set. The rank of the matrix $\mathbf{H}$ (or $\mathbf{J}$) is given by the number of non-zero eigenvalues and can be related to the number of independent
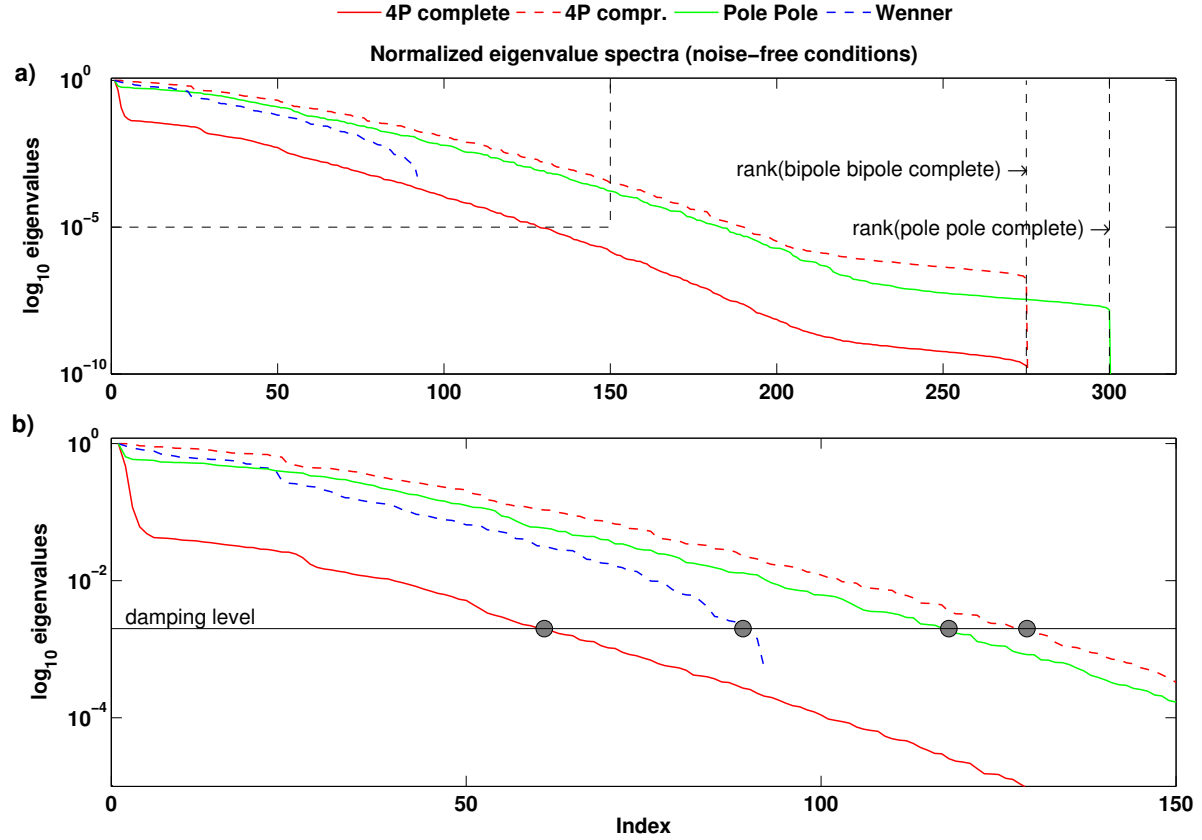
Figure 5.2 – Eigenvalue spectra of the Hessian matrix for four-point (bipole-bipole) configurations, normalized with respect to the dominant eigenvalue. Diagram (a) shows eigenvalues versus eigenvalue number (index) computed for complete and comprehensive data sets. Diagram (b) is an enlargement of the initial portion within the boxed region in diagram (a). Corresponding eigenvalues for the pole-pole and Wenner data sets are shown for comparison.

measurement configurations. This is why both the complete and comprehensive data sets have the same number of non-zero eigenvalues. It is interesting to note that the shapes of the spectra of the complete and comprehensive data sets are quite different.

The implications of the different shapes are best understood, when the regularization effects are also considered. Regularization essentially flattens the eigenvalue spectra beyond a certain threshold level. Depending on the level of data noise, we can set a realistic threshold, below which no significance would be attached to the eigenvalues. This is indicated schematically by the horizontal solid line in Figure 5.2. The intersections of the eigenvalue spectra and this horizontal line separate the portions of the resolved model space (to the left of the intersection) and the unresolved null space (to the right of the intersection) (Maurer *et al.*, 2009). For geoelectric problems, the horizontal threshold line is usually well above the smallest non-zero eigenvalue. Since the null space of the comprehensive data set is significantly smaller than that of the complete (basis) data set, it is expected that inversion results based on a comprehensive data set are superior. Figure 5.2 also indicates that a Wenner data set is expected to provide superior imaging properties than a complete data set, but inferior properties than a comprehensive and

a pole-pole data set.

Figures 5.3a and 5.3c show the tomographic inversion results for the comprehensive and complete data sets, respectively. Clearly, the comprehensive data set provides a superior tomogram. In particular, the deeper resistive block is much better resolved. Figure 5.3b shows the diagonal elements of the model resolution matrix (equation 5.5). For better comparison, we have plotted in Figure 5.3d the relative resolution which is the ratio of the model resolution of the complete noise-free data set to that of the comprehensive noise-free data set. The relative resolution of the complete data set degrades with increasing depth, as expected for a surface array resistivity experiment.

Figures 5.3a to 5.3d demonstrate that reconstructing a comprehensive data set out of a noise-free complete data set leads to a better conditioned inverse problem and thus to an improved resolution. This is interesting from a theoretical point of view, but the important question that remains to be answered concerns the applicability of such a reconstruction in the presence of realistic noise. Geoelectric data are typically contaminated with ambient noise of a particular (fixed) voltage level and some instrumental noise that is usually proportional to the voltage measured. On the basis of our experience with measured data sets, we have chosen a noise model with 70 mV ambient noise and 0.1% relative noise. Furthermore, we assumed the injected currents to be 1 A.

With such a noise model, we have contaminated the comprehensive and complete data sets. Furthermore, we have reconstructed a comprehensive data set out of the noise-contaminated complete data set. With the knowledge of the noise model we could establish appropriate data covariance matrices $\mathbf{C}_D^{-1}$ for the "measured" comprehensive and complete data sets. For the reconstructed data set, the matrix $\mathbf{C}_D^{-1}$ had to be computed using the error propagation law (i.e., in forming the linear combination from among the relevant basis configurations, the absolute errors from all relevant combinations are simply added). Since the reconstruction procedure for bipole-bipole data is a relatively complicated superposition of up to 6 different basis electrode configurations, the errors can grow quite substantially. More details on the superposition and error propagation procedures are described in Appendix 5.12.1.

Inversion results for the noise-contaminated data sets are shown in Figures 5.3e to 5.3j. Compared with the optimal reference solution in Figure 5.3a, the quality of all tomograms is decreased. The noise-contaminated "fully measured" comprehensive data set (Figure 5.3e) resolves the shallow blocks quite well, but the deep conductive block is less well resolved compared with Figure 5.3a. These observations are in accordance with the relative resolution plot shown in Figure 5.3f, which indicates a considerably decreased resolution than the noise-free comprehensive data set (Figures 5.3a and 5.3b). Results from the complete data set shown in Figures 5.3g and 5.3h, are even worse. The deep conductive block is not visible in the tomogram. Again, this is predicted by the relative resolution plot in Figure 5.3h.
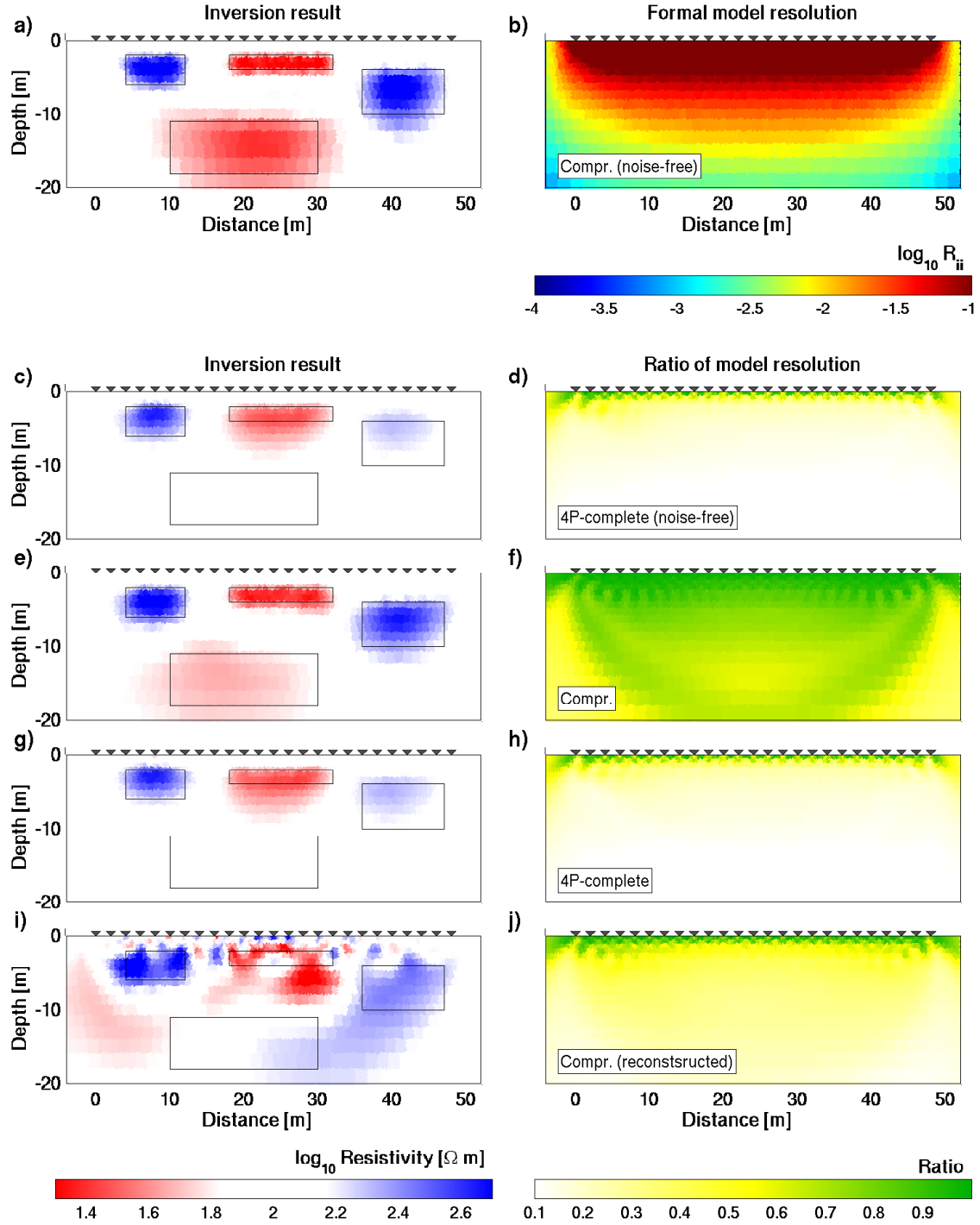
Figure 5.3 – Model resolution and inversion results for the 4- point configurations. Diagram (a) shows the true model and diagram (b) shows the model resolution for the noise-free comprehensive data sets. Diagrams (c), (e) (g) and (i) show inversion results for the noise-free complete, noisy "measured" comprehensive, noisy complete and noisy reconstructed comprehensive data sets, respectively. Diagrams (d), (f), (h) and (j) show the corresponding relative model resolution plots, where the ratio is taken with respect to the noise-free comprehensive data set.

The tomogram computed from the reconstructed comprehensive data set is shown in Figure 5.3i. A comparison of the relative resolution plots in Figures 5.3f, 5.3h and 5.3j indicates that the quality of this tomogram should lie between those in Figures 5.3a and 5.3c. This is not the case. Accumulation of errors during the superposition did not allow reliable tomograms to be obtained. The discrepancy between the predicted quality of the tomogram in Figure 5.3j and the actual result in Figure 5.3i is most likely caused by non-linear effects that led the inversion converge in a local minimum.

Our computations have demonstrated that a noise-free comprehensive data set is more suitable for tomographic inversions than a noise-free complete data set, and that the reconstruction of a comprehensive data set using a noise-contaminated complete data set does not provide reliable results.

5.6 Parallel data acquisition of complete three-point (pole-bipole) data sets
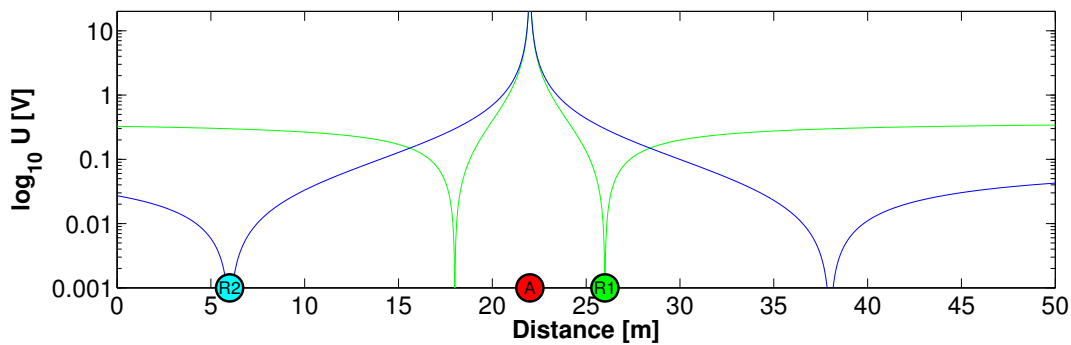
Figure 5.4 – Voltage distributions for pole-bipole configuration over a homogeneous earth with the current source at position A. The green curve is the voltage relative to a reference electrode at position R_1, whereas the blue curve is the voltage relative to a reference electrode at position R_2.

A possible option for speeding up the data acquisition would be to simultaneously record several configurations at once. On the basis of a fully distributed multi-electrode array described in Stummer *et al.* (2002), we have developed a new system that is capable of swiftly performing parallel scans, such that with a n-electrode array $n - 3$ voltage measurements (two current injecting electrodes, one reference electrode and $n-3$ measuring electrodes) can be performed simultaneously. More details of the acquisition system are provided in Appendix 5.12.2.

Parallelizing the acquisition of a complete 4-electrode data set, as proposed by Xu and Noel (1993), would be quite difficult and would result in an overly large amount of redundant measurements. In combination with the unfavorable error propagation properties, described in the previous section and Appendix 5.12.1, this makes complete

four-point data sets unsuitable for our purposes.

An obvious alternative solution would be to record pole-pole data, from which any four-point configurations could be reconstructed. Pole-pole configurations are amenable to parallel recordings. A complete pole-pole data set could be recorded with only n parallel scans. As discussed in Maurer and Friedel (2006), pole-pole data have favorable resolution properties, and reconstruction of a comprehensive four-point data set using noise-free pole-pole data would further increase the quality of the tomograms underneath the electrode array. However, it is well known that pole-pole data suffer from serious capacitive and inductive noise problems caused by the long cable that connects the remote potential electrode. Therefore, they are of limited use in urban areas where high ambient noise levels may be present.

A better alternative would be to record geoelectric data using pole-bipole configurations. Here, only one mobile current electrode (the source) is involved. The other injecting electrode (the sink) is kept fixed at some remote distance from the array, which makes the measurements less susceptible to ambient noise because electromagnetic noise pickup is not an issue on the current lines. Pole-bipole configurations can be rapidly acquired using a parallel recording system, and a complete pole-bipole data set can be recorded with only $2n$ parallel scans. The situation is illustrated in Figure 5.4. Current is injected at electrode position A, and a reference electrode R_1 is chosen. With such a setup, all the remaining electrodes can measure simultaneously the potential differences with respect to electrode R_1. The resulting voltages (assuming for illustrative purposes a homogeneous halfspace) are displayed in Figure 5.4 by the green curve. At 4 m distance from the current source A, the measured potential difference would be zero. In the case of a heterogeneous subsurface structure, zero potential differences may occur at slightly different locations. A second set of measurements using another reference electrode R_2 is required to avoid very low potential differences (see blue curve in Figure 5.4), that could be overwhelmed by noise.

The measurements described in Figure 5.4 form a complete data set, such that any other pole-bipole configurations (i.e., a comprehensive pole-bipole data set) can be reconstructed. This is illustrated in Figure 5.5. The potential difference between the electrodes labeled N_1 and N_2 can be reconstructed from the measured potential differences between R_1 and N_1 and R_1 and N_2. Alternatively, one could add the potential differences between R_2 and N_1 and R_2 and N_2. Since the reconstruction process requires only adding two measured voltages (not up to six, as in the bipole-bipole case), this is less susceptible to accumulation of measurement errors.

Practical implementation of the concept described above requires decisions concerning (i) the positioning of the reference electrodes R_1 and R_2 and (ii) the choice of R_1 or R_2 for reconstructing a comprehensive pole-bipole data set. To obtain high potential differences, for electrodes remote from the source we suggest placing electrode R_1 close
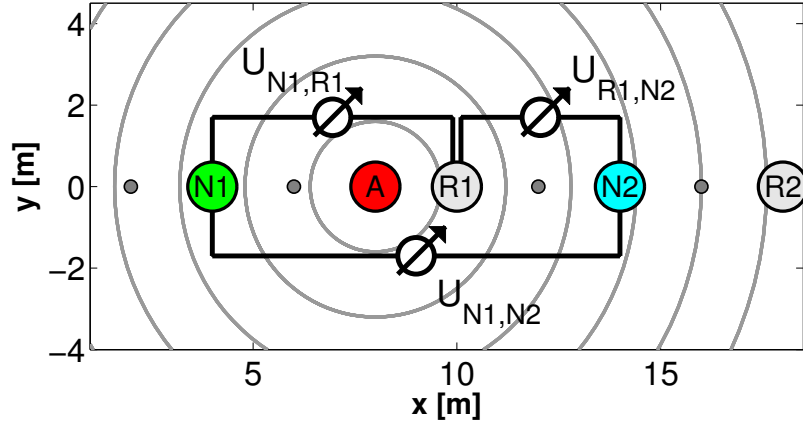
Figure 5.5 – Principle of pole-bipole data reconstruction. The electric field generated by a current source A and a current sink located at infinity is a conservative vector field, with an associated scalar potential. Measuring the potential differences U_{N_1,R_1} and U_{R_1,N_2} allows reconstructing the voltage drop U_{N_1,N_2} by algebraic addition $U_{N_1,N_2} = U_{N_1,R_1} + U_{R_1,N_2}$.

to the injecting electrode. The second reference electrode R_2 should be placed at some distance, such that it yields high potential differences at receiver electrodes close to the source. The choice of either R_1 or R_2 for reconstructing a comprehensive data set is governed by the expected reconstruction error (using a prescribed error model). Only the reconstruction with the reference electrode that leads to the smaller reconstruction error is retained.

5.7 Tomographic inversion of complete and comprehensive pole-bipole data sets

To explore the capabilities and limitations of complete and comprehensive pole-bipole data sets, similar computations to those described for the four-point configurations were performed. Figure 5.6 shows the eigenvalue spectra of the Hessian matrices (or equivalently, the squared singular values of the sensitivity matrices) computed for the complete and comprehensive pole-bipole data sets. The spectra for the comprehensive four-point and pole-bipole data sets are similar, which indicates that comparable inversion results can be achieved. The spectrum for the complete pole-bipole data is clearly superior to the corresponding four-point spectrum in Figure 5.2.

In Figures 5.7a and 5.7b, the tomogram and the corresponding resolution matrix for an error-free comprehensive pole-bipole data set are shown. As predicted by the eigenvalue spectra in Figure 5.6, the results are comparable to the error-free "measured" comprehensive four-point data set (Figures 5.3a and 5.3b). The tomogram and the relative resolution (with respect to Figure 5.7b) obtained for the noise-free complete pole-bipole data set are shown in Figures 5.7c and 5.7d. In contrast to the result for the noise-free complete data set using a four-point configuration (Figures 5.3a and 5.3c), the
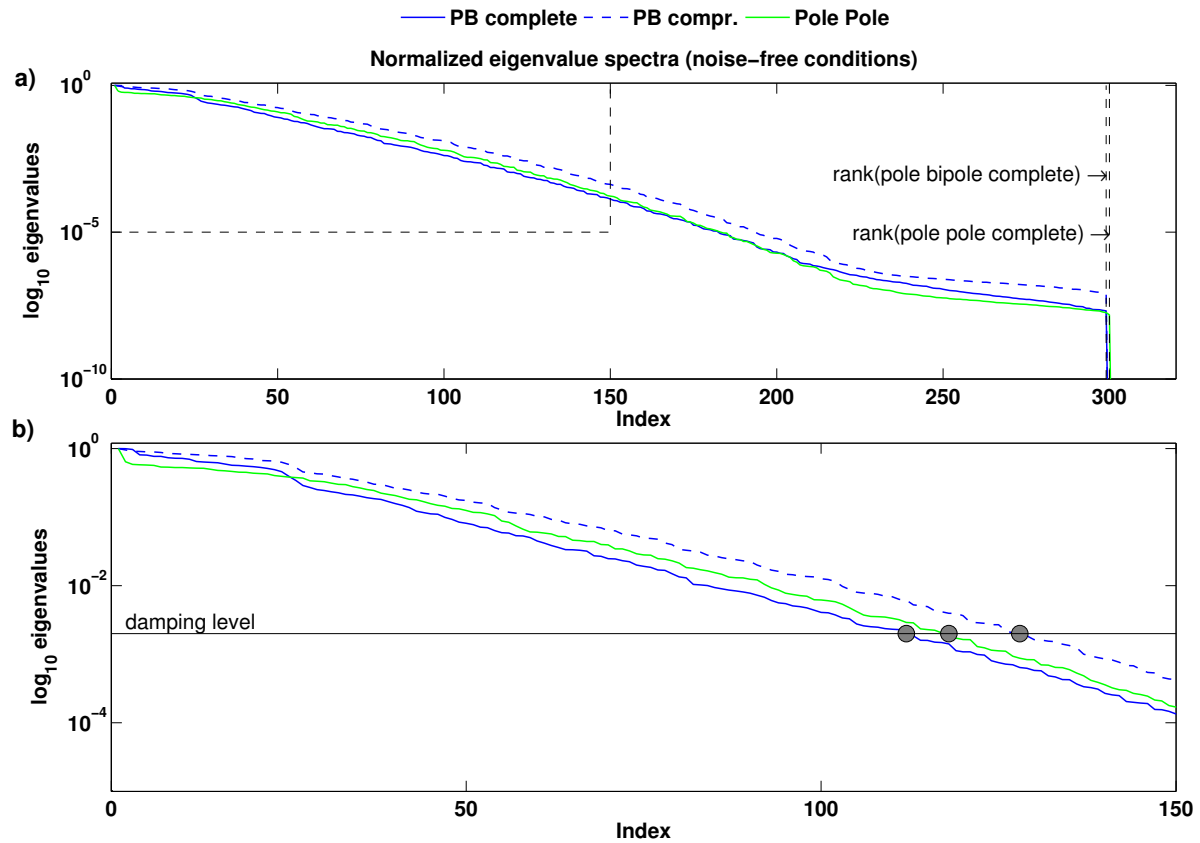
Figure 5.6 – Eigenvalue spectra of the Hessian matrix for three-point (pole-bipole) configurations, normalized with respect to the dominant eigenvalue. Diagram (a) shows eigenvalues versus eigenvalue number (index) computed for complete and comprehensive data sets. Diagram (b) is an enlargement of the initial portion within the boxed region in diagram (a). Corresponding eigenvalues for the pole-pole data set are shown for comparison.

result for the complete pole-bipole data set is very similar to that of the comprehensive data set (Figure 5.7a).

By analogy with the results shown in Figure 5.3, the comprehensive and complete pole-bipole data sets were subsequently contaminated using the same noise model. Tomograms and relative resolution plots are shown in Figures 5.7e to 5.7j. The tomogram for the measured noisy comprehensive data set (Figure 5.7e) provides a hint of the deep conductive block, but its resolution is significantly below that of the noise-free data sets (Figures 5.7a and 5.7c). The signature of the deep conductive block using the noisy complete data set is even fainter (Figure 5.7g), but it is still superior to its four-point counterpart in Figure 5.3g. The reconstructed comprehensive data set resolves the deep conductive block quite well, but there are also a few artifacts in the shallow part of the model (Figure 5.7j). They are likely the result of error accumulations during the reconstruction process.
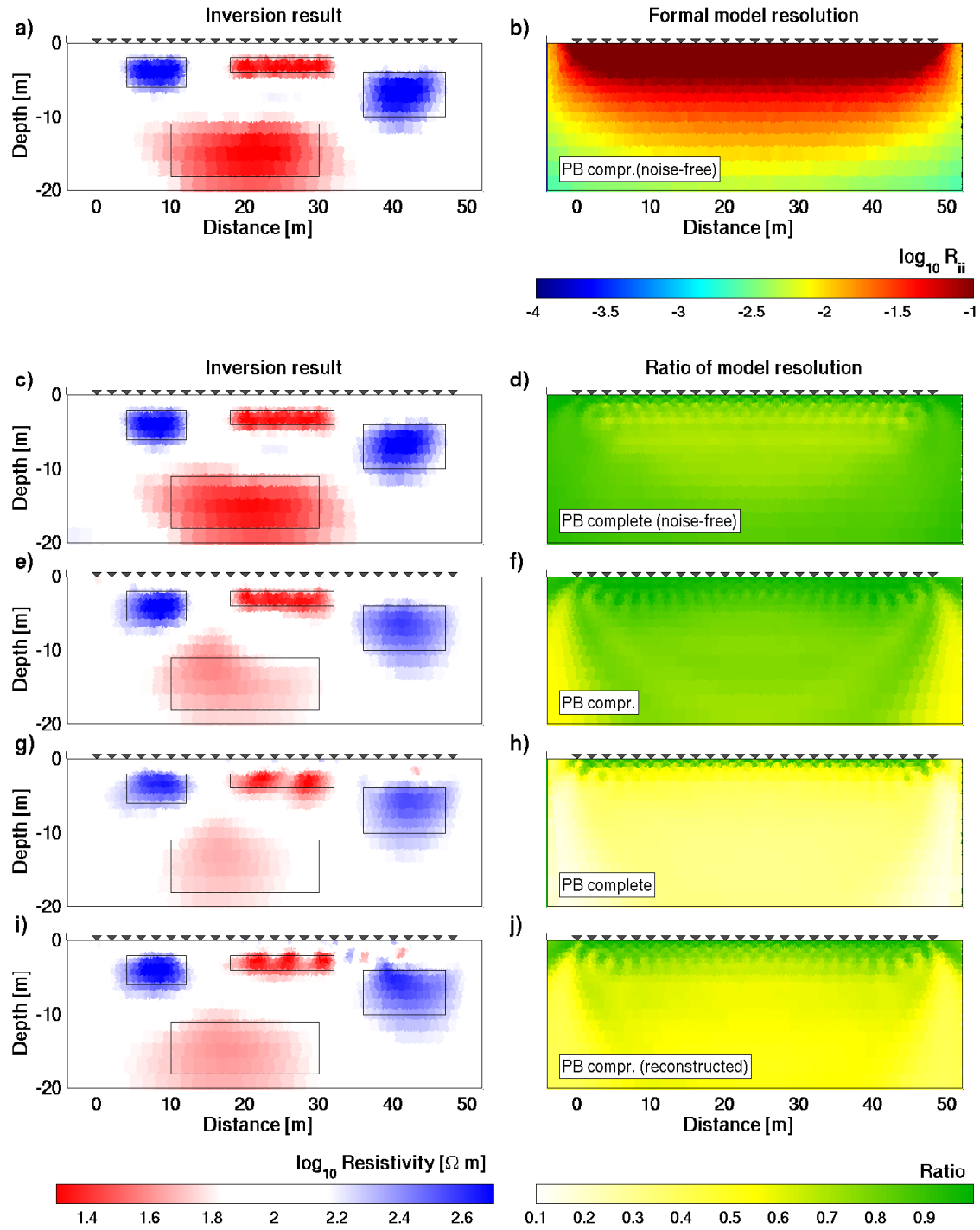
Figure 5.7 – Model resolution and inversion results for the three-point configurations. Diagram (a) shows the true model and diagram (b) shows the model resolution for the noise-free comprehensive data sets. Diagrams (c), (e), (g) and (i) show inversion results for the noise-free complete, noisy "measured" comprehensive, noisy complete and noisy reconstructed comprehensive data sets, respectively. Diagrams (d), (f), (h) and (j) show the corresponding relative model resolution plots, where the ratio is taken with respect to the noise-free comprehensive data set.

5.8 Case study – Stetten landfill
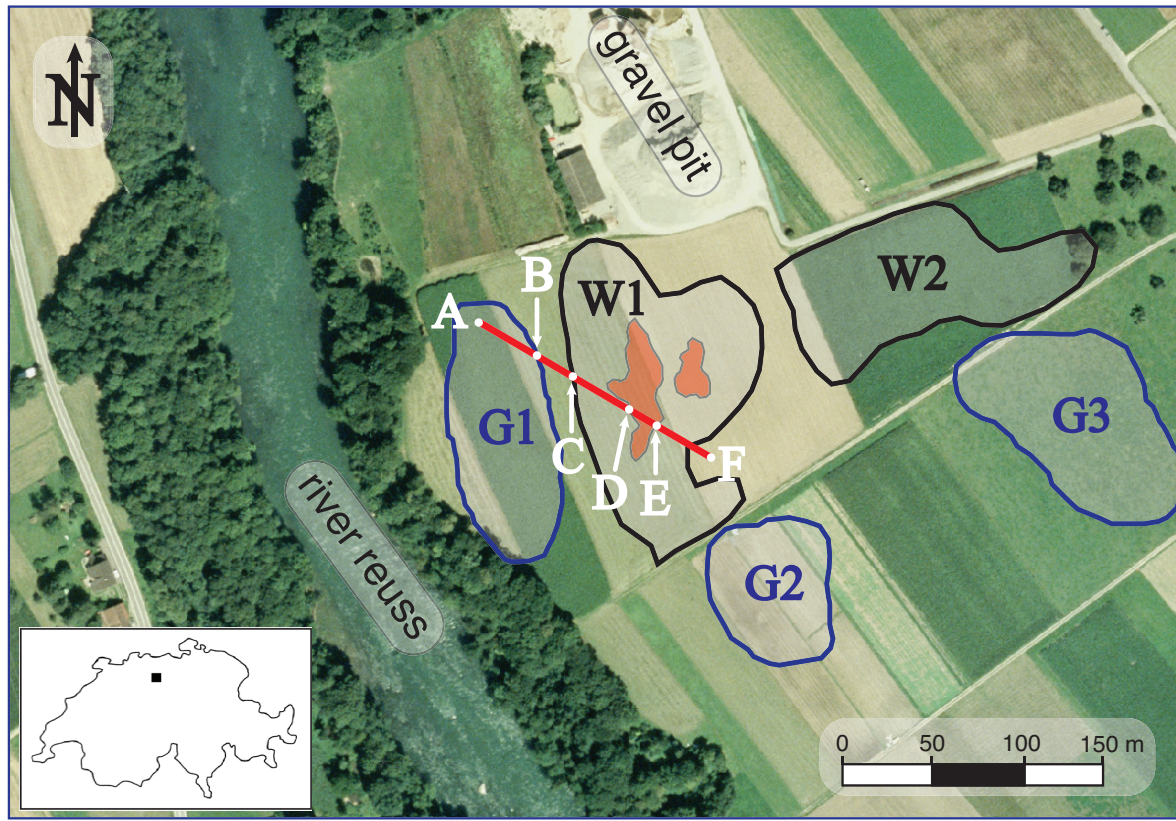
Figure 5.8 – Air photo of Stetten landfill resistivity test site. Comprehensive and complete pole-bipole data sets were recorded along the electrode profile indicated by the red line. Extensive previous geophysical measurements revealed the borders of shallow gravel lenses (marked as regions G1, G2 and G3) and two distinct waste deposit bodies (marked as regions W1 and W2). High conductivities in excess of 0.1 S/m were recorded by EM-31 measurements below the zones marked in red.

Numerical experiments have indicated that parallel recording of complete and comprehensive pole-bipole data sets could be powerful options for obtaining optimal subsurface images. This has been further investigated at a field test above a former waste disposal site near Stetten, Switzerland (Green *et al.*, 1999). The landfill contains heterogeneous industrial waste that was dumped into a disused gravel pit before being covered by a 0.8 m layer of soil. Vertical-gradient magnetic and frequency-domain electromagnetic data were used to define the lateral boundaries of the landfill and the location of buried metallic objects (Lanz *et al.*, 1999). Tomographic inversions of densely spaced seismic refraction data allowed the base of the landfill to be delineated over a wide area (Lanz *et al.*, 1998). Detailed characteristics of the shallow host sediments were provided by the results of 2D and 3D high-resolution seismic reflection and georadar surveys (Lanz *et al.*, 1996, 1994; Green *et al.*, 1999), electrical resistivity mapping, and electrical resistivity sounding (Lanz *et al.*, 1998), and information obtained from several shallow drillholes (Lanz *et al.*, 1998).

Figure 5.8 is an annotated areal photograph of the area of investigation,. Regions marked *W1* and *W2* indicate the locations of the waste dumps, whereas *G1* to *G3* indicate the locations of unexploited gravel lenses. Within *W1*, electromagnetic measurements delineated particularly conductive areas (marked in red, see also (Lanz *et al.*, 1999)).

Geoelectric data were recorded with the new acquisition system described in Appendix 5.12.2. Fifty electrodes were placed at 3 m spacing along a profile between points *A* and *F* (see Figure 5.8). A "complete" data set was recorded with 50 x 2 = 100 parallel scans (4,500 configurations). As reference electrodes (see Figures 5.5 and 5.6) we chose one of the electrodes nearest to the injecting electrode and a second one at a distance from the injecting electrode of 12 m. Data acquisition was completed in 17 minutes. Additionally, we collected a full comprehensive data set involving 50 x 49 = 2450 parallel scans (117,600 configurations), which was completed in about five and a half hours.

Since the parallel scans performed for the comprehensive data set comprise all possible combinations of injecting and reference electrodes, we could make use of reciprocity for checking the data quality. This revealed that the ambient noise level was very high. Only 4,264 of the 4,800 measurements of the complete data set, and 65,000 out of the 117,600 measurements of the comprehensive data set could be retained for the tomographic inversions.

Inversion results for the measured comprehensive data set are shown in Figures 5.9a and 5.9b. The diagonal elements of the resolution matrix displayed in Figure 5.9a indicate that interpretable structure can be expected down to a depth of about 20 m. In Figure 5.9b gravel lens *G1* is revealed by the shallow orange-yellow coloured zone towards the left of the section, having relatively high resistivities of 200 - 800 Ωm. The signature of the waste pit *W1* is found between the marker points *C* and *F* (Figure 5.6). The highly conductive feature ($\approx$ 20 - 30 Ωm) depicted in white extends to a depth of about 10 m. Strictly speaking, the profile intersects the highly conductive area only between marker points *D* and *E*, but its signature is also visible between *C* and *D* due to 3D (out-of-plane) effects, which always influence resitivity measurements (see Figure 5.8). Near point *E*, there is an isolated resistive feature, which most likely represents a concrete block dumped into this industrial waste pit.

The tomogram obtained with the complete pole-bipole data set is shown in Figure 5.9c. The main features observed in Figure 5.9a also appear in this tomogram. However, the conductive feature is somewhat blurred and additional surficial resistive anomalies are observed between marker points *E* and *F*. They are considered to be artifacts. The resistivities of about 100 Ωm in the poorly resolved areas at the bottom of the tomogram represent the initial model. This indicates that the complete pole-bipole basis data set provides no useful information at greater depth. Although the formal resolution for the
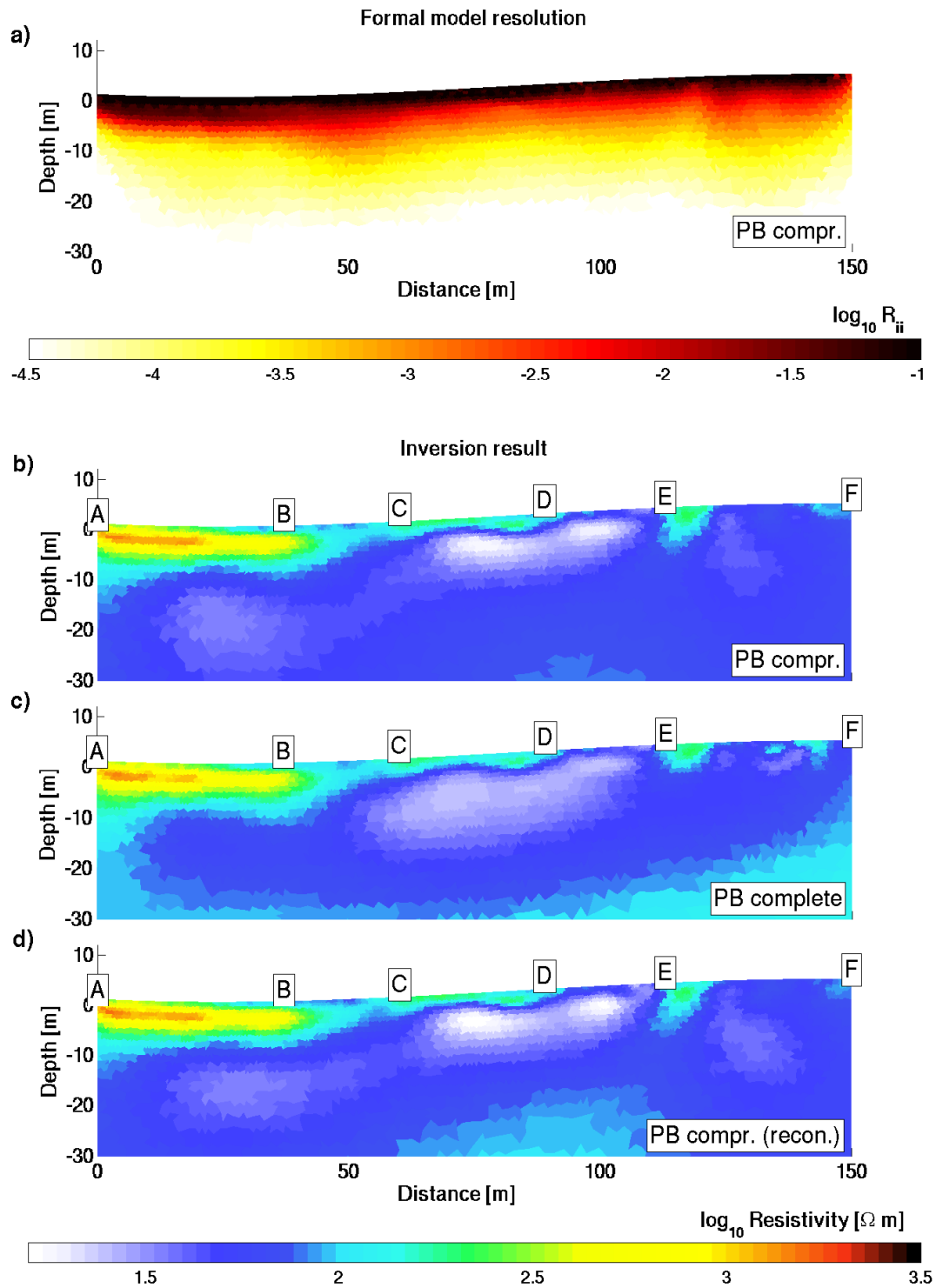
Figure 5.9 – Stetten field site formal model resolution (diagram a) for the comprehensive pole-bipole data set and tomograms (diagrams b-d) for the recorded comprehensive data set (diagram b), complete data set (diagram c) and the reconstructed comprehensive data set (diagram d). The latter was constructed out of the basis electrode configurations underlying diagram (c).

comprehensive data set (Figure 5.9a) is also quite low at these depths, it is at least capable of predicting the average subsurface resistivities.

Inversion results with a reconstructed comprehensive pole-bipole data set (using the complete data set described in Figure 5.9c) are shown in Figure 5.9d. Within the well-resolved uppermost 20 m, there is a very good match between the results using the measured (Figure 5.9b) and the reconstructed (Figure 5.9d) comprehensive data sets, thereby confirming the usefulness of the reconstruction approach. At greater depth, we observe some remnants of the initial model, but they are much less pronounced than in Figure 5.9c.

5.9   Discussion

Our investigations revealed several interesting properties of comprehensive and complete four-point (bipole-bipole) and three-point (pole-bipole) data sets. The most important result is that reconstructing a comprehensive pole-bipole data set from a complete pole-bipole data set is feasible and useful. In combination with a fully parallel data acquisition system this proved to be very efficient for acquiring a small 2D profile of data across a buried waste disposal site. The true potential of the approach proposed becomes evident when considering large 3D deployments that include more than 100 electrodes. Transferring the measuring strategy from 2D to 3D is straightforward. Two current injections at each electrode position are required, and the choice of the two reference electrodes R_1 and R_2 can be made in a similar manner to that described for the 2D setup. Likewise, the choice of R_1 or R_2 for the reconstructions is identical for 2D and 3D deployments.

Determining reliable data weights to form $\mathbf{C}_D^{-1}$ is generally important for tomographic inversions, but it is particularly critical for the reconstruction approach. It might therefore be advisable to establish an appropriate error model prior (and possibly posterior) to a survey. The ambient noise level (e.g., due to self potentials, telluric currents, electromagnetic interference, etc) could be determined by means of passive measurements when no current is injected, and an estimate of the voltage-dependent error could be identified with repeated measurements using different injection currents. Alternatively, one could perform reciprocal measurements, by exchanging current and potential electrodes, for estimating the data errors.

Once a reliable complete data set is acquired, there is considerable flexibility for the subsequent tomographic inversions. Generally, we recommend reconstructing a comprehensive data set, but conceptually it is also possible to reconstruct only partial data sets. This could be useful, when the noise conditions exhibit high spatial variations. Another scenario, in which partial reconstructions could be useful, includes experiments that focus on a particular part of the subsurface. After an initial inversion of the com-

plete data set, one may concentrate on a subsurface area of particular interest. This can be achieved by reconstructing only configurations that contribute to illuminating the area(s) of interest. Identifying such configurations with "posteriori experimental design" will be a topic of future research.

An important feature of the acquisition strategy proposed is that no à priori assumptions on the subsurface structure are required before the survey. This is a clear advantage compared to the sequential approaches of Stummer *et al.* (2004) and Wilkinson *et al.* (2006), which rely on sensitivity patterns computed for a particular resistivity model.

5.10   Conclusions

Key results of our investigations can be summarized as follows.

1. Sequential experimental design, as proposed recently, is not suitable for designing large-scale geoelectrical 2D or 3D surveys involving more than 50 electrodes.

2. As an alternative strategy, we propose measuring complete (or basis) data sets from which comprehensive data sets can be reconstructed by superposition. Complete data sets are usually quite small and can thus be recorded within a reasonable time. Comprehensive data sets allow full exploitation of the information content offered by geoelectrical data.

3. In the absence of noise, complete four-point configuration data sets allow comprehensive data sets to be reconstructed. Comparisons of eigenvalue spectra and model resolution values demonstrate that comprehensive data sets provide significantly superior tomographic images than complete data sets. In the presence of realistic noise, reconstruction of comprehensive four-point data sets is not advisable, because the errors that accumulate through the reconstruction process may become unacceptably large.

4. Acquisition of complete pole-bipole data sets and subsequent reconstruction of comprehensive pole-bipole data is less susceptible to error accumulations. Even in the presence of realistic noise, excellent results can be achieved. This has been demonstrated using both synthetic and observed data sets.

5. Complete pole-bipole data sets can be recorded efficiently with parallel data acquisition systems. For an n-electrode array only 2n parallel scans are required.

5.11   Acknowledgments

5.12   Appendix

5.12.1   Error propagation involved in reconstructing comprehensive data sets from complete (basis) data sets

Reconstructing a comprehensive (or any other appropriate) data set from a complete (basis) data set involves the algebraic addition of measured potential differences

$$U^{rec} = \sum_{i=1}^{N} f_i U_i^{compl}, \tag{5.6}$$

where U_i^{compl} can be any of the potential readings contained in the complete data set and f_i are linear factors that are either plus or minus one. Obviously such a superposition is only meaningful for potential differences recorded with the same current injection strength. Therefore, prior to the reconstruction process, all potential differences in the basis data set are linearly scaled to a source signal strength of $1A$. Uncertainties in the measurements U_i^{compl} propagate through the reconstructed potential values according to the error propagation law. This needs to be carefully taken into account when computing à priori model covariance matrices $\mathbf{C}_M^{-1}$ required for inverting reconstructed data sets. For this purpose, we assume, that the potential readings U_i^{compl} in the basis data set are contaminated with a certain percentage p of relative noise and a constant noise level ΔU_c yielding absolute potential errors:

$$\Delta U_i^{compl} = \Delta U_c + p/100 \cdot U_i^{compl} \tag{5.7}$$

According to the error propagation law, resulting absolute errors for reconstructed potential values U^{rec} (Equation 5.6) are

$$\Delta U^{rec} = \sum_{i=1}^{N} \left| \frac{\partial U^{rec}}{\partial U_i^{compl}} \right| \cdot |\Delta U_i^{compl}| = \sum_{i=1}^{N} |f_i \cdot (\Delta U_c + p/100 \cdot U_i^{compl})|, \tag{5.8}$$

such that the absolute errors from the relevant basis configurations simply add up. Based on an estimated error model (i.e. appropriate values for p and ΔU_c) a data covariance

matrix $\mathbf{C}_M^{-1}$ can then be obtained from the inverse of the squared relative data errors:

$$\mathbf{C}_M^{-1} = \mathrm{diag}\left(\left[\frac{U_j^{rec}}{\Delta U_j^{rec}} \right]^2 \right) \tag{5.9}$$

To identify the linear combinations (Equation 5.6) required to reconstruct any four-point (bipole-bipole) measurement configuration from four-point complete data sets, either the representation formula introduced by Lehmann (1995) or the approach based on primary pole-pole data sets by Xu and Noel (1993) can be used. As the representation formula is relatively complicated to implement and, more importantly, is restricted to the basis four-point data set described in (Lehmann, 1995), we briefly demonstrate the approach by Xu and Noel (1993). Given a primary pole-pole data set $\vec{d}_{pp} \in \Re^{n_{pp}}$, a complete data set $\vec{d}_{basis} \in \Re^{n_{basis}}$ and an arbitrary data set $\vec{d}_r \in \Re^{n_r}$ that is to be reconstructed, it is relatively simple to find linear maps $\mathbf{A} \in R^{n_{basis} \times n_{pp}}$ and $\mathbf{B} \in R^{n_r \times n_{pp}}$ such that

$$\mathbf{A}\,\vec{d}_{pp} = \vec{d}_{basis} \quad \text{and} \quad \mathbf{B}\,\vec{d}_{pp} = \vec{d}_r. \tag{5.10}$$

Such linear maps are commonly applied during geoelectric data inversions when calculating four-point sensitivities (or forward solutions) from pole-pole sensitivities (or forward solutions). If the data set in $\vec{d}_{basis}$ is truly complete, then the linear combinations required to reconstruct $\vec{d}_r$ from $\vec{d}_{basis}$ are given by the linear map

$$\mathbf{D} = \mathbf{B} \cdot \mathbf{A}^{-g}, \tag{5.11}$$

where $\mathbf{A}^{-g}$ is the generalized inverse of the matrix $\mathbf{A}$. The linear combinations in $\mathbf{A}$ involve the addition of up to six measurements in $\vec{d}_{basis}$ and therefore lead to large error accumulations according to Equation 5.8 and consequently to small data weights in the data covariance matrix $\mathbf{C}_M^{-1}$ (Equation 5.9), thereby effectively degrading the resolution capability of the data set $\vec{d}_r$.

In contrast to the rather complicated process described above, reconstructing any pole-bipole data set out of the complete pole-bipole data set described in section 5.6 is straightforward, because it only involves the linear combination of two basis configurations as illustrated in Figure 5.5. More importantly, since for each reconstructed data point an optimal reference electrode can be selected and since only two basis configurations are added, error accumulations are usually not an issue.
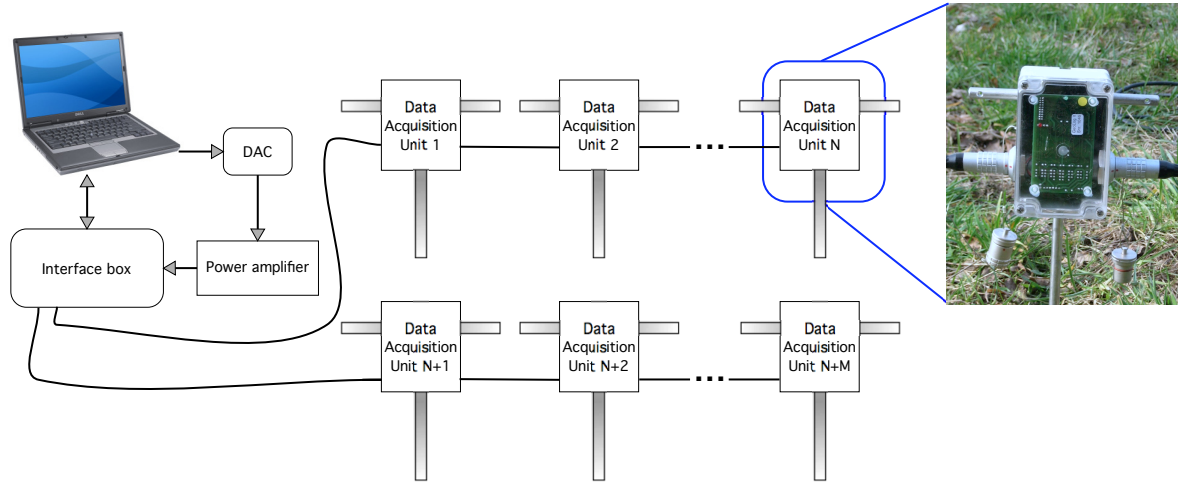
Figure 5.10 – Schematic layout of the fully distributed data acquisition system *ETH-DCMES-II*.

5.12.2 ETH-DCMES-II: a new tool for parallel acquisition of large geoelectrical data sets

ETH-DCMES-II is an extension of the multi-electrode array ETH-DCMES described in Stummer *et al.* (2002). This experimental (non-commercial) system offers several unique features that are generally useful for fast and reliable acquisition of geoelectrical data, and particularly suitable for the measuring strategies described in this paper. The general concept of *ETH-DCMES-II* is shown in Figure 5.10. Each electrode is equipped with a Data Acquisition Unit (DAU) that contains switching relays, a 24 bit A/D converter, a microprocessor, random access memory, serial interfaces and rechargeable batteries. The individual DAUs are connected by four wires to an interface box (IFB), which is connected to a standard laptop computer. The current design of the IFB allows up to 124 DAUs to be hooked up. With some minor modifications it is possible to extend the system to several IFBs.

Arbitrary current source waveforms (e.g., square wave, sine wave, chirp signal) can be generated on the computer and fed via a D/A converter into a battery-driven amplifier that produces up to 300 V and 100 mA. Conceptually, more amplifiers could be serially connected to increase the maximum voltage. The source current fed into the electrode array is monitored by a special DAU that is located in the IFB.

Communication between the DAUs and the computer is performed via a serial interface. Each DAU can configure its electrode to act either as current sink or source, reference or measuring electrode. Typically, current is injected over two electrodes, one electrode acts as a potential reference, and all other electrodes measure simultaneously the voltage with respect to the reference. The resulting voltages are digitized at the measuring DAUs and temporarily stored in the DAUs random access memory.

After completion of a parallel scan, the operator can download all the voltage wave-

forms to the computer for further analyses in the laboratory (e.g. for extracting induced polarization parameters). Due to the serial communication, such a download can be time-consuming. Alternatively, it is possible to simultaneously start data analysis programs on all DAUs that compute the voltage parameters required for the subsequent tomographic inversions (e.g., maximum voltage amplitudes and the associated variances). The results of the DAU-controlled analyses typically include only a few numbers that can be transferred swiftly back to the computer. The operator can upload any suitable data analysis programs to the DAUs. Choice of an appropriate algorithm can even be made in the field.

The batteries included in the DAUs can be charged at any time (e.g. when the system is idle). Since the capacity of the batteries allows the system to be operated up to 12 hours, recharging is typically done overnight.

Chapter 6

Conclusions and Outlook

The overall goal of my thesis was to improve data acquisition and data inversion schemes such that efficient large-scale 3D geoelectric field surveys become feasible. This required improvements of (i) the data acquisition hardware, (ii) the numerical forward modelling and inversion algorithms, and (iii) the experimental design. In the following, I will summarize the most significant achievements of my thesis work, and I will outline where I see a need for further research.

6.1 Main achievements

6.1.1 *ETH-DCMES-II*

The *ETH-DCMES* data acquisition system presented by Stummer *et al.* (2002), has been further developed and improved in several important ways to take full advantage of its parallel recording capabilities and to improve its robustness, mobility, versatility and field handling. Besides numerous minor technical improvements, the data acquisition units (DAUs) were redesigned to allow processing of the voltage time series. As a consequence, the time-consuming transfer of the recorded voltage waveforms can now be avoided, which increases substantially the data acquisition speed in the parallel recording mode. Performance tests conducted during a 3D field survey revealed that in distributing the data analysis, the recording time could be reduced down to a quarter of the time previously required. Robust and reliable waveform analysis algorithms for sinusoidal and rectangular voltage waveforms have been developed and tested with synthetic and observed data.

The overall handling of the *ETH-DCMES* has been improved by replacing the bulky and heavy source (including its power supply) with a newly developed light-weight and battery-driven current source. Furthermore, the new data acquisition system can now be controlled with a standard notebook computer. These improvements allow the *ETH-DCMES-II* to be employed in rugged terrain not accessible by vehicle.

6.1.2 Efficient 2.5D/3D numerical modelling and inversion

The solution to the numerical forward modelling problem is the most challenging and time-consuming part of 3D geoelectric data inversions. Therefore, a large part of my research was devoted to the development of an optimized forward solver, exploiting several novel techniques. I have employed the finite element method for solving the governing differential equation using an unstructured domain discretization. This allowed arbitrary topography to be incorporated, and the domain discretization to be refined (made more dense) or coarsened wherever necessary.

Moreover, I addressed two major problems of geoelectric forward modelling, namely (i) singularities near the source electrodes and (ii) truncation of the computational domain at the artificial ground boundaries. Traditional approaches for both of these issues require model discretizations with a large number of grid points. To deal more efficiently with the source electrode singularities, I employed a novel singularity removal scheme based on a fast multipole boundary element method. To reduce inaccuracies caused by the limited computational domain, I employed infinite elements. By means of extensive numerical tests I demonstrated that the combined application of singularity removal and infinite elements allows the number of grid points to be reduced by a factor of $\approx$ 6-10 compared with traditional finite-element methods. This facilitates the application of modern sparse direct matrix solvers for realistic 3D inversion problems, which greatly speeds up the computations.

Despite the seemingly ever increasing power of computers, the inversion of full 3D geoelectrical data sets remains a challenging and time-consuming task. I have implemented optimized data inversion procedures that are based on solving the normal equations within each iteration of a Gauss-Newton type minimization. This allows almost arbitrarily large data sets to be inverted, which is essential for analyzing data sets from large-scale 3D geoelectric field surveys. The only limiting factor is the number of inversion blocks in the model, which governs the size of the Hessian matrix in the normal equations.

To keep the size of the Hessian matrix to within manageable limits, special attention was paid to the parameterization of the inversion blocks. Besides restricting the size of the Hessian matrix, the inversion block parameterization is also of key importance to reduce the under-determined component of the inversion problem. Two approaches, based on clustering of the forward mesh cells, have been implemented. Both allow the parameterization to be adapted to the resolving power of the data sets involved.

The inversion procedures were tested extensively with synthetic 2D and 3D data sets. Furthermore, they were applied successfully to large 2D and 3D field data sets recorded over a buried waste-deposit site in Switzerland.

6.1.3 Experimental design

Since sequential experimental design, as proposed recently by Stummer *et al.* (2004) and Wilkinson *et al.* (2006), is not practical for designing large-scale 3D geoelectrical surveys, I have devised a novel recording strategy that is based on complete pole-bipole data sets (in the sense of Xu and Noel (1993)), from which comprehensive pole-bipole data sets can be reconstructed.

By means of an eigenanalysis of the Hessian matrix and computing the model resolution matrices I have demonstrated that such a reconstruction could also be beneficial for complete four-point data sets, as proposed by Xu and Noel (1993) and Lehmann (1995). However, in the presence of noise, such four point reconstructions become unstable. In contrast, pole-bipole reconstructions are shown to be very useful, offering improvements in resolution and image quality, even in the presence of realistic noise.

Complete pole-bipole data sets can be acquired very efficiently with fully parallelized systems, such as the *ETH-DCMES-II*. This was demonstrated during a field experiment over the buried waste disposal site, referred to earlier. Furthermore, comparisons of tomographic inversions using reconstructed and effectively measured comprehensive pole-bipole data sets confirmed our theoretical results.

6.2 Areas of future research

6.2.1 Improvements to the *ETH-DCMES-II*

Ethernet-based data bus

Modern Ethernet-based data buses allow much higher data transfer rates than the RS-485 data bus currently employed in the *ETH-DCMES-II* system. Ethernet-based communication would thus allow recorded full waveforms to be transferred back to the central computer in a small fraction of the time currently required. The data transfer rate of the RS-485 data bus is limited to 38.5 kBit/s to ensure error-free transfer over a maximum cable length of 1.2km (Stummer *et al.*, 2002). In contrast, Ethernet data busses are available that support data transfer rates of either 10, 100 or 1000 MBit/s, depending on the cable-type used. Only RG-58 coaxial cables, offering a data transfer rate of 10 MBit/s, support sufficiently large maximum cable lengths (500m). However, coaxial cables are relatively heavy and delicate to handle. Furthermore, they are not flexible enough to be coiled up easily. Fiber cables could be used as an alternative. This would require an Ethernet–to–Fiber media converter attached to the field computer. Fiber cables feature a maximum cable length of about 40km and very high data transfere rates. But this would require relatively expensive Fiber–to–Ethernet converters build into each DAU. Furthermore, fiber cable connections are very sensitive and thus

might easily break.

A better solution would be to employ so-called Ethernet extenders. These lightweight and inexpensive devices can be connected to a standard 10/100 MBit twisted pair Ethernet connection. They increase the maximum cable length allowed from 100m up to 10km by reducing the maximum transfer rate down to 4.6 MBit/s, which is still 120 times faster than the 38.5 kBit/s offered by the RS-485 data bus. A single twisted pair of copper cable is sufficient for the data bus connecting the DAUs to the central unit. A multiport-repeater with four channels could be combined with four Ethernet extenders to support four data bus cables, each with a maximum cable length of 10km and a data transfer rate of 4.6 MBit/s. These components could be placed inside the interface-box. Only a single standard Ethernet connection would be required on the field computer to communicate with all DAUs.

GPS-based automatic position detection

Accurate determination of the electrode locations occupied during a geoelectric field campaign is essential for reliable inversions (Zhou and Dahlin, 2003). Usually electrode positions are measured with handheld differential GPS devices or even measuring tapes, which is quite error-prone.

Each DAU could be equipped with a GPS chip for automating the positioning. Integrated GPS chips are nowadays routinely embedded in cell phone devices. They are small in size (less than 5 by 5 millimetres), low-cost (around ten dollars each) and have a low power consumption of less than 15mW. The latter is important, considering the limited battery capacity of the DAUs. A power consumption of less than 15mW would certainly be acceptable in comparison with the 100mW power consumption of the DAUs. Each time the DAUs would have to be moved (e.g. during a roll-along procedure), a broadcast message would be send to all DAUs asking them to acquire their actual position with their on-board GPS chips. Subsequently the GPS chips could be deactivated (or put into a sleep mode) to save battery power. A continuously running GPS base-station placed at a fixed location would be employed to support differential GPS. Automatic GPS position determination by the DAUs would alleviate the current laborious field surveying procedure, especially during 3D field campaigns involving a large number of electrode locations.

Improved waveform analysis algorithms

Generally, the analysis algorithms developed for sinusoidal and rectangular voltage waveforms proved to work reliably. However, visual inspection of voltage waveforms revealed that (i) too many measurements may be filtered out based on the misfit parameter returned by the DAUs, and (ii) questionable measurements caused by technical problems
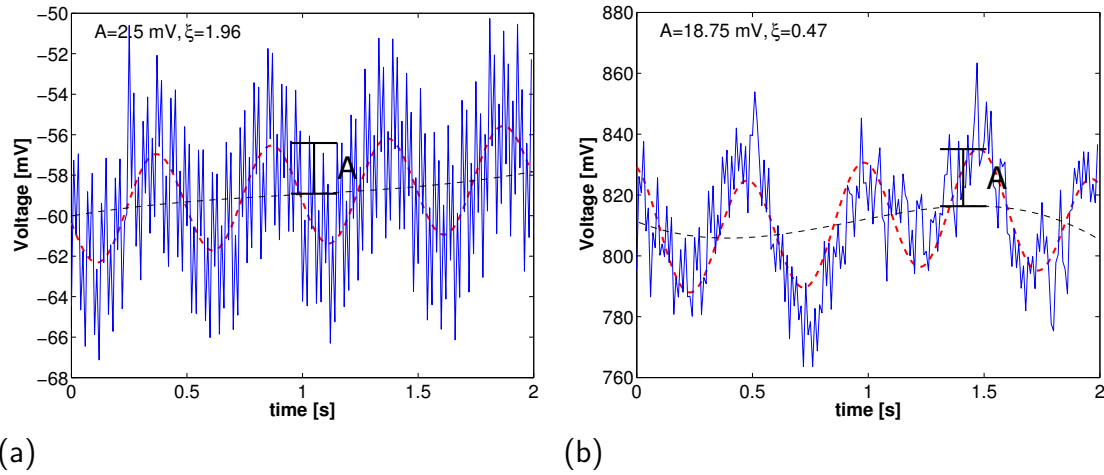
Figure 6.1 – Problematic waveform signals recorded during the 3D field survey at the Stetten waste-deposit site. The signal waveform in diagram (a) is masked by strong high frequency noise due to a large geometry factor of the electrode configuration used (i.e low voltage level of signal). Diagram (b) shows a waveform recorded by a mal-functioning DAU. The red dashed lines indicates the fit estimated by the corresponding DAUs; A is the resolved signal amplitude and ξ is the data misfit parameter that quantifies the quality of the data fits.

with the DAUs may not be identified.

Both problems only occurred for a small fraction of the waveforms downloaded for test purposes. Case (i) usually occurs for voltage waveforms that are overshadowed by strong high-frequency noise. Figure 6.1(a) shows an example of such a waveform. Recordings based on these waveforms would be automatically excluded from the data set due to the large data misfit parameter returned by the DAU.

However, in most of the cases the DAUs were nevertheless able to estimate the voltage signal amplitude reliably. To resolve this problem, a low-pass filter could be applied to the recorded voltage waveforms prior to fitting the voltage data to a mathematicl function appropriate to the current waveform.

Problem (ii) is more severe. The origin of these questionable measurements could not be clearly identified. Based on the shape of the signals recorded (Figure 6.1(b)), I suspect that they are caused by a bad contact between the DAUs and the metal stakes. The redesigned DAUs are equipped with a small metal spring that establishes the electrical contact between the DAUs and the electrodes. A larger spring or alternatively a second spring could be attached to improve the electrical coupling.

For improved recognition of questionable signals, information from all DAUs involved in a parallel scan should be taken into account. Any odd or spurious measurements would most likely be recognized as outliers in a generally spatially slowly varying voltage distribution. Such visual data control is currently implemented in the acquisition software by mapping the voltage values determined for a single parallel scan – however, automatic filters should be developed to simplify the process.

Acquisition of induced polarization data

Induced polarization (IP) measurements are used in several environmental applications, for example for distinguishing sand from clay and in the mining industry (mainly for detecting metal sulphides). Measurements are either performed in the time-domain or in the frequency-domain. Interrupted square-wave source signals are used in the time-domain, and the IP effect (chargeability) is determined from the decay characteristics of the voltage waveform. In the frequency-domain, a sequence of harmonically alternating current waveforms is employed, and the IP effect recognised as a frequency dependence in the measured voltage (or apparent resistivity).

The *ETH-DCMES-II* is capable of injecting almost arbitrary source signal waveforms and voltage recordings with a sampling rate of up to 1KHz. Adaptive waveform analysis algorithms can be developed and deployed on the DAUs. Therefore, the *ETH-DCMES-II* has the ability to acquire induced polarization data, but this option has not yet been exploited.

IP measurements with the *ETH-DCMES-II* system (e.g., based on a few sinusoidal alternating current injections with varying frequencies) would have to include a cross-correlation of the measured voltage waveforms with the injected current waveforms for identifying phase-shifts. This would require the current waveforms, acquired with the DAU located at the interface box to be distributed to all other DAUs. Alternatively, all voltage waveforms could be downloaded (perhaps using the fast Ethernet option discussed previously) to the central computer, and the cross-correlations could be performed later in the laboratory.

6.2.2   Future developements on Forward and Inverse Algorithms

Support for subsurface (borehole) electrodes

The inversion of geoelectric data recorded in boreholes is currently not yet fully supported by my forward and inverse solvers. Both the 2.5D and 3D forward solvers support singularity removal for subsurface electrodes only in the presence of a flat topography, where the singular potential can be determined analytically. The boundary element method, employed for estimating the singular potentials with surface electrodes in the presence of topography, needs to be extended. This can be accomplished by adapting the boundary conditions of the Laplace equation employed for determining the singular potentials (Equation 3.16 in section 3.5). Additionally, the clustering algorithms for constructing the inversion blocks (section 4.2) would need to be modified slightly.

Adaptive forward solvers

The finite-element method, as it is currently employed for the forward solver described in Chapter 3, is based on a fixed set of finite-element basis functions. Mesh refinements have to be performed during the initial mesh generation process.

Adaptive mesh refinements could be applied for optimizing the finite element meshes. This is usually implemented using iterative algorithms. After a forward solution has been computed on an initial (coarse) domain disretization, an appropriate error estimator (see Ainsworth and Oden, 1997, for an overview of different implementations) is applied to identify elements that need to be refined. This process is repeated until a sufficiently accurate solution is obtained. In addition to spatial mesh refinements ("h-refinements"), the polynomial degree of the finite-element shape functions can be increased or decreased ("p-refinements"). Adaptive methods should be applied to the non-singular (secondary) potential fields to avoid excessive refinements due to numerical singularities close to the source electrodes.

Initial tests using h-refinements have revealed that the iterative process required to achieve an adaptive forward discretization slows down the overall solution process severely, but it should be noted that these tests were performed with conventional preconditioned conjugate gradient equation solvers. Conceptually, multigrid equation solvers, capable of taking the hierarchical structure of the refined mesh into account, may give a better performance.

An interesting alternative for solving elliptic differential equations based on adaptive wavelet basis functions is described in (Cohen *et al.*, 2001). Barinka *et al.* (2001) demonstrated the efficiency of this method for the Poisson and the Helmholtz equations. Adaptive wavelet techniques employ an iterative approach in which an initial approximate solution is obtained by using only a few wavelet basis functions. The accuracy of the solution is then successively improved by introducing additional basis functions.

This method has several advantages compared to the more traditional finite element and finite difference methods. The expansion of the wavelet basis is purely data driven, such that additional details are only introduced in those regions where they are required. Furthermore, adding or removing basis functions does not require the existing domain discretization to be modified. Finally, wavelet-based algorithms allow inexpensive and efficient diagonal preconditioners to be applied.

6.2.3 Future developments of data acquisition strategies

The data acquisition and reconstruction scheme proposed in Chapter 5 was discussed only for 2D data sets. Extending this approach to 3D field surveys is straightforward. The presented pole-bipole data set can easily be acquired on 3D (aerial) electrode deployments. As for 2D electrode profiles, the source (injecting) electrode is sequentially
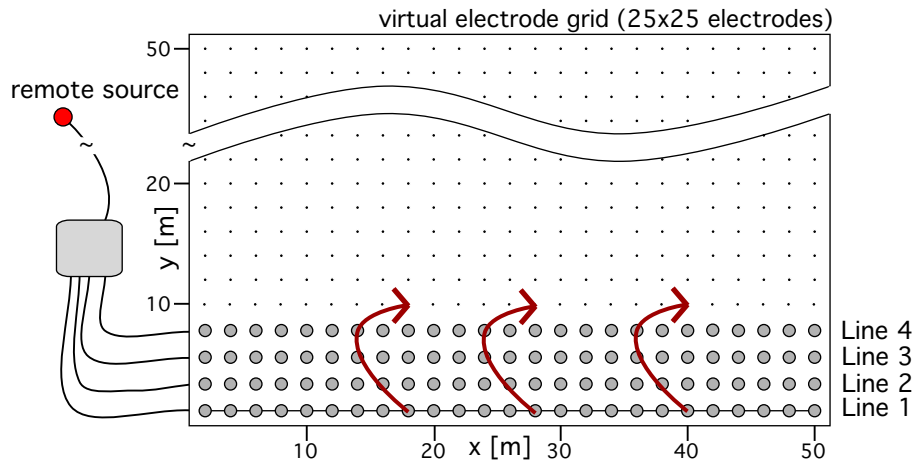
Figure 6.2 – Roll-along scheme employed during the 3D field campaign at the Stetten waste disposal site. Within each step of the roll-along procedure one electrode line was moved after a complete set of pole-bipole parallel measurements were taken.

placed on each of the locations within a predefined electrode deployment. For each source electrode position, two parallel scans with two different reference electrodes are acquired. The choice of the reference electrodes as well as the subsequent data reconstruction process can be performed in a similar manner as described in Chapter 5.

Efficient 3D roll-along strategies

A major difference between 2D and 3D data acquisition concerns the way the electrodes are placed in the field. Covering a large area under investigation with a limited number of electrodes usually requires roll-along strategies (widely practised in the seismic industry) to be employed. In order to obtain maximum subsurface information at minimal cost, suitable deployments of electrodes should be found, such that the effort for moving the electrodes is minimized and sufficient 3D coverage in the x and y directions (Figure 6.2) is achieved. For the 3D field campaign at the buried waste disposal site near Stetten (Chapter 4), the roll-along strategy depicted in Figure 6.2 was employed. For each of the electrode deployments, complete pole-bipole data sets were acquired. The roll-along procedure proved to be efficient in terms of the effort required for moving the electrodes. Moving one electrode line at a time resulted in maximum subsurface coverage. Such data sets also contain redundant information that can be used for quality control. Moving two or three lines at once would provide a faster 3D roll-along, but with a less dense measurement sampling in the y-direction (Figure 6.2). It remains to be investigated whether the expected loss of subsurface information justifies the enhanced acquisition speed. Conceptually, more complicated roll-along techniques could be employed. For example, after completion of the measurements on the first electrode deployment, line 1 could be moved further away in the y direction. The only requirement is that the

procedure can be carried out efficiently. Alternatively, the roll-along procedure could be repeated in the x-direction. Resolution studies and/or synthetic model studies should be carried out to gain more insight into the properties of the different roll-along options.

"A-posteriori" experimental design

Comprehensive three-point data sets have been reconstructed for the synthetic and measured complete data sets presented in Chapter 5. Conceptually, any subset of the comprehensive data set could be reconstructed. A future topic of investigation could be to assess which partial data reconstructions would be most suitable for specified subsurface targets. A-posteriori experimental design strategies (i.e. based on the algorithms presented by Stummer *et al.* (2004) and Wilkinson *et al.* (2006)) could be applied to identify useful reconstructions.

Theoretical aspects of the proposed data reconstruction process

Xu and Noel (1993) and Lehmann (1995) demonstrated that any three- or four-point configurations can be reconstructed from complete three- or four-point data set by simple algebraic additions. This raises the question as to how the augmentation of a measured complete data set by means of data reconstructions influences its capability to resolve subsurface conductivity structures. From a physical point of view, such a data augmentation is not expected to provide additional information because only linear combinations of measured quantities are supplied (and the rank of the Hessian matrix should not change). However, from a mathematical point of view, augmenting a data set with reconstructed measurements can be interpreted as a preconditioning of the Hessian matrix in the normal equation. In Chapter 5, it was demonstrated that improved inversion results can be obtained by such a process, provided the measured data sets are complete and error propagation is properly taken into account.

Augmenting a complete data set with reconstructed data yields a sensitivity matrix $\mathbf{G} = \mathbf{D} \cdot \mathbf{G_c}$, where $\mathbf{G_c}$ is the sensitivity matrix of the measured data set and $\mathbf{D}$ is a matrix that performs simple linear combinations on $\mathbf{G_c}$. A representation of the sparse matrix $\mathbf{D}$ can be obtained in a relatively simple manner for any three- or four-point data reconstructions as described by Xu and Noel (1993). It would be enlightening to analyze in detail the properties of the matrix $\mathbf{D}$ and its influence on the eigenvalue spectrum of the Hesssian matrix and the corresponding model resolution matrix. This may not only provide a better theoretical understanding of the benefits of the reconstruction process, but may also allow reconstructions to be performed in an optimal manner (e.g. in the presence of a spatially irregular noise pattern).

Appendix A

A new boundary-element-based singularity removal approach for geoelectric forward solver

Mark Blome, Hansruedi Maurer

EAGE Near Surface Conference
Palermo, Italy, September 4–7, 2005

A.1 Summary

We present a new singularity removal technique for 3D finite-element forward calculations of the geoelectric equations in the presence of significant topography. The technique, which is based on the Trefftz boundary-element method (TBEM), allows the singular potential to be calculated numerically and subtracted from the finite-element equations. A numerical experiment demonstrates that the technique is accurate and computationally very efficient.

A.2 Introduction

During the past few decades, much effort has been put into the development of numerical solutions of the 3D geoelectrical forward problem. Many solutions found in the literature are based on the finite-difference technique of (Dey and Morrison, 1979a). Alternatively, finite-element solutions that allow the implementation of unstructured meshes have been

proposed (e.g. Pridmore *et al.*, 1981). This is particularly useful for taking into account topography effects.

Finite-difference and finite-element calculations suffer from singularities that occur at the source electrode positions. Lowry *et al.* (1989) presented a procedure for efficiently removing these singularities. They subtract an analytical homogeneous halfspace solution prior to discretization of the governing equations. This technique has been routinely applied to flat-earth models, but it has its limitations in the presence of significant topography. Here, we show that the singular potential can be estimated numerically in an efficient manner via the Trefftz method.

A.3   Theory

In 3D geoelectric modeling, the Poisson equation with appropriate boundary conditions needs to be solved:

$$
\begin{cases}
\nabla \cdot (\sigma(x,y,z)\nabla V) = -I\delta(|\vec{r} - \vec{r_i}|) & \text{in } \Omega \\
\qquad\quad \partial V/\partial \mathbf{n} = 0 & \text{on } \Gamma_1 \ , \\
\qquad\qquad V = f(x,y,z) & \text{on } \Gamma_2
\end{cases}
\tag{A.1}
$$

where $\sigma(x,y,z)$ denotes the spatially varying conductivity, $\vec{r_i}$ is the current source position, I is the current density, and Ω is the domain under consideration with boundary Γ separated into a surface (Γ_1) and the ground (Γ_2). We derive the finite-element formulation to equation A.1 by a weighted residual approach

$$
\int_\Omega R\omega \ d\Omega = \int_\Omega [\nabla \cdot (\sigma \nabla V) + I\delta(|\vec{r} - \vec{r_i}|)]\omega d\Omega = 0,
\tag{A.2}
$$

where R is the residual and ω are the weighting functions. After applying Greens integral theorem to equation A.2, the resulting weak Galerkin formulation can be discretized using various finite-element types. We use tetrahedral elements with linear form functions. This discretized form leads to a sparse system of linear equations that can be solved effectively with appropriate numerical methods.

In Lowry *et al.* (1989)'s singularity removal technique, the potential field in equation A.1 is separated into an anomalous (V_a) and a normal part (V_n), whereby $V(x,y,z) = V_a(x,y,z) + V_n(x,y,z)$. Moving the known normal potential field to the right side in equation A.1 leads to:

$$
\nabla \cdot (\sigma(x,y,z)\nabla V_a) = -\nabla \cdot ((\sigma(x,y,z) - \sigma_0)\nabla V_n) \text{ within } \Omega
\tag{A.3}
$$

The problem is reduced to determining only the non-singular potential field that results from the conductivity anomalies. Once the non-singular potential is found, the
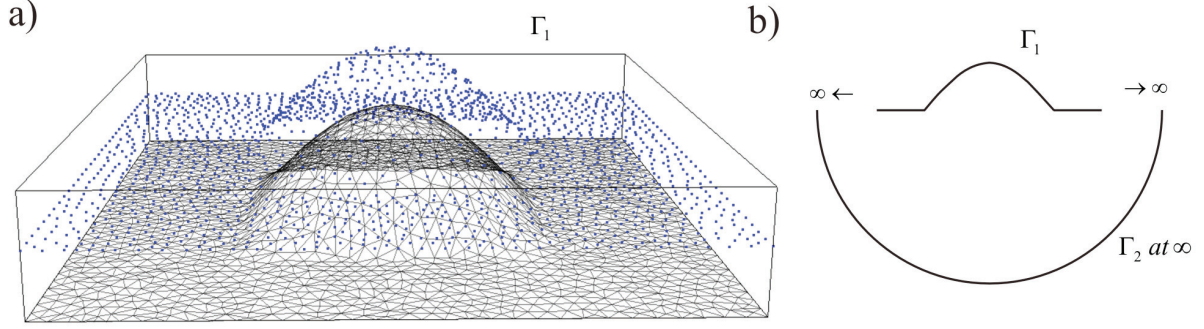
Figure A.1 – (a) A typical surface mesh with the corresponding set of representing sources used in the TBEM. (b) The integration principle.

singular potential is added to yield the total electrical potential.

In the singularity removal approach of (Lowry *et al.*, 1989), V_n is given by an analytical solution for a homogeneous halfspace. This may be a poor representation of V_n in the presence of topography. We seek an alternative method for accurately and swiftly determining V_n in the presence of significant topographic relief. Our solution is based on the Trefftz boundary-element method (TBEM; Kita and Kamiya (1995)), which is a variant of the boundary-element methods (Brebbia, 1978). The solution is approximated by a superposition of functions $u_i^*(\vec{r})$ that a priori satisfy laplaces equation:

$$
\begin{cases}
u(\vec{r}) = & u_p + \sum_{i=1}^{N} a_i u_i^*(\vec{r}) = u_p + \vec{a}^T \cdot \vec{u}^*(\vec{r}) \\[4mm]
q(\vec{r}) = & \dfrac{\partial u(\vec{r})}{\partial \vec{n}} = \dfrac{\partial u_p(\vec{r})}{\partial \vec{n}} + \sum_{i=1}^{N} a_i \dfrac{\partial u_i^*(\vec{r})}{\partial \vec{n}} = q_p + \vec{a}^T \cdot \vec{q}^*(\vec{r})
\end{cases}, \qquad (A.4)
$$

where u_p is the particular homogeneous halfspace solution to equation A.1. The unknown parameters a_i are determined such that the approximate solution $u(\vec{r})$ and its normal derivative at the boundary ($q(\vec{r})$) satisfy the boundary conditions by means of a weighted-residual approach:

$$
\int_{\Gamma_1} (u(\vec{r}) - \widehat{u})\omega_1 \, d\Gamma_1 - \int_{\Gamma_2} (q(\vec{r}) - \widehat{q})\omega_2 \, d\Gamma_2 = 0, \qquad (A.5)
$$

where $\widehat{u}$ and $\widehat{q}$ represent the prescribed boundary conditions on Γ_1 and Γ_2, respectively. The discretized form of equation A.5 leads to a dense symmetric matrix with only $N \times N$ entries, where N is the number of interpolation functions employed. For complicated domains (e.g., in the presence of topography), the functions $u_i^*(\vec{r})$ can be constructed by using so-called representing sources (Mayergoyz *et al.*, 1983). The strategy is depicted in Figure A.1a. The representing sources are located above the topographic surface at a certain height d_s. For $\vec{r}_i$, the ith representing source location, $u_i^*(\vec{r})$ and $q_i^*(\vec{r})$ are given

by:

$$u_i^*(\vec{r}) = \frac{d_s}{|\vec{r} - \vec{r}_i|}, \quad q_i^*(\vec{r}) = \frac{\partial u_i^*(\vec{r})}{\partial \vec{n}}, \tag{A.6}$$

The integrations in equation A.5 have to be carried out along the boundary as shown schematically in Figure (A.1b; Yokoi and Senchez-Sesma (1998)). The surface is extended virtually to infinity, such that the ground Γ_2 is at infinity and hence all integral contributions along Γ_2 in equation A.5 vanish. Thanks to the TBEM, the integration along Γ_1 can be truncated at a moderate distance from the topographic region without significant loss of accuracy; the singular potential over the flat part of the surface rapidly approaches the analytical flat-earth solution, which is included in $u(\vec{r})$. To model an infinitely extended surface over an unbounded domain, it is, therefore, sufficient to integrate along the inner part of Γ_1 (Figure A.1a).

After the unknown coefficients $\vec{a}^T$ have been found, the singular potential is available in a half-analytical form (equation A.4). This makes the TBEM very memory efficient, since only N coefficients a_i need to be saved for each singular potential. As the system matrix resulting from equation A.5 does not depend on the source location, it needs to be inverted only once for a given set of electrodes. The remaining operations are simple backward substitutions.

A.4   Numerical Example
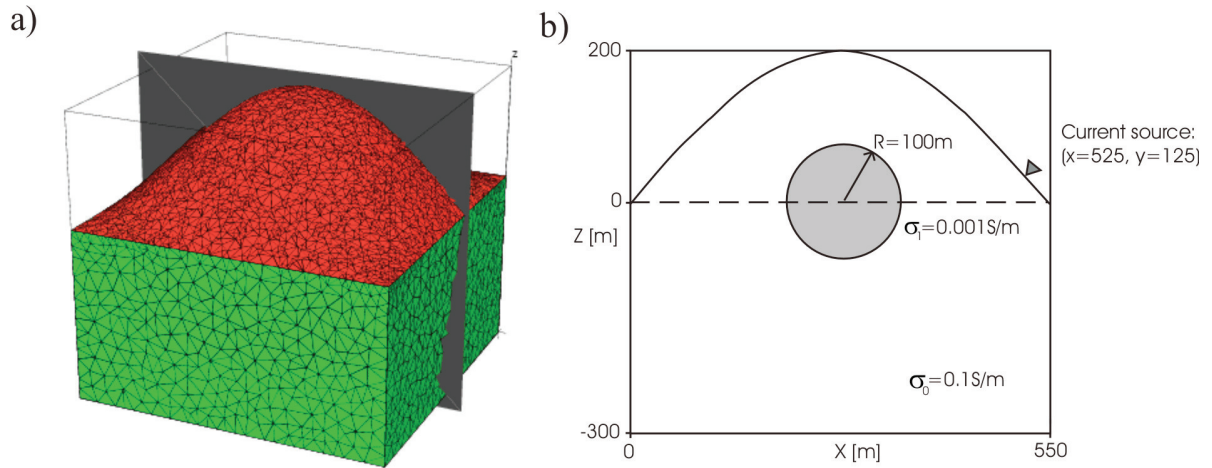
Figure A.2 – Test model. (a) The tetrahedral finite-element mesh representing the conductivity model and (b) a vertical cut through the conductivity model.

The new singularity removal approach is applied to a simple synthetic model that includes topography. Figure A.2a shows the finite-element mesh used in the calculations, whereas Figure A.2b outlines a vertical cut through the conductivity model at the position indicated by the grey plane in Figure A.2a. It consists of a resistive sphere

embedded in a more conductive homogeneous domain. A current source is placed close to the margin of the topographic region.
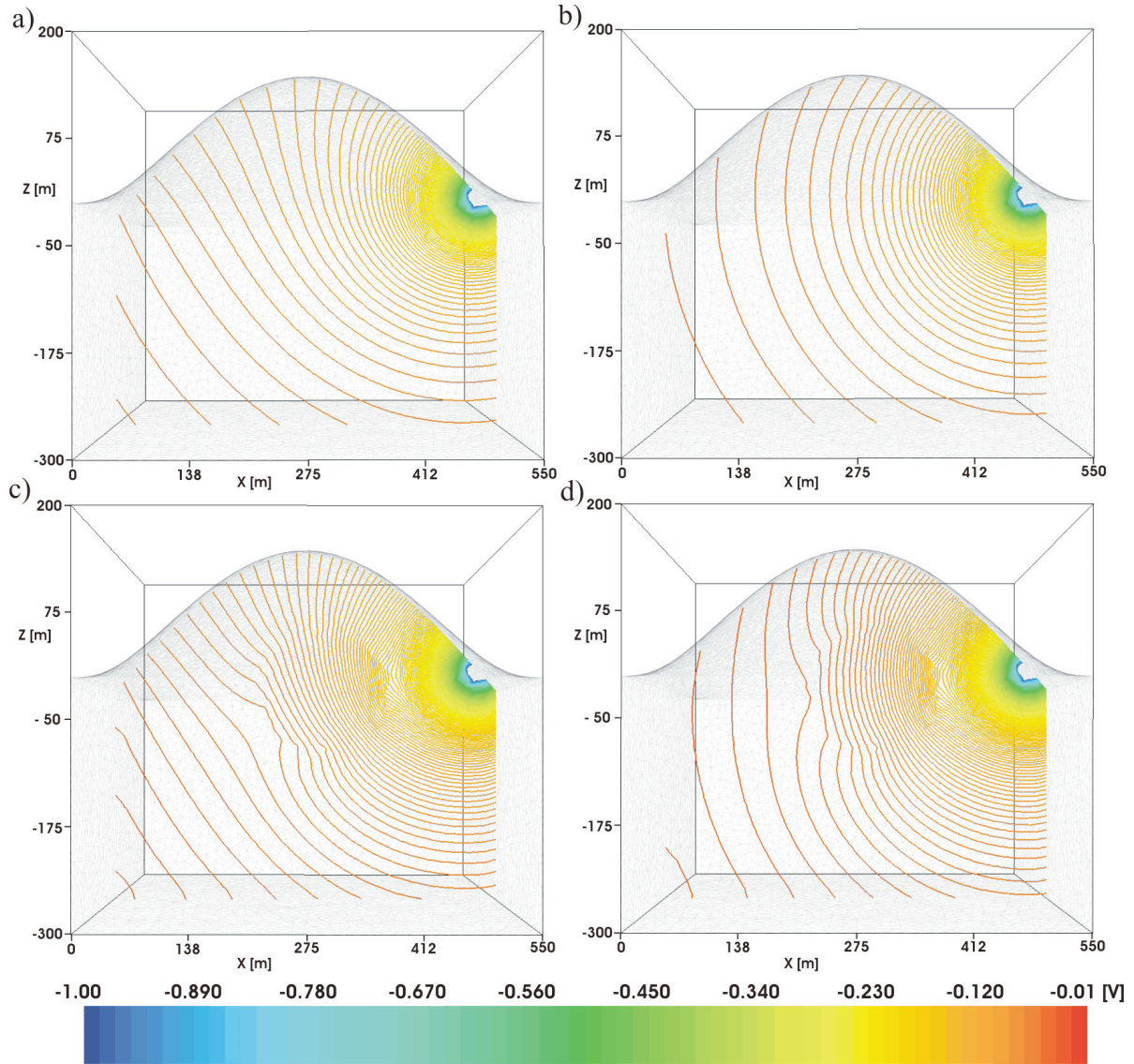
Figure A.3 – Numerical results for the model shown in Figure A.2 . (a) and (b) show the singular potential estimated numerically using the TBEM and analytically using a flat-earth solution, respectively. (c) and (d) show the corresponding finite-element solutions for the total potential V.

The singular potential computed with the TBEM is displayed in Figure A.3a. For comparison, the analytical halfspace solution is plotted in Figure A.3b. The boundary condition at the surface requires the contour lines to be perpendicular to the topography, which is obviously only the case in Figure A.3a. The total potentials computed using the singular potentials of Figures A.3a and A.3b are shown in Figures A.3c and A.3d, respectively. The errors in the singular potential field in Figure A.3b propagate through to the total potential field, thus polluting the solution (Figure A.3d). In contrast, the new singularity removal scheme yields physically reasonable results (Figure A.3c); again,

the contour lines should be perpendicular to the topography.

A.5   Conclusions

We have introduced a novel singularity removal approach based on the Trefftz boundary-element method. It allows the singularity removal, which has become an indispensable tool for geoelectric forward solvers, to be used even in the presence of pronounced topography. Because the solution is a function series, the method can be incorporated easily into existing finite-element codes. Its high accuracy stems from the fact that the topographic surface is modeled as an infinitely extended surface over an unbounded domain. Clearly, the construction of such a model with comparable accuracy using a finite-element mesh would be a very demanding and time-consuming task.

Appendix B

Advances in 3d geoelectric forward solver

Mark Blome, Hansruedi Maurer

4th International Symposium on Three-Dimensional Electromagnetics
Freiberg, Germany, September 27–30, 2007

B.1 Summary

The introduction of multi-electrode data acquisition systems during the 1980's and 1990's has significantly improved the acquisition speed of geoelectrical surveying, such that relatively large 3-D data sets can now be collected with moderate field effort. However, despite the seemingly ever increasing power of computers, full 3-D geoelectrical data inversions remain challenging and time-consuming tasks. We present technical advances in solving the 3D geolectrical forward problem, which is the computationally most expensive part of the inversion process. Major problems are typically caused by (i) singularities near the source electrodes and (ii) truncation of the computational domain at the model boundaries. Traditional approaches to overcoming these problems require model discretizations with a large number of grid points. To deal more efficiently with the source electrode singularities, we employ a novel singularity removal scheme based on a fast multipole boundary element method, and to cope with inaccuracies due to the limited computational domain, we use infinite elements. Extensive tests of our new

forward solver demonstrate that a high degree of accuracy can be achieved with modest computational grids.

B.2 Introduction

During the past decades much effort has been put into the development of numerical solutions of the 3D geoelectrical forward problem. Most published solutions are based on the finite-difference method (Mufti, 1976; Dey and Morrison, 1979a) or the finite-element method (Coggon, 1971; Pridmore *et al.*, 1981). Our forward solver is based on the finite-element technique and uses unstructured tetrahedral meshes, thus allowing for the incorporation of complicated 3-D topographies and varying mesh densities.

B.3 Theory

B.3.1 Finite-element equations

The governing equation for the geoelectric forward problem is given by the Poisson equation

$$\nabla \cdot (\sigma \nabla U) = -I_0 \delta(r - r_s) \text{ in } \Omega, \tag{B.1}$$

which results from the equation of continuity for a current density I_0 injected at a source position r_s into a domain Ω with an arbitrary conductivity distribution σ. By applying appropriate boundary conditions at the surface (Γ_s) and at the computational boundaries in the earth (Γ_g),

$$\frac{\partial U}{\partial n} = 0 \text{ on } \Gamma_s, \qquad \frac{\partial U}{\partial n} + \nu U = 0 \text{ on } \Gamma_g \tag{B.2}$$

the electrical potential U at any position r in Ω can be determined using the finite-element method. A formulation of equation B.1 suitable for the finite element method can be obtained by applying Galerkins criterion and Green's first identity:

$$\int_\Omega \sigma \nabla U \cdot \nabla \omega d\Omega - \int_\Gamma \sigma \omega \frac{\partial U}{\partial n} d\Gamma = -\int_\Omega I_0 \delta(r - r_s) \omega d\Omega, \tag{B.3}$$

where ω represents the shape functions required to approximate U within a finite element (e.g. Kost (1994)). We discretize the computational domain by unstructured tetrahedral finite elements using linear or quadratic shape functions to yield a sparse linear system of equations that can be solved effectively with appropriate numerical methods.

B.3.2   Singularity removal

The solution of the geoelectric forward problem contains singularities at the source electrode positions due to the δ-function in equation B.1. Consequently, inaccuracies that occur close to the source electrode positions could severely distort the inversion process. An obvious strategy to handle these inaccuracies is to refine the mesh locally around the source electrode positions. Unfortunately, this greatly increases the number of unknowns in the forward problem, significantly increasing the computational costs. Lowry *et al.* (1989) presented a procedure to remove these singularities by separating the singular part of the solution (U^n) from the non-singular part (U^a): $U = U^a + U^n$.

To account for the singular part of the potential, an analytical homogeneous halfspace solution with σ_0 equal to the conductivity at the source electrode position, is usually employed. Moving the known singular potential field to the right side, equation B.1 leads to a modified Poisson equation

$$\nabla \cdot (\sigma(r)\nabla U^a) = -\nabla \cdot ((\sigma(r) - \sigma_0)\nabla U^n) \tag{B.4}$$

where the δ-function on the right side has vanished. The problem is reduced to determining only the non-singular potential field that results from the conductivity anomalies. This technique has been routinely applied to flat-earth models, but it is not applicable in the presence of pronounced topography. In this case, an analytical expression for the singular potential does not exist. It must be computed numerically. Among the available numerical methods, the boundary element method (BEM) is well suited for this purpose (see statements concerning equation B.6).
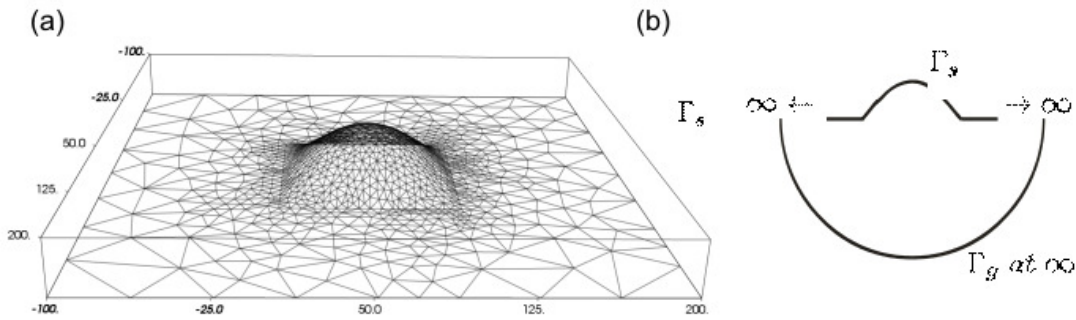
Figure B.1 – (a) A typical surface mesh used in the fast multipole BEM (b) The integration principle.

To derive the boundary integral equation, we use again Galerkin's criterion (Sauter and Schwab, 2004):

$$\int_\Omega \nabla \cdot (\sigma_0 \nabla U_h)\omega d\Omega = 0, \tag{B.5}$$

where U_h is the solution of the homogeneous Poisson equation (Laplace equation) and ω

is the corresponding Green's function. We solve for (U_h) under the modified boundary conditions and add the inhomogeneous part U_i (halfspace solution) afterwards to yield the total singular potential U_n. Applying Green's first identity twice yields the boundary integral equation

$$\int\limits_\Gamma \frac{\partial U_h}{\partial n}\omega d\Gamma - \int\limits_\Gamma U_h \frac{\partial \omega}{\partial n} d\Gamma + \frac{1}{2}U_h(r) = 0, \tag{B.6}$$

which does not contain volume integrals. Only the boundary of the domain Ω needs to be discretized, resulting in a substantial reduction of the number of unknowns in the equations to be solved. Furthermore, the absence of volume integrals permits the underground boundaries Γ_g to be moved to infinity (see Figure B.1 b). As U_h approaches 0 at infinity, the boundary integrals along Γ_g vanish. Along the surface boundary (Γ_s), the integration can be truncated after a limited distance from the source (i.e. where $\frac{\partial U_h}{\partial n}$ approaches 0) and thus only the inner part of Γ_s needs to be discretized. Figure B.1 (a) shows an example triangular mesh used for the BEM.

To evaluate rapidly the singular potentials, we employ a fast multipole BEM (FM-BEM) developed by Hackbusch and Nowak (1989) and implemented by Lage (1995). In addition to the standard advantages of the BEM, this implementation has almost the same beneficial scaling behavior of the computational costs as the FE and FD methods.

B.3.3   Open boundary handling via infinite elements
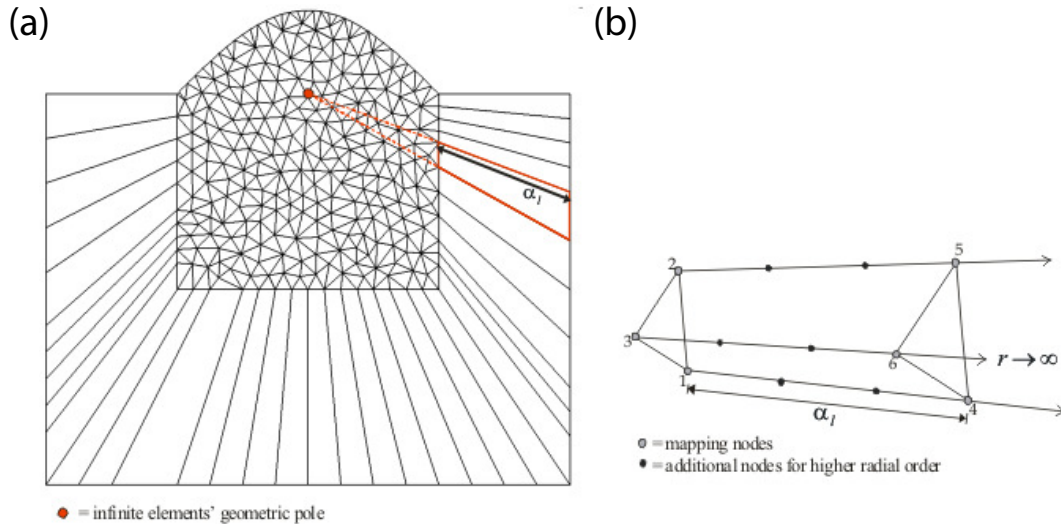
Figure B.2 – (a) Cross-section through a 3D FE mesh with infinite elements attached to the underground boundaries (b) Sketch of a sample infinite element.

When solving for the potential field unbounded domains occur in the geoelectric equations. Commonly, these unbounded domains are handled by "truncating" the computational domain sufficiently far from the injecting electrodes. Mixed type boundary condi-

tions in combination with decreasing mesh density towards the underground boundaries has proved to be efficient and reasonably accurate (Rücker *et al.*, 2006). Nevertheless, a significant fraction of the unknowns in the finite-element equations is only needed to assure the continuation of the potential field towards the underground boundaries. If these additional unknowns could be avoided, significant reductions of the overall computational costs could be achieved.

Infinite elements, originally developed in the field of acoustic radiation (Bettes, 1987), provide a cost-effective and elegant alternative to deal with open boundary problems. Instead of truncating the domain at certain distances away from the electrodes, a simple mapping technique allows the outer domain to be modeled by infinite elements that enable the integration to be carried out to infinity in radial directions. Infinite elements feature special shape functions that permit the potential to decay in radial direction:

$$\phi_j = 1/2 S_i(\xi, \eta)(1 - \nu) P_i^{(2,0)}(\nu), \tag{B.7}$$

where $P_i^{(2,0)}(\nu)$ are Jacobi polynomials, $S_i(\xi, \eta)$ are conventional linear shape functions defined in the plane perpendicular to the radial direction and ξ, η and ν are the local coordinates in the reference element. We employ Astley-Leys elements developed by Astley *et al.* (1998b). The infinite elements are attached to the boundary Γ_g of the FE mesh (see Figure B.2).

B.4   Numerical example
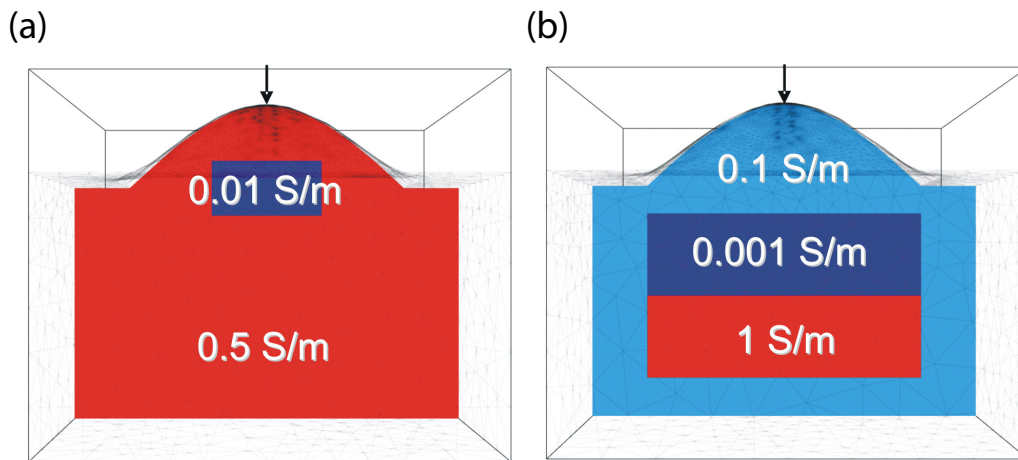
Figure B.3 – (a) Cuboid and (b) layered block models. The source electrode is located on top of the topographic relief as indicated by the black arrows.
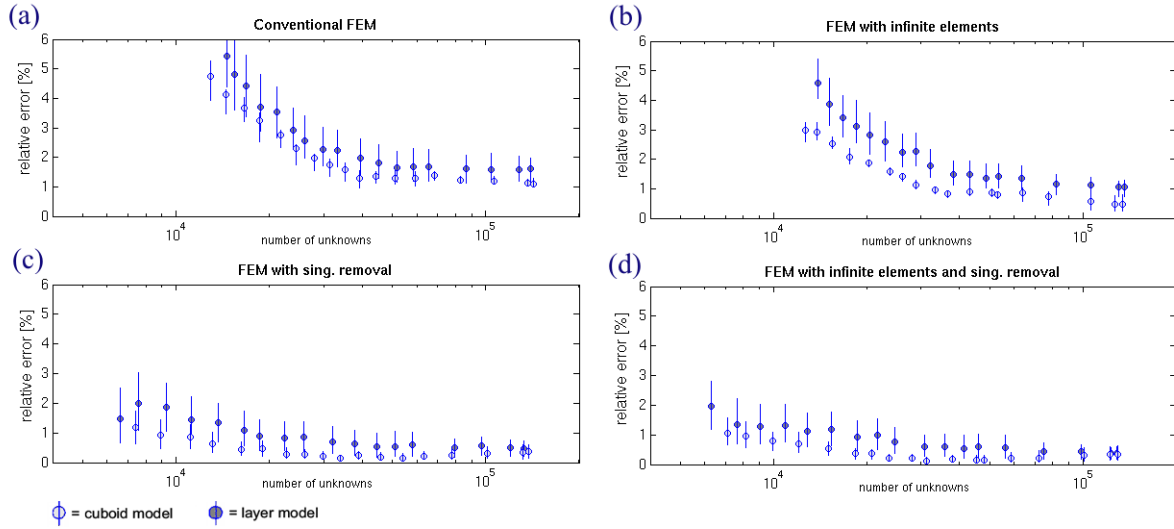
Figure B.4 – Median relative solution errors (in %) for a series of meshes with increasing number of unknowns. For (c) and (d), in which singularity removal has been applied, no local mesh refinement around the source electrodes was used, and for (b) and (d), in which infinite elements where used, the outer part of the mesh was not discretized.

Numerical simulations were carried out for 2 different conductivity models that include a cuboid-shaped anomaly or a stack of three layers (see Figure B.3). Both models are distinguished by substantial topography. For each model, we performed calculations on a series of meshes with an increasing number of unknowns. All calculations were compared to reference solutions that where obtained on extremely dense FE meshes equipped with second-order shape functions (each requiring more than 1 million unknowns). Figure B.4 shows the median errors relative to the reference solutions together with the 25 and 75 percentiles (error bars). All calculations where carried out using first-order shape functions. For the conventional FE calculations (Figure B.4 a), a mixed boundary condition was used, whereas for the FE calculations with singularity removal (Figure B.4 c), a dirichlet boundary condition was considered for the non-singular part of the potential.

For the calculations based on the conventional FEM (see Figure B.4 a), the solution for the coarsest mesh shows a median relative error of $\approx 4.7\%$ and $\approx 5.5\%$ for the cuboid and layered models, respectively; with an increasing number of unknowns the relative error decreases until it reaches a more-or-less stable value of $\approx 1.2 - 1.6\%$ for $\approx 83000 - 86000$ unknowns. The error plot for the FE calculations with infinite elements (Figure B.4 b) shows quite similar characteristics, but in this case the $1.2 - 1.6\%$ relative errors are achieved with a much smaller number of unknowns (i.e. $\approx 29000 - 38000$).

The performance of the forward solver is increased substantially when the singularity removal is activated (Figure B.4 c). For the cuboid model a relative error of $< 1.2\%$ is reached with ≈ 7400 unknowns whereas for the layer model a relative error of $< 1.6\%$ is reached with ≈ 11000 unknowns. Finally, by estimating the singular potentials with

the FM-BEM and applying the infinite elements to calculate the non-singular potential part, we gain a further, rather slight increase in the overall solution accuracy (Figure B.4 d).

B.5   Conclusion

Application of BEM-based singularity removal and infinite elements improves the efficiency of 3D geoelectrical forward modeling substantially. This is primarily due to the fact that both techniques produce accurate solutions with a relatively small number of unknowns. This is particularly important, because the computation time required for solving the finite-element equations scales roughly with the square of the number of unknowns.

If the number of unknowns can be kept reasonably low, direct matrix solvers become a very attractive option for solving the finite-element equations. Once the finite-element system matrix is decomposed, the solutions for a multitude of electrode positions can be obtained by simple back substitutions. This will further boost the performance of our forward solver.

Appendix C

ETH-DCMES-II

C.1 Field Set-Up

The following components are required to operate the *ETH-DCMES-II* during a field survey:

ETH-DCMES-II

- Interface box (RS-232 cable, power cable, Y-cable for 2 batteries, 2 x 12V batteries)
- Current source (link adapter to interface box, power connector to battery, USB-cable, 1 x 12V battery)
- N DAUs (N four wire cables, spare DAUs, 2 magnets)
- N metal stakes (2 hammers)
- Field notebook (with Matlab, *EconSeries* device driver, *ETH-DCMES-II* device driver and GeoLog GUI installed)
- Toolbox

Remote source (optional)

- 3-5 remote cables (200m length each)
- 2 metal stakes
- cable connector for remote source DAU
- warning plate and road bridges

Battery charging

- Extension power cord

- Power supply unit (60V/10A output capability)

- 4 x 12V truck batteries (if main supplies are not available)

- Connecting cable (IFB to power supply)

Previous to any field survey it should be ensured that the internal batteries of all DAUs that are to be deployed in the field have been charged and that all DAUs are working properly. Additionally, a few spare DAUs ready for operation should be prepared.

The electrodes (metal stakes) should be placed across the area of interest in such a way that groups of up to 31 DAUs can be formed and connected to one of the four field data bus channels of the interface-box. The electrodes should be placed at equidistant spacing in the X- and Y-directions. The maximum possible spacing is limited by the length of the four-wire cables (5m) used to interconnect the DAUs. Usually, the DAUs are pre-configured (i.e. daisy-chained to the four-wire cables) and packed into boxes each containing 11 or 12 DAUs. Thereby, they can easily be deployed in the field. When attaching the DAUs to the metal stakes, it is important to make sure that the DAUs are properly clipped onto the stakes. Otherwise a poor contact between the DAUs and the metal stakes may result. In the worst case, this might not be detected during contact resistance measurements resulting in poor quality voltage signals. The first DAU in each of the four chains needs to be connected to one of the four field bus channel sockets on the interface-box (denoted *X10* to *X13*).

Two 12V batteries connected in parallel are required to power the interface-box via its power supply socket (*X1*). After power-supply is established, the LCD display on the interface-box should either display the input voltage or the current drawn by the connected DAUs (depending on the setting of the display switch). The field computer needs to be connected to the interface-box by a RS-232 serial link cable. It is important to firmly screw-in the RS-232 cable to both the field computer and the interface-box. A loose RS-232 cable connection might lead to problems during the communication to the DAUs.

The current source must be connected by a four-wire cable to the IFB's *X2* jack. It requires a 12V DC power supply, by a single 12V battery pack. A universal serial bus (USB) cable is used to control the current source with the field computer. The current source should only be switched on shortly before the data acquisition starts due to its relatively large power consumption even without any signal output. At this stage, the field computer should be started up and the GeoLog measurement software should be launched and configured as described in the following.

C.2 The GeoLog Software - Users Manual

Recoding 3*D* geoelectric data sets with the highly flexible *ETH-DCMES-II* data acquisition system requires a sophisticated measurement software. Within the framework of this thesis such a measurement software has been developed with the aim of automating the acquisition of geoelectric data sets without limiting the versatility of the *ETH-DCMES-II*. The measurement software allows conventional and parallel bipole-bipole, pole-bipole and pole-pole data sets to be recorded, where either full waveforms are transferred back to the field laptop or only a few numbers characterizing the recorded waveforms. Arbitrary source waveforms can be injected and corresponding data analysis software modules can be uploaded to the individual DAUs. For 3*D* data acquisitions, a roll-along strategy has been implemented.

The software comprises two main building blocks: (i) The DCMES-II device driver, that handles all low-level communication to the DAUs and the current source, and (ii) the graphical user interface, that is used to setup all necessary parameters for a field survey, to automate and supervise the measurement process and to handle the acquired data. Both components have been developed with the following main objectives in mind:

Fast data acquisition The measurement software and especially the device driver is geared towards fast data acquisitions in parallel measurement mode. This is mainly achieved by (i) minimizing idle cycles during communication to/from the data loggers and (ii) distributing the data pre-processing to the individual data loggers.

Data safety The graphical user interface is designed such that recorded data is saved immediately after it is received from the individual DAUs. Additionally, the DAUs diagnostics (battery status, operation readiness, etc.) and all the user-applied settings (measurement parameters, electrode deployment configurations) are saved automatically. In case of abrupt interruption of the software (e.g. due to a malfunction of the field notebook), the measurement software can be restarted to continue the measurement where it was interrupted. At most the very last measurement configuration needs to be repeated.

Data control The measurement software allows the recorded measurements including full waveforms (in case they were recorded) to be inspected while the software continues acquiring data. This way, possible issues (e.g. regarding the electromagnetic noise conditions, too low injecting currents or inappropriate gain settings, can be identified in an early stage during the field campaign.

Robustness against DAU breakdown Especially during long field surveys, it may happen that one or several data loggers are experiencing problems e.g. due to a too low battery voltage. Affected data loggers can easily be excluded from the

measurements or exchanged by available spare data loggers without the need of re-acquiring already obtained measurements.

3D data acquisition The measurement software allows the definition of 3D roll-along recording strategies. In each step of the roll-along procedure, the actual positions of the DAUs are displayed in the graphical user interface to ensure smooth field operations during the survey.
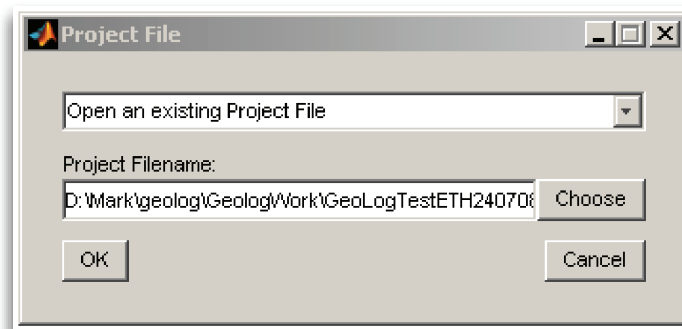
Measurement Setup

Figure C.1 – Initial start-up window of the GeoLog software. The user is asked to either create a new project or load-in a project that was previously created.
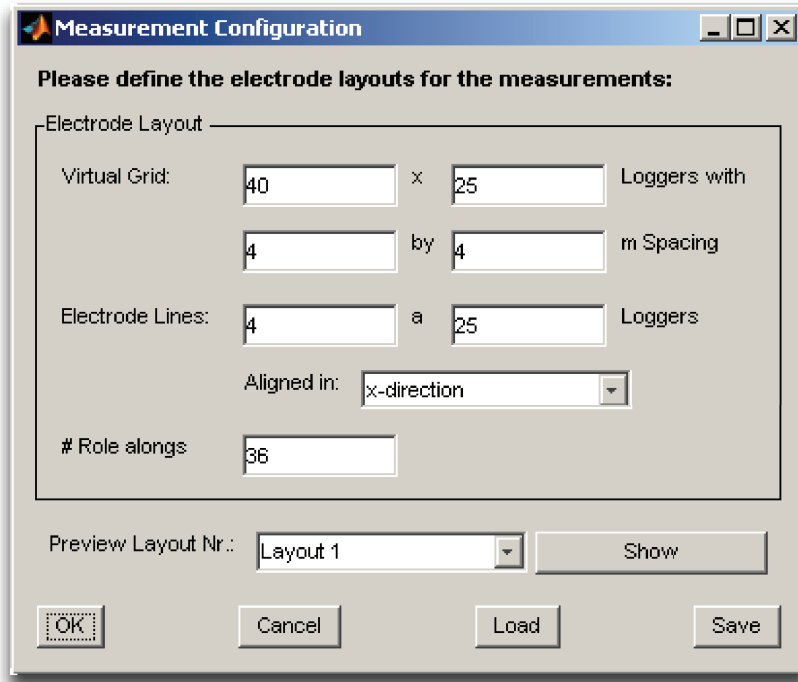
Once the measurement program has been started in Matlab by

```
addpath ( genpath ( '~/ subversion / geolog / GeologGui ' ) ) ;
MeasGui ;
```

the user is requested to either create a new measurement project or load-in a project that was previously generated (Figure C.1). Note that all files related to a certain measurement project (acquired data, applied measurement configurations, diagnostics of the DAUs, etc) are stored within a single folder.

Creating a new measurement project requires the user to enter all parameters describing the electrode deployments that are used during the field campaign (Figure C.2). For that purpose, a virtual grid of electrodes, on which the $3D$ roll-along steps are carried out, needs to be specified. The software also supports acquisition of conventional measurements on $2D$ electrode deployments. In that case, a single electrode line needs to be specified and the number of roll-along steps must be set to one. Electrode deployments, referred to as "Layouts" in the software, can be previewed with the "Show" button.

Clicking "OK" will bring up the device driver dialogue (Figure C.3), that allows initialization of the communication between the field notebook and the *ETH-DCMES-II*'s
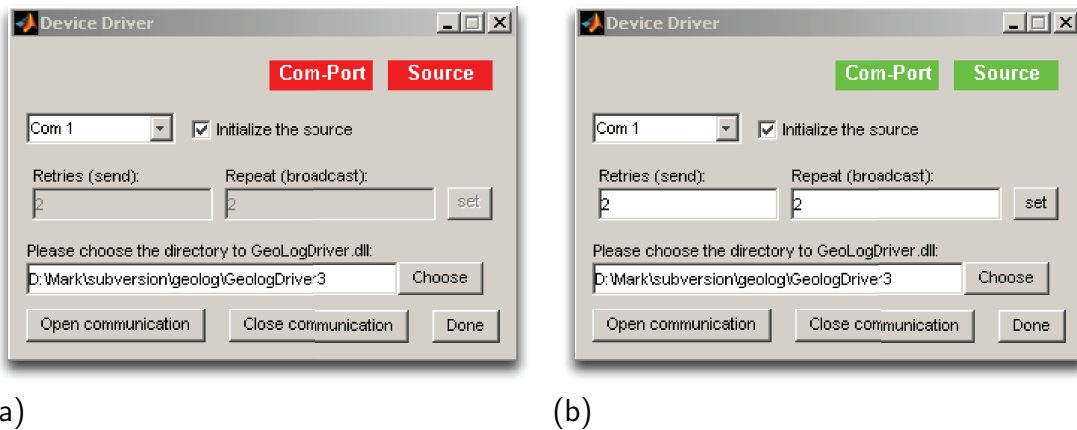
Figure C.2 – Parameters required for 3*D* roll-long schemes. A virtual grid of electrodes needs to be defined together with the number of roll-along steps employed in the *Y*- or *X*-directions. For conventional 2*D* electrode layouts (i.e. geoelectrical profiling), a single electrode line with the number of roll-along steps set to one needs to be specified.

(a)   (b)

Figure C.3 – (a) Device driver dialogue. The folder containing the *ETH-DCMES-II* device driver (GeoLogDriver.dll) needs to be specified. Subsequently, after the current source and the Interface Box are attached to the field notebook, communication to the *ETH-DCMES-II* can be initiated with the "Open communication" button (b).

current source and interface-box. The corresponding low-level functionalities are implemented in a C++ device driver (files "GeoLogDriver.dll" and "GeoLogDriver2.h"). After the folder containing the driver files has been specified and both the interface-box and the current source have been connected properly to the field notebook, communications with the *ETH-DCMES-II* can be initialized by pressing the "Open communication" button. A successful initialization of communications with the current source and the

interface-box, respectively, is indicated by the corresponding text-fields turning green (Figure C.3).

Subsequently, the number of retries for commands to any of the DAUs can be specified. The default number is two, meaning that if a DAU does not respond within 100ms or if it was unable to interpret a command (e.g. due to electromagnetic noise along the communication wire), the corresponding command is resent at most two times before an error is returned by the device driver. This setting does not apply to broadcast commands (sent to all DAUs), to which DAUs never respond. To ensure a reliable field operation, certain broadcast commands necessary to set-up and start parallel measurements, will automatically be repeated n times as specified in the text-field labelled "Repeat (broadcast)". The device driver dialogue can be brought up any time later from within the software's main window.
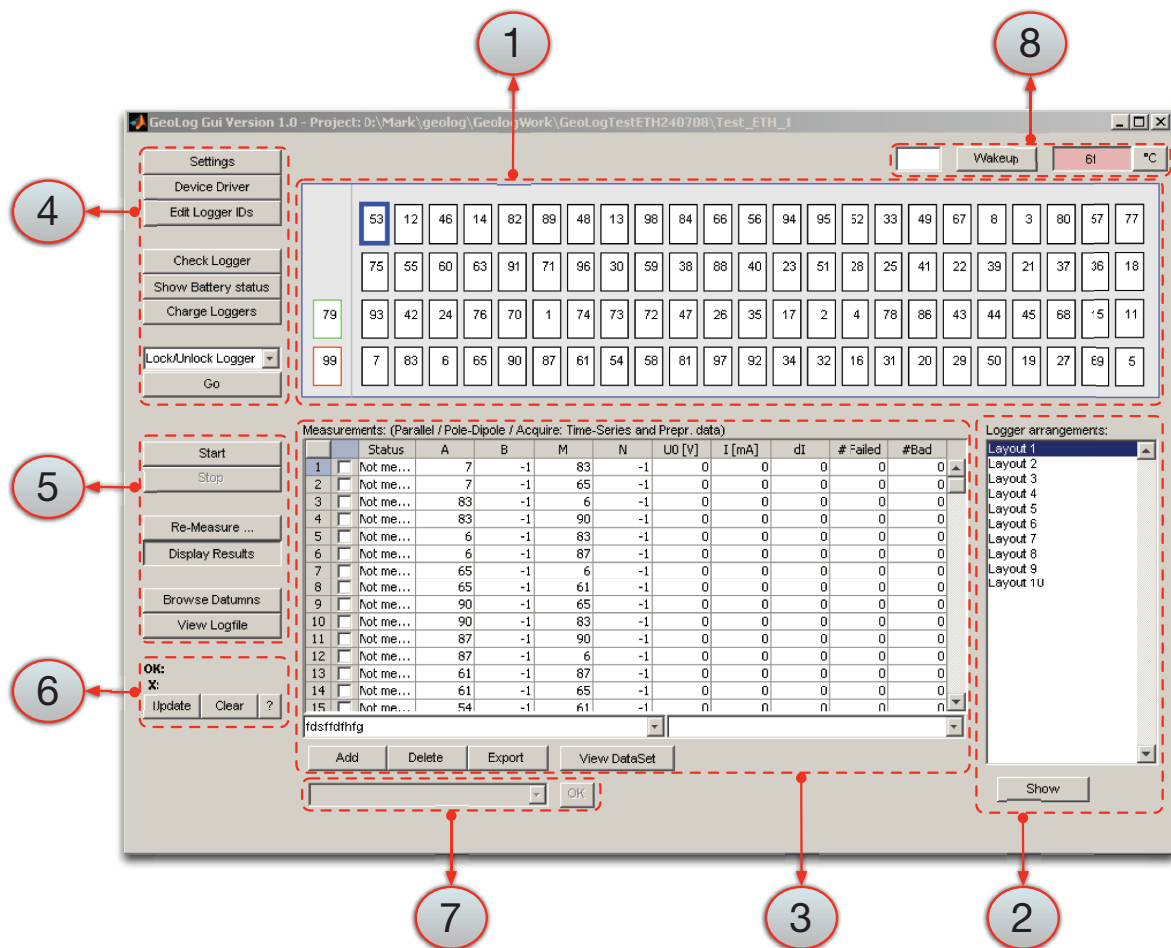
Figure C.4 – Main panel of the GeoLog software. It allows the definition, acquisition and inspection of geoelectric data sets defined on any of the specified electrode deployments.

Closing the device driver dialogue with the button "Done" will bring up the main window of the GeoLog software (C.4). The window is separated in several functional groups as indicated by the numbers in figure (C.4). It allows the definition, acquisition

and visual inspection of geoelectric data sets on any of the defined electrode deployments.

The logger display panel at the top of the measurement window (1) reflects the positions of the DAUs (as they are placed in the field) for any of the electrode deployments used. On the left side in the logger display panel the DAU responsible for logging the injected source current (usually DAU number 99, which is located inside the interface-box) is shown. Furthermore IDs of the remote source and remote reference DAUs (in case they are employed) are displayed. DAUs in the logger display can be selected e.g. to obtain information about their diagnostic parameters (battery status, internal temperature, current consumption), to upload customized data analysis software modules or to exclude them from future measurements (in case they are experiencing problems).

The "Logger arrangements" panel (2) on the right side allows switching the measurement display to one of the defined electrode deployments (this is also possible while the software is acquiring data). The logger display (1) will update to reflect the actual arrangement of the DAUs and the data table (3) will show one of the data sets defined on the selected layout. An arbitrary number of data sets can be defined for each of the logger arrangements. Typically, during a field campaign, a contact resistance measurement and optionally a few full waveform recordings are conducted on each of the electrode deployments in addition to the data set that is used in the employed measurement strategy. The left pull-down menu below the data table selects the different data sets and the right pull-down menu shows detailed status messages (e.g. error messages) for the measurement currently selected in the data table. Deselecting the checkbox-field in the first column of the data table marks the corresponding measurement to be re-measured. All measurements selected in such a way will be repeated automatically the next time a measurement is started. Before data can be acquired with the *ETH-DCMES-II*, certain acquisition parameters must be defined ("Settings", (4)), the IDs of the DAUs employed in the field need to be entered ("Edit Logger IDs", (4)) and the operation readiness of all DAUs needs to be checked ("Check Loggers", (4)). Subsequently, a variety of data sets that are to be acquired can be defined ("Add", (3)). The individual steps required are described in the following.

Entering IDs of the DAUs employed

Figure C.5 shows the panel used to enter the IDs of the DAUs in the order as they are placed in the field. Optionally, the source logger's ID (which is 99 by default) can be changed. For pole-bipole acquisitions, a remote source DAU needs to be employed. The corresponding ID must be entered in the text-field labelled "Remote source logger". Similarly, in case pole-pole data sets are to be acquired, the ID of a remote reference logger needs to be entered. Occasionally, it might be necessary to exclude certain DAUs from the measurements (e.g. due to a breakdown or due to obstacles in the field).

Figure C.5 – Graphical user interface that allows the IDs off all DAUs employed in the field to be entered. Optionally, remote source and remote reference DAU IDs can be provided.

This can be achieved by selecting a DAU in the logger display panel and subsequently pressing the button "Lock/unlock logger". Pressing the button "Scan for Loggers" will automatically scan for DAUs connected to the *ETH-DCMES-II* with IDs in the range of $1 - 100$. The ID table will subsequently be filled with the IDs of all detected DAUs. This option may be convenient for lab experiments or to charge the DAUs in the field.

Acquisition parameters

Previous to any data acquisitions, certain acquisition parameters need to be defined. Figure C.6 shows the dialogue box used to enter these parameters:

Source Settings

- **Amplitude [V]:** Source waveform amplitude. Selecting "automatic" will estimate the voltage amplitude automatically previous to each data acquisition based on a given target current strength.
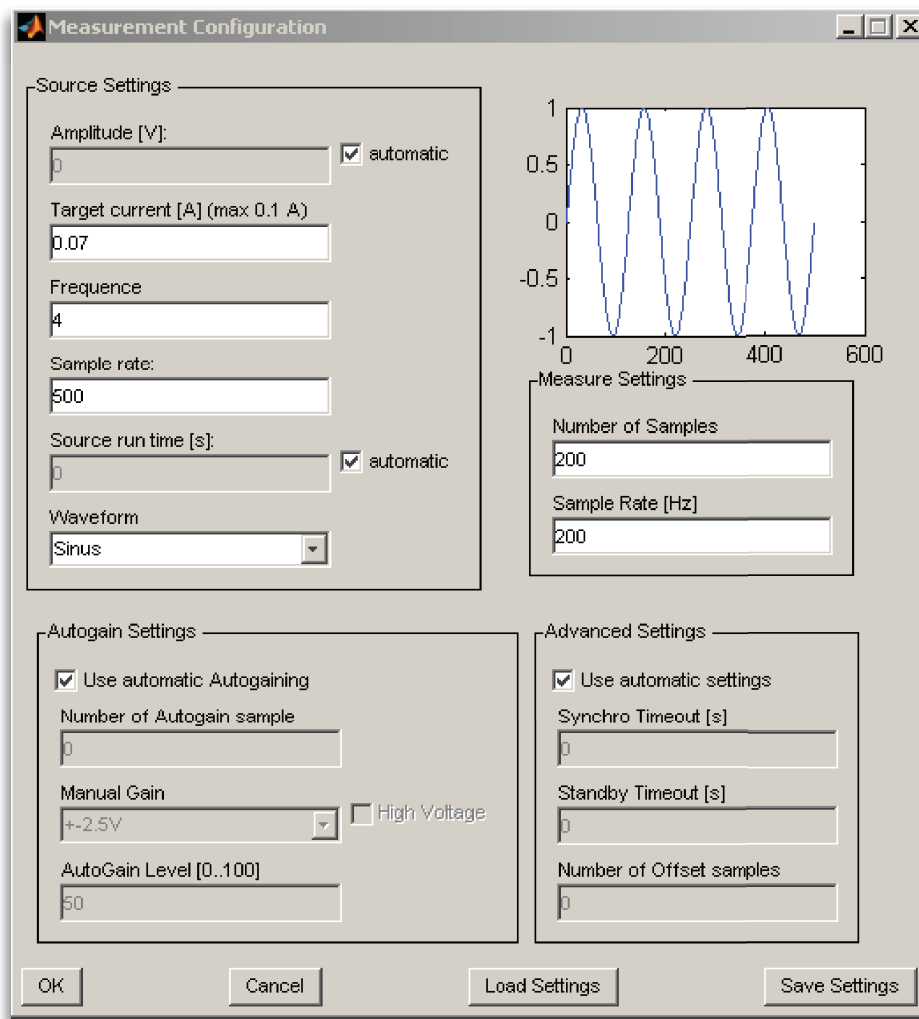
Figure C.6 – Acquisition parameter dialog box. Usually, it is sufficient to specify settings describing the source waveform and defining the number of samples to be acquired by the DAUs. "Autogain Settings" and "Advanced settings" should be left unchanged in most cases.

- **Frequence:** Source signal frequency in [Hz]

- **Sample rate:** Source signal sampling rate (between 30Hz and 50KHz), usually about 500Hz.

- **Source run time:** Defines the length of the source waveform in seconds. In most cases the "automatic" option should be used for which the length of the source waveform is automatically adjusted to the number of samples recorded by the DAUs.

- **Waveform:** Either sinusoidal, rectangular or linearly swept frequency chirp source waveforms can be used. Note that the software module currently deployed on the DAUs only supports analysis of sinusoidal and rectangular source waveforms.

Measure Settings

- **Number of Samples:** Number of samples to be acquired by the DAUs (e.g. 200).

- **Sample Rate [Hz]:** Samples per second to be taken by the DAUs (e.g. 100).

Autogain Settings These settings should only be changed in some rare cases – autogain is used by default.

- **Number of Autogain Samples:** Number of samples to be taken for automatic gain adjustment on the DAUs.

- **Manual Gain:** In most cases automatic gain selection is recommended. However, in certain cases (e.g. for passive ambient noise recordings), it might be necessary to specify the gain manually.

- **AutoGain Level [0..100]:** Maximum gain to be used (the default value is 50%)

Advanced Settings These settings should always be left unchanged ("Use automatic settings"). However, in some rare cases it might be necessary do adjust these settings.

- **Synchro Timeout [s]:** Time in seconds for the DAUs to wait after they have been configured for a measurement before the measurement is actually initiated.

- **Standby Timeout [s]:** Time in seconds the DAUs will wait after a measurement is finished before returning to standby mode. Note that the acquired data (and optionally pre-processing results) need to be transferred back to the operating computer before this time-out runs out. Otherwise previously acquired measurements will be lost.

- **Number of Offset Samples:** Number of samples to be acquired by the individual DAUs before the actual measurement starts (these samples will not be recorded).

Checking the operation readiness of the DAUs

To assure that all employed DAUs are ready to acquire data, their operation readiness and internal battery condition need to be checked (button "Check Logger" in the main GeoLog window). Figure C.7 shows the panel used for this purpose. A wakeup-signal should be sent to all DAUs in a first step to make sure that all DAUs are listening for commands from the field computer (button "Logger Wakeup"). Pressing "check All" will require all DAUs to return information about their diagnostics. All DAUs that do not respond within a certain time (usually 200ms) will be listed in the table as "not responding". Furthermore, an error message will appear for all DAUs for which (i) the internal application is not running or is not ready and (ii) the internal battery voltage is too low. In the first case, re-uploading the DAUs application should solve the problem
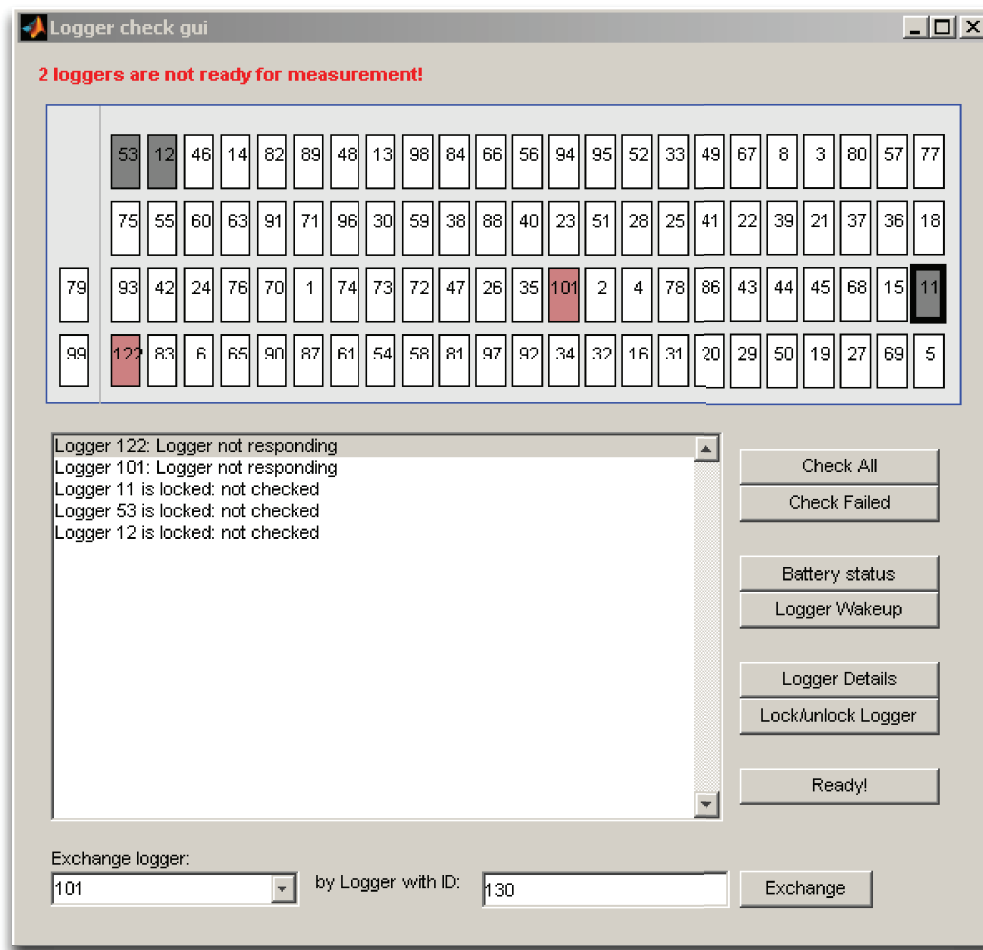
Figure C.7 – User interface that allows the operation readiness of all employed DAUs to be checked conveniently.

whereas in the latter case the DAU should be replaced. There are several possible reasons for a DAU to not respond to commands from the field computer:

- Too low battery voltage

- The DAU might be in standby mode. Usually, the wakeup-signal should bring the DAU in receiving mode. In case of doubt, it may help to wakeup the DAU manually by placing a strong magnet close to the front of its casing (the DAUs electronics board includes a magnet switch). If successful, the DAUs LED will blink upon start-up to display the DAU's internal battery voltage.

- The DAU might not be connected properly to the data bus cable.

- The cable connection to the DAU might be damaged. In this case all DAUs attached to the data bus after the DAU that is not responding are usually not responding as well.

• The RS-485 communication chip or any other part of the DAU might be damaged.

The button "Battery status" will illustrate the battery status of all DAUs graphically in the logger display panel. If DAUs that are experiencing problems are exchanged then the corresponding IDs need to be updated. This can be done in the lowermost part of the panel. Alternatively, DAUs can be locked (i.e. excluded from all future measurements) by selecting them in the logger display panel and clicking "Lock/unlock Logger".

Defining data sets
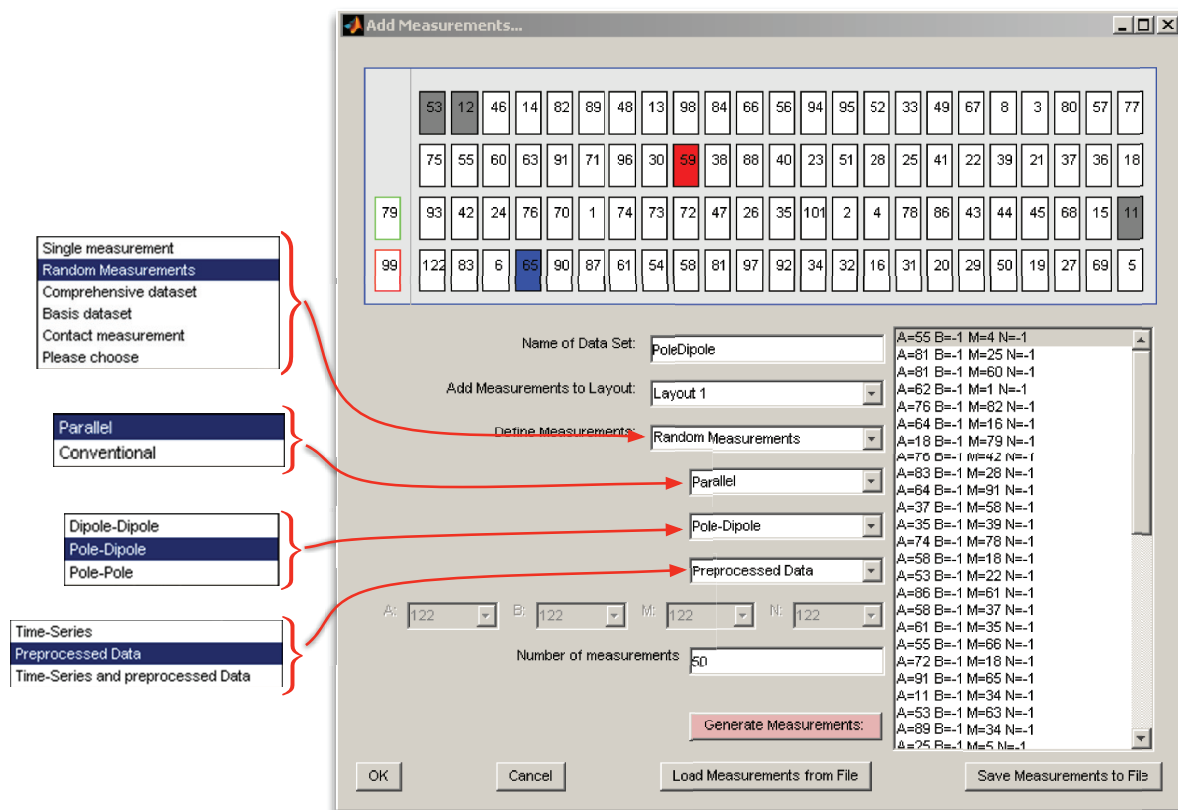
Figure C.8 – Panel that allows sets of electrode configurations be added to the measurement project. Arbitrary pole-pole, pole-bipole and bipole-bipole parallel or sequential data sets can be defined.

Selecting "add" in the main panel of the GeoLog software (Figure C.4, number (3)) allows a data set that should be acquired to be added to the measurement project (Figure C.8). Please note that data sets are always added only to the currently selected logger layout ("Logger arrangements" panel, (2) in Figure C.4). The GeoLog software allows pole-pole, pole-bipole and bipole-bipole parallel or sequential data sets to be acquired. In each case, either the full waveform or only the results of waveform pre-processing on the DAUs can be transferred back to the central computer. After selecting the appropriate settings, pressing the button "Generate Measurements" will generate the

requested measurement configurations. They can be previewed simply by clicking on the individual entries in the list; the logger display panel will highlight the corresponding DAUs to visualize the configuration.

Before adding the generated data set to the measurement project by clicking "OK", a valid data set name needs to be entered in the text-field labelled "Name of Data Set". Note that the filename where the recorded data will later be saved to is defined by the project name, the layout on which the data is recorded and the name the data set is given. These filenames have the following form:

'<project name>/<data set name>_<Layoutnumber>.mat'.

It is also possible to add the selected data set on all electrode layouts at the same time. This is convenient for roll-along strategies where typically the same data set is acquired on all electrode deployments. Note that when adding a contact resistance measurement, the user is asked whether he would like to test the contact resistances for all electrode locations or only for the ones that where actually moved from the last to the current electrode deployment. Support for arbitrary data sets can be added to the panel displayed in Figure C.8 by modifying the Matlab functions "GLAddMeasurements()" and "GLGenMeasSet()" appropriately.

Data acquisition

Once all necessary configurations are done and all DAUs are ready to acquire data, acquisition of the selected data set can be started by clicking "Start" in the main window of the GeoLog software ((5) in Figure C.4). The software will issue a wakeup signal, check all DAUs and then sequentially acquire data for all the measurement configurations listed in the data table.

Figure C.9 shows a measurement in progress. The logger display panel (1) displays graphically the configurations that are currently being acquired. DAUs that returned data with a too low signal-to-noise ratio during a measurement will be highlighted in yellow. Detailed error messages for potentially arising problems during the data acquisition are displayed in the popup-box below the data table (3). Full waveforms or preprocessed data received from the DAUs can be viewed during the measurement process by activating the "View DataSet" button (4). The progress bar in the bottom of the window will show the estimated remaining time until the data acquisition is finished.

Data quality control

Once the acquisition of a data set is finished and the acquisition of the data set to be acquired next has been initiated, it is recommended to visually check the quality of the recorded data. Thereby problems with any of the DAUs or too low data quality can be
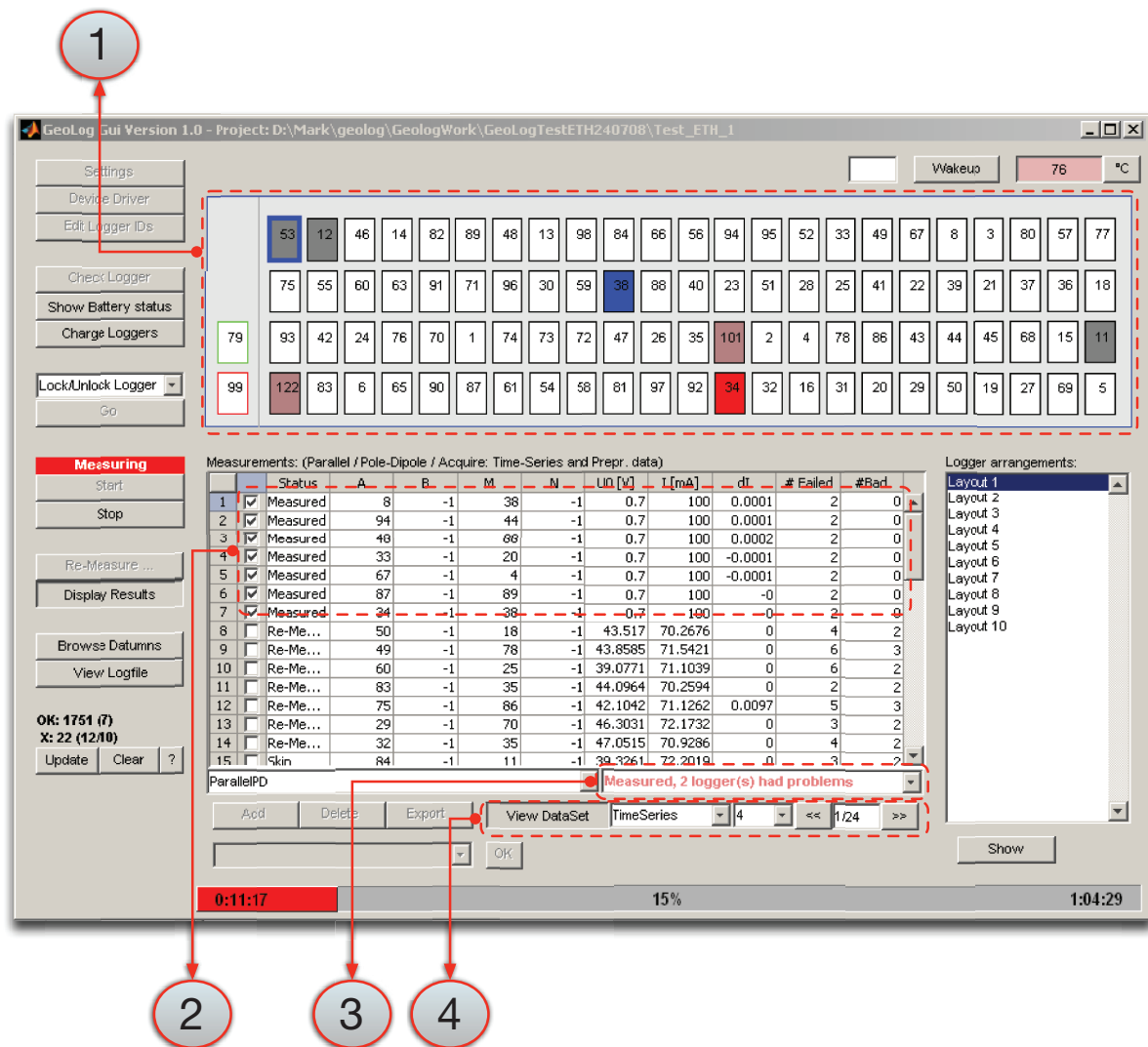
Figure C.9 – Main window of the GeoLog software currently acquiring a data set. The software shows all necessary information required to supervise the measurement process. Data sets can be inspected visually while the data acquisition is running.

detected at an early stage during the field campaign and appropriate counter-measures can be taken.

Clicking the button "Browse Data" in the main window of the GeoLog software will bring up a graphical user interface (Figure C.10) that allows visual inspection of the acquired data. Recorded potential differences, apparent resistivities, data quality parameters (among others) can be displayed in a map-style fashion on top of the positions of the DAUs or in the form of histogram and line plots (see Figure C.10). Clicking the "<<" and ">>" buttons on the left side of the GUI allows scrolling through the individual parallel scans. Information for all measurements belonging to a single parallel scan are displayed in the data table. The displayed data set can be filtered (e.g. by the geometry factor) or sorted as necessary.
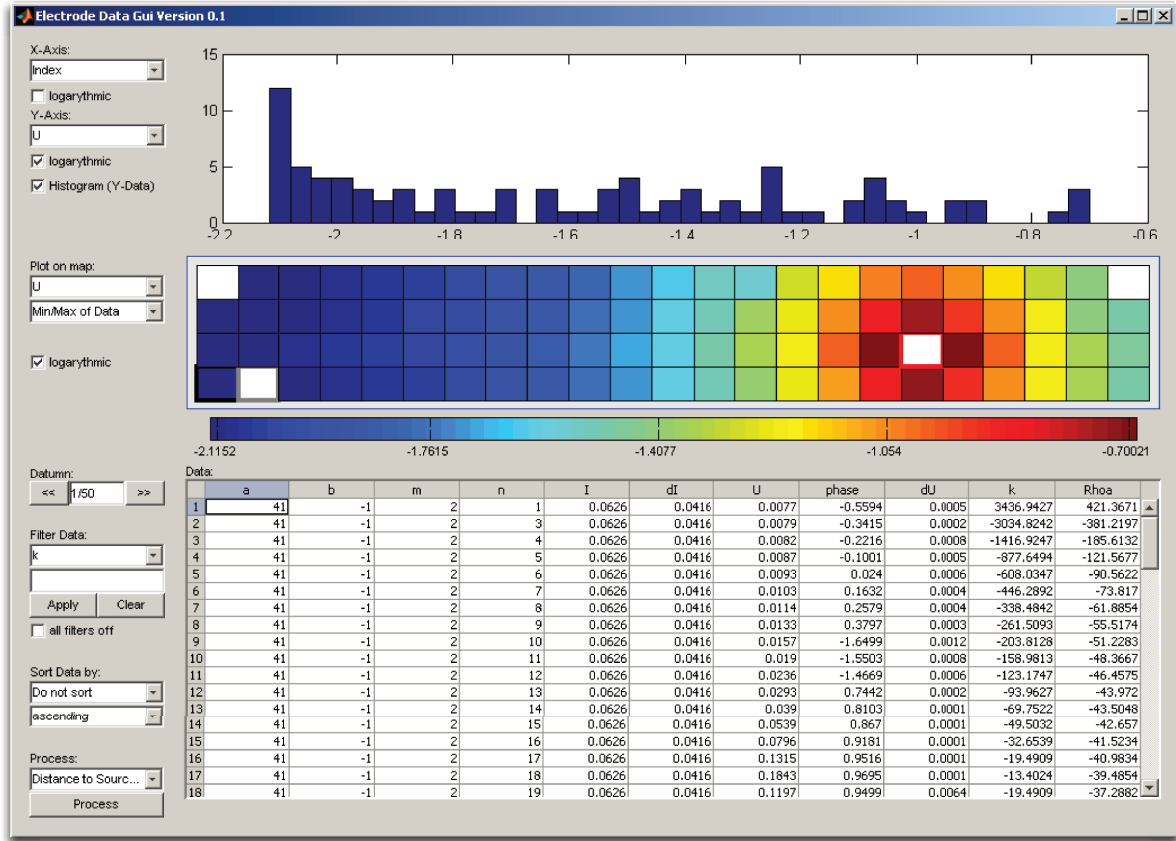
Figure C.10 – Visual inspection of the acquired data. Recorded potential amplitudes, apparent resistivities, data quality parameters (among others) can be plotted on top of the positions of the DAUs to detect possible issues with any of the DAUs in an early stage of the field campaign.

Exporting acquired data sets

Geoelectric data sets recorded with the GeoLog data acquisition software are stored in Matlab binary files. Besides the full potential waveforms (in case they were recorded) these files contain additional information including the IDs of the DAUs, data about the ambient noise characteristics (as returned by the individual DAUs), error codes and internal book-keeping data required by the GeoLog software. An export GUI (Figure C.11) is used to process and export these data sets to a format suitable for geoelectric data inversions.

The export panel allows the user to select the data sets (recorded on the individual electrode deployments) that should be processed and combined to a single data set during the export process. Note that contact resistance data sets and data sets for which only the full waveforms have been recorded cannot be exported. For each of the individual data sets, a filter can be defined to exclude measurements recorded by certain DAUs. Furthermore, all measurements can be excluded for which a certain DAU acted as reference electrode, current source or current sink. This option is useful for eliminating unreliable measurements recorded by DAUs that experienced technical problems during
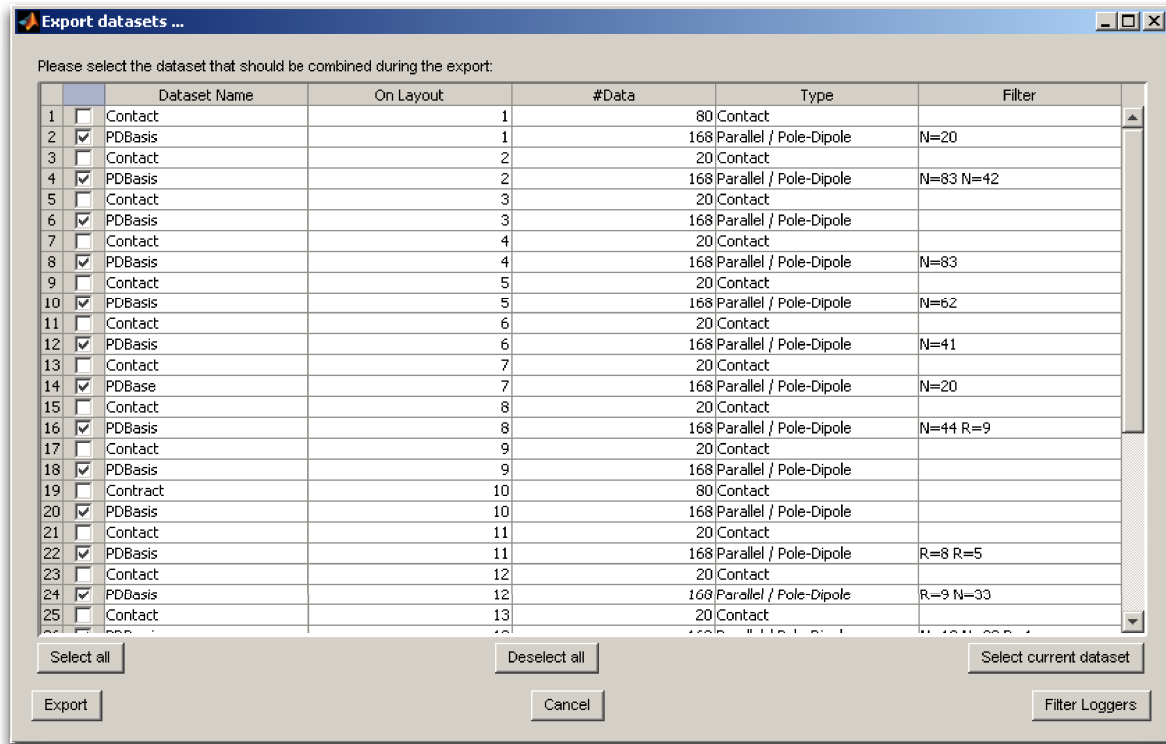
Figure C.11 – Data export dialog of the GeoLog measurement software. It allows all data sets recorded on the individual electrode deployments to be processed, combined to a single data file and exported in a format suitable for geoelectric data inversion.

the field survey.

The exported data set will be saved to a Matlab binary file and additionally to a clear-text file that can be loaded in Matlab by the function "readinv3dfile()" (for further processing) or opened with the Matlab GUI "EleDataGui()". The exported files are located in the project directory under the filenames:

'<project name>/<project name>[.mat/.txt]'.

Note that all data sets that have been processed during the data export are also saved (prior to combining them to a single data set) under the following filenames:

'<project name>/<data set name>_<Layoutnumber>[.mat/.txt]'.

C.2.1 *ETH-DCMES-II* device driver

The GeoLog measurement software relies on functionalities implemented in a C++ device driver. The main building blocks of the device driver, that handles all low-level communications to the *ETH-DCMES-II*, are illustrated in Figure C.12. It consists of the following components:

Source Driver The source driver controls the data acquisition board employed in the current source. It manages the digital–to–analogue-conversion of the current wave-
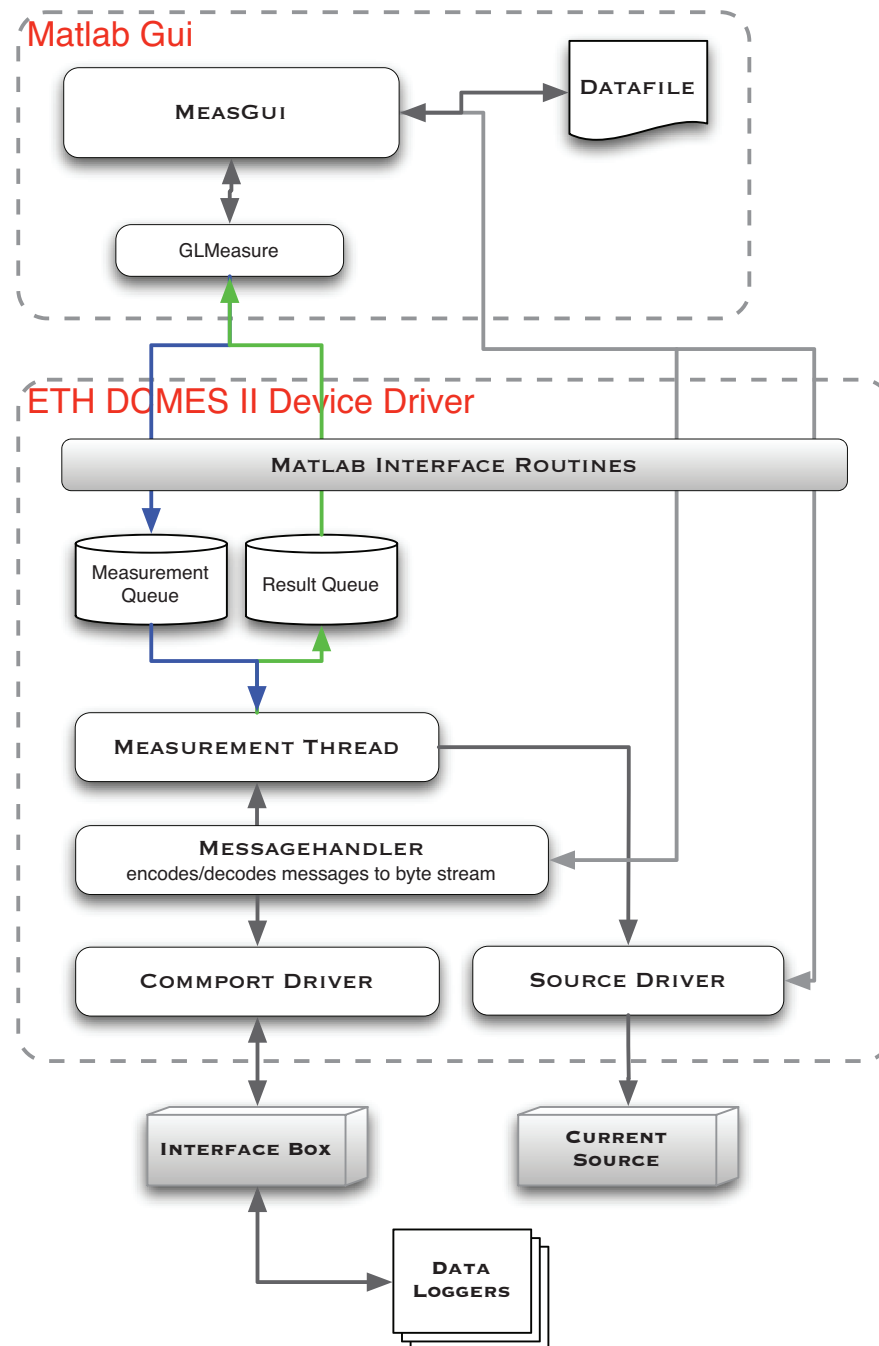
Figure C.12 – General structure of the GeoLog measurement software. The graphical user
  interface is implemented in Matlab whereas for performance and stability reasons all device-
  related functionality is implemented as a C++ device driver. The device driver allows
  measurements to be performed asynchronously without interfering with the Matlab GUI.

form generated in Matlab and it controls estimation of source signal voltage amplitudes. Furthermore, it monitors the temperature of the power amplifier located inside the source.

Com-port driver The Com-Port driver controls all low-level communications passing through the RS-232 serial link of the field computer, i.e. it handles byte streams send to or received from all DAUs connected to the field data bus.

Message handler All commands send to the DAUs are composed and subsequently transformed to byte streams by the message handler. Similarly, it decodes all messages received from the DAUs.

Measurement thread The measurement thread manages the acquisition of geoelectric data sets with the *ETH-DCMES-II*. All measurements are performed asynchronously in a separate thread to avoid interference with the GeoLog measurement software.

Virtual logger driver The C++ device driver can be compiled in a simulation mode in which an arbitrary number of DAUs are simulated by the "Virtual logger driver". In this way further developments or debugging of the GeoLog software can be performed without actually employing the *ETH-DCMES-II*. Synthetic potential readings (and full waveforms) are generated based on analytical homogenous half-space solutions.

Matlab interface routines All functionalities implemented in the C++ device driver are accessible from within Matlab through these interface routines.

C.3 Technical details of the *ETH-DCMES-II*

Technical details on the *ETH-DCMES-II* are documented in the following Figures. Figure C.13 shows the individual steps required to acquire parallel, (serial) four-point and contact resistance measurements with the *ETH-DCMES-II* and Figures C.14 to C.18 show electric curcuit diagrams of the Interfacebox and a data acquisition unit, respectively.
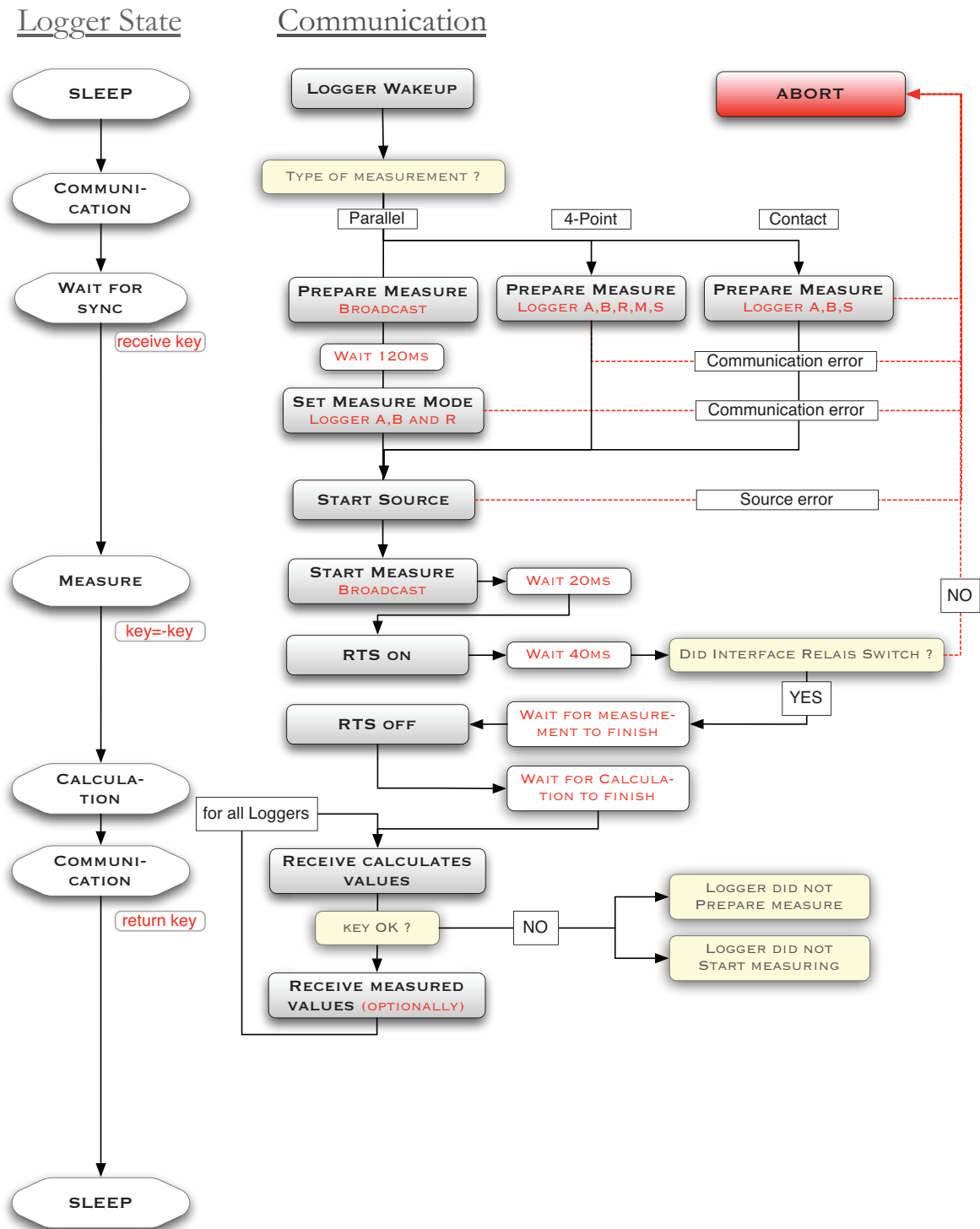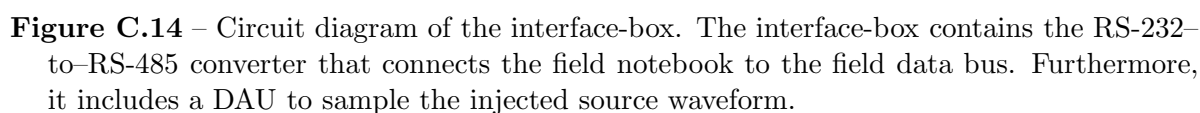
Figure C.13 – Flow diagram of the individual steps required to acquire parallel, (serial) four-point and contact resistance measurements with the *ETH-DCMES-II*. The left side shows the state of the DAUs during the individual steps performed.
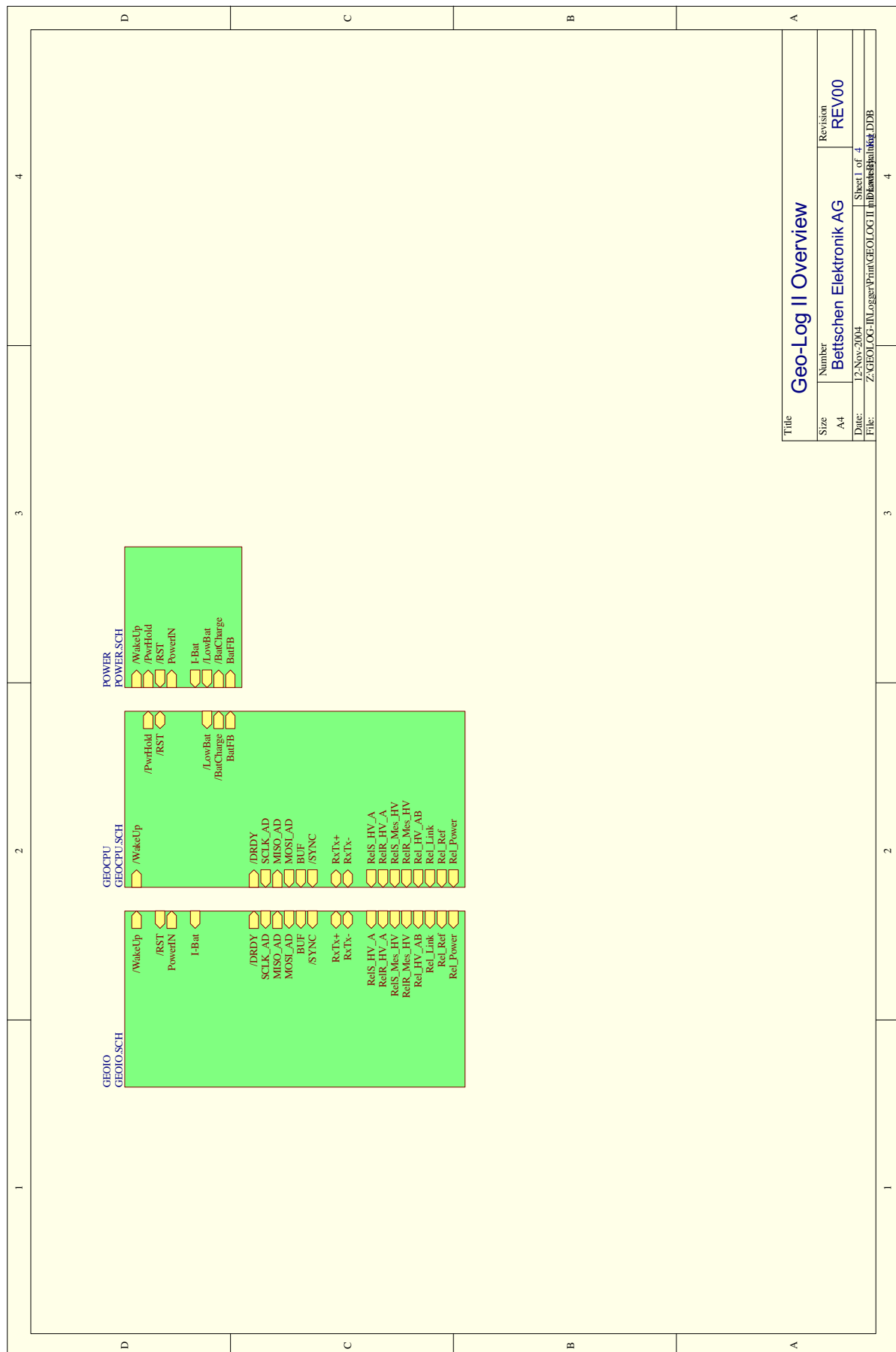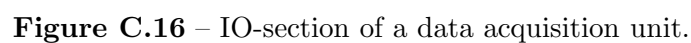
Figure C.14 – Circuit diagram of the interface-box. The interface-box contains the RS-232–to–RS-485 converter that connects the field notebook to the field data bus. Furthermore, it includes a DAU to sample the injected source waveform.

Figure C.15 – Connection scheme of a data acquisition unit (DAU).

Figure C.16 – IO-section of a data acquisition unit.
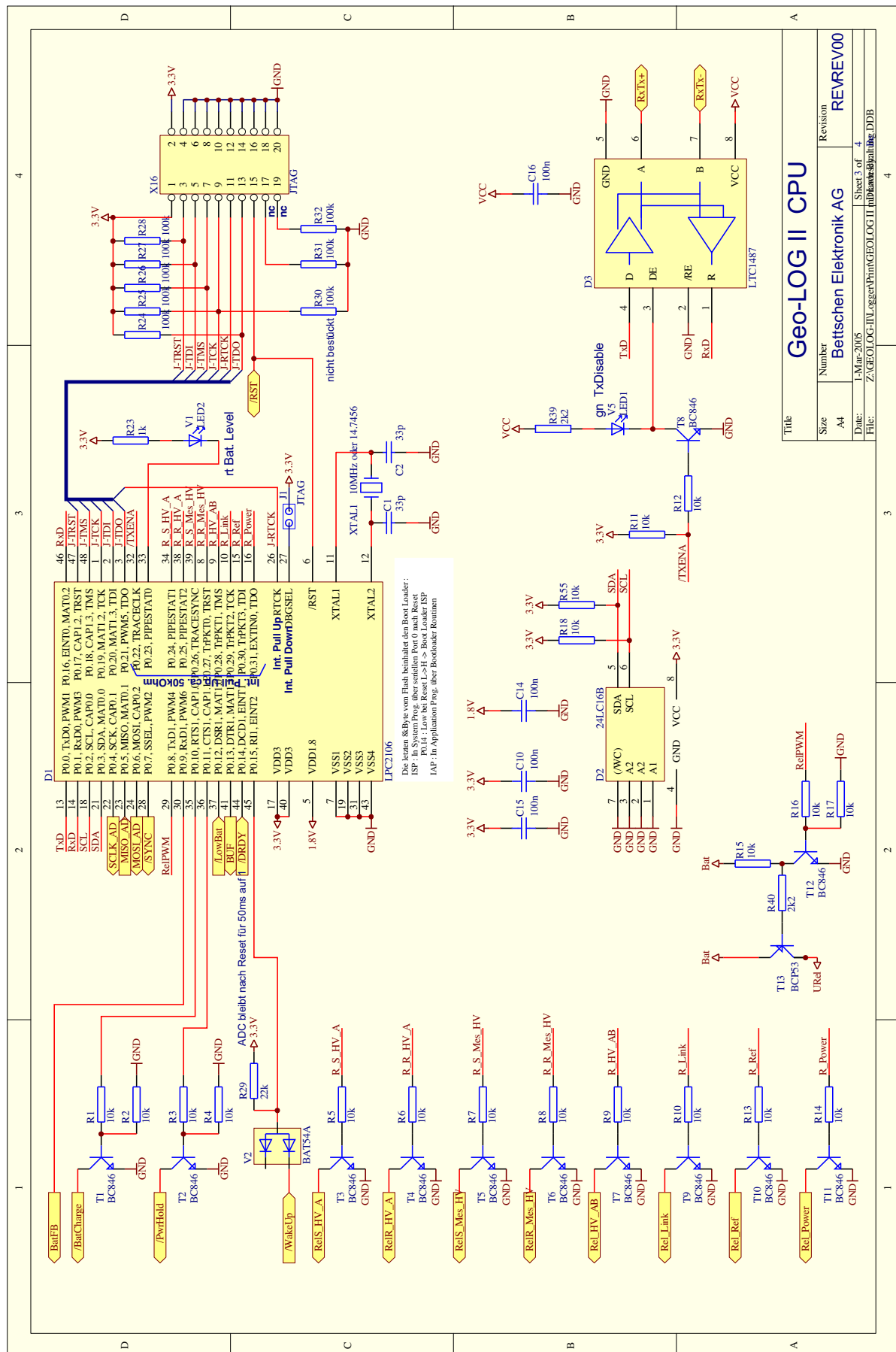
Figure C.17 – Digital section of a data acquisition unit comprising CPU, RAM, clock signal generator, and RS-485 interface.

Figure C.18 – Power section of a data acquisition unit comprising precision voltage reference, automatic battery charging circuit and input switch matix.
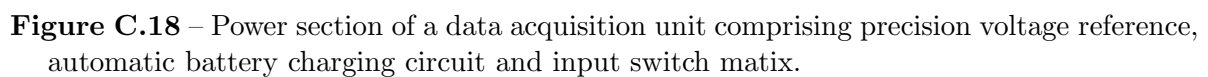
Bibliography

Ainsworth, M. and Oden, J. (1997). A posteriori error estimation in finite element analysis. *Computer Methods in Applied Mechanics and Engineering*, **142**, 1–88.

Akeret, F. (2003). Experimental design in der geoelektrik mit multielektroden systemen. *Diplomarbeit ETH*.

Anderson, B., Bryant, I., Lülig, M., Spies, B., and Helbig, K. (1994). Oilfield anisotropy: Its origins and electrical characteristics. *Oilfield Rev.*, **6**(4), 48–56.

Astley, R. J., Macaulay, G. J., Coyette, J. P., and Cremers, L. (1998a). Three-dimensional wave-envelope elements of variable order for acoustic radiation and scattering. part i. formulation in the frequency domain. *Journal Of The Acoustical Society Of America*, **103**(1), 49–63.

Astley, R. J., Coyette, J. P., and Cremers, L. (1998b). Three-dimensional wave-envelope elements of variable order for acoustic radiation and scattering. Part II. Formulation in the time domain. *Journal Of The Acoustical Society Of America*, **103**(1), 64–72.

Barinka, A., Barsch, T., Charton, P., Cohen, A., Dahlke, S., Dahmen, W., and Urban, K. (2001). Adaptive wavelet schemes for elliptic problems implementation and numerical experiments. *Siam Journal On Scientific Computing*, **23**(3), 910–939.

Barker, R. (1979). Signal contribution sections and their use in resistivity studies. *Geophys. J. Internat.*, **59**(1), 123–129.

Barker, R. D. (1989). Depth of investigation of collinear symmetrical four-electrode arrays. *Geophysics*, **54**(8), 1031–1037.

Barth, N. and Wunsch, C. (1990). Oceanographic experimental design by simulated annealing. *J. Phys. Ocean.*, **20**(9), 1249–1263.

Bettes, P. (1987). A simple wave envelope example. *Commun. Appl. Numeri. Methods*, **3**, 77–80.

Binley, A., Daily, W., and Ramirez, A. (1997). Detecting leaks from environmental barriers using electrical current imaging. *Journal of Environmental and Engineering Geophysics*, **2**(1), 11–19.

Blome, M., Maurer, H., and Schmidt, K. (2009). Advances in three-dimensional geoelectric forward solver techniques. *Geophys. J. Int.*, **176**(1), 740–752.

Brebbia, C. A. (1978). *The Boundary Element Method for Engineers*. Pentech Press, London.

Broyden, C. (1972). *Numerical Methods for unconstrained optimizations*. Academic Press.

Buselli, G. and Lu, K. (2001). Groundwater contamination monitoring with multichannel electrical and electromagnetic methods. *J. Appl. Geophys.*, **48**(1), 11–23.

Butler, D., editor (2005). *Near Surface Geophysics*. Society Of Exploration Geophysicists.

Capiti, I. (2007). Multi-electrode system ETH-DCMES II. *diploma thesis, ETH Zürich, Switzerland*.

Cherkaeva, E. and Tripp, A. C. (1996). Optimal survey design using focused resistivity arrays. *IEEE Trans. Geosci. Remote Sensing*, **34**(2), 358–366.

Christensen, N. B. (1989). AC resistivity sounding. *First Break*, **7**(11), 447–452.

Coggon, J. H. (1971). Electromagnetic and electrical modeling by the finite element method. *Geophysics*, **36**(1), 132–155.

Cohen, A., Dahmen, W., and Devore, R. (2001). Adaptive wavelet methods for elliptic operator equations: Convergence rates. *Mathematics Of Computation*, **70**(233), 27–75.

Coscia, I., Marescot, L., Maurer, H., Greenhalgh, S., and Green, A. (2008). Experimental design for cross hole electrical resistivity tomography data sets. *EAGE Near- Surface Meeting, Cracow, Poland, September 2008*.

Curtis, A. (1999). Optimal experiment design: cross-borehole tomographic examples. *Geophys. J. Int.*, **136**(3), 637–650.

Dahlin, T. (1989). *The development of a cable system for vertical electrical sounding and a comparison of the Schlumberger and Offset Wenner methods*. Ph.D. thesis, Lund University.

Dahlin, T. and Loke, M. H. (1998). Resolution of 2d wenner resistivity imaging as assessed by numerical modelling. *J. Appl. Geophys.*, **38**, 237–249.

Dahlin, T. and Zhou, B. (2001). A numerical comparison of 2D resistivity imaging with eight electrode arrays. In *7th Meeting of the Environmental and Engineering Geophysical Society (European Section)*, pages 977–983. Environ. and Eng. Geophys. Soc., Euro. Section.

deGroot Hedlin, C. and Constable, S. (1990). Occam's inversion to generate smooth, two-dimensional models from magnetotelluric data. *Geophysics*, **55**(12), 1613–1624.

Dey, A. and Morrison, H. F. (1979a). Resistivity modeling for arbitrarily shaped three-dimensional structures. *Geophysics*, **44**(4), 753–780.

Dey, A. and Morrison, H. F. (1979b). Resistivity modelling for arbitrarily shaped two-dimensional structures. *Geophys. Prospect.*, **27**, 106–136.

Dieter, K., Paterson, N., and Grant, F. (1969). IP and resistivity type curves for three-dimensional bodies. *Geophysics*, **34**, 615–632.

Dongarra, J., Ducroz, J., Hammarling, S., and Duff, I. (1990). A set of level 3 basic linear algebra subprograms. *Acm T Math Software*, **16**(1), 1–17.

Dreyer, D. and von Estorff, O. (2003). Improved conditioning of infinite elements for exterior acoustics. *International Journal For Numerical Methods In Engineering*, **58**(6), 933–953.

Ellis, R. G. and Oldenburg, D. W. (1994). The pole-pole 3-d dc-resistivity inverse problem: a conjugate-gradient approach. *Geophys. J. Internat.*, **119**, 187–194.

Evjen, H. M. (1938). Depth factors and resolving power of electrical measurements. *Geophysics*, **3**, 78–95.

Farquharson, C. G. and Oldenburg, D. W. (2004). A comparison of automatic techniques for estimating the regularization parameter in non-linear inverse problems. *Geophys. J. Internat.*, **156**(3), 411–425.

Frauenfelder, P. and Lage, C. (2002). Concepts – an object-oriented software package for partial differential equations. *Mathematical Modelling and Numerical Analysis*, **36**(5), 937–951.

Frey, P., Borouchaki, H., and George, P. (1996). Delaunay tetrahedralization using an advancing-front approach. *5th International Meshing Roundtable*, pages 31–43.

Friedel, S. (1997). *Umweltgeophysik*, chapter Hochauflösende Geoelektrik - Geoelektrische Tomographie, pages 131–151. Ernst und Sohn, Berlin.

Friedel, S. (2000). *Über die Abbildungseigenschaften der geoelektrischen Impedanztomographie unter Berücksichtigung von endlicher Anzahl und endlicher Genauigkeit der Meßdaten.* Ph.D. thesis, Universität Leipzig, Shaker Verlag, Aachen.

Friedel, S. (2003). Resolution, stability and efficiency of resistivity tomography estimated from a generalized inverse approach. *Geophys. J. Internat.*, **53**(2), 305–316.

Furman, A., Ferré, T., and Warrick, A. (2004). Optimization of ERT surveys for monitoring transient hydrological events using perturbation sensitivity and genetic algorithms. *Vadose Zone J.*, **3**, 1230–1239.

Geselowitz, D. B. (1971). An application of electrocardiographic lead theory to impedance plethysmography. *IEEE Trans. Biomed. Eng.*, **BME-18**, 38–41.

Gish, O. and Rooney, W. (1925). Measurement of resistivity of large masses of undisturbed earth. *J. of Geoph. Research*, **30**(4), 161–188.

Gisser, D., Isaacson, D., and Newell, J. (1988). Theory and performance of an adaptive current tomography system. *Clin. Phys. Physiol. Meas.*, **9**(Suppl. A), 35–41.

Gosh, D. (1971). The application of linear filter theory to the direct interpretation of geoelectrical resistivity sounding measurements. *Geophys. Prospect.*, **19**, 192–217.

Green, A. G., Lanz, E., Maurer, H., and Boerner, D. E. (1999). A template for geophysical investigations of a small landfill. *The Leading Edge*, **18**(2), 248–254.

Greengard, L. and Rokhlin, V. (1987). A fast algorithm for particle simulations. *J. Comput. Phys.*, **73**(2), 325–348.

Greenhalgh, S., Zhou, B., Greenhalgh, M., Marescot, L., and Wiese, T. (2009). Explicit expressions for the frèchet derivatives in 3d anisotropic resistivity inversion. *Geophysics*, **74**, 31–43.

Griffiths, D. H. and Turnbull, J. (1985). A multi-electrode array for resistivity surveying. *First Break*, **3**(7), 16–20.

Griffiths, D. H., Turnbull, J., and Olayinka, A. I. (1990). Two-dimensional resistivity mapping with a computer controlled array. *First Break*, **8**(4), 121–129.

Günther, T. (2004). *Inversion methods and Resolution Analysis for the 2D/3D Reconstruction of Resistivity Structures from DC Measurements.* Ph.D. thesis, University of Mining and Technology, Freiberg, Germany.

Günther, T., Rücker, C., and Spitzer, K. (2006). Three-dimensional modelling and inversion of DC resistivity data incorporating topography - II. Inversion. *Geophys. J. Internat.*, **166**(2), 506–517.

Hackbusch, W. and Nowak, Z. (1989). On the fast matrix multiplication in the boundary element method by panel-clustering. *Numerische Mathematik*, **54**, 463–491.

Hallof, P. G. (1957). *On the interpretation of resistivity and induced polarization measurements*. Ph.D. thesis, MIT, Cambridge, Massachusetts, USA.

Herwanger, J. V., Pain, C. C., Binley, A., de Oliveira, C. R. E., and Worthington, M. H. (2004). Anisotropic resistivity tomography. *Geophys. J. Internat.*, **158**(2), 409–425.

Hestenes, M. S. (1952). Method of conjugate gradients for solving linear systems. *J. Res. Nat. Bur. Standards*, **49**, 409–436.

Hvozdara, M. and Kaikkonen, P. (1998). An integral equations solution of the forward d.c. geoelectric problem for a 3-d body of inhomogeneous conductivity buried in a halfspace. *J. Appl. Geophys.*, **39**, 95–107.

Isaacson, D. (1986). Distinguishability of conductivities by electric current computed tomography. *IEEE Trans. Med. Imag.*, **5**, 91–95.

Karypis, G. and Kumar, V. (1995). A fast and high quality multilevel scheme for partitioning irregular graphs. In *International Conference on Parallel Processing*, pages 113–122.

Keller, G. V. and Frischknecht, F. C. (1966). *Electrical methods in geophysical prospecting*. Pergamo Press Inc., Oxford.

Kemna, A. (2000). *Tomographic Inversion of Complex Resistivity: Theory and Application*. Ph.D. thesis, Ruhr Universität Bochum.

Kirk, B., Peterson, J., Stogner, R., and Carey, G. (2006). libmesh: a c++ library for parallel adaptive mesh refinement/coarsening simulations. *Engineering with Computers*, **22**, 237–254.

Kita, E. and Kamiya, N. (1995). Trefftz method: an overview. *Advances in Engineering Software*, **24**(1), 3–12.

Knödel, K., Krummel, H., and Lange, G. (1997). *Geophysik*. Springer-Verlag, Berlin.

Kost, A. (1994). *Numerische Methoden in der Berechnung elektromagnetischer Felder*. Springer-Verlag.

Kunetz, G. (1966). *Principles of Direct Current Resistivity Prospecting.* Gebrüder Borntraeger.

LaBrecque, D. J., Miletto, M., Daily, W., Ramirez, A., and Owen, E. (1996). The effects of noise on occam's inversion of resistivity tomography data. *Geophysics*, **61**(2), 538–548.

Lage, C. (1995). *Analyse, Entwurf und Implementation von Randelementmethoden.* Ph.D. thesis, Inst. f. Prakt. Math., Universitaet Kiel.

Langer, R. (1933). An inverse problem in differential equations. *American Society of Mathematics Journal*, **29**(2), 814–820.

Lanz, E., Jemmi, L., Müller, R., Green, A. G., Pugin, A., and Huggenberger, P. (1994). Integrated studies of Swiss waste disposal sites: Results from georadar and other geophysical surveys. In *5th Internat. Conf. on Ground Penetrating Radar (GPR 1994)*, pages 1261–1274.

Lanz, E., Pugin, A., Green, A. G., and Horstmeyer, H. (1996). Results of 2- and 3-d high-resolution seismic reflection surveying of surficial sediments. *Geophys. Res. Lett.*, **23**(5), 491–494.

Lanz, E., Maurer, H., and Green, A. G. (1998). Refraction tomography over a buried waste disposal site. *Geophysics*, **63**(4), 1414–1433.

Lanz, E., Boerner, D. E., Maurer, H., and Green, A. G. (1999). Landfill delineation and characterization using electrical, electromagnetic and magnetic methods. *J. Environ. Eng. Geophys.*, **3**(4), 185–196.

Lanz, E. B. (1998). *Integrated geophysical studies of a composite landfill and its surroundings.* Ph.D. thesis, Institute of Geophysics, Swiss Federal Institute of Technology, Zürich, Switzerland.

Lee, T. (1975). An integral equation and its solution for some two and three-dimensional problems in resistivity and induced polarization. *Geophysical Journal*, **42**, 81–95.

Lehmann, H. (1995). Potential representation by independent configurations on a multielectrode array. *Geophys. J. Internat.*, **120**(2), 331–338.

Li, Y. and Spitzer, K. (2002). Three-dimensional DC resistivity forward modelling using finite elements in comparison with finite-difference solutions. *Geophys. J. Internat.*, **151**(3), 924–934.

Li, Y. and Spitzer, K. (2005). Finite element resistivity modelling for three-dimensional structures with arbitrary anisotropy. *Physics of the Earth and Planetary Interiors*, **150**(1–3, special issue), 15–27.

Loke, M. H. and Barker, R. D. (1996a). Practical techniques for 3d resistivity surveys and data inversion. *Geophys. Prospect.*, **44**(3), 499–523.

Loke, M. H. and Barker, R. D. (1996b). Rapid least-squares inversion of apparent resistivity pseudosections by a quasi-newton method. *Geophys. Prospect.*, **44**, 131–152.

Lowry, T., Allen, M. B., and Shive, P. N. (1989). Singularity removal: A refinement of resistivity modeling techniques. *Geophysics*, **54**(6), 766–774.

Ma, Q. (2002). The boundary element method for 3-d DC resistivity modeling in layered earth. *Geophysics*, **67**(2), 610–617.

Maurer, H. and Boerner, D. E. (1998). Optimized and robust experimental design: a non–linear application to em sounding. *Geophys. J. Internat.*, **132**, 458–468.

Maurer, H. and Friedel, S. (2006). Outer-space sensitivities in geoelectrical tomography. *Geophysics*, **71**(3), G93–G96.

Maurer, H., Holliger, K., and Boerner, D. E. (1998). Stochastic regularization: Smoothness or similarity ? *Geophys. Res. Lett.*, **25**(15), 2889–2892.

Maurer, H., Boerner, D. E., and Curtis, A. (2000). Design strategies for electromagnetic geophysical surveys. *Inverse Problems*, **16**, 1097–1117.

Maurer, H., Greenhalgh, S., and Latzel, S. (2009). Frequency and spatial sampling strategies for crosshole seismic waveform spectral inversion experiments. *Geophysics*, **in press.**

Mayergoyz, I., Chari, M., and Konrad, A. (1983). Boundary galerkin's method for three-dimensional finite element electromagnetic field computation. *IEEE Transactions on Magnetics*, **19**(6), 2333–2336.

McGillivray, P. and Oldenburg, D. (1990). Methods for calculating fréchet derivatives and sensitivities for the non-linear inverse problem: A comparative study. *Geophys. Prospect.*, **38**(5), 499–524.

Mendonca, C. A. (2003). The face-current concept and its application to survey design in electrical exploration. *Geophysics*, **68**(3), 900–910.

Menke, W. (1984). Geophysical data analysis: Discrete inverse theory. *Academic Press, Orlando FL.*

Mufti, I. R. (1976). Finite-difference resistivity modeling for arbitrarily shaped two-dimensional structures. *Geophysics*, **41**(1), 62–78.

Nabighian, M. N. (1987). *Electromagnetic Methods in Applied Geophysics*, volume 1–3. Society of Exploration Geophysics.

Olayinka, A. I. and Yaramanci, U. (2000). Assessment of the reliability of 2d inversion of apparent resistivity data. *Geophys. Prospect.*, **48**, 293–316.

Oldenburg, D. W. and Li, Y. (1994). Inversion of induced polarization data. *Geophysics*, **59**(9), 1327–1341.

Oldenburg, D. W. and Li, Y. (1999). Estimating depth of investigation in DC resistivity and ip surveys. *Geophysics*, **64**(2), 403–416.

Olivar, A., de Lima, L., Hedison, K., and Porsani, J. (1995). Imaging industrial contaminant plumes with resistivity techniques. *J. Applied Geophys.*, **34**(2), 93–108.

Pain, C., Herwanger, J., Saunders, J., Worthington, M., and de Oliveira, C. R. E. (2003). Anisotropic resistivity inversion. *Inverse Problems*, **19**, 1081–1111.

Pain, C. C., Herwanger, J. V., Worthington, M. H., and Oliveira, C. R. E. d. (2002). Effective multidimensional resistivity inversion using finite-element techniques. *Geophys. J. Internat.*, **151**(3), 710–728.

Park, S. K. and Van, G. P. (1991). Inversion of pole-pole data for 3-d resistivity structure beneath arrays of electrodes. *Geophysics*, **56**(7), 951–960.

Patera, A. (1984). A spectral element method for fluid dynamics – laminar flow in a channel expansion. *Journal of Computational Physics*, **54**, 468–488.

Pelton, W. H., Rijo, L., and Swift, C. M. (1978). Inversion of two-dimensional resistivity and induced-polarization data. *Geophysics*, **43**(4), 788–803.

Pridmore, D. F., Hohmann, G. W., Ward, S. H., and Sill, W. R. (1981). An investigation of finite-element modeling for electrical and electromagnetic data in three dimensions. *Geophysics*, **46**(7), 1009–1024.

Robinson, E. S. and Coruh, C. (1988). *Basic exploration geophysics.* John Wiley & Sons Ltd.

Roy, A. (1972). Depth of investigation in Wenner, three-electrode and dipole-dipole DC resistivity methods. *Geophys. Prospect.*, **20**, 329–340.

Roy, A. (1978). A theorem for direct current regimes and some of its consequences. *Geophys. Prospect.*, **26**, 442–463.

Roy, A. and Apparao, A. (1971). Depth of investigation in direct current methods. *Geophysics*, **36**(5), 943–959.

Rubin, Y. and Hubbard, S. (2005). *Hydrogeophysics*. Springer Dordrecht, Berlin.

Rücker, C., Günther, T., and Spitzer, K. (2006). Three-dimensional modelling and inversion of DC resistivity data incorporating topography - I. Modelling. *Geophys. J. Internat.*, **166**, 495–505.

Sasaki, Y. (1994). 3-d resistivity inversion using the finite-element method. *Geophysics*, **59**(12), 1839–1848.

Sauter, S. and Schwab, C. (2004). *Randelementmethoden*. Teubner.

Schenk, O., Gartner, K., Fichtner, W., and Stricker, A. (2001). Pardiso: a high-performance serial and parallel sparse linear solver in semiconductor device simulation. *Future Generation Computer Systems*, **18**(1), 69–78.

Schenk, O., Röllin, S., and Hagemann, M. (2003). Recent advances in sparse linear solver technology for semiconductor device simulation matrices. In *Proceedings of the 2003 International Conference on Simulations of Semiconductor Processes and Devices*, pages 103–108.

Schleifer, N. (2002). Anwendung der spektralen induzierten polarisation in der archäologischen prospektion. *Dissertation, Fachbereich Geowissenschaten/Geographie, Johan Wolfgang Goethe Universität, Frankfurt am Main*, pages 31–53.

Schlumberger, C. (1920). *Étude sur la Prospection Électrique du Sous-sol*. Gultier-Villars et Cie, Paris.

Schwarz, H. and Waldvogel, J. (2004). *Numerische Mathematik (5. Auflage)*. Teubner Verlag.

Shewchuk, J. R. (1996). Triangle: Engineering a 2D Quality Mesh Generator and Delaunay Triangulator. In M. C. Lin and D. Manocha, editors, *Applied Computational Geometry: Towards Geometric Engineering*, volume 1148 of *Lecture Notes in Computer Science*, pages 203–222. Springer-Verlag.

Si, H. and Gaertner, K. (2005). Meshing piecewise linear complexes by constrained delaunay tetrahedralization. *Proceedings of the 14th International Meshing Roundtable*, pages 147–163.

Slater, L. and Reeve, A. (2002). Investigating peatland stratigraphy and hydrogeology using integrated electrical geophysics. *Geophysics*, **76**(2), 365–378.

Smith, N. and Vozoff, K. (1984). Two-dimensional DC resistivity inversion for dipole-dipole data. *IEEE Transctions on Geoscience and Remote Sensing*, **GE-22**(1), 21–28.

Spitzer, K. (1995). A 3-d finite-difference algorithm for DC resistivity modelling using conjugate gradient methods. *Geophys. J. Internat.*, **123**(3), 903–914.

Spitzer, K. (1998). The three-dimensional DC sensitivity for surface and subsurface sources. *Geophys. J. Internat.*, **134**, 736–746.

Stefanescu, S., Schlumberger, C., and Schlumberger, M. (1930). Sur la distribution électrique potentielle autour d'une prise de terre ponctuelle dans un terrain à couches horizontales, homogènes et isotropes. *J. Phys. Radium*, **1**(4), 132–140.

Stummer, P. (2003). New developments in electrical resistivity imaging. *Diss. ETH, No. 15034, Zürich, Switzerland.*

Stummer, P., Maurer, H., Horstmeyer, H., and Green, A. (2002). Optimization of DC resistivity data acquisition: real-time experimental design and a new multielectrode system. *IEEE Transactions on Geoscience and Remote Sensing*, **40**(12), 2727–2735.

Stummer, P., Maurer, H., and Green, A. (2004). Experimental design: Electrical resistivity data sets that provide optimum subsurface information. *Geophysics*, **69**(1), 120–139.

Tarantola, A. (1987). *Inverse Problem Theory*. Elsevier.

Tripp, A. C., Hohmann, G. W., and Swift, C. M. (1984). Two-dimensional resistivity inversion. *Geophysics*, **49**(10), 1708–1717.

Van, G., Park, S., and Hamilton, P. (1991). Monitoring leaks from storage ponds using resistivity methods. *Geophysics*, **56**(8), 1267–1270.

Wang, T., Fang, S., and Mezzatesta, A. (2000). Three-dimensional finite-difference resistivity modeling using an upgridding method. *Geoscience and Remote Sensing, IEEE Transactions on*, **38**(4), 1544–1550.

Ward, S. H. (1990). *Geotechnical and Environmental Geophysics*, chapter Resistivity and Induced Polarization Methods, pages 147–189. Investigations in Geophysics No. 5. Soc. Expl. Geophys.

Weller, A., Seichter, M., and Kampke, A. (1996). Induced-polarization modelling using complex electrical conductivities. *Geophys. J. Internat.*, **127**(2), 387–398.

Weller, A., Brune, S., Hennig, T., and Kansy, A. (2000). Spectral induced polarisation at a medieval smelting site. In *Proceedings of the 6th Meeting Environmental and Engineering Geophysics (EEGS-ES)*, volume 11, Bochum, Germany.

Wilkinson, P. B., Meldrum, P. I., Chambers, J. E., Kuras, O., and Ogilvy, R. D. (2006). Improved strategies for the automatic selection of optimized sets of electrical resistivity tomography measurement configurations. *Geophys. J. Internat.*, **167**(3), 1119–1126.

Xu, B. and Noel, M. (1993). On the completeness of data sets with multielectrode systems for electrical resistivity surveys. *Geophys. Prospect.*, **41**, 791–801.

Xu, S.-Z., Zhao, S., and Ni, Y. (1998). A boundary element method for 2-d DC resistivity modeling with a point current source. *Geophysics*, **63**(2), 399–404.

Yaramanci, U. (2000). Geoelectric exploration and monitoring in rock salt for the safety assessment of underground waste disposal sites. *J. Appl. Geophys.*, **44**(2-3), 181–196.

Yilmaz, O. (2001). *Seismic data processing*. Society of Exploration Geophysicists.

Yokoi, T. and Senchez-Sesma, J. (1998). A hybrid calculation technique of the indirect boundary element method and the analytical solutions for three-dimensional problems of topography. *Geophys. J. Int.*, **133**(1), 121–139.

Zhang, J., Mackie, R. L., and Madden, T. R. (1995). 3-d resistivity forward modeling and inversion using conjugate gradients. *Geophysics*, **60**(5), 1313–1325.

Zhao, S. and Yedlin, M. J. (1996). Some refinements on the finite-difference method for 3-d DC resistivity modeling. *Geophysics*, **61**(5), 1301–1307.

Zhe, J., Greenhalgh, S., and Marescot, L. (2007). Multichannel full waveform and flexible electrode combination resistivity imaging system. *Geophysics*, **72**, 57–64.

Zhody, A. A. R., Anderson, L. A., and Muffler, L. J. P. (1973). Resistivity, self-potential, and induced-polarization surveys of a vapor-dominated geothermal system. *Geophysics*, **38**(6), 1130–1144.

Zhou, B. and Dahlin, T. (2003). Properties and effects of measurement errors on 2d resistivity imaging surveying. *Near Surface Geophysics*, **1**(3), 105–117.

Zhou, B. and Greenhalgh, S. A. (1999). Explicit expressions and numerical calculations for the frechet and second derivatives in 2.5d helmholtz equation inversion. *Geophys. Prospect.*, **47**(4), 443–468.

Zhou, B. and Greenhalgh, S. A. (2001). Finite element three-dimensional direct current resistivity modelling: accuracy and efficiency considerations. *Geophys. J. Internat.*, **145**(3), 679–688.

Zhou, B. and Greenhalgh, S. A. (2002). Rapid 2-d/3-d crosshole resistivity imaging using the analytic sensitivity function. *Geophysics*, **67**(3), 755–765.

Zhou, B., Greenhalgh, M., S, and Greenhalgh (2009). 2.5-d/3-d resistivity modelling in anisotropic media using gaussian quadrature grids. *Geophys. J. Internat.*, **176**(1), 63–80.

Zienkiewicz (1977). *The finite element method*. McGraw Hill, London.

Acknowledgments

Without the support, contributions and personal encouragement of many people inside and outside the ETH, this PhD thesis would never have been finished. I am greatly thankful for all the help I received during the scientific and personal expedition I undertook that eventually (finally!) resulted into this thesis.

Foremost, I would like to express my gratitude to my supervisors Prof. Hansruedi Maurer and Prof. Alan Green for offering me this challenging research topic. Without the great research group that Alan Green established here at the ETH and without his constant, inspiring scientific (not to mention the administrative) support to the whole group, none of the work I did would have been possible. I am especially thankful to Hansruedi for continuously providing great ideas, for believing in my abilities to finish this project and for always being patient with me (which, I guess, sometimes wasn't too easy). Due to his vast knowledge and his amazing ability to improvise he always had an alternative solution at hand when I got stuck somewhere. Without the extra effort he undertook during the last stage of my PhD, I would not have been able to meet my final deadline.

I am particularly grateful to Prof. Stewart Greenhalgh, who, even before he joined the thesis committee, contributed to the quality of my work with fruitful discussions and by thoroughly reading and considerably improving my manuscripts. I always enjoyed discussing my work with him due to his in-depth knowledge about anything related to geophysics and due to his respectful and humble way of addressing my research. Furthermore, I would like to thank Prof. Andreas Weller for kindly serving as an external examiner for my thesis.

During the course of my PhD project I had the chance to work together with many great people. I would especially like to thank Prof. Christoph Schwab for helpful advice on the boundary element method and Thomas Günther for helpful discussions on meshing and finite element techniques. I greatly acknowledge the effort Thomas Günther and Carsten Rücker undertake to provide the geoelectric community with their inspiring open-source inversion packages. Special thanks go to Dr. Olaf Schenk for extending his direct matrix solver *Pardiso* for my research. A big thanks goes to Kersten Schmidt for closely working with me on the multipole boundary element method and to the Seminar of Applied Mathematics for providing their *Concepts* class library.